Mathematical Modelling and Computational Simulation Studies of Flagellate Motility

Benjamin J. Walker

Wadham College

University of Oxford

A thesis submitted for the degree of

DPhil in Mathematics

Trinity 2021

Acknowledgements

I would like to thank my supervisor Eamonn Gaffney for his invaluable and unwavering support. His insight, guidance, questionable working hours, and curiosity have made this experience singularly enjoyable, for which I am unspeakably grateful. I am also most thankful for my collaborators and friends, Kenta Ishimoto and Richard Wheeler, without whom I would have missed out on so much science and so much fun.

Thank you also to my friends and family, particularly my parents Sally and Jeremy and my partner Sophia, for being beside me throughout.

Contents

Abstract

In this thesis, we explore different topics in the broad field of microscale swimming, focussing on microswimmers that propel themselves via slender appendages known as flagella. There is a wealth of biological examples, including helically driven bacteria, such as *E. coli*, and the well known and well studied human spermatozoon. Commensurate with this variety of examples from which microswimmer study draws inspiration and motivation, potential applications of developed understanding of this microscale world are also broad, spanning industry and medicine, particularly with the recent advent of synthetic microswimmers.

Driven by open questions in both biology and the theory of swimming at low Reynolds number, we investigate the behaviours of two flagellated organisms, one canonical and one lesser studied, in a range of computationally simulated microenvironments, from confined to multiswimmer settings. We form approximate dynamical systems for each of these model scenarios, averaging over the relatively short period of the flagellar beat, enabling thorough analysis of the dynamics via the resulting phase planes. Fundamental to these studies is knowledge of the motion of the flagellum, which we seek out from experimental data for the swimmer *Leishmania mexicana*, though we later relax this assumption of kinematic knowledge and move to consider the so-called elastohydrodynamic problem, in which fluid dynamics and elasticity can reshape the flagellar beat. We look towards realising systematic improvements to the accuracy of modern elastohydrodynamic techniques and, further, significantly broaden the scope of recent efficient methodologies to address the three-dimensional motion of slender elastic bodies in viscous fluid.

Chapter 1

Introduction

1.1 The swimming problem

Ubiquitous across nature, the flagellum is canonically a long slender organelle and is known to perform a variety of functional roles in a wide range of organisms, similar in form to the related cilium. Conserved across most eukaryotic flagella is the iconic '9+2' axoneme [1], a cytoskeletal structure formed of a central pair of singlet microtubules surrounded by nine microtubule doublets that is present along the length of the flagellum beyond the basal body. Shown in Figure 1.1(a) is a schematic depicting the cross-section of an axoneme, where the outer microtubule doublets are universally numbered by their position relative to the central pair. Repeated movement of the outer microtubules relative to one-another, driven by the action of molecular motors, can give rise to flagellar beating, utilised by a plethora of organisms to provide motility at the microscale. Perhaps the best-known example of a flagellated microswimmer is the human spermatozoon, with its single beating flagellum providing motility in the female reproductive tract (see Figure 1.1(b)). Well studied both experimentally and theoretically, further examples include the biflagellate *Chlamydomonas* [2–6], the family of parasitic organisms *Trypanosomatidae* [7–11], and the wider class of spermatozoa [12–15], the latter in particular exhibiting diverse external morphology across organisms [16].

The motility of flagellates is often vital for the success of the organism. For instance, the motile trypanosomes are typically required to perform a series of directed migrations in their insect vectors to achieve delivery to their host species, in some cases the host species being humans [7]. In mammals, a loss of motility amongst spermatozoa inhibits successful navigation of the female reproductive tract, established *in vitro* by Wallach et al. [17] and Coetzee et al. [18] and of great pertinence to

the large research area that is human fertility medicine. Owing to the wide-reaching importance of motility and the range of complex microenvironments in which flagellates occur *in vivo*, there has been extensive experimental and theoretical study into the behaviours of flagellated microswimmers in confined geometries and non-trivial background fluid flows, both of which we will later consider in more detail.

The theoretical study of microswimmers is typically performed by analysis and solution of the Stokes equations, the low-Reynolds-number limit of the Navier-Stokes equations for a Newtonian fluid. The assumption of a Newtonian fluid medium is common in the study of microswimmers, despite the rheological details of some *in vivo* media being complex and highly non-linear, or simply unknown. For example, the human spermatozoon repeatedly transitions between Newtonian and viscoelastic media in the female reproductive tract, whilst the precise rheology of the sandfly-vector midgut environment inhabited by the trypanosome *Leishmania* during its life cycle remains unknown. There has been detailed study of viscoelastic media in reference to microscale swimming, with an early analysis for an undulating sheet presented by Chaudhury [19], whilst Fulford et al. [20] considered a beating filament. Further, owing to the biological relevance and prevalence of viscoelastic fluids, there have been numerous recent works on the topic, ranging from studies of swimming efficiency to an investigation into collective behaviours [21–30]. However, in what follows, we will assume that any fluid medium under consideration is Newtonian, following a significant body of microswimmer study that is itself rich in biological application and theory [31], with many open questions remaining.

We state the familiar three-dimensional (3D) Stokes equations for an incompressible Newtonian fluid in a domain Ω with smooth boundary $\partial\Omega$ as

$$\mu\nabla^2\boldsymbol{u} = \nabla p\,, \quad \nabla\cdot\boldsymbol{u} = 0\,, \tag{1.1}$$

where we write $\boldsymbol{u}$ for the fluid velocity measured in the inertial laboratory frame, p for the associated pressure, and μ for the dynamic viscosity of the fluid. As mentioned previously, these linear equations result from the vanishing-Reynolds-number limit of the Navier-Stokes equations, where here we define the Reynolds number as $Re = \rho UL/\mu$ for a typical flow speed U, characteristic lengthscale L, and density ρ. The Reynolds number represents the ratio between inertial and viscous effects, with a low Reynolds number corresponding to small-scale, slow-moving, or highly viscous flows. The study of a particular microswimmer often gives rise to natural choices of velocity and lengthscale. For the human spermatozoon, appropriate scales are $U = 35\,\mu\mathrm{m\,s^{-1}}$ and $L = 60\,\mu\mathrm{m}$, corresponding to a typical swimming speed and cell length [34, 35],

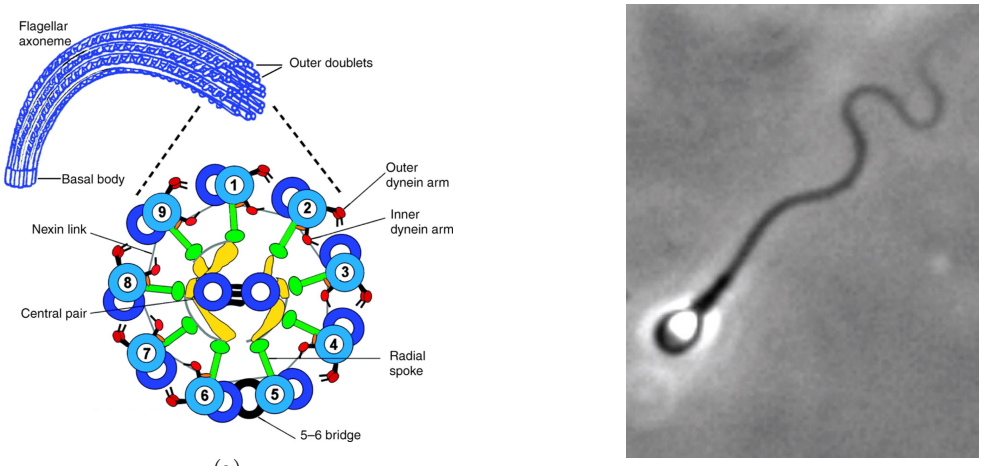

(a) (b)

Figure 1.1: (a) A schematic cross-section of the flagellum, composed of nine outer microtubule doublets arranged around a central pair. This cross-section looks down the flagellum from base to tip. Reproduced from Lindemann and Lesich [32] with permission. (b) An example micrograph of a flagellated organism, the human spermatozoon, captured in a high viscosity medium in which it achieves motility via actuation of its single flagellum. Reproduced from Gaffney et al. [33] with permission.

yielding a Reynolds number on the order of 10^{-3} in the case of a watery medium with $\rho/\mu \sim 1 \times 10^6\,\mathrm{s\,m^{-2}}$, thus demonstrating the applicability of the Stokes equations in modelling this flagellate's swimming behaviour. Whilst it may be convenient to take the advective timescale L/U, flagellar beating is often periodic, with there commonly being a natural choice of timescale given by their beat frequency f. Analogously to the Reynolds number, we define the frequency Reynolds number as $Re_f = \rho f L^2/\mu$, representing the importance of the inertial term $\partial_t \boldsymbol{u}$ in the Navier-Stokes equations in relation to the viscous terms. For the case of the human spermatozoon described above, with a beat frequency of around 15 Hz in a watery medium [36], the frequency Reynolds number is on the order of 10^{-2}, sufficiently small to justify the neglect of the non-steady term in the Navier-Stokes equations when modelling flagellate motility. Of note, inertial effects can have a significant relative effect in the far-field, as in Oseen's approximation for the motion of a sphere [37], but the small magnitude of such flows entails that they are often neglected.

The typical condition prescribed in the far-field for Stokes flow in an unbounded region is that the fluid velocity due to any disturbance decays to zero at spatial infinity, and we will see that the fundamental solutions to the Stokes equations in free space satisfy this condition. When additional boundaries are introduced to the fluid domain, the far-field condition applies away from them, with the boundaries having appropriate accompanying conditions, such as the common no-slip condition.

In the swimming problem, it is often assumed that the time-evolving configuration of a swimmer in a swimmer-fixed reference frame is known, for instance, from digital videomicroscopy, allowing us to prescribe kinematic no-slip boundary conditions at the swimmer surface [31]. Under this assumption, the swimming problem may be formulated in terms of the *a priori* unknown linear and angular velocities $\boldsymbol{U}$ and $\boldsymbol{\Omega}$ of the swimmer, given in the laboratory frame and with angular velocity measured relative to a point in the swimmer-fixed frame, noting that zero Reynolds number entails that this need not be the swimmer centre of mass. The latter observation arises from consideration of the angular momentum of the swimmer, wherein the rate of change of angular momentum is dependent on the choice of reference point only via linear momentum, with this contribution vanishing in the limit of zero Reynolds number. We will focus initially on the solution of the Stokes equations given these kinematic boundary conditions and prescribed boundary motion, though we will later consider in detail the more complex case of an elastohydrodynamic coupling between flagellum and fluid.

Now with the two additional vector unknowns $\boldsymbol{U}$ and $\boldsymbol{\Omega}$, in order to close the system we require two additional vector constraints, which are force and torque-free conditions upon the swimmer, appropriate in the inertialess regime of the Stokes equations and equivalent to the zero-Reynolds-number limit of Newton's Second Law. Stated explicitly in terms of the total force $\boldsymbol{F}$ and torque $\boldsymbol{L}$ exerted on a swimmer by the fluid, they are

$$\boldsymbol{F} + \boldsymbol{F}_{\text{ext}} = \boldsymbol{0}\,, \quad \boldsymbol{L} + \boldsymbol{L}_{\text{ext}} = \boldsymbol{0}\,, \tag{1.2}$$

where $\boldsymbol{F}_{\text{ext}}$ and $\boldsymbol{L}_{\text{ext}}$ are external applied forces and torques. We will in general consider $\boldsymbol{F}_{\text{ext}} = \boldsymbol{L}_{\text{ext}} = 0$, with the microswimmers in theoretical study typically assumed to be neutrally buoyant, as evidenced for sperm by Winet et al. [38], for example. However, gyrotactic effects, arising from gravitational torques, are known to be pertinent to the study of some microorganisms, especially flagellated algae [39].

1.2 Solution of the Stokes equations

When solving the Stokes equations, it should be first noted that the formulation is not explicitly dependent on time, with solutions for flow velocity and pressure being reliant on only the instantaneous configuration of the domain and boundary conditions. With time therefore only a parameter in the flow problem, this leads to a natural time-marching procedure for the solution of the swimming problem: at each instant, the instantaneous swimming velocities $\boldsymbol{U}$ and $\boldsymbol{\Omega}$ are found given the known

domain geometry and boundary conditions, then the positions of any swimmers or otherwise-evolving boundaries are stepped forwards in time. There is a broad and well known range of existing solvers for the positional ordinary differential equations, with a typical methodology in the study of microswimmers being that of Heun's scheme [40]. Thus, we will instead focus on solution methods for the instantaneous flow problem that are particular to the Stokes equations.

In order to determine the desired swimming velocities at each instant, it is necessary to solve the full swimming problem, including seeking the flow solution. The Stokes equations admit well known fundamental solutions to their singularly forced equivalent,

$$\mu\nabla^2\boldsymbol{u} = \nabla p - \delta(\boldsymbol{x}-\boldsymbol{x}_0)\hat{\boldsymbol{F}}\,, \tag{1.3}$$

where a point force $\hat{\boldsymbol{F}}$ has been introduced to the fluid at $\boldsymbol{x}_0$. The solution for the fluid velocity in this singularly forced case is given explicitly by the Oseen tensor $\mathbb{J}$ as

$$\boldsymbol{u}(\boldsymbol{x}) = \hat{\mathbf{F}}\cdot\mathbb{J}(\boldsymbol{x}-\boldsymbol{x}_0)\,, \quad \mathbb{J}(\boldsymbol{r}) \coloneqq \frac{1}{8\pi\mu}\left(\frac{\mathbf{I}}{\|\boldsymbol{r}\|}+\frac{\boldsymbol{r}\boldsymbol{r}}{\|\boldsymbol{r}\|^3}\right), \tag{1.4}$$

with the above fundamental solution being termed the Stokeslet [41], referred to also as the free-space velocity Greens function. The $O\left(1/\left\|\boldsymbol{x}-\boldsymbol{x}_0\right\|\right)$ behaviour exhibited by the Stokeslet as $\boldsymbol{x}\to\infty$ is characteristic of solutions to the Stokes equations, with fluid disturbances decaying to zero in the far-field. Taking derivatives of the Stokeslet with respect to $\boldsymbol{x}_0$ gives rise to additional fundamental solutions of the Stokes equations, for example the stresslet and the rotlet, which, by linearity, may be used to construct solutions to the original equations via so-called singularity methods [42]. Analogous to the Greens functions of Laplace's equation, modified Greens functions satisfying certain flow boundary conditions may be constructed for particular geometries, with the singularly forced Stokes flow problem in a half space giving rise to the so-called Blakelet when $\boldsymbol{u}=0$ on a plane boundary [43]. Similar expressions exist for periodic flows [44, 45], as well as for flows in the exterior of a rigid sphere and other simple geometries [46]. However, in the study of microswimmers, the relevant fluid domain Ω is often more complex, in general being taken to be the exterior of any swimmers in combination with any additional boundaries. The flagellated swimming problem is one such case, with the flagellum constituting a geometrically complex moving boundary whose actuation may be coupled to the surrounding fluid.

Hence, whilst there are circumstances that readily admit analytic solutions of the Stokes equations, such as those of the canonical Stokes drag calculation for a sphere moving in a viscous fluid [47], the complex geometries involved in posing

the flagellated swimming problem in general inhibit analytic progress. Thus, there has been significant work towards the development of approximate and numerical schemes for efficient and accurate solution of the swimming problem, and there now exist numerous methods for obtaining approximate solutions to the equations and constraints that govern microscale swimming.

1.2.1 Resistive force theory

The simplest, but least accurate, solution procedure utilises *resistive force theory* (RFT), first presented by Hancock in the publications of 1953 and 1955 [13, 41], and in common use due to its simplicity. Resistive force theory applied to flagella offers a leading-order solution for the fluid velocity on the surface of the flagellum that is linear in the applied force at that point, with errors logarithmic in the aspect ratio of the flagellum when away from the flagellum ends [48]. Explicitly, far from any boundaries and decomposing the centreline velocity of the flagellum into components $\boldsymbol{U}_t$ and $\boldsymbol{U}_n$, respectively tangential and normal to the flagellum centreline, for constants η and ξ we have the linear relationship

$$\boldsymbol{U}_t = \eta \boldsymbol{f}_t, \quad \boldsymbol{U}_n = \xi \boldsymbol{f}_n \,, \tag{1.5}$$

where the local force density applied to the fluid by the flagellum $\boldsymbol{f}$ has been decomposed into tangential and normal components $\boldsymbol{f}_t$ and $\boldsymbol{f}_n$. The constants ξ and η proposed by Gray and Hancock [13] are related at leading order by $\eta/\xi = 2$, representing the drag anisotropy associated with slender bodies, with the constants given as

$$\eta = \frac{\log(2/\epsilon) - 0.5}{2\pi\mu}, \quad \xi = \frac{\log(2/\epsilon) - 0.5}{4\pi\mu}, \tag{1.6}$$

for flagellum aspect ratio ϵ. The values of these coefficients and their ratio, dependent on the aspect ratio and geometry of the slender body, are correct in the limit of a vanishingly thin flagellum [49] and were later refined by Lighthill [50], though resistive force coefficients with a ratio of two remain in use [51]. In application to the swimming problem, resistive force theory may be used to give the total forces and torques acting on a swimmer due to the prescribed motion of one or more flagella in terms of the flagellar beat pattern and the swimming velocities $\boldsymbol{U}$ and $\boldsymbol{\Omega}$. These are computed as integrals along the centreline of the flagellum, following application of Newton's Third Law. When coupled with the force and torque-free conditions of Equation (1.2), the instantaneous swimming velocities may then be determined simply, though typically only to an accuracy of $\log(1/\epsilon)$ [52].

A significant drawback of RFT is that it is a purely local theory, with it failing to take into account the effects of proximity to fluid boundaries or indeed to the non-local distribution of forces, and therefore is sometimes referred to as local drag theory [31]. Owing to its local nature, its accuracy is limited when it is applied to bodies in close proximity to one another or to boundaries, or in application to individual flagella that exhibit high curvatures. Refinements to resistive force theory have been considered to account for fluid boundaries, as reviewed and expanded upon by Brennen and Winet [53], evaluated by Ramia et al. [54] and Walker et al. [55], and with the additional recent work of Man et al. [56] providing a correction for nearby low-amplitude flagella.

1.2.2 Slender-body theory

Tailored to the study of flagella-like morphologies, *slender-body theory* (SBT) can be thought of as a significant non-local refinement of resistive force theory, with the leading-order SBT solution corresponding to RFT, and was proposed initially in the mid 1970s then built upon by Johnson and others [49, 52, 57–59]. In slender-body theory, the slenderness of a flagellum or filament is exploited to approximate the surrounding fluid motion as an integral over the body's centreline, with solution via SBT then proceeding by computing the unknown force density that forms part of the integrand, typically discretised along the centreline to yield a system of linear equations. For force density $\boldsymbol{f}$ distributed along the centreline, the integral expressions for the fluid velocity $\boldsymbol{u}$ at a point $\boldsymbol{x}_0$ as given by a variety of slender-body theories have the general succinct form

$$\boldsymbol{u}(\boldsymbol{x}_0) = \int \boldsymbol{K}(\boldsymbol{x}_0, \boldsymbol{x}) \boldsymbol{f}(s) \, \mathrm{d}s \,, \tag{1.7}$$

where the centreline location $\boldsymbol{x} = \boldsymbol{x}(s)$ is a function of the flagellum arclength parameter s and $\boldsymbol{K}$ is a particular choice of integral kernel, with which an appropriate range of integration is associated. A common and perhaps minimal ansatz of this form takes $\boldsymbol{K}$ to be the Oseen tensor of Equation (1.4), explicitly setting $\boldsymbol{K}(\boldsymbol{x}_0, \boldsymbol{x}) = \mathbb{J}(\boldsymbol{x} - \boldsymbol{x}_0)$. This yields the integral equation

$$\boldsymbol{u}(\boldsymbol{x}_0) = \frac{1}{8\pi\mu} \int \left(\frac{\mathbf{I}}{|\boldsymbol{x} - \boldsymbol{x}_0|} + \frac{(\boldsymbol{x} - \boldsymbol{x}_0)(\boldsymbol{x} - \boldsymbol{x}_0)}{|\boldsymbol{x} - \boldsymbol{x}_0|^3} \right) \cdot \boldsymbol{f}(s) \, \mathrm{d}s \,, \tag{1.8}$$

with integration being performed over the entire length of the filament.

Though superior to resistive force theory in that it captures non-local hydrodynamics, slender-body theory formulated as above necessitates the evaluation of a

singular line integral when $\boldsymbol{x}_0$ lies on the centreline, posing significant numerical challenge. Indeed, the ansatz must be posed with care in this case, with refined arguments such as the matched asymptotic expansions of Keller and Rubinow [58] and Johnson [52] required. Numerous works have modified the simple formulation above to achieve a numerically viable solution method that includes the self interaction of flagella, with significant recent examples being the modification of the integral kernel by Tornberg and Shelley [60] and Shelley and Ueda [61]. Due to its overall simplicity and typical algebraic accuracy [52], SBT has seen widespread use in modern low-Reynolds-number hydrodynamics, from studies of filament sedimentation to spermatozoon swimming stability, in the latter case being used in a hybrid scheme with another method of solution, the boundary element method [12, 40, 60, 62–65].

1.2.3 Boundary element method

Considered the most computationally intensive but accurate method of solution, the boundary element method (BEM), first used numerically by Youngren and Acrivos [66] and later comprehensively implemented by Pozrikidis [67], recasts Stokes equations into integral equations over the boundary of the domain $\partial\Omega$. Following the formulation of Pozrikidis via the Lorentz reciprocal relation, the solution for the flow velocity $\boldsymbol{u}$ at a point $\boldsymbol{x}_0$ in the interior of the fluid domain is given by

$$\begin{aligned} u_j(\boldsymbol{x}_0) = &- \frac{1}{8\pi\mu} \int\limits_{\partial\Omega} G_{ij}(\boldsymbol{x}, \boldsymbol{x}_0) f_i(\boldsymbol{x}) \, \mathrm{d}S(\boldsymbol{x}) \\ &+ \frac{1}{8\pi} \int\limits_{\partial\Omega} u_i(\boldsymbol{x}) T_{ijk}(\boldsymbol{x}, \boldsymbol{x}_0) n_k(\boldsymbol{x}) \, \mathrm{d}S(\boldsymbol{x}) \,, \end{aligned} \tag{1.9}$$

where $i, j, k \in \{1, 2, 3\}$, f_i are the components of surface traction, and $\boldsymbol{n}$ is the surface normal directed into the fluid. Here, the integral kernels G_{ij} and T_{ijk} are velocity and stress Greens functions of Stokes flow, defined in terms of the solutions of the singularly forced Stokes equations (1.3) as

$$u_i(\boldsymbol{x}) = \frac{1}{8\pi\mu} G_{ij}(\boldsymbol{x}, \boldsymbol{x}_0) \hat{F}_j \,, \quad \sigma_{ik}(\boldsymbol{x}) = \frac{1}{8\pi} T_{ijk}(\boldsymbol{x}, \boldsymbol{x}_0) \hat{F}_j \,, \tag{1.10}$$

where σ denotes the Cauchy stress tensor. As an example, one may choose the free-space Greens functions, whereby $G_{ij}(\boldsymbol{x}, \boldsymbol{x}_0)$ is simply a scalar multiple of the Oseen tensor $\mathbb{J}(\boldsymbol{x} - \boldsymbol{x}_0)$ as defined in Equation (1.4), though in general more complex Greens function such as the aforementioned Blakelet may be used. Given the expression (1.9) for the flow velocity $\boldsymbol{u}$ at any point in the domain and in our case of prescribed boundary motion, BEM solution schemes attempt to find the unknown surface traction on

the swimmer surface. This is typically achieved by considering a discretisation of the modified equation

$$\begin{aligned} u_j(\boldsymbol{x}^\star) = &- \frac{1}{4\pi\mu} \int_{\partial\Omega} G_{ij}(\boldsymbol{x}, \boldsymbol{x}^\star) f_i(\boldsymbol{x}) \, \mathrm{d}S(\boldsymbol{x}) \\ &+ \frac{1}{4\pi} \overset{PV}{\int_{\partial\Omega}} u_i(\boldsymbol{x}) T_{ijk}(\boldsymbol{x}, \boldsymbol{x}^\star) n_k(\boldsymbol{x}) \, \mathrm{d}S(\boldsymbol{x}) \,, \end{aligned} \tag{1.11}$$

where $\int^{PV}$ denotes a Cauchy principal value integral in the second summand. This modified equation explicitly relates the fluid velocity at a point $\boldsymbol{x}^\star$ on the boundary of the domain to the boundary tractions. These integrals are weakly singular, with considerable care being required to evaluate them numerically. However, some computational difficulty can be avoided given particular additional conditions, as one of the surface integrals in Equations (1.9) and (1.11) may be removed analytically. For example, for bodies with zero net force and torque, the first integral, known as the single layer potential, can be eliminated as in Pozrikidis [45, 67] to reduce the equation to one with only a single surface integral, which in this case is known as the double layer formulation of the boundary integral equations.

Since the boundary integral equations for Stokes flow as presented are exact, the accuracy of boundary element methods is determined by the accuracy of the discretisation and machine precision, in comparison to the inherent loss of accuracy introduced in the formulation of slender-body theory and resistive force theory. This accuracy comes at the cost of needing to solve a large dense linear system to determine the boundary tractions, though notably only the boundary of the domain must be discretised. It is, however, this discretisation that is a major drawback of the BEM compared to other methods, requiring non-trivial consideration to appropriately represent the time-evolving $\partial\Omega$ by a small number of simple surface elements. There is freedom in the choice of surface elements used, with three-node linear triangles and six-node quadratic triangles being the simplest elements in common use, though only the latter of the two allows for local curvature to be captured in the discretisation [67]. The full extent of the dependence of the solution on the properties of the surface discretisation remains to be explored, with numerically established convergence typically being used to ascertain solution accuracy [40].

Given a surface discretisation, the unknown tractions are approximated by finite elements and the integrals on the mesh are computed via specialised quadrature rules [68]. Solution of the resulting linear system, which includes the unknown swimming velocities, is computationally challenging due to the size and density of the coefficient

matrix, in addition to the significant cost involved in approximating the singular integrals incurred when forming the system. Additionally, the gauge freedom in the pressure p must be handled systematically, with an example approach being to fix this freedom by enforcing that the normal boundary traction has a surface mean of zero, without loss of generality. Despite the computational cost of the boundary element method, its use is often preferable to less-accurate methods when capturing the geometry of a problem is thought to be of importance. Recent study has demonstrated that swimmer morphology can greatly affect even qualitative aspects of swimming behaviours [63] and, thus, boundary element methods are commonly applied to the swimming problem [28, 63, 69–73].

1.2.4 Singularity representations and regularised Stokeslets

Analytically tractable in comparison to the boundary element method, an alternative approach to the swimming problem is to consider microswimmers as collections of singular solutions to the Stokes equations. The most basic example is perhaps to represent a spherical swimmer as a single point force, giving the flow solution as that of the Stokeslet. However, as we have assumed torque and force-free conditions for swimming, the appropriate minimal singularity representation of a swimmer is a force dipole, or *stresslet*, corresponding to two opposing point forces being brought together. As mentioned previously in Section 1.2, an expression for the stresslet may be obtained by differentiating the fluid velocity solution of the Stokeslet with respect to the location of the point force, and the representation of a swimmer by a stresslet is known to inherently satisfy the force and torque-free conditions of swimming [45]. The characteristic flow field due to a stresslet is shown in Figure 1.2 beside that of a Stokeslet, where the far-field decay of the stresslet can be seen to be faster than that of the Stokeslet, corresponding to $O\left(1/\left\|\boldsymbol{x}-\boldsymbol{x}_0\right\|^2\right)$ behaviour of the stresslet away from the singularity.

Simple singularity representations of microswimmers can provide the leading order flow solution in the far field of the swimmer [31], and may additionally be used to examine the hydrodynamic interactions between multiple swimmers with computational ease, as was performed recently in the population-level analysis of Ishimoto and Gaffney [74]. However, it is clear that the modelling of a complex microswimmer by a small collection of singularities in general neglects the morphological details of the swimmer, previously noted to be significant in determining swimmer behaviour. A natural extension of this method is to introduce additional singularities distributed across the surface of the swimmer to better represent the geometry, reminiscent of

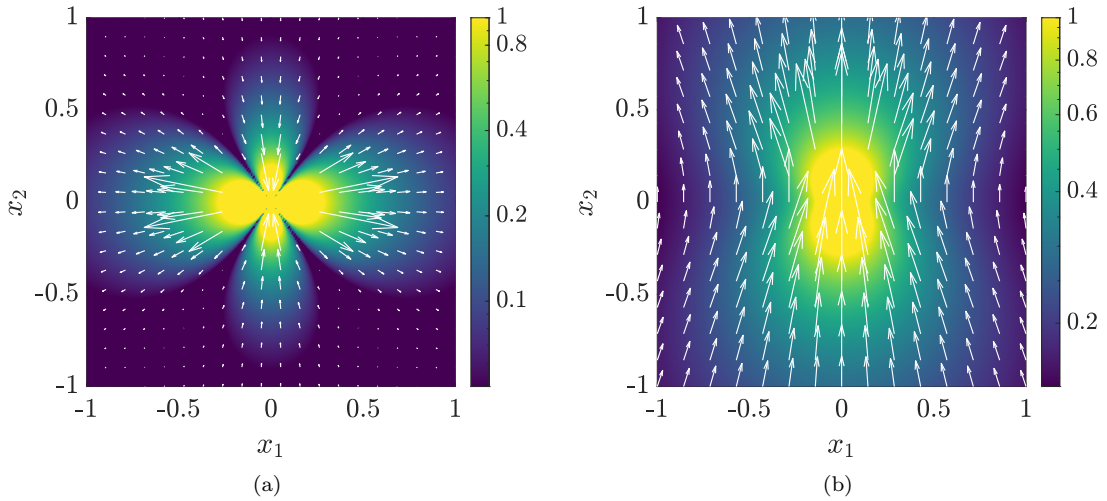

Figure 1.2: The characteristic flow fields corresponding to (a) the stresslet and (b) the Stokeslet, each with unit strength. The decay of the stresslet can be seen to be faster than that of the Stokeslet, corresponding to the $O\left(1/r\right)$ and $O\left(1/r^2\right)$ far-field behaviour of each singularity, respectively, with the flow magnitude indicated by colour (scaled logarithmically and individually for visual clarity). The flow field of the Stokeslet is not dissimilar from the classical solution of a rigid sphere moving in a viscous fluid. Here, r denotes the Cartesian distance from the origin. The displayed axes are of the laboratory frame, with the singularities located at the origin of this frame and directed along the labelled x_2 axis.

slender-body theory and the boundary integral formulation. However, this approach leads to expressions for the fluid velocity that become singular close to the boundary, which is both unphysical and computationally problematic.

First presented by Cortez in 2001, the method of regularised Stokeslets seeks to resolve this issue [75]. Whilst previous methods seek solutions to the singularly forced Stokes equations (1.3), Cortez instead considers the solution with a regularised forcing term, dependent on some small non-zero parameter ϵ and an example of which being $\phi_\epsilon(\boldsymbol{x}-\boldsymbol{x}_0)\hat{\boldsymbol{F}}$ for

$$\phi_\epsilon(\boldsymbol{r}) = \frac{15\epsilon^4}{8\pi(\|\boldsymbol{r}\|^2+\epsilon^2)^{\frac{7}{2}}}\,. \tag{1.12}$$

Given such a smoothed force, a solution analogous to the Stokeslet can be found, with the solution converging to the Stokeslet in the limit $\epsilon \to 0$. These regularised Stokeslets may then be used in place of singularities to represent applied forces, yielding a regular solution to the approximate fluid problem. The work of Cortez has since been significantly extended and applied to the study of microswimmers, seeing use in boundary element implementations [70], a construction analogous to the Blakelet having been found[1] [76], and with numerous applications to flagellate and filament

[1]The original publication of Ainley et al. [76] contains an error in the form of the regularised image system and a corrected version is presented by Smith [70].

motion [77–81]. This includes a regularised version of slender-body theory for the study of thin filaments, wherein the regularisation parameter ϵ is commonly assumed to be approximately equal to the radius of the flagellum, eliminating the problem of singular line integrals usually inherent to the methodology [82]. My recent work leveraged the freedom present in the choice of regularisation parameter to generate an algebraically accurate theory for slender bodies with a non-uniform cross-sectional radius [83], which we will later utilise and expand upon in Chapter 5.

1.3 Theory of microscale swimming

1.3.1 Seminal works and hydrodynamic classification

There exists a rich classical theory of swimming at low Reynolds number, stemming from the seminal work of Taylor in 1951 [84]. Taylor considered the motion of an infinite sheet induced by travelling waves of displacement, extending an initial analysis to include the interaction of a neighbouring sheet. The latter part of this study began the theoretical investigation into the phenomenon of flagellar and ciliary synchronisation, whereby nearby flagellated and ciliated swimmers are observed to beat in synchrony despite an initial phase difference [85, 86]. There has been significant work examining the complex hydrodynamics that govern the interaction of nearby filaments, investigated using a range of methodologies, from the approach of Taylor [87] to modern singularity and regularised Stokeslet methods [88–91]. Further theoretical work utilises asymptotic methods [92], in addition to a wealth of recent experimental evidence of flagellar synchronisation through hydrodynamic interactions [93–96].

Following Taylor's initial work, there has been significant development of a more general theory of microscale swimming, applied to a host of model swimmers not restricted to flagellates. Summarised in detail in the review of Lauga and Powers [31], swimmers may be classified hydrodynamically as *pushers* or *pullers* depending on their characteristic flow field[2]. Pullers achieve propulsion by drawing fluid inwards along their axis of motion before pushing it out perpendicular to their swimming direction. The canonical puller is *Chlamydomonas*, a biflagellated alga with a large spherical body that uses a breaststroke-like motion to swim, though numerous additional examples may be found in the parasitic family *Trypanosomatidae*. *Chlamydomonas* in particular has been the subject of extensive theoretical and experimental works [97, 98], though, in general, pusher swimmers are the better-studied of the two

[2]An additional category of swimmer, *neutral*, also exists, though they are less common in hydrodynamic studies. One such organism is the ciliate *Paramecium*.

classes. A significant body of research into pusher dynamics pertains to the mammalian spermatozoon, itself classified hydrodynamically as a pusher due to the net expulsion of fluid along its axis of motion [99–102]. This is broadly similar to the bacterium *Escherichia coli*, which utilises a rotating helical bundle of flagella to provide motility [103, 104]. A schematic of pusher and puller behaviour is reproduced from Lauga and Powers [31] in Figure 1.3, with idealised spermatozoa and *Chlamydomonas* shown as example pushers and pullers.

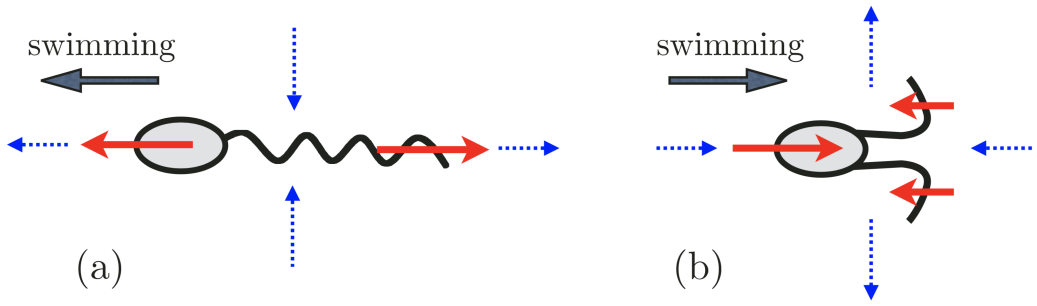

Figure 1.3: A schematic characterisation of (a) pushers and (b) pullers, with flow direction shown in blue and forces shown in red. Pushers draw fluid in from their sides and push it outwards along their axis of motion, whilst pullers perform the reverse action. Figure reproduced from Lauga and Powers [31] with permission.

Classification as a pusher or a puller may be quantified explicitly in terms of simple singularity representations of swimmers. Comparison of Figure 1.2a and Figure 1.3a suggests that the characteristic flow field of a pusher may be well represented by that of a stresslet, with the qualitative fluid behaviour appearing to be the same. The implications of such a simplistic singularity representation may be analytically explored, yielding simple descriptions of pairwise swimming behaviour, dynamics near boundaries, and far-field flow behaviours of collections of pusher swimmers. For example, the swimming of two nearby pushers may be seen directly to be mutually attractive and stabilising, tending towards a configuration with the swimmers parallel and beside each other [31]. There is an analogous singularity description of puller swimmers, corresponding simply to a reversal of the dipole direction and, hence, of the resulting flow field from that of pushers. Derived from this reversal of dynamics is a corresponding reversal of behaviour, with two nearby pullers orienting away from each other and swimming apart. This reversal of instantaneous swimming velocity and time-evolving behaviour highlights an important duality between the swimming behaviours of pushers and pullers.

This pusher-puller duality is additionally captured in the study of an important class of microswimmer models, *squirmers*. Squirmers are model microswimmers that

can induce fluid flow and motility by low-amplitude surface deformations or ciliary beating, typically taken to have approximately axisymmetric or spherical morphology [105, 106], and have been introduced as models of the ciliate *Paramecium* and colonies of the alga *Volvox carteri* [107, 108]. The fluid flows induced by squirmers are typically modelled as a tangential slip velocity on the swimmer surface, with the analytical solution found by an expansion in spherical harmonics, as performed in the recent work of Pak and Lauga [109]. The classical solutions of Blake [105] and Lighthill [106] yield a solution for the swimming velocity of a spherical squirmer that is proportional to a low-order coefficient of the expanded squirmer slip velocity, notably corresponding to the mode that characterises the swimmer as a pusher or a puller [78]. It is the sign of this coefficient that determines the classification of the swimmer; thus, the classification of a squirmer as either a pusher or a puller determines the sign of the swimming velocity, whereby each case may be thought of as the reversal of the other.

1.3.2 Time reversibility

This relationship between pusher and puller dynamics extends beyond simple singularity representations and idealised squirmer models, resultant of a simple property of the Stokes equations. We have already noted that the Stokes equations lack an explicit dependence on time, hence, by linearity, we can see that for any solution pair $(\boldsymbol{u}, p)$ the reversed flow given by $(-\boldsymbol{u}, -p)$ is also a solution of the governing equations, subject to a reversal of boundary conditions. In the context of the swimming problem, this reversal corresponds precisely to a reversal of swimming velocities and any boundary actuation or slip velocities. Thus, there is indeed a precise duality between the swimming of pushers and pullers, with the solution corresponding to a given pusher being exactly the time-reversal of the same swimmer but with puller characteristics.

This may be most easily thought of in the context of a monoflagellated swimmer such as the human spermatozoon, which typically beats its flagellum with a base-to-tip travelling wave of displacement. The spermatozoon is a pusher, with the tipward beating of its flagellum on average drawing in fluid from the sides and expelling it along the long axis of the flagellum, achieving propulsion 'head first'. The time-reversal of the spermatozoon therefore attains the opposite motion, achieving 'tail-first' movement via reversed actuation of the flagellum in the form of a tip-to-base travelling wave. Crucial for this reversibility property to apply is precise equality in morphology of the puller and pusher swimmers, in addition to the precise reversal of boundary conditions. When this holds, however, studying the behaviours of a

swimmer that may be a puller or a pusher depending on circumstance becomes much less complex, with detailed study of one case simply being the reversal of the other.

The duality of low-Reynolds-number swimming also leads to a significant result that is contrary to intuition gained from motion at higher Reynolds numbers. Presented by Purcell in print in 1977, the Scallop theorem demonstrates that attempting to swim via a time-reversible or reciprocal deformation of a cell, like that of the scallop with a single hinge, yields no net motion at zero Reynolds number for Newtonian fluids [110]. In the context of our flagellated example, the theorem states that the swimmer would undo its previous motion should it at some point precisely reverse its flagellar kinematics, a property of swimming in Stokes flow that is not present at higher Reynolds numbers. Further, this result is dependent only on the configurations in the swimmer-fixed reference frame, and notably not on the rate at which a swimmer changes between configurations, consistent with the interpretation of Stokes flows as being inertia free. The theorem again stems from time being merely a parameter in the swimming problem, and is a direct consequence of time-reversibility. The Scallop theorem implies that motion at zero Reynolds number must be achieved via non-reciprocal swimmer deformation, for example the aforementioned travelling-wave flagellar beating of spermatozoa or the breaststroke-like gait of *Chlamydomonas*. A non-reciprocal motion has even been demonstrated in the case of a simple model three-sphere swimmer, suggested as a possible simple scheme to be employed by artificial microswimmers [111].

1.3.3 Swimming near a boundary

Swimming at the microscale may rarely be considered to occur in free-space, with other swimmers and boundaries often playing a crucial role in an organism's function as well as impacting significantly on their dynamics. As an example, human spermatozoa are known to interact with the oviductal epithelium in the Fallopian tubes, with disrupted boundary interactions suggested by Suarez and Pacey to be associated with reductions in fertility [112]. The theoretical effects of boundaries have been well documented in many cases, there being studies of singularity swimmers, squirmers, and pushers near to boundaries [63, 69, 78, 103, 113]. Singularity representations of swimmers give rise to the prediction that pushers will align parallel to a no-slip infinite wall, providing their angle of attack is sufficiently shallow, and will additionally be attracted to the boundary. By time reversibility, or as can be seen directly from the singularity representations of Spagnolie and Lauga [78], puller swimmers undergo the opposite motion, orienting perpendicular to a wall and moving away from it.

However, singularity models of swimmers arise from consideration of far-field flows, whilst interactions with boundaries necessitate the consideration of near-field interactions that may not be captured by these representations. Indeed, we may not expect pusher and puller swimmers to behave as predicted by singularity models. This is evident even within the classes of pusher and puller, where fundamentally different behaviours are observed for the simplest swimmers, as illustrated by the contrast between a force-dipole puller, which deflects from boundaries [31], and the spherical puller squirmer, which swims stably near boundaries [113]. Thus, detailed examination of near-boundary dynamics is necessitated to fully capture the exhibited behaviour of a swimmer, additionally noted to be highly sensitive to swimmer morphology [114].

The rich boundary behaviours of swimmers more complex than simple squirmer or singularity models are not tractable in general via analytic methods, with the dynamics of flagellates being an example where there has instead been significant numerical study [40, 63, 69, 100, 104]. Much of this study has been directed towards pushers with long flagella relative to their bodies, the most notable example being spermatozoa. By the aforementioned time reversibility, we may additionally infer the behaviours of spermatozoa-like pullers from previous works, though we may not comment on the swimming of microorganisms with significantly different morphologies. Example such swimmers are the numerous large-bodied *Trypanosomatidae*, whose swimming behaviours are yet to be studied in detail and therefore represent a significant gap in current understanding. Hence, in Chapter 2, we will consider the dynamics of such a large-bodied puller in the presence of a solid no-slip boundary, circumstances thought to be of particular pertinence to the *Trypanosomatidae* life cycle.

1.3.4 Response to background flows

Microscale swimming may be intuited to be dominated by background flows, sweeping away any untethered bodies with the prevalent flow direction. However, it has been observed that many microswimmers utilise ambient flows as guidance cues, in some cases resulting in net motion upstream, contrary to the dominant background fluid direction and our accompanying intuition. A pertinent example of such a swimmer is the human spermatozoon, which, when placed in a background shear flow, has been observed to reorient in response to the flow when near to a planar boundary [115, 116]. This is in agreement with behaviours seen in high-accuracy boundary element simulations of model spermatozoa [99], with similar rheotactic behaviours being exhibited by the bacteria *Bacillus subtilis* and the canonical *Escherichia coli* [117, 118]. The work

of Molaei and Sheng, in particular, found that the tumbling of *E. coli* was promoted by the presence of a shear flow, apparently counteracting the previously observed suppression of bacterial tumbling resultant of the presence of a boundary [119]. This suggests an intricate interplay between the effects of confinement and background flows on swimming. Hence, the hydrodynamic response of small-scale motile organisms requires careful analysis of the interaction between swimmer and environment. As is the case with swimming behaviours in general, the dynamics of large-bodied flagellated swimmers in response to background flows remain unexplored. Thus, in Chapter 3, we will examine the responses of such monoflagellates to a particular but common and physically realisable background flow [14, 99, 115, 117].

Whilst many recent studies have predominantly considered the effects of both boundaries and non-trivial background flows on swimming at the microscale, a rich theory accompanies the dynamics of swimmers in bulk flow. The classical work of Jeffery [120] explored the effects of a background shearing flow on particle dynamics in the bulk, studying the motion of an ellipsoid. Exploiting the simple geometry of the particle, Jeffery solved the governing equations explicitly, yielding, in the most basic case, a formula for the period of rotation of the body, T, in terms of the shearing rate, γ, of the background flow and the aspect ratio of the ellipsoid, r. This well known relation may be stated simply as

$$T = \frac{2\pi}{\gamma}\left(r + \frac{1}{r}\right) \tag{1.13}$$

and highlights a linear relation between the period of rotation and the inverse of the shearing rate of the background flow. The existence of such a simple relation between the far-field fluid flow and the dynamics of this model particle suggests a possible simple representation of the motion of more-complex microswimmers, though it is *a priori* unclear as to the effects of interacting timescales and non-trivial geometries on the bulk behaviours of actively beating flagellated swimmers. Kantsler et al. [115] propose a similar but phenomenological linear relationship between swimming velocities and the background flow rate, potentially enabling efficient study of microswimmer populations and supplementing the descriptions of Pedley and Kessler [5] and Bearon and Grünbaum [121], though the validity of such a model is yet to be established. Hence, a further aim of Chapter 3 will be to explore in detail the dynamics of a sample microswimmer in the bulk when it is exposed to a shearing flow, attempting to ascertain the degree to which simple linear relationships between flow parameters and swimmer velocities capture the behaviours of flagellated microswimmers, at least *in silico*.

1.3.5 Interactions between swimmers

Whilst much work has considered the dynamics of isolated swimmers, microswimmers in nature are often found in company. As we noted above, Taylor's seminal work on microswimmers included a theoretical investigation of swimmer-swimmer interactions using infinite sheets as model flagella [84]. Such sheet models are still in use, for example the recent work of Olson and Fauci [89] that investigated the attraction and alignment of nearby sheets and filaments, which included flagellar elasticity and a study of synchronisation. A similar study of pairwise interactions represented spermatozoa by a collection of beads [122], finding that the two model swimmers can attract each other through swimmer-fluid interactions. In these latter two studies, however, with each of them approximating complex spermatozoan morphology via sheets or beads, it is unclear as to the extent to which their presented results are applicable to spermatozoa.

The interactions of swimmers with simpler morphologies have also been considered. A detailed investigation of the pairwise behaviours of spherical squirmers was performed by Ishikawa et al. [108], with reference to the genus of ciliated microorganisms *Opalina*. Their study exploited the linearity of the flow problem alongside the simplicity of the swimmer shape to describe in general the interactions between these two model microorganisms. This provided greater modelling fidelity than that of simple singularity models, which, as noted in Section 1.3.1, predict the mutual attraction of puller-type swimmers and repulsive behaviours in pushers. Refined models of swimmers may be required in order to capture the details of microscale swimming, as noted by Ishimoto and Gaffney [113] and Ishimoto [114] for the cases of boundary swimming and directed taxis, with the effects of cellular geometry unable to be *a priori* dismissed in generality.

With the human spermatozoon being a widely studied microorganism of obvious pertinence to human fertility medicine, often swimming in crowded microenvironments and typically possessing an intricate cellular morphology, high-accuracy exploration of its pairwise dynamics is both lacking and likely of pertinence to the theory of microscale swimming and a wider scientific community. Hence, the study of such a model organism will form the focus of Chapter 4 of this thesis, in which we aim to elucidate long-time behaviours of a swimming pair of model cells from a range of physically relevant initial configurations, building upon the objectives of Ishikawa et al. [108] though extended to flagellated swimmers.

Performing simulation on a larger scale though at reduced accuracy, recent works have attempted to model the collective behaviours of significant populations of microswimmers, ranging up to simulations of thousands of swimmers. Schoeller and Keaveny [123] utilise the force coupling method to simulate up to a thousand individual swimmers [124], each consisting of a flexible flagellum and an ellipsoidal head. Schoeller and Keaveny note that the full time-dependent flow fields of individual swimmers play a significant role in the dynamics, hence, care should be taken in capturing these flows. In parallel to the work of Schoeller and Keaveny, Ishimoto et al. [72] introduce the idea of representing the time-varying flow field around a swimmer via a number of regularised Stokeslets, in application to the human spermatozoon. Utilising principal component analysis to identify significant modes of the flow, Ishimoto et al. are able to capture approximately 90% of the cumulative variance of the flow field about its mean using only five modes, thereby enabling large-scale simulation of swimmers that retains a high degree of near-field fidelity. Such a study in two spatial dimensions was subsequently performed and reported in the work of Ishimoto and Gaffney [74], where clustering of spermatozoa was noted to occur and be dependent on the details of fluid viscoelasticity. However, the accuracy of this recent model in predicting the dynamics of nearby swimmers is yet to be investigated. Hence, as an additional objective of Chapter 4, we will attempt to ascertain the degree to which this simple scalable methodology is able to predict pairwise swimming interactions.

1.3.6 Beyond prescribed kinematics

Many studies of flagellate motion, including those that constitute the first research Chapters of this thesis, rely upon prior knowledge of flagellar kinematics. These kinematics are often the basis for idealised analytical study, or given as inputs to computational simulation frameworks, with a typical desired output being the path of a virtual swimmer, for instance. Whilst such results can be informative, revealing a hydrodynamic mechanism for the upstream rheotaxis of human spermatozoa [99], for example, they necessarily neglect the potentially complex fluid-structure interactions, termed *elastohydrodynamics*, that give rise to the flagellar gait. Whilst the neglect of such couplings might be thought to be motivated by sought simplicity, which indeed their absence can confer, it is often the result of a combination of two distinct but related issues: computational tractability and data availability.

The latter of these problems represents a fundamental barrier to the widespread elastohydrodynamic modelling of flagellated organisms. In posing the elastohydrodynamic problem for a flagellum driven by internal molecular motors, the prescription

of kinematic data is replaced by the specification of the mechanical action of these molecular motors. Whilst kinematic flagellar data may be acquired with relative ease for a host of organisms, owing to advances in videomicroscopy and subsequent image processing [125, 126], data relating to the activity and action of intraflagellar motors is not so readily available, requiring detailed and practically complex measurements of mechanical properties of the flagellum, for instance. Hence, with the required data lacking, the move to replace kinematic studies with elastohydrodynamic models has been hindered, though numerous idealised and hypothesised forms of molecular motor activity have nevertheless been proposed and studied [127–133]. The continuation of such efforts may eventually serve to solve or circumvent the data availability problem, opening up a wealth of future elastohydrodynamic studies of flagellated organisms, though progress in this area has been limited somewhat by the other issue of elastohydrodynamic enquiry, that of computational tractability.

Indeed, the coupled elastohydrodynamics of a slender filament in a viscous fluid are well known to be plagued by severe numerical stiffness, as noted in the recent and comprehensive review of du Roure et al. [134]. However, stemming from the transformative work of Moreau et al. [51], which we will later consider in detail, computational studies of the two-dimensional motions of planar filaments have been rendered tractable. Further, this work has already been extended by myself and others to include improved-accuracy hydrodynamics via slender-body theory [55, 135], with efforts beginning to address the problem of actively driven flagella [136]. Despite these augmentations of the original RFT-based approach of Moreau et al., there remains significant scope for improving upon the accuracy of the employed slender-body theories, with these approaches providing little guarantee of the satisfaction of the hydrodynamic no-slip condition that is routinely applied on the surface of an object in flow, for instance. Hence, as the primary aim of Chapter 5, we will seek to utilise the recent and flexible regularised slender-body theory of Walker et al. [83] to produce a framework for two-dimensional elastohydrodynamic study that affords justified hydrodynamic accuracy.

Each of these approaches, however, is limited to filament motion in two dimensions. Whilst there are examples of flagella that beat in a largely planar manner, such as those of *Leishmania mexicana* [137], the inability to simulate the motion of filaments in three dimensions significantly restricts the applicability of these elastohydrodynamic methodologies, with the complex three-dimensional beating observed in spermatozoa unable to be considered, for instance. Thus, in the final research Chapter of this thesis, we will aim to generalise the approach of Moreau et al. [51]

to three spatial dimensions, seeking to enable the consideration of filament elastohydrodynamics in much greater generality than has previously been computationally tractable.

1.4 Thesis summary

In summary, this thesis will seek to consider a number of open problems related to various aspects of flagellate motility and its study, from examining the swimming behaviours of particular model flagellated organisms to the generation of new techniques and methodologies used for investigating the fluid-structure interactions of filaments. Chapter 2 will aim to explore the motion of the parasitic organism *Leishmania mexicana*, a large-bodied puller-type microswimmer that is significantly distinct from previously studied organisms. We will begin by presenting a novel methodology for the automated identification of flagella from videomicroscopy data, enabling the subsequent large-scale analysis of flagellar kinematics that elucidates the form of the *Leishmania* beat. Utilising the resulting kinematic description of the beat of these flagellates, we will extensively consider its swimming behaviours in the proximity of boundaries via a reduction of the dynamics to an approximate plane autonomous system, simulating swimmer motion using the boundary element method. In doing so, we identify a mechanism of boundary approach unseen in smaller-bodied swimmers, which we hypothesise to be of pertinence to the *Leishmania* life cycle and the biological setting in which they may be found.

In Chapter 3, we will continue our study of puller-type swimmers, considering in this case the effects of a candidate background flow on the swimming behaviours of model flagellates with *Leishmania*-like morphology. By first examining a swimmer in an unbounded domain, we will compare the exhibited periodic rotational motion of the flagellate with the Jeffery's orbits of passive ellipsoidal particles, and note remarkable agreement. Maintained across a range of background flow rates, this agreement suggests an approach for the approximation of swimmer motion in such experimentally realisable flows, the theoretical utility of which we will additionally aim to demonstrate. Having explored both background flows and confined geometries individually, in the remainder of Chapter 3, we will consider these circumstances in combination, documenting the predicted behaviours of our idealised swimmer and proposing a methodology for the dynamic switching of long-time behaviours of swimmers *in vitro*.

With microswimmers often being present in multiplicity, in Chapter 4, we will aim to report on the hydrodynamic interactions of a pair of synchronised model spermatozoa, making use of a bespoke high-accuracy boundary element computational framework as in Chapters 2 and 3. Considering the swimming pair from a range of initial conditions, we will reduce their pairwise dynamics to a two-dimensional autonomous system in their relative separation and orientation, validating such an approximation and using it to predict long-time dynamics of the flagellates. We will seek to compare our predictions against previous theoretical and experimental studies, commenting on the importance of high-accuracy methodologies for the detailed quantification of the dynamics of nearby swimmers. In the latter portion of Chapter 4, we will additionally present a comparison of our predictions against the recently introduced technique of Ishimoto and Gaffney [74], which represents a flagellated swimmer by a small number of time-varying regularised Stokeslets.

Having considered model swimmers with prescribed beating patterns, in the remainder of this thesis we will focus instead on the topic of filament elastohydrodynamics. In Chapter 5, we will aim to improve upon the hydrodynamic accuracy of recent two-dimensional methodologies, incorporating a recent regularised slender-body theory of non-uniform filaments [83]. This will necessitate the development of a semi-analytic framework, in which we will analytically compute slender-body integrals along portions of the filament to accelerate computation. We will also rigorously quantify the discretisation and approximation errors incurred throughout, yielding a justified computational foundation for accurate two-dimensional elastohydrodynamic study. In Chapter 6, we will then lift similar recent ideas in elastohydrodynamics to three spatial dimensions, removing the planar restriction that accompanies contemporary efficient methods to enable study of a wide range of elastohydrodynamic settings. Making use of a simple resistive force theory, we will encounter and circumvent issues of singular parameterisation in three dimensions, resulting in an efficient framework for filament simulation that reduces computational demands by several orders of magnitude over similar approaches.

We will conclude this thesis with a discussion of the presented material in the broader context of flagellate motility, summarising the key contributions of this work and touching upon directions for future study.

Chapter 2

The boundary behaviours of *Leishmania mexicana*

In this Chapter, as a first investigation into microscale swimming, we will introduce and consider a model monoflagellated organism, *Leishmania mexicana*. Determining its flagellar kinematics from videomicroscopy, we will then enquire into its swimming dynamics in the presence of an infinite no-slip boundary, utilising boundary element computations and methods of dimensionality reduction to investigate behaviours that may be pertinent to the life cycle of this human parasite. The content of this Chapter has been published in the Journal of Theoretical Biology and Scientific Reports (Walker et al. [125, 138]).

2.1 Introduction and motivation

The unicellular parasitic eukaryotes of the family Trypanosomatidae are the cause of many major human diseases, including African trypanosomiasis and New World leishmaniasis [139]. Those of the genus *Leishmania*, transmitted to humans by the bite of a sandfly, affect around four million individuals globally [140]. A prominent cause of cutaneous leishmaniasis in the Americas, *L. mexicana* are a popular focus of recent research, owing to their complete development cycle being observable *in vitro* [141]. In the highly motile promastigote stage of their life cycle, a stage defined by morphology and as shown in Figure 2.1, they utilise a single flagellum for locomotion, protruding from their anterior cell body and predominantly beating with a tip-to-base planar wave, the latter being common to all trypanosomatidae [10, 142–146]. Their viability in the sandfly-vector midgut is thought to depend upon their ability to navigate effectively [147], with it being widely accepted that their survival in this low-Reynolds-number environment is reliant upon attachment to the nearby epithelium

during one stage of their life cycle [148, 149]. In fact, the precise driving mechanism of the tip-first boundary approach of *Leishmania* promastigotes remains unknown, and is hypothesised by Bates [149] to simply be a consequence of their flagellum-first swimming direction. However, the effects of potential hydrodynamic factors remain to be considered in detail. Contrastingly, in many *Leishmania*-sandfly pairings, the mechanism of epithelial binding has been well explored, having been evidenced to be dependent upon the major *Leishmania* surface glycoconjugate, *lipophosphoglycan* (LPG) [150–154]. Following a developmental process termed metacyclogenesis, and an accompanying change in LPG, the epithelial binding is reversed, resulting in the detachment of the promastigote from the midgut surface [151]. Hence, we will seek to examine the mechanics of *Leishmania* upon approach to, and movement away from, a boundary. In doing so, we will aim to consider how the cell may control its location in the sandfly midgut, in its need to both approach and leave the gut epithelium at different stages of its life cycle. Seeking to employ a kinematic model of the swimmer, this will necessitate the quantification of kinematic flagellar data from digital videomicroscopy of swimming *Leishmania mexicana*, with the details of the beat pattern currently unknown.

A direct consequence of locomotion via tip-to-base flagellar beating, *Leishmania* spp.[1] are hydrodynamically classified as *pullers*, achieving propulsion by drawing fluid along the length of the flagellum before then pushing out the fluid at the sides, similar to the mechanism caricatured in Figure 1.3. In Section 1.3.3, we noted that dynamics even within the classes of pusher and puller are sensitive to the resolution of the modelling of swimmers. Hence, refined models of cellular swimmers are required to elucidate their boundary dynamics, as illustrated by the rich boundary behaviours observed for flagellate pushers, such as *E. coli*, mammalian spermatozoa, and the biflagellate puller *Chlamydomonas* in recent extensive work [40, 97, 99–104]. However, corresponding studies of monoflagellated pullers, either observational or simulation-based, are comparatively lacking and, hence, there is extensive scope for the investigation of the boundary behaviours of a flagellated puller such as *L. mexicana*.

In particular, additional to their differing hydrodynamic classification, *Leishmania* promastigotes are also morphologically distinct from the better-studied pusher monoflagellates. Accumulation behaviours are reported to be sensitive to variations in swimmer morphology [114], whilst appeal to time-reversal symmetry to infer puller behaviour from pusher behaviour requires the same cellular morphology. Hence, due

[1] *Leishmania* spp. here means species of *Leishmania*, a catch-all phrase for all species.

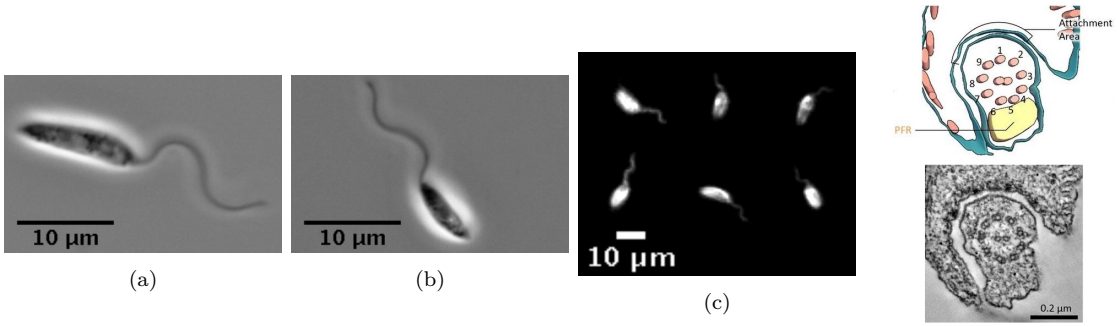

(a) (b) (c) (d)

Figure 2.1: Sample frames from *L. mexicana* promastigote videomicroscopy, between two coverslips (a),(b), and in the bulk, as presented in montage form for (c). We observe that the lengthscales of the body and flagellum are approximately equal, with the cell body being approximately ellipsoidal in shape. Flagellar beating can be seen to be both sinusoidal and planar in character, in both a confined environment and in the bulk. (d) The ultrastructure of *Leishmania mexicana* showing an accessory flagellar structure, the paraflagellar rod (PFR), which can be seen here alongside the axoneme and is present along the length of the flagellum. Reproduced from Wheeler et al. [155] with permission. Sample videomicroscopy is from Dr Richard Wheeler's laboratory, reproduced with permission.

to its distinct morphology, *Leishmania* swimming behaviour cannot be inferred from previous studies of swimmers, with the lengthscales of the flagellum and cell body being approximately equal, each on the order of 10 µm (see Figure 2.1). In contrast, for a typical human spermatozoon this ratio approaches one-tenth, with the spermatozoon cell body being substantially shorter than the attached flagellum [34, 156].

The smaller cell body of such spermatozoa also enables the use of approximate analytic techniques, such as resistive force theory, in studying their motility [49]. As touched upon earlier in Section 1.2.1, this has been implemented classically for the spermatozoa of the sea urchin *Psammechinus* by Gray and Hancock [13], where hydrodynamic interactions between the two cell components are either neglected or treated simplistically. Given the comparable scales of the cell body and flagellum in *Leishmania*, such an approach is inappropriate [49], with methods treating the flagellum and cell body comparably being more natural, and indeed, accurate. Thus, a full and high-accuracy numerical study is necessitated to fully capture the hydrodynamics and resulting behaviours of *Leishmania*.

Hence, in this Chapter, we will detail the digital extraction and analysis of the flagellar waveform of *Leishmania mexicana* in a typical growth medium. Having sought a low-dimensional expansion of the observed kinematics via standard Fourier analysis [157, 158], we will use a high-accuracy boundary element computational framework to perform a number of *in silico* experiments [67], our primary objective being to document the complex long-term behaviour of a virtual promastigote in the presence

of a planar boundary. Further, we will use beat-averaged phase planes to classify and quantify behaviours in the near and far-field of a boundary, drawing simulation-based behavioural comparisons with classical pushers such as the human spermatozoon. Our final objective of this Chapter will then be to examine the hypothesis that hydrodynamic interaction is sufficient for eliciting the noted tip-first boundary approach of *L. mexicana* promastigotes and, additionally, that repulsive boundary interactions drive the separation of promastigotes from a boundary.

2.2 Methods

Before we begin to explore the swimming behaviours of *Leishmania mexicana*, we will first summarise the methods used and the techniques applied. In this Chapter, we will largely make use of existing hydrodynamic techniques and approaches. As such, we will only briefly outline the standard methods used, whilst describing novel or non-standard approaches in detail.

2.2.1 Determining flagellar kinematics

This section very briefly summarises methods developed for extracting flagellar kinematics from videomicroscopy, detailed in Walker et al. [125].

Flagellar kinematics were extracted via novel automated analysis in the ImageJ macro language from imaging data captured by Dr Richard Wheeler, with details on image capture given in Appendix 2.A. Data was preprocessed into a binary mask via standard techniques, yielding a representation akin to that shown in Figure 2.2(b). From this mask, the flagellum was identified as a region of consistent observable width, despite the presence of an accessory structure supplementing the flagellum known as the paraflagellar rod (see Figure 2.1(d)). The width of the binary representation of the swimmer is computed using the medial axis transform, encoding the width along the cell midline and defined in more detail in Appendix 2.B. A simple analysis of the distribution of the transform values yields the flagellum as the region corresponding to the modal value, a heuristic that proves to be sufficient to adequately and automatically segment the flagellum from the 126-cell dataset of approximately 150,000 frames. Indeed, due to the conserved morphology of flagella across eukaryotic organisms, this method is expected to be applicable to a wide range of flagellates, having recently been applied to bovine spermatozoa [159], for instance.

The results of the image analysis were given relative to a cell-fixed reference frame with coordinates $\boldsymbol{x} = (x_1, x_2, x_3)$. This frame is defined as having x_1 directed along

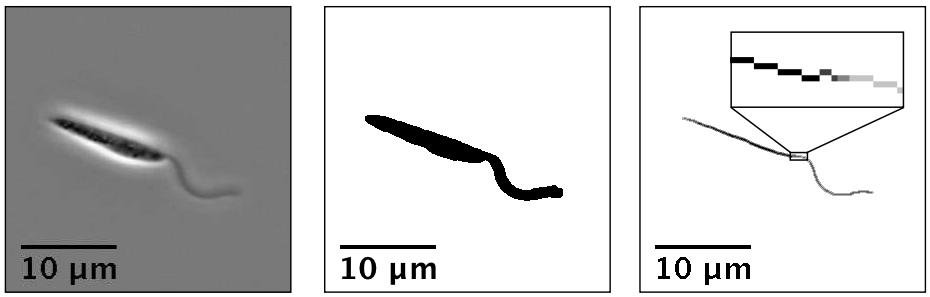

Figure 2.2: A sample frame taken from phase contrast videomicroscopy of a *L. mexicana* promastigote. (a) Original frame. Despite the presence of an accessory structure supplementing the flagellum, the paraflagellar rod, at the recorded resolution the flagellum appears to be of approximately constant width. (b) Result of processing (a) into a binary image, following background subtraction and noise reduction. Existing methods of flagellum extraction are unable to automatically identify the flagellum in this image, typically requiring user input at this stage. (c) Result of the medial axis transform applied to (b), encoding the width of the cell along the medial line as colour. Shown inset is an enlarged section of the transform.

the axis joining the body centroid to the visible base of the flagellum, with the base being placed at the origin and having coordinates $\boldsymbol{x}_0$ in the inertial laboratory frame (see Figure 2.3). In a similar analysis of mammalian spermatozoa [63, 160], a rigid attachment of the flagellum to the cell body was assumed due to the presence of structural components, such as outer dense fibres, which provided sufficient information to rotate the captured data into the cell-fixed frame. Indeed, this would be appropriate for *Leishmania* at the true attachment site inside the flagellar pocket, where microtubule structures bind the flagellum to the cell body [161, 162]. However, our captured data provides an exterior view at a resolution such that the perceived flagellar attachment appears free, and at a site that we will refer to as the base, distinct from the true flagellar attachment zone within the flagellar pocket. Thus, relaxing the constraint of rigid attachment is suitable here, and indeed this provides good agreement with observed waveforms. Hence, the cell body rotation is instead used to determine the cell-fixed frame orientation in the inertial frame, with the flagellar base $\boldsymbol{x}_0$ being the centre of rotation here and throughout. Approximate wavelengths and amplitudes were computed similarly to Gadelha et al. [10], where appropriate, along with an approximation to the cell body length. A standard decomposition of the resulting waveform data into Fourier modes was then performed [157, 158], where an expansion of low dimension was sought for use in numerical simulations. The results of this analysis are presented later in Section 2.3.1.

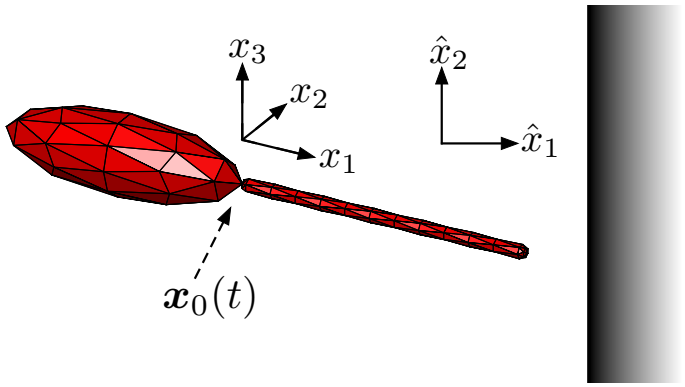

Figure 2.3: A three-dimensional computational representation of the virtual promastigote with undeformed flagellum, where 80 triangular elements (red) have been used to mesh the cell body surface for illustration purposes (see Appendix 2.C). The location of flagellar attachment at time t is denoted $\boldsymbol{x}_0(t)$ in the laboratory frame and is the origin of the cell-fixed reference frame whose axes, $x_1x_2x_3$, are depicted. A solid boundary lies in the laboratory frame plane $\hat{x}_1 = \text{constant}$.

2.2.2 Governing equations

Using typical length, velocity, and time scales given in Wheeler et al. [156] and Wheeler [163], we non-dimensionalise the Stokes equations with a lengthscale $L = 10\,\mu\text{m}$ and a velocity scale $U = 1\,\mu\text{m}\,\text{s}^{-1}$, and scale pressure with $\mu U/L$, taking the advective timescale L/U and using the dynamic viscosity of water at 25 °C. With a typical *Leishmania* flagellar beat frequency of 20 Hz, this yields both a Reynolds number and a frequency Reynolds number on the order of 10^{-3}, with the inertialess limit of the Stokes equations therefore appropriate here. For a given surface S, which typically will represent the promastigote surface, we reiterate the following integral representation for the instantaneous flow velocity $\boldsymbol{u}$ relative to the inertial frame at a point $\boldsymbol{x}^\star$ on the surface, with coordinates given in the body-fixed frame and following Pozrikidis [67],

$$\begin{aligned} u_j(\boldsymbol{x}^\star) = &-\frac{1}{4\pi\mu}\int_S G_{ij}(\boldsymbol{x},\boldsymbol{x}^\star) f_i(\boldsymbol{x})\,\mathrm{d}S(\boldsymbol{x}) \\ &+\frac{1}{4\pi}\overset{PV}{\int_S} u_i(\boldsymbol{x}) T_{ijk}(\boldsymbol{x},\boldsymbol{x}^\star) n_k(\boldsymbol{x})\,\mathrm{d}S(\boldsymbol{x})\,. \end{aligned} \tag{2.1}$$

As in Chapter 1, G_{ij} and T_{ijk} are velocity and stress Green's functions of three-dimensional Stokes flow, to be prescribed later, $\boldsymbol{n}$ is the surface normal directed into the fluid, f_i are the components of the surface traction, and $\int^{PV}$ denotes a principal value integral in the second summand. The velocity may be decomposed into background, cell, and disturbance velocities as in Ishimoto and Gaffney [63], where the cell linear and angular velocities, $\boldsymbol{U}$ and $\boldsymbol{\Omega}$, are *a priori* unknown in the

inertial frame and must be solved for along with the boundary tractions, subject to the additional force and torque-free constraints formulated in Equation (1.2). Explicitly, imposing the hydrodynamic no-slip condition on the surface of the swimmer allows us to write

$$\boldsymbol{u}(\boldsymbol{x}^\star) = \underbrace{\boldsymbol{U} + \boldsymbol{\Omega} \times (\boldsymbol{x}^\star - \boldsymbol{x}_0)}_{\text{rigid body velocity}} + \boldsymbol{u}_r \,, \tag{2.2}$$

where $\boldsymbol{u}_r$ is the velocity of $\boldsymbol{x}^\star$ relative to the cell body and $\boldsymbol{x}_0$ is the base of the flagellum and the origin of the cell-fixed frame. As we will be prescribing flagellar kinematics in this Chapter, this latter term is known, being identically zero for points on the cell body and generally non-zero for points on the flagellum. Thus, we are able to combine this with Equation (2.1) to pose an integral equation for the tractions f_i and body velocities $\boldsymbol{U}$ and $\boldsymbol{\Omega}$, imposing a background flow of zero here and throughout this Chapter. Though we will not do so here, non-trivial background flows may be accounted for by the simple subtraction of a known Stokes flow $\boldsymbol{u}_b$ from $\boldsymbol{u}$, with standard Green's functions of Stokes that decay to zero at spatial infinity then applicable to the disturbance flow $\boldsymbol{u} - \boldsymbol{u}_b$, exploiting the linearity of the governing equations.

2.2.3 The virtual promastigote

In order to model the swimming behaviour of *Leishmania*, we introduce a neutrally buoyant *virtual promastigote*, which here will have an idealised geometry that is similar to wild-type promastigotes (see Figures 2.1 and 2.3). In particular, we construct our idealised promastigote using an axisymmetric prolate ellipsoid to represent the cell body, which differs slightly from observed *L. mexicana* promastigotes, as the latter typically exhibit limited body curvature along their long axis (see Figure 2.1 for typical examples). With reference to the non-dimensionalisation scales of Section 2.2.2, we prescribe a non-dimensional body length of 1.1, with circular cross-sections of diameter 0.35, consistent with a typical promastigote lengthscale of 10 µm and corresponding to a non-dimensional flagellum length of 1.3. In turn, we model the latter by introducing a slender capped cylinder of non-dimensional width 0.03 that attaches to the body at the origin of the cell-fixed frame. The flagellum shape in the cell-fixed frame is described by a general parameterisation

$$\boldsymbol{x} = \boldsymbol{H}(\xi, t) \,, \quad \xi \in [0, \xi^\star(t)] \,, \tag{2.3}$$

where the quantity $\xi^\star(t)$ is chosen such that the arclength of the flagellum is conserved, and we enforce that $\boldsymbol{H}(0,t) = \boldsymbol{0}$, ensuring flagellar attachment occurs at the same

location on the body for all times t. Where it is appropriate to define a beat plane in the cell-fixed frame, we will assume, without loss of generality, that such a plane is spanned by unit vectors in the x_1 and x_2 directions, so that there is no beating in the x_3 coordinate direction (see Figure 2.3). Flagellum material velocities in the inertial frame at a given time t are approximated from positional information using a central differences scheme optimised for double precision arithmetic [164].

2.2.4 Numerical scheme

Given the instantaneous velocity of the flagellum in the cell-fixed frame, which we will later determine from videomicroscopy, we proceed to solve the boundary integral equations of three-dimensional Stokes flow over the discretised virtual promastigote surface, closing the system with the conditions of force and torque–free swimming as described in Section 1.1. The numerical implementation used here builds upon work undertaken during my undergraduate degree studying rigid particles in flow [165], to which we direct the interested reader for details of the discretisation and numerical formulation. Geometry, surface tractions, and surface velocities are interpolated using a mesh of N nodes, yielding a linear system of $3N+6$ scalar equations in $3N+6$ scalar unknowns, including the components of swimming velocity $\boldsymbol{U}$ and angular velocity $\boldsymbol{\Omega}$. Details of the computational mesh are given in Appendix 2.C. We additionally enforce, without loss of generality, that the normal boundary traction has a surface mean of zero, eliminating the pressure non-uniqueness inherent in Stokes flow, and solve the resulting system for the virtual promastigote velocities and surface tractions. Throughout, we use the Blakelet for the integral kernel G_{ij} in Equation (2.1) [43], along with the accompanying form of T_{ijk}, which ensures that the solutions satisfy a no-slip condition on a specified planar boundary. Denoting coordinates in the laboratory frame by $\hat{\boldsymbol{x}} = (\hat{x}_1, \hat{x}_2, \hat{x}_3)$, we typically specify this stationary boundary as $\hat{x}_1 = 0$.

Having computed instantaneous promastigote velocities at a time t, we use Heun's method with timestep $\mathrm{d}t$ to update the position and orientation of the cell in the inertial frame, as detailed in Smith et al. [40], with positional evolution of the flagellum base point $\boldsymbol{x}_0$ following the predictor-corrector scheme

$$\boldsymbol{x}_0(t+\mathrm{d}t) = \boldsymbol{x}_0(t) + \frac{\mathrm{d}t}{2}\left[\boldsymbol{U}(t) + \boldsymbol{U}(t+\mathrm{d}t)\right] \tag{2.4}$$

and cell orientation being dealt with similarly. Here, $\boldsymbol{U}(t+\mathrm{d}t)$ is approximated via a predictor step, in which the predicted location of the cell-fixed frame is given by $\tilde{\boldsymbol{x}}_0(t+$

$\mathrm{d}t) = \boldsymbol{x}_0(t) + \mathrm{d}t\,\boldsymbol{U}(t)$ and other quantities are analogously computed. An adaptive timestepping scheme is employed in order to increase accuracy when approaching the boundary, where velocities are expected to be highly sensitive to boundary separation and body configuration. Typically, one hundred timesteps per period of the flagellar beat are employed, increasing by a factor of ten when approaching the boundary.

Noting that surface interactions such as steric forces often occur between cells and substrates, but also are highly variable between different solutes and substrates [166], we proceed to additionally consider a surface force. Whilst an attractive surface force will simply tend to induce binding once a cell is sufficiently close to a boundary wall, the impact of a repulsive potential is ambiguous *a priori*, with the potential to reflect the cell away from the boundary or to induce stable swimming for a cell that would otherwise crash into the boundary. Hence, we consider a repulsive boundary force via a surface potential, as introduced by Ishimoto and Gaffney [167] and motivated by Klein et. al's measurements [166]. The resulting force per unit area in non-dimensional form is given by

$$\boldsymbol{f}_{\text{wall}}(\boldsymbol{x}) = g\frac{e^{-d/l}}{1-e^{-d/l}}\boldsymbol{n}\,, \tag{2.5}$$

where d is the boundary separation, $\boldsymbol{n}$ is the outward-facing normal of the boundary, and $l = 0.02,\ g \propto \hat{\mu}/\hat{T}$ are the effective range and strength of the force, chosen such that a strong short-range repulsion is represented, with strength scaling with dimensionless viscosity $\hat{\mu}$ and beat period $\hat{T}$.

Our implementation has been verified in free-space against the work of Ishimoto and Gaffney [63] on use of spermatozoan geometries and by reproducing the Jeffery's orbits of ellipsoidal particles [120], whilst the implementation of the Blakelet was compared with the software library BEMLIB [67].

2.2.5 Construction of phase planes

In an effort to gain a more complete picture of the virtual promastigote dynamics without performing numerous costly individual simulations, we will attempt to simplify the dynamics via its restriction to a plane autonomous system, as shown parameterised in Figure 2.4. Specifically, we proceed by equating the third coordinate vectors of the inertial and cell-fixed frames, so that the motion and beat plane lie in the plane $\hat{x}_3 = 0$. We additionally average over a single beat period, as in Ramia et al. [54], enabling a parameterisation by boundary separation and orientation alone, which we denote by h and θ respectively (see Figure 2.4). We define the separation to be the distance from the flagellar attachment point to the wall, and the orientation

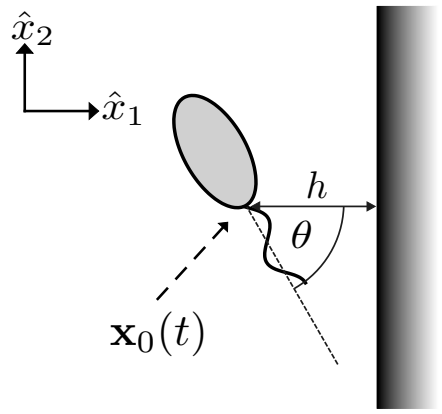

Figure 2.4: Schematic showing the planar configuration of a virtual promastigote, where boundary separation is denoted h, being measured from the flagellum attachment point $\boldsymbol{x}_0$. The clockwise angular displacement of the cell-fixed frame from the laboratory frame is denoted θ, as shown, such that $\theta = 0$ corresponds to perpendicular approach towards the boundary.

to be the clockwise angle between the body-fixed x_1-axis and the boundary normal. We can then form the representation

$$\begin{aligned} \dot{h} &= F(h, \theta)\,, \\ \dot{\theta} &= G(h, \theta)\,, \end{aligned} \tag{2.6}$$

where a dot denotes a time derivative and F and G represent the process of boundary element simulation and subsequent phase averaging. Note that we may identify $-\dot{h} \equiv \bar{U}_1$ and $-\dot{\theta} \equiv \bar{\Omega}_3$, the phase-averaged linear velocity in the $\hat{x}_1$ direction and the rate of rotation about the $\hat{x}_3$ axis, respectively. That the numerical simulations are consistent with the restriction of planarity is confirmed *a posteriori*, owing to the assumed symmetry of the virtual promastigote, together with an *a posteriori* validation that the phase-dependent dynamics is sufficiently accurate compared with full simulations so as to be highly informative, highlighting that the reduced system is indeed representative of the full dynamics. Such comparison is presented in more detail in Chapters 3 and 4, in which we confirm the relevance of planar investigations and validate the beat-averaged phase-plane approximation via direct comparison with full simulations. All behavioural predictions of the reduced system are further validated by the detailed consideration of the full motion of the virtual swimmer.

2.3 Results

2.3.1 *L. mexicana* exhibit simple flagellar kinematics

Analysis of the temporal Fourier spectra of the *L. mexicana* flagellar beat for a sample of 126 cells between two cover slips revealed a single prominent planar beat frequency

in the range of 26 Hz to 34 Hz, clearly observable along the entire flagellum length (see Figure 2.5(b)). The lack of other significant modes suggests that a decomposition into a single sinusoid is appropriate for representing the flagellar beat. Thus, we opt to define the non-dimensional beat parameters of amplitude, wavelength, and frequency, denoted A, λ, and f, respectively, and assume the functional form

$$\begin{aligned} x_1(\xi, t) &= \xi\,, \\ x_2(\xi, t) &= A\left[\sin\left(\frac{2\pi}{\lambda}\xi + 2\pi f t\right) - \sin\left(2\pi f t\right)\right]\,, \\ x_3(\xi, t) &= 0 \end{aligned} \tag{2.7}$$

in the cell-fixed frame. Under this assumption, amplitudes and wavelengths were approximated, with the averaged results being shown in Figure 2.5(a). Here, we set $A = 0.18$, $\lambda = 1.3$, and $f = 2.8$ for use in simulations, recovering a typical long-wavelength flagellar beat (see Supplementary Movie 1 of Walker et al. [138]) and noting that the results that follow are not sensitive to variations in these parameter choices. Good agreement between the model flagellar beat and that extracted from data is shown in Figure 2.5(c), demonstrating a remarkably simple flagellar kinematics, not dissimilar to that of *L. major* and the classically studied *Crithidia oncopelti* [10, 144]. Additionally, it is noted that, whilst this planar beat pattern was seen in confined promastigotes (see Appendix 2.A), such beating is also observed in the bulk and no non-planar beating is exhibited (see Figure 2.1(c)). Furthermore, from analysing observations of the human spermatozoon, it has also been reported that monoflagellate beating is unchanged near to a boundary to the resolution that can be observed with typical microscopy [63, Appendix A]. Therefore, we adopt our model beat pattern both in the far and near-field of boundaries, and assume that there is not significant variation in this waveform due to hydrodynamic boundary effects.

2.3.2 Virtual promastigote beat plane aligns towards the perpendicular

Long-time simulations of virtual promastigotes revealed a tendency of the cells to align their beat plane normal to the boundary when h, the cell-boundary distance, was sufficiently small. This may be explained by a simple torque balance argument, especially due to the cell body size, and exemplifies a general observation that pullers tend to align perpendicular to boundaries [31, 78]. In this instance, and with reference to Figure 2.6, the no-slip boundary induces increased drag on the near-side of the cell body in comparison to the far side. This difference results in a torque, which, when

Feature	Mean (± S.D.)
Dominant frequency	31.4 ± 9.42 Hz
Flag. wavelength	8.79 ± 1.99µm
Flag. amplitude	1.77 ± 0.877µm
Flag. length	14.9 ± 4.90µm
Body length	9.81 ± 3.29µm
Body width	3.5µm [156]
Flagellum width	0.3µm [156]

(a)

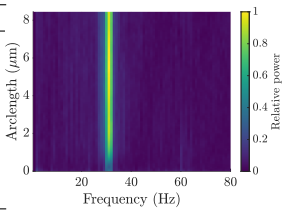

(b)

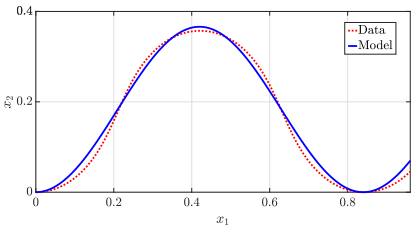

(c)

Figure 2.5: (a) Typical cell parameters as computed from an analysis of *L. mexicana* videomicroscopy of 126 cells, along with body and flagellum widths from Wheeler et. al. [156]. The flagellar beat amplitude is noted to be approximately half the typical cell body width. (b) The Fourier power spectrum for a sample cell. A strong dominant frequency band can be seen around 28Hz, present for the entire length of the flagellum. Power is shown normalised and arclength is measured from the flagellum base. (c) A flagellar waveform extracted from videomicroscopy (red, dotted) plotted against a model beat with a single sinusoid (blue, solid), showing excellent agreement both in space and in time (time not shown). Coordinates as shown are dimensionless.

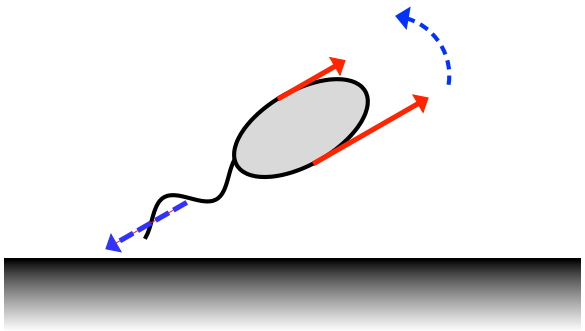

Figure 2.6: Physical mechanism of morphology-dependent drag-based rotation. The no-slip boundary induces increased drag on the near side portion of the cell in comparison to the far side (red, solid), generating a net torque that causes cell reorientation, in addition to the typical promastigote movement towards the boundary (blue, dashed).

combined with the constraint of torque-free swimming, drives reorientation towards the perpendicular, significantly more so than is present when the body size is reduced. The difference in hydrodynamic drag across the virtual promastigote may be explicitly computed by prescribing an instantaneous cell velocity and orientation in place of the force-free and torque-free conditions, the results of which are shown in Table 2.1 for various swimmer configurations and body lengthscales, with the flagellum fixed and straight. These figures demonstrate the existence of a notable drag difference between near and far sides of the swimmer and, in particular, the dependence of this difference on body size, supporting the conclusion that increased cell body size is a factor in the hydrodynamic promotion of promastigote reorientation. This behaviour, and likewise the observations that follow, are observed to be robust to small changes in cell aspect ratio and beat parameters (see Appendix 2.D).

		θ/π				Body length			
		0.2	0.3	0.4	0.5	0.11	0.44	0.77	1.1
h	0.6	·	·	11.0	13.5	2.8	3.9	6.9	11.0
	0.8	·	8.7	7.2	8.3	1.4	2.2	4.3	7.2
	1.0	·	5.1	5.1	5.7	0.9	1.5	3.0	5.1
	1.2	3.5	3.9	3.9	4.1	0.6	1.1	2.3	3.9

Table 2.1: Percentage increase in hydrodynamic drag between the bulk and wall-facing sides of a virtual promastigote moving along the axis of the flagellum, with the flagellum straight. Relative drag difference is shown for various configurations in phase space in the first section of the table for a virtual promastigote with typical morphology as described in Section 2.2.3, with the drag differential being greatest for low separations h. The dependence of this drag difference on swimmer body morphology is captured by the second part of the table, where we fix $\theta/\pi = 0.4$ and vary the length of the swimmer body whilst preserving its aspect ratio. Increased body lengthscale is seen to significantly increase the relative drag difference and, thus, a strong dependence of the resultant forcing of the swimmer on body morphology is highlighted. Boundary separation h and body length are non-dimensional, and configurations that result in intersection with the boundary are omitted.

2.3.3 Virtual promastigotes reorient to promote boundary collision via distal flagellar tip

Upon a collision-bound approach to a planar boundary, in the absence of additional repulsive surface forces, we observe the remarkable reorientation of the virtual promastigote such that the distal tip of the flagellum is promoted as the point of contact. This is visible in numerous individual simulations, the behaviour also being captured by the phase plane of Figure 2.7(b), to be detailed later, where we see a rapid change in the angle θ when in close proximity to the boundary. This may again be partially explained by the general tendency of pullers to align perpendicular to a wall, but the large magnitude of the effect suggests that it is also resultant of the same morphology-dependent mechanism as the beat plane reorientation described above. Indeed, this is

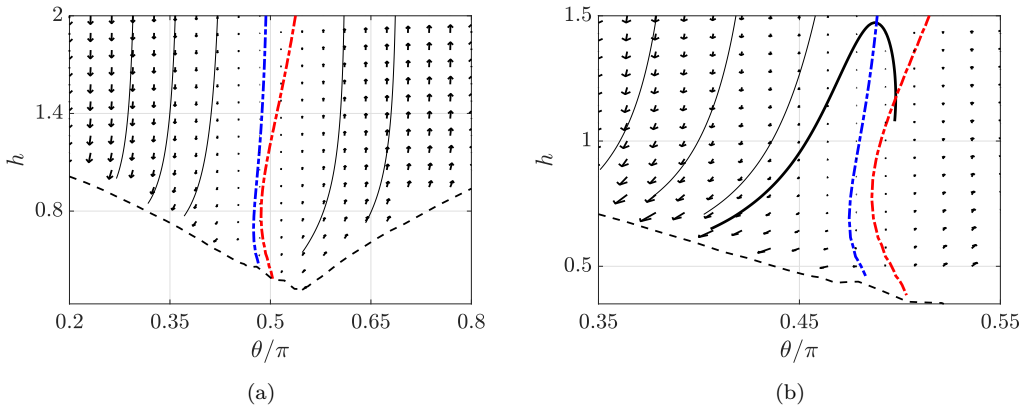

Figure 2.7: Beat-averaged phase planes approximating virtual promastigote motion near a boundary. Sample trajectories are shown as black lines, with the black dashed line separating off the region where configurations intersect with the boundary. Nullclines of the separation h and orientation θ are shown as dashed lines (blue and red, respectively), with the h nullcline approaching $\theta = \pi/2$ as h becomes large. (a) We observe a spectrum of dynamics, with boundary collision occurring in the left half of the phase plane, and reorientation away from the boundary in the right half. For cells approaching from the far-field ($h \to \infty$, $|\theta| < \pi/2$), the trapping regions of the phase plane allow only boundary collision for most values of θ, though this reasoning does not apply to the right of the red θ nullcline. Indeed, long-time simulation confirms that deflection may be observed if $\theta = \pi/2$ initially. The phase plane appears to have no stable fixed points or periodic orbits, corresponding to a lack of stable boundary swimming. (b) Higher resolution phase plane highlighting drag-based reorientation. Trajectories can be seen to curve rapidly in the direction of decreasing θ as they approach the boundary. A sample computed trajectory (heavy line) appears to exhibit a non-monotonic change in h.

confirmed by repeating simulations with greatly reduced body size, where the effects are seen to be substantially decreased, consistent with the quantitative observations shown in Table 2.1. Thus, both beat plane orientation and the specifics of boundary approach are dependent upon virtual promastigote morphology and together result in the flagellar tip being the primary point of surface contact.

2.3.4 Swimming is unstable in the absence of a surface force

As described in Section 2.2.5, employing temporal averaging of the dynamics, we compute a phase plane in order to deduce long-time behaviour (see Figure 2.7(a)). Partitioning phase plane trajectories by the h nullcline (which approaches $\theta = \pi/2$ in the far-field, depicted blue, dashed), we observe that almost all virtual promastigotes approaching the boundary from the far-field will eventually collide with the boundary (see Supplementary Movie 2 of Walker et al. [138]). Similarly, almost all trajectories that initially face away from the boundary exhibit a monotonic increase in boundary separation and relative angle, with those that are sufficiently close to the boundary undergoing deflection, in which θ initially increases and then approaches a constant

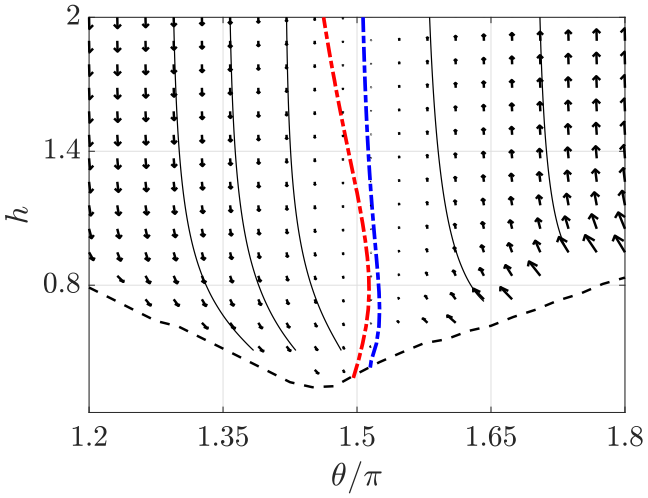

Figure 2.8: Beat-averaged phase plane approximating the motion near a boundary for a virtual pusher with the same morphology as the virtual promastigote of Figure 2.3. Sample trajectories are shown as black lines, with the black dashed line separating off the region where configurations intersect with the boundary. Nullclines of the separation h and orientation θ are shown as dashed lines (blue and red respectively), with the h nullcline approaching $\theta = 3\pi/2$ as h becomes large. Having reversed the propagation direction of the flagellar beat, we recognise the time-reversed behaviour of the virtual promastigote, subject to a shift in θ (cf. Figure 2.7(a)). Noting the sign of $\dot{\theta}$ near the θ-nullcline, we see that it is a stable attractor, located at $\theta \approx 3\pi/2$.

value as promastigote-wall separation grows.

However, the phase plane shows a region where non-monotonic change in h appears plausible (see Figure 2.7(b)), suggesting that those promastigotes beginning on trajectories in the region between the h and θ nullclines will initially move away from the boundary, but will subsequently undergo reorientation towards the surface and eventually collide with it. Contrastingly, such behaviours are not observed in full simulations. However, this is not a significant conflict given the magnitude of the error introduced by the phase plane averaging process, which is typically of the order 10^{-6}, comparable to the $\dot{\theta}$ values seen in this limited region of the phase plane near the nullclines. Therefore, the approximate behaviour need not accurately reflect the full dynamics local to this region. Thus, overall, we see a dichotomy of behaviours exhibited by the virtual promastigote, those of collision with or deflection away from the boundary, with no mechanism for stable boundary swimming. This is confirmed by long-time simulation of virtual promastigotes with $\theta \approx \pi/2$ initially, which orient away from the boundary rather than swimming stably (see Supplementary Movie 3 of Walker et al. [138]).

In order to compare these behaviours against those of an appropriate pusher swimmer, we reverse the direction of beat propagation in the flagellum and simulate the

resulting motion. The behaviour of this pusher is captured by a phase plane (see Figure 2.8), where we observe that the θ nullcline is a stable attractor of the system, located at $\theta \approx 3\pi/2$ and corresponding to swimming approximately parallel to the boundary. In long-time simulations of the full system, we in fact observe stable boundary swimming at a constant separation h, which differs slightly from the beat-averaged system due to the previously described beat-cycle-averaging errors near the system nullclines. In explanation of this stable swimming with reference to the virtual promastigote, we firstly note that a change in beat propagation direction is in fact equivalent to a reversal of time in the flagellar kinematics of Equation (2.7), subject to a phase shift. As detailed in Section 1.3.2, with time appearing only as a parameter in the governing equations, the solution to the time-reversed problem is simply the reversal of the original problem. Therefore, we recover the reversed behaviour of the virtual promastigote in the behaviours of this pusher and, in the place of unstable motion, observe stable parallel swimming near the θ nullcline in a region where $\dot{h}$ is near-vanishing. Additionally, we examine the effects of a significant decrease in cell body size by further modifying the virtual promastigote, reducing the body volume by two orders of magnitude, and repeating the above analysis. From long-time simulation, we note that the stable swimming of the altered pusher may still be observed, albeit at a different boundary separation h, whilst the puller behaviour remains unstable. Thus, our results suggest that hydrodynamic classification is a more significant factor than morphology in determining the stability of boundary swimming.

2.3.5 Repulsive surface forces do not give rise to stable boundary swimming

The repulsive surface potential of Section 2.2.4 is now introduced to the system. Due to the short range over which the resulting repulsive force is non-negligible, the previous phase plane analysis that does not account for the surface force holds throughout most of the phase space. However, due to the varying distance of the flagellum from the boundary throughout a single beat period, phase averaging is not appropriate to determine the dynamics very near to the boundary. Hence, numerous long-time simulations were performed (see Figure 2.9 for an example) to ascertain the motion of the virtual promastigote when in close proximity to the boundary, following which the phase plane of Figure 2.7(a) is used to examine further behaviour.

One might envisage the existence of a periodic motion, with the torque induced by the surface potential orienting the cell into a configuration where it will again collide

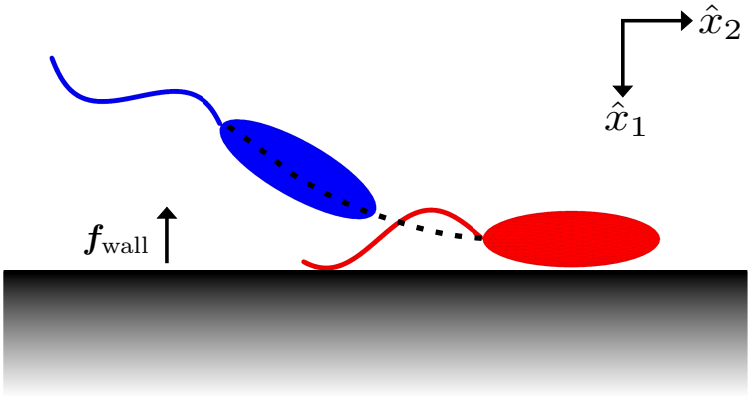

Figure 2.9: The simulated motion of a virtual promastigote in close proximity to a boundary, accounting for a repulsive surface potential. The computational mesh is shown for the initial configuration (red), parallel to the boundary, and the configuration after ca. 1.4 s (blue). The approximate time-averaged path of the attachment point is also shown (black, dashed). We observe that the promastigote orients away from the boundary and thereafter moves off into the bulk. See Supplementary Movie 4 of Walker et al. [138] for the full motion.

with the boundary, and such motion repeats *ad infinitum*. This phenomenon could not be observed for all conducted *in silico* experiments with typical parameter values and cell configurations, which we reason is due to the strong repulsive boundary character.

We observe that the only exhibited behaviour is deflection away from the boundary, with the surface repulsive force causing reorientation of the promastigote such that it falls into the deflective regime, which is observed to be unchanged for reasonable variation in force strength due to the short-range nature of the surface potential. Thus, the inclusion of a repulsive surface potential of physically reasonable character to model boundary contact forces does not give rise to stable boundary swimming of virtual promastigotes and, instead, promotes their eventual deflection.

Reversing the direction of beat propagation, we examine the near-boundary behaviour of the morphologically equivalent pusher, which, due to the repulsive surface force, may not be inferred by time reversal of the puller behaviour. In contrast to the deflection observed for the puller, in this case, we in fact see that the swimmer aligns approximately parallel to the boundary, approaching a stable separation from the wall after an initial period of transition, qualitatively similar to the non-deflective behaviour of small-bodied pushers [40] and as exemplified in Supplementary Movie 5 of Walker et al. [138]. Thus, our results further evidence the significance of hydrodynamic classification in determining boundary behaviours and suggest, in this case, the subdominance of body morphology in effecting stable boundary swimming.

2.4 Discussion and conclusions

In this Chapter, we have identified and described a novel model flagellar waveform of *L. mexicana* promastigotes, observing a simple planar dynamics in 126 cells that lends itself to simple parameterisation and subsequent simulation. Using this model beat pattern, we have observed and explored the boundary behaviours of a virtual axisymmetric promastigote, an idealised hydrodynamic puller with a significant body lengthscale relative to its flagellum.

We have seen that swimming near a boundary in the absence of surface forces is unstable for virtual promastigotes, with trajectories resulting either in immediate deflection away from the boundary or eventual collision with the surface. This behaviour may not be deduced from previous observations of puller microswimmers, owing to the swimmer's distinct morphology and the reported sensitivity of boundary behaviours to swimmer geometry [114]. Here, promastigotes that initially swim away from a boundary may be captured if sufficiently close, undergoing reorientation that results in their collision with the surface. Drawing comparison with *in vivo* promastigotes, this may provide hydrodynamic explanation for the epithelial attachment observed in the sandfly midgut that precedes promastigote metacyclogenesis, established to be necessary for the survival of *Leishmania* promastigotes [148, 149].

Further, we have noted that the time-reversibility of the governing equations allows us to immediately compare the dynamics of pushers and pullers near boundaries in scenarios without repulsive surface forces. Whilst our results have shown that no stable boundary swimming occurs in the case of our virtual promastigote puller, we observed the stable motion of morphologically equivalent pushers, with the latter swimming parallel to the boundary irrespective of the presence of short range repulsive boundary forces. This is in agreement with the known behaviour of the smaller-bodied human spermatozoon, a pusher that can maintain stable parallel swimming next to a planar boundary [40, 100, 101, 168]. A significant reduction in cell body size is not observed to drastically alter the behaviour of the virtual pusher, with only the height of stable swimming being affected. Thus, our results show that the stable boundary swimming of monoflagellates in quiescent fluid is highly dependent on the method of locomotion, and less so to specific changes in morphological scales.

We have also seen that a change in surface character, from a scenario in the absence of surface forces to one with a short range surface force, reduces the prevalence of surface-bound trajectories, with those that would previously have ended in collision now being reoriented into the deflective regime. This promotion of deflective

behaviour in the presence of additional repulsive effects is consistent with wild-type promastigotes, where a change in LPG during metacyclogenesis is thought to result in cell detachment from midgut epithelium, followed by taxis towards the sandfly foregut [151]. Indeed, we are drawn to conjecture that this taxis is aided by the transfer of promastigotes into the bulk and away from the no-slip boundary, so that cells are more susceptible to convection by background flows. Such flows may be associated with sandfly regurgitation, stimulated by the parasite's production of promastigote secretory gel in their infective form [169]. Thus, the hydrodynamic interaction behind the deflection of virtual promastigotes may be responsible for *in vivo* movement of promastigotes into the bulk, and could therefore facilitate the transmission of the infective form of the parasite from vector to host.

However, whilst we have noted that stable boundary swimming of virtual promastigotes does not occur with a repulsive surface potential, this is not the case for the human spermatozoon [63, 160]. Differing in both hydrodynamic classification and cell morphology, it is not clear in the context of the presented results which feature drives the contrasting behaviours observed when accounting for short range surface forces, as time-reversibility is lost due to the boundary force. However, the above results indicate that cell morphology may not have significant impact in general on stable surface swimming. Thus, the observed behavioural differences between virtual promastigotes and human spermatozoa are hypothesised to be primarily resultant of the contrasting methods of locomotion.

Remarkably, we have observed a morphology-dependent mechanism for the promotion of tip-first boundary collision for virtual promastigotes near non-repulsive boundaries. We hypothesise that this mechanism may provide an explanation for the observed behaviour of *in vivo* promastigotes, where flagellum-first attachment is well documented. This behaviour lacks an evidenced driving mechanism, though it has been postulated to be due to the flagellum-first nature of *Leishmania* swimming [149]. Here *in silico*, our study of virtual promastigotes suggests a refined mechanism, whereby the comparatively large body size of the promastigote results in the emergence of drag-based reorientation of notable magnitude, highly dependent on body lengthscale, aligning the virtual flagellum such that the distal tip initiates boundary contact.

In Appendix 2.D, we have examined the behavioural effects of changing body lengthscale and aspect ratio, demonstrating that reported behaviours are robust to typical observed variation in these morphological parameters. There remains significant scope in future work to relax the assumption of body axisymmetry in order

to more accurately model *Leishmania* promastigotes and determine the impact of symmetry-breaking body geometry on boundary behaviours. One might expect there to be a significant dependence of behaviour on aspects of cell morphology, with certain realistic *Leishmania* promastigote body curvatures breaking all symmetry and, thus, adding further complexity to the dynamics. Additionally, the classification of boundary and general swimming behaviours for the different morphologies of promastigotes observed in sandflies, which is more diverse than in culture, is likely to be highly relevant in the continued study of *Leishmania* spp. and in the general investigation into hydrodynamic pullers with flagellum-scale cell bodies.

In summary, in this first research Chapter, we have investigated in detail the boundary behaviours of a flagellated puller, a virtual *L. mexicana* promastigote equipped with a determined planar tip-to-base beat pattern, and have observed that stable boundary accumulation does not feature amongst the range of exhibited behaviours, irrespective of the inclusion of repulsive surface forces. Instead, long-time promastigote behaviour may be divided into two distinct categories based on initial location and orientation: those that are deflected away from the boundary, and those that collide tip-first with the boundary. However, whether or not these behaviours are truly representative of *Leishmania* promastigotes in their microenvironments requires further exploration. Nevertheless, our results suggest that the observed behaviour in the sandfly vector midgut may be explained by the hydrodynamic interactions between a promastigote and a boundary, enabling cell attachment and subsequent detachment at life cycle stages appropriate for *Leishmania* survival and virulence. In particular, we have seen that boundary collision via the distal tip of the flagellum is promoted mechanically in virtual promastigotes by a combination of a large cell body and tip-to-base beating, evidencing a remarkable morphology-dependent hydrodynamic mechanism of boundary approach.

Appendix

2.A Videomicroscopy of *L. mexicana*

High framerate videos of *Leishmania mexicana* were generated similarly to previously described in Wheeler [163] by Dr Richard Wheeler, University of Oxford. Promastigote *L. mexicana* (WHO strain MNYC/BZ/62/M379) were grown in M199 supplemented with 10% FCS and 50 µM HEPES·HCl pH 7.4, and maintained in exponential growth between approximately 10^6 and 10^7 cells/ml. For high framerate videos, plain glass slides and coverslips were first blocked by immersion in 1% bovine serum albumen for 30 s, then washed with distilled water. An approximately $2 \times 1\text{cm}^2$ rectangle was drawn on the blocked slide with a hydrophobic barrier pen, to which 1 µl *L. mexicana* culture in logarithmic growth was added, then a blocked coverslip was added giving a ca. ∼5 µm sample depth. 200 and 400 frame/s videos between 4 and 9 s long were captured with an Andor Neo v5.5 sCMOS camera using phase contrast illumination on a Zeiss Axio Observer inverted microscope with a 63× N.A. 1.3 Plan-Neofluar objective (420881-9970-000) and a N.A. 0.55 long working distance condenser. Sample frames can be seen in Figure 2.1.

For visualising *L. mexicana* waveforms in the bulk, a 250 µm thick adhesive plastic square was applied to a glass slide to make a deep chamber, in which 10 µl *L. mexicana* culture was placed, then a coverslip added. Images were captured at a focal plane mid-way through the sample depth, using dark field illumination and a long working distance 10× N.A. 0.45 Plan-Apochromat objective (1063-139). Many cells lay with their cell body and flagellum entirely in the focal plane, consistent with a planar flagellar beat (see Figure 2.1(c)).

2.B The medial axis transform

The medial axis transform may be thought of as the pixel-wise product of a Euclidean distance map and a skeletonisation, with the distance map encoding at each point

the shortest distance to a point not included in the binary mask. As an example, consider the binary image shown in Figure 2.2b, obtained via a prefiltering and image intensity thresholding of Figure 2.2a, where the black region identifies the cell body and flagellum. Skeletonising the region gives a curve of the shape shown in Figure 2.2c, where we are choosing to skeletonise such that the skeleton of a connected region is also connected. Taking the product of the resulting curve with a distance map of the original binary image yields the greyscale image of Figure 2.2c, with points of greater magnitude, shown darker in this figure, corresponding to regions of greater width. Examples of the medial axis transform applied to simple shapes are shown in Figure 2.B.1.

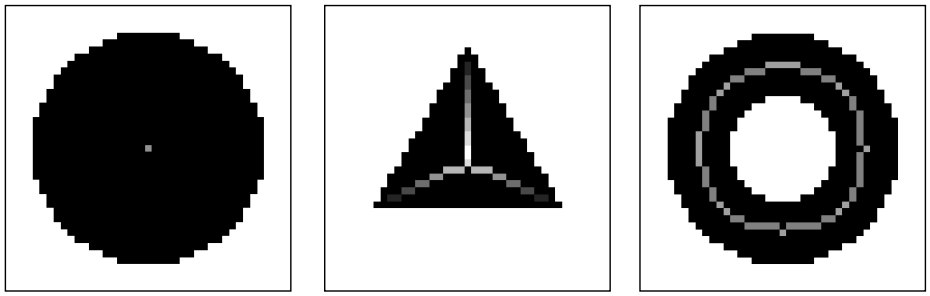

Figure 2.B.1: Examples of the medial axis transform applied to simple low-resolution shapes. The original image is shown in black, with the results of the transform superimposed in greyscale, where brighter pixels correspond to higher values of the transform and, thus, wider sections of the original shape. (a) A simple disk is mapped to a single point by the transform, with the radius of the disk encoded in the transform. (b) A triangular region is reduced to the skeleton shown, with the encoded width decreasing away from the skeleton and triangle's shared centre. (c) An annulus is transformed to a circle along its medial line, with a constant width-profile subject to artefacts of the rasterisation.

2.C Meshing the virtual promastigote

Both icosahedral and triangulated-cubic meshes were considered for the discretisation of the virtual promastigote body, with an icosahedral mesh being used in practice. Subdivision was performed by the bisection of existing edges, increasing the element count by a factor of four per subdivision. For the flagellum, a cylindrical mesh with spherically capped ends was used, with the vertices being constructed in equispaced circular bands and triangular elements constructed between them. In simulations, a mesh of 320 elements was used for the cell body, and 324 for the flagellum. At lower mesh refinements, high sensitivity of simulation results on mesh geometry was noted, with a low resolution symmetry-breaking icosahedral mesh producing artefacts

in long-time simulations. Thus, simulation results were verified at higher mesh resolutions, where artefacts were of negligible magnitude. The computational mesh used throughout this chapter is sufficiently refined so as to yield convergence of swimmer linear and angular velocities to within 1% of the limiting value, with errors measured via a standard infinity norm.

2.D Effects of body morphology

Given the reported variation in *Leishmania* promastigotes [156, 170], we examine the effects on swimming of altering the morphological parameters describing the swimmer body. With the body length of typical promastigotes varying approximately between 7 µm and 17 µm [156], we simulate the motion of modified virtual promastigotes with body lengths sampled from this range. Here, we fix the body aspect ratio to be that of the original virtual promastigote, and show sample kinematics in Figure 2.D.1 for a single initial configuration. Figure 2.D.1(a) presents the motion of swimmers when a repulsive boundary force is included. We observe that, despite differing in body lengthscale, the swimmers follow qualitatively similar paths in phase space and exhibit the same overall behaviours. The larger-bodied swimmers are seen to undergo reduced reorientation and displacement in phase space when compared with smaller-bodied virtual swimmers, consistent with larger bodies having increased overall drag as well as increased near-wall hydrodynamic resistance. Without repulsive short range surface forces, the same level of qualitative agreement is present, as evident from the time series of Figure 2.D.1(b), with increased reorientation towards the boundary for larger-bodied swimmers.

Similar consideration of variation in body aspect ratio from that of the virtual promastigote yields qualitatively unchanged dynamics, where additionally we observe that decreases in aspect ratio result in reduced swimmer velocities and correspondingly shortened trajectories in phase space for a given simulation time. With the virtual promastigote previously having had an aspect ratio of ~ 3.14, here the aspect ratio was sampled from the range 2-5, capturing the typical variation seen in *Leishmania* promastigotes [156]. Hence, we have seen that the reported behaviours of virtual promastigotes are robust to observed variations in both aspect ratio and body lengthscale.

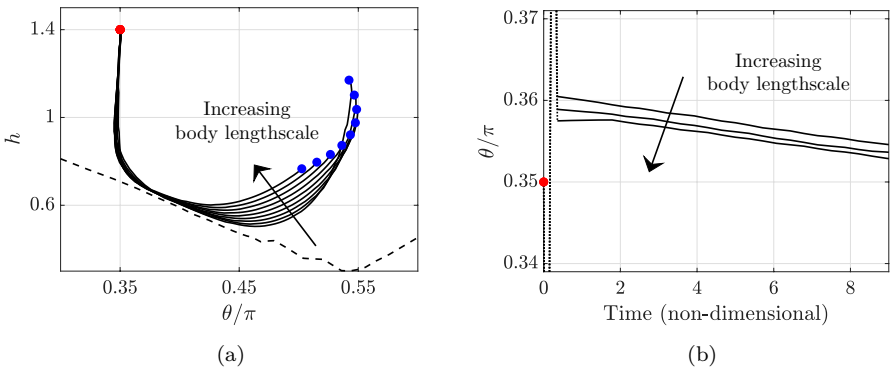

Figure 2.D.1: Simulated swimming of virtual promastigotes with differing body lengthscales. (a) Beginning from a sample initial condition of $(\theta, h) = (0.35\pi, 1.4)$, with the initial location in phase space being shown in red and the simulation endpoints in blue, the smoothed paths of virtual swimmers are depicted as black curves. We simulate virtual promastigotes with a modified body lengthscale, where the aspect ratio of the body is kept fixed and the length of the body is sampled from a range of 7 µm to 17 µm, representing typical variation in *Leishmania*. The black dashed line approximately separates off configurations that represent intersection with the boundary. We observe qualitatively unchanged swimming behaviour in the presence of a repulsive surface potential, with reduced deflection being seen for larger-bodied swimmers. (b) From simulating the swimmers in the absence of short range boundary forces, halting prior to boundary contact, we show a smoothed time series plot of the evolution of θ/π, with the initial configuration of all cells being $(\theta, h) = (0.35\pi, 1.4)$ and lengthscales sampled from the same range as in (a). Greater alignment towards the boundary is observed for swimmers with increased body lengthscales. The dotted section of the curve shows an initial unsmoothed transient, with the common initial value highlighted in red.

Chapter 3

The response of monoflagellate pullers to a shearing flow

In the previous Chapter, we considered the motion of a model microswimmer in the presence of a infinite planar boundary, prescribing an idealised beat pattern for the relative motion of the flagellum that we identified from videomicroscopy data. For this particular puller swimmer, *Leishmania mexicana*, we hypothesised that certain aspects of its swimming may lead to behaviour that is appropriate for its life-cycle stages, speculating upon the impact of background flows on its movement *in vivo*. Motivated by this latter remark and the unknown effects of flow on such a swimmer, in this Chapter, we will consider the behaviour of this model puller in a candidate background flow, both in unbounded and semi-infinite domains. We will again employ high-accuracy boundary element methods that capture the distinctive morphology of this swimmer, exploring the complex, though in some cases surprisingly simple, interactions between this flagellate and a background flow. The content of this Chapter has been published in Physical Review E (Walker et al. [171]).

3.1 Introduction

In the microscale world of unicellular swimmers, the background dynamics of the environment may seem to dominate cell motion. However, such motile microorganisms can be guided by background flows, enabling the directed taxis of cells in their microenvironment. For example, a background shear flow is seen to influence the swimming direction of mammalian spermatozoa near a boundary [99, 115, 116], and bias the orientation of *E. coli* both in the proximity of a planar boundary and in the bulk fluid [117, 118]. Such a directed response to background flow, known as rheotaxis, is hypothesised in some cases to be a contributing factor to the function

or survival of the swimmer, as for the canonical human spermatozoon [14, 99], for instance. Rheotaxis is widely prevalent in nature across a range of scales, being commonly observed in fish [172] and additionally exhibited amongst insects [173]. In terms of microscale swimming, the rheotaxis of squirmers has been considered in detail [114, 174], a biological example being the ciliated microorganism *Opalina* [105, 113, 175]. With regards to flagellated swimmers, recalling the common classification of microswimmers into pullers and pushers[1], the behaviours of pushers are better studied than those of pullers, with particular recent focus on the boundary accumulation of flagellates such as the mammalian spermatozoon and the bacterium *E. coli* [40, 99, 100, 103, 104]. In particular, rheotaxis of mammalian spermatozoa has been known to occur for over a hundred years [176] and has recently been explained in more detail with reference to its potential biological significance [14, 38, 115, 177, 178]. Given the lack of analogous knowledge regarding pullers, examples of which include the insect pathogens *Crithidia* spp. and related genera, as well as the genus of plant pathogens *Phytomonas*, there is therefore extensive scope to expand on current understanding and examine bulk puller response to background flows, as well as the additional effects of boundary proximity.

In doing so, we will return once again to consider the model hydrodynamic puller of Chapter 2, *Leishmania mexicana*, which we recall is a parasitic monoflagellate of the genus *Leishmania* that is responsible for a major tropical human disease. They utilise a tip-to-base flagellar beat to achieve locomotion, as quantified in Section 2.3.1, common to the motile life cycle stages of all species of the family *Trypanosomatidae*, including the aforementioned genera *Crithidia* and *Phytomonas* [10, 142–146]. During their life cycle stage in the sandfly midgut, *Leishmania* promastigotes, characterised by their particular morphology and exemplified in Figure 2.1, are known to migrate towards the foregut following detachment from midgut epithelium [151]. They have also been observed at this stage to induce regurgitation in the vector by the secretion of promastigote secretory gel into their environment [169, 179]. The precise role of such regurgitation is unknown, but we suggested in the concluding remarks of Chapter 2 that it may aid in the taxis of promastigotes in the bulk fluid. However, any possible rheotactic effects of background flows near boundaries have previously not been considered for *Trypanosomatidae*, even for Newtonian media, with only their dynamics in quiescent fluid explored in Chapter 2. Thus, in this Chapter, our objective is to examine the effects of ambient Newtonian flow on the boundary

[1] As noted previously, an additional category, *neutral*, also exists, though is less prevalent in contemporary study.

swimming of this monoflagellated puller. Such a study will not only elucidate the behaviour of *Leishmania* in experimental settings and microfluidic devices, but also inform our understanding of its behaviour *in situ*, subject to the caveat that the rheology in the sandfly midgut is unknown.

Hence, we will investigate the response of motile monoflagellates to a shearing flow, with particular reference to the morphology and swimming characteristics of the *Leishmania mexicana* promastigote. Our candidate background flow, a shear flow, is one in which the fluid moves in non-mixing layers, may be generated experimentally near boundaries in microfluidic channels [117], and has previously been used to study the rheotaxis of human spermatozoa [14, 99, 115]. Indeed, the phenomenological model of Kantsler et al. [115] proposes a simple linear relationship between flagellate velocities and the parameters describing a background shear flow. If valid, such a model may be extended to the study of microswimmer populations, supplementing the prior descriptions of swimmer suspensions of Pedley and Kessler [5] and Bearon and Grünbaum [121] and, more generally, facilitating further study into the behaviours of flagellate and active particle populations, with the latter as reviewed by Bechinger et al. [180]. Thus, we additionally aim to ascertain, to high precision, the level of agreement between free-space flagellate swimming and a simplified description of their response to shear flows.

To proceed, following much of the formulation of Chapter 2, we will first recapitulate the boundary element formulation of the governing equations and, for clarity, detail the construction of a virtual swimmer. Further, we will again use the technique of phase-averaging to provide an approximate quantification of virtual monoflagellate swimmers in free space and exposed to a shearing flow, drawing comparisons with classical studies of non-motile bodies. We will then vary body lengthscales and flagellar kinematics in order to compare hydrodynamic classifications and the impacts of morphology in the scenarios of bulk and boundary swimming, seeking to comment on the effects and the implications for guidance via time-dependent shearing rates. Our final objective will then be to use the above to comment on the effects of shear flows on the boundary swimming of virtual *Leishmania* and once again discuss potential relevance to *in vivo* promastigotes.

3.2 Methods

3.2.1 The virtual monoflagellate

In order to simulate the motion of monoflagellates, we will again utilise a general idealised computational representation: the virtual monoflagellate. In this Chapter, we will cast the virtual monoflagellate in dimensional form, seeking to enable simple interpretation of the parameters of any imposed background flows. Equipped with an axisymmetric ellipsoidal body and a long attached flagellum, the construction of a universal virtual monoflagellate enables the study of a variety of flagellated swimmers, here focussing on the *Leishmania mexicana* promastigote. We model such a virtual promastigote as having a large prolate body, with typical major and minor axes of 11 µm and 3.5 µm, respectively, and a flagellum of length 13 µm, using the typical measurements of Wheeler et al. [156]. More explicitly than in Chapter 2, we define two reference frames, a laboratory and a swimmer-fixed frame, with coordinates $\hat{x}_1\hat{x}_2\hat{x}_3$ and $x_1x_2x_3$, respectively, as shown in Figure 3.2.1 and where the major axis of the ellipsoidal body lies along the x_1 axis. The origin of the swimmer-fixed frame in the laboratory frame is denoted $\boldsymbol{x}_0(t)$ and is the location of flagellar attachment to the swimmer body. The surface of the monoflagellate is typically meshed using 644 triangular elements, inherited from Chapter 2, with more elements being utilised for verification purposes and a coarse example being shown in Figure 3.2.1.

To complete a kinematic description of the swimmer, we prescribe a planar beat pattern for the flagellum, as is evidenced to be typical for *Leishmania* in Figure 2.1 and observed in other microswimmers, and adopt the convention that the beat lies in the plane specified by $x_3 = 0$. In particular, we use the description of *Leishmania* beating identified in Section 2.3.1, with the flagellum centreline being parameterised explicitly by ξ in the swimmer-fixed frame as

$$\begin{aligned} x_1(\xi,t) &= \xi\,, \\ x_2(\xi,t) &= A\left[\sin\left(\frac{2\pi}{\lambda}\xi + 2\pi f t\right) - \sin\left(2\pi f t\right)\right], \\ x_3(\xi,t) &= 0 \end{aligned} \tag{3.1}$$

for parameters $\lambda = 13\,\mu\text{m}$, $f = 28\,\text{Hz}$, and $A = 1.8\,\mu\text{m}$. Here, $\xi \in [0, \xi^\star]$, where $\xi^\star$ is chosen to conserve the flagellum length over time and the form of $x_2(\xi,t)$ is such that the proximal base of the flagellum is attached to the swimmer body for all time t. The above parameter choices give a typical free-space swimming speed of approximately $1.5\,\mu\text{m}\,\text{s}^{-1}$ to $2\,\mu\text{m}\,\text{s}^{-1}$, of similar magnitude to reported *Leishmania*

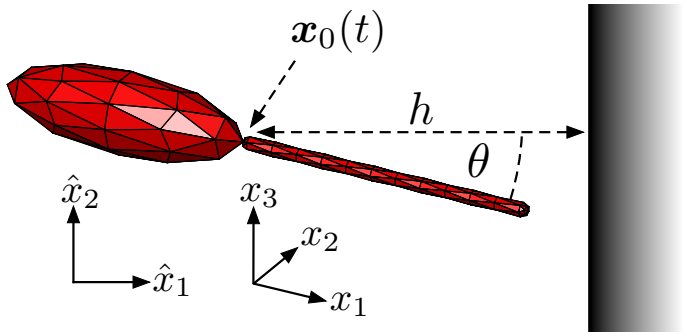

Figure 3.2.1: Computational representation of a monoflagellate. We model monoflagellated swimmers with an axisymmetric ellipsoidal body and an attached flagellum, as shown here for a virtual promastigote. The attachment location is denoted $\boldsymbol{x}_0(t)$ in the laboratory reference frame $\hat{x}_1\hat{x}_2\hat{x}_3$, and forms the origin of the swimmer-fixed reference frame $x_1x_2x_3$. Planar boundaries will typically be specified by $\hat{x}_1 =$ constant, with the accompanying swimmer separation h and orientation θ shown.

motion *in vitro* [156]. The analysis that follows is robust to small changes in beating parameters, but the full effects of significant deviation are not explored here in detail. When briefly considering the motion of pusher swimmers, we will typically retain the virtual promastigote swimmer parameters, subject to reversals in beating direction and variations in body lengthscale, but no other morphological changes.

3.2.2 Governing equations and solution

The now-familiar governing equations of motion, the incompressible Newtonian Stokes equations of Equation (1.1), are solved as described in Section 2.2.2, though we here recapitulate the governing equations and solution method for both clarity and completeness. A reader familiar with the methodology described in Chapter 2 may safely skip to the final paragraph of this section, where the imposed background flow is described.

For fluid velocity $\boldsymbol{u}$, expressed in the inertial laboratory frame, and pressure p, we seek to solve the dimensional equations

$$\mu\nabla^2\boldsymbol{u} = \nabla p\,, \quad \nabla\cdot\boldsymbol{u} = 0\,, \tag{3.2}$$

where μ is the dynamic viscosity of the fluid and these equations are imposed in the exterior of the domain Ω, which we will typically take to represent the exterior of the closed volume of a microswimmer. We enforce the additional conditions of force and torque-free swimming to close the system, as is typical for swimmers at small scale under the additional assumption of neutral buoyancy [31], removing the pressure

gauge freedom as in Chapter 2. The solution of these equations via the boundary element method is given by Pozrikidis [67], explicitly as the solution of

$$\begin{aligned} u_j(\boldsymbol{x}^\star) = &- \frac{1}{4\pi\mu} \int_S G_{ij}(\boldsymbol{x}, \boldsymbol{x}^\star) f_i(\boldsymbol{x}) \, \mathrm{d}S(\boldsymbol{x}) \\ &+ \frac{1}{4\pi} \int_S^{PV} u_i(\boldsymbol{x}) T_{ijk}(\boldsymbol{x}, \boldsymbol{x}^\star) n_k(\boldsymbol{x}) \, \mathrm{d}S(\boldsymbol{x}) \,, \end{aligned} \tag{3.3}$$

shown here for a surface S that will typically represent the surface of the swimmer. Here, $\boldsymbol{x}^\star$ is a point on S with coordinates given in the swimmer-fixed frame, f_i are the components of surface traction, and $\boldsymbol{n}$ is the surface normal directed into the fluid domain. Additionally, G_{ij} and T_{ijk} are velocity and stress Green's functions of three-dimensional Stokes flow and $\int^{PV}$ in the second summand denotes a principal value integral.

Prior to solution, it is useful to decompose the fluid velocity into a known background and an unknown disturbance flow, denoted by $\boldsymbol{u}_b$ and $\boldsymbol{u}_d$, respectively, expressed in the laboratory frame and following the work of Ishimoto and Gaffney [63]. Hence, we prescribe $\boldsymbol{u} \to \boldsymbol{u}_b$ in the far field and away from any boundaries, and the decomposition gives the appropriate condition at infinity for the unknown disturbance flow as $\boldsymbol{u}_d \to 0$. On boundaries, including the swimmer surface, we impose the no-slip condition. In order to prescribe these conditions, we may utilise the free-space or Blakelet integral kernels in Equation (3.3) [43], with the latter additionally enforcing the no-slip condition on a specified planar boundary and noting that both choices yield solutions satisfying the far-field condition.

We may readily compute the solution of Equation (3.3) for a known swimmer configuration in order to determine the instantaneous swimmer linear and angular velocities in the laboratory frame, taking μ throughout to be the dynamic viscosity of water at 25 °C. We then employ a second-order timestepping scheme to compute swimming trajectories, as detailed in Smith et al. [40] and Chapter 2.

The implementation of the boundary element method was verified against the work of Ishimoto and Gaffney [63], with sample simulations in agreement for the cases of bulk swimming and motion near a boundary. The integral kernels used in the solution of the boundary integral equations were compared with the implementations of Pozrikidis [67], showing agreement to machine precision. Final verification was also performed against the analytic solution of Jeffery [120] for passive ellipsoidal particles, with discretisation parameters being chosen to give solutions of sufficient accuracy and precision (1% difference from the limiting value). Where simulations

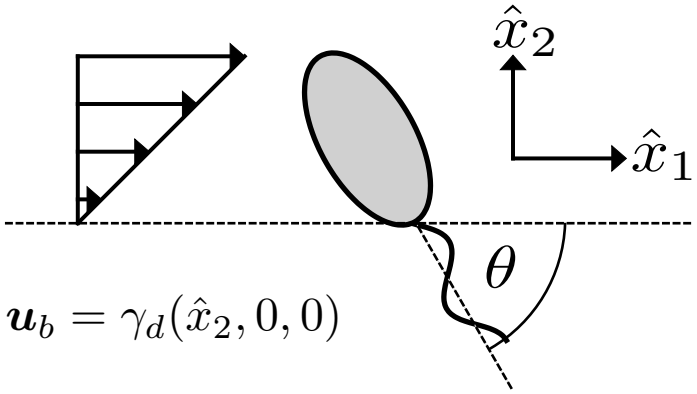

Figure 3.2.2: Describing planar flagellate motion in the bulk. Shown for a virtual promastigote, we define θ to be the clockwise angle between the swimmer-fixed major axis, x_1, and the principal axis of the shear flow, $\hat{x}_1$, with the flow specified in dimensional form as $\boldsymbol{u}_b = \gamma_d(\hat{x}_2, 0, 0)$, expressed in and relative to the laboratory frame. The monoflagellate's beating plane lies in the plane of the background shearing flow (see Appendix 3.A for results concerning the more general case).

include solid boundaries and will result in collision between the swimmer and the surface, simulations are halted when the distance between swimmer and boundary reaches ca. 2 nm.

In studying the response of virtual monoflagellates to a shearing flow in the bulk, we will prescribe $\boldsymbol{u}_b = \gamma_d(\hat{x}_2, 0, 0)$, where γ_d is a dimensional shearing rate and the frame coordinates are as shown in Figure 3.2.2, whereas study near a planar boundary given by $\hat{x}_1 = 0$ will entail $\boldsymbol{u}_b = \gamma_d(0, -\hat{x}_1, 0)$ to satisfy the no-slip condition at the boundary. A biologically appropriate choice of γ_d is unknown in the context of *Leishmania* and, thus, we will typically take γ_d such as to give a non-washout flow that nonetheless influences the swimmer.

3.2.3 Phase-averaged analysis

With phase-averaged analysis proving to be a useful lens into the behaviours of virtual promastigotes in Chapter 2, we seek to apply the same principal to a monoflagellate in shear. This is partly to reduce the computational costs of simulation, which can be prohibitively high due to the high mesh resolutions required for sufficient accuracy, but primarily to enable us to apply principles of dynamical systems theory in the study of swimmer motion. In order to obtain these averaged dynamics, we simulate a swimmer in a given configuration at multiple points over its beat period, typically 20 or 40 sample points, and average the computed linear and angular velocities over the beat.

In free-space, we will initially align the swimmer along the direction of shear, aligning the beating plane of the virtual flagellate with the plane of the shear. The

orientation may then be described by the single clockwise angle θ, as shown in Figure 3.2.2. This significant restriction of the initial condition greatly simplifies the dynamics and enables analysis of an otherwise computationally complex scenario, exploiting body symmetry and the planar nature of the background flow.

We make a similar simplification to the dynamics near a planar wall given by $\hat{x}_1 = 0$, considering motion in a plane $\hat{x}_3 =$ constant and parameterising by orientation θ and separation h. Here, θ is defined as the clockwise angle between the swimmer-fixed x_1 axis and the $\hat{x}_1$ axis of the laboratory frame, and the dimensional separation h is the perpendicular distance from the attachment point $\boldsymbol{x}_0(t)$ to the boundary, shown in Figure 3.2.1. This gives a two-dimensional autonomous system, comparable with known analytic results for squirmers [181, 182] and reduced from the four-dimensional dynamics that would allow rotations out of the plane of the shear. Of note, whilst these dynamics are initiated in particular planes, the subsequent motion is unrestricted. The relevance of the study of these dynamics in describing the full system is examined and evidenced in Appendix 3.A. Comparisons between the predictions of the constrained dynamics and long-time simulations of the full dynamics, in particular pertaining to swimmers that are not aligned with described planes, highlight remarkable agreement between the two systems. Thus, the use of the above dimensionally reduced systems is justified for exploring the more general behaviours of the swimmers considered here.

3.2.4 Repulsive boundary forces

Reported *in vitro* for the bacterium *Staphylococcus aureus* by Klein et al. [166], strong repulsive boundary forces act between cells and boundaries. In order to capture the effects of such surface forces, including the effects of contact with the boundary, we can include short-range repulsive boundary forces of steric origin, given per unit surface area and scaling in strength with the ratio of fluid viscosity and dimensional beating period, μ/T_d. Following Ishimoto and Gaffney [167] and the approach taken in Chapter 2, we explicitly give the force per unit area in dimensional form as

$$\boldsymbol{f}_{\text{wall}}(s) = g\frac{\mu}{T_d}\frac{e^{-s/l}}{1-e^{-s/l}}\boldsymbol{n}\,, \tag{3.4}$$

for outward-pointing unit boundary normal $\boldsymbol{n}$, boundary separation s, non-dimensional scaling $g = 1250$ chosen to represent a strong force relative to other scales in the model, and characteristic decay length $l = 0.2\,\mu\text{m}$ that is much smaller than the cell scale, in line with the force lengthscales observed in Klein et al. [166]. We will refer

to a boundary equipped with this force as *repulsive*, whilst a boundary without such a potential will be described as *passive*.

3.3 Results

3.3.1 Virtual monoflagellate rotation in the plane may be partially approximated by passive ellipsoids in the bulk

Due to a lack of symmetry-breaking features in the bulk, virtual pushers equipped with a planar flagellar beat are observed to turn in a shear flow aligned with their beat plane (see Figure 3.2.2). The evolution and period of the rotation are calculated using phase-averaged analysis, with the evolution of the angular displacement of the cell shown over dimensional time in Figure 3.3.1(a). The phase-averaged planar motion is compared and verified against long-time simulation of the full system, and good agreement is observed. The angular motion is similar in character to the well known Jeffery's orbits of passive ellipsoidal particles in shear flow [120]. Thus, the orbits were compared against the dynamics of axisymmetric ellipsoidal particles with appropriate dimensional period of rotation T_d, choosing the aspect ratio $r > 1$ of each ellipsoid as that given by Jeffery's formula,

$$T_d = \frac{2\pi}{\gamma_d}\left(r + \frac{1}{r}\right), \tag{3.5}$$

which we recall from Section 1.3.4. One such comparison is shown in Figure 3.3.1(b), between a passive ellipsoid and an active virtual promastigote, where only slight quantitative differences are observed between the two. Thus, the phase-averaged angular dynamics of our large-bodied puller may be approximately captured by a Jeffery's orbit for a given shear rate, but the same ellipsoid *a priori* may not be a suitable replacement across a range of shearing rates. In fact, analysis of the dimensional period T_d as a function of shearing rate γ_d revealed that a single choice of ellipsoid is indeed appropriate for a range of background flow rates ($r \approx 5.49$ for the virtual promastigote), and shows remarkable agreement with the functional form given in Equation (3.5), as shown in Figure 3.3.1(c). Hence, we conclude that the rotational motion of flagellated pullers with large cell bodies and a planar beat pattern in non-washout flow may be reasonably approximated by the Jeffery's orbit of an appropriate passive ellipsoid, the aspect ratio of which may be determined by simple phase-averaged analysis and curve fitting.

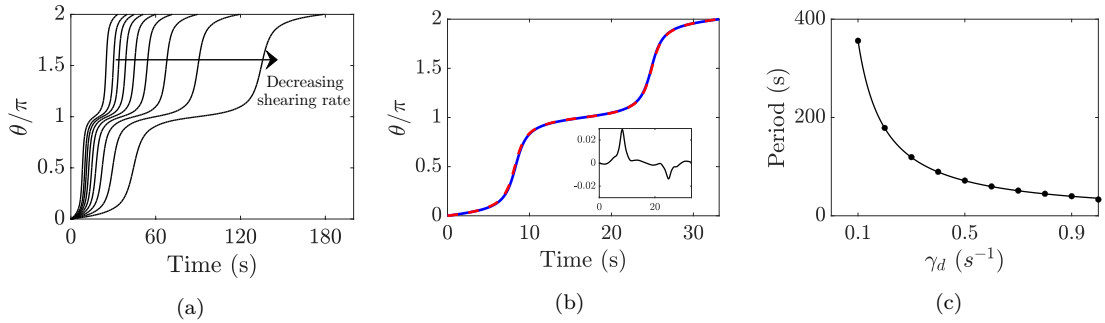

Figure 3.3.1: Free-space angular evolution of virtual monoflagellates, as predicted by phase-averaging, in comparison to passive ellipsoids. (a) Temporal evolution of the angular displacement of a virtual promastigote in the bulk over one full rotation for background shear flow of shearing rates between $0.2\,\mathrm{s}^{-1}$ and $1\,\mathrm{s}^{-1}$. Here, the period of rotation is seen to increase as shearing rate decreases. (b) The Jeffery's orbit of an ellipsoidal particle in shear flow with the same period as the virtual promastigote is shown for $\gamma_d = 1\,\mathrm{s}^{-1}$ (blue, solid), showing remarkably similar dynamics to the corresponding promastigote orbit (red, dashed). The residual plot is inset, displaying absolute errors on the order of 10^{-2}. (c) The dimensional period of promastigote rotation as a function of dimensional shearing rate (black dots). The periods of the promastigote rotation exhibit the same dependence on shearing rate as Jeffery's orbits, as given by the smooth curve for a single fitted effective aspect ratio.

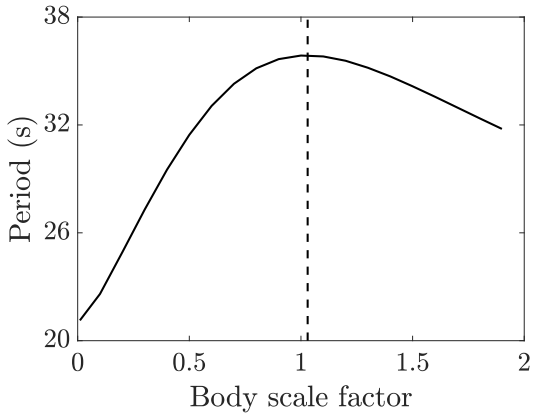

Figure 3.3.2: Period of rotation for virtual puller monoflagellates in shear flow of rate $\gamma_d = 1\,\mathrm{s}^{-1}$, for a range of body lengthscales. Body lengthscale is shown as a scaling factor applied to the typical promastigote body parameters introduced in Section 3.2.1, where a scaling of 1 corresponds to the typical *Leishmania mexicana* lengthscale. The maximum period of rotation is highlighted by the dashed vertical line and occurs for a scaling ca. 1, that corresponding approximately to a typical promastigote.

By the time-reversibility of the governing equations and boundary conditions, this method of approximation is also valid for a pusher with the same morphology and beat characteristics, obtained as a result of reversing the direction of flagellar beating. Thus, the efficacy of approximating angular dynamics with Jeffery's orbits is independent of whether the swimmer is a pusher or a puller.

The above analysis was repeated for a range of body lengthscales, whilst retaining body symmetry and flagellum lengthscale, with the resulting periods of rotation shown in Figure 3.3.2. Here, we have fixed the shearing rate $\gamma_d = 1\,\mathrm{s}^{-1}$, along with flagellum morphological and beating parameters. The resulting curve highlights a maximal period of rotation, corresponding approximately to the body lengthscale of the virtual promastigote. Thus, likely coincidentally, *Leishmania mexicana* promastigotes of typical length appear to exhibit the largest period of rotation for variations in body scale.

3.3.2 Guided bulk swimming may be achieved using temporally evolving shearing flows, and readily approximated

Coupling the angular evolution of a monoflagellate with its linear velocity completely describes the phase-averaged planar motion of such a swimmer. Computing the phase-averaged linear velocity of the swimmer for given background flow rate γ_d and orientation θ, notably less expensive computationally than full long-time simulation, it is possible to simulate the approximate long-time motion of the microswimmer and determine the effects of a variable background shearing rate. It is thereby feasible to obtain an approximate swimming trajectory without large computational cost given a prescribed time-varying background flow.

Via the same method, it is also possible to approximately determine the set of all possible swimming paths from a partially prescribed configuration for a specified background flow. We consider a swimmer in a background shear flow $\boldsymbol{u}_b = \gamma_d(\hat{x}_2, 0, 0)$, expressed in the laboratory frame and here with $\gamma_d = 1\,\mathrm{s}^{-1}$. Additionally assuming that the initial swimmer position is known, we take this position to be the origin of the laboratory frame, without loss of generality. Supposing that the unknown initial orientation of the swimmer is distributed uniformly in $[0, 2\pi]$, as might be a naive assumption for an unknown flagellate, we see in Figure 3.3.3(a) that the most probable positions after some fixed time may be identified with the regions of increased point density, with paths being shown after 2 s and qualitatively robust to large variations in simulation interval and shearing rate. Refining the distribution of initial orientation

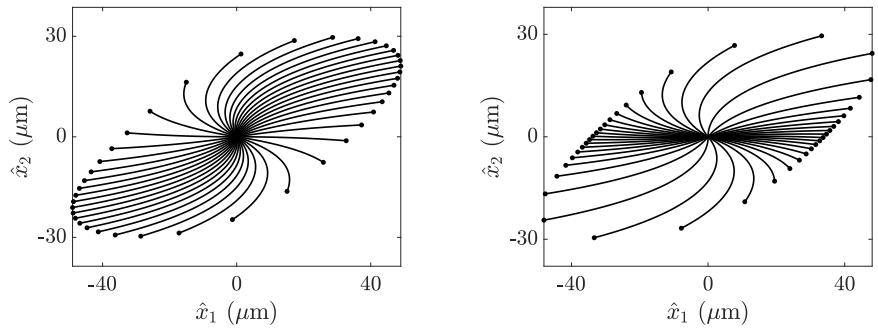

Figure 3.3.3: Swimmer trajectories computed from phase-averaged analysis, initialised at the origin of the laboratory frame in a background shear flow and shown after 2 s. (a) Trajectories with initial orientation sampled from a uniform distribution. The density of endpoints provides a naive estimate of the probability of initially randomly oriented swimmers being in a given region after a specified time. (b) Trajectories where initial orientation is sampled according to the distribution of orientations during a Jeffery's orbit. A differing distribution of endpoints to (a) can be clearly seen, giving a markedly different quantification of how the location evolves for a swimmer with unknown orientation. Here, the background shear flow is prescribed in the laboratory frame as $\boldsymbol{u}_b = \gamma_d(\hat{x}_2, 0, 0)$, where results are shown for $\gamma_d = 1\,\mathrm{s}^{-1}$ and are qualitatively robust to changes in both shear rate and simulation length, in that stark differences between endpoint distributions remain evident.

using the dynamics of the Jeffery's orbit approximation, uniformly sampling over a period, we obtain the profile shown in Figure 3.3.3(b), exhibiting a stark contrast in distribution and showing greater likelihood of travel along the axis of the flow than the naively distributed approach, as might be reasonably expected.

In addition, we theorise that one may inform the specification of background flows using the same phase-averaged analysis in an attempt to prescribe a swimming path, thereby enabling the guidance of a swimmer along a specified path by dynamic changes in background shearing rate. As an example of this, a simple path shown as a black dotted curve in Figure 3.3.4 was prescribed for the typical virtual promastigote, informed by Figure 3.3.3 and aiming to guide the swimmer in a fixed direction. Taking the intended direction of guidance to be along that of the shear flow, an appropriate shearing rate evolution was determined from phase-averaged analysis. For such a rotationally symmetric path, only a single shear reversal is required, with the reversal time being half the period of rotation. Long-time simulation of the swimmer in this time-dependent background flow illustrates good agreement between the predicted and fully simulated paths, particularly on a short timescale. Agreement is improved by temporally refining the simulation of the full system and, thus, this comparison validates the efficacy of both the phase-averaged approximation and the proposed method of swimmer guidance. However, the lessening of agreement towards the latter

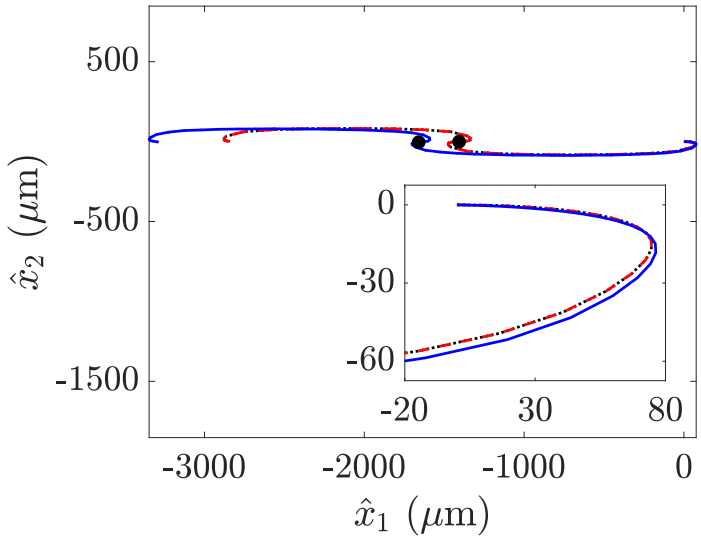

Figure 3.3.4: The shear-guided swimming path of a monoflagellate in a specified time-dependent shear. The phase-averaged approximation (red, dashed) is observed to closely resemble the long-time simulation of the swimmer (blue, solid), beginning from the origin of the laboratory frame with x_1 parallel to $\hat{x}_1$. The locations of background flow reversal, corresponding to a specific time and switching the shearing rate from $\gamma_d = 1\,\mathrm{s}^{-1}$ to $\gamma_d = -1\,\mathrm{s}^{-1}$, are highlighted on the paths (black, filled). The prescribed path is shown as a black dotted curve, seen to coincide with the phase-averaged approximation. Inset is the initial section of the trajectory. Quantitative agreement is improved with increased refinement of the phase-averaged and long-time simulations, but computation of the latter is prohibitively expensive. Overall good agreement, though naturally worsening with duration, over such a timescale (60 s) further validates the phase-averaged approximation and the resulting method of path prediction.

portion of the motion indicates a potential sensitivity of this method of guidance to error, with the largest source of error in this case being the minor but accumulating disparity between the phase-averaged methodology, which was used to determine the appropriate reversal time, and the long-time simulation. Indeed, though not visible at the resolution of Figure 3.3.4, small differences in the $\hat{x}_2$ coordinate can result in large changes in swimmer path due to the background flow, the magnitude of which is proportional to this coordinate. Thus, care may be warranted when further investigating this modality of control and its practical robustness.

3.3.3 Shearing flow in general does not induce stable boundary taxis in virtual promastigotes

In order to characterise the behaviours of virtual monoflagellates near a passive no-slip boundary in the presence of shear flow, we compute a time-averaged phase plane as described in Section 3.2.3, where orientation θ is as shown in Figure 3.2.1. An example of such a phase plane is shown in Figure 3.3.5(a), where we have simulated a virtual promastigote in moderately strong shear flow of dimensional shearing rate $\gamma_d = 1\,\mathrm{s}^{-1}$

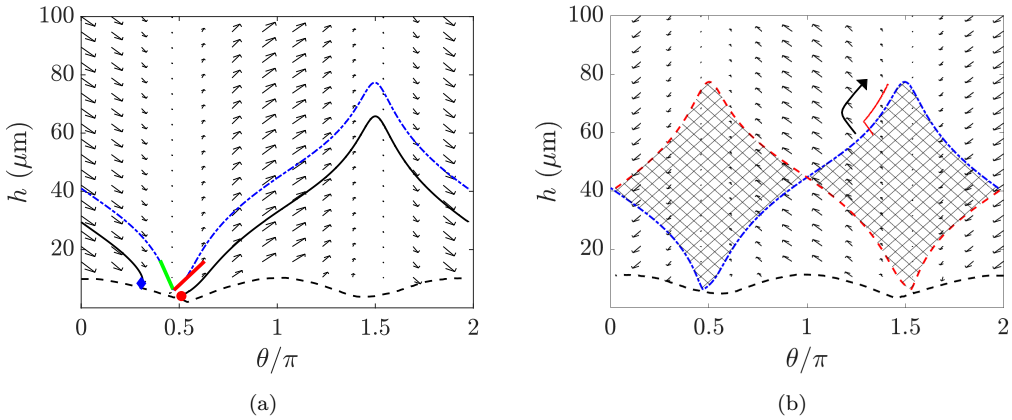

Figure 3.3.5: Phase planes describing the phase-averaged dynamics of a large-bodied puller in shearing flow of rate $\gamma_d = 1\,\mathrm{s}^{-1}$ near a no-slip planar boundary. The black dashed line separates off the region of the phase plane where configurations intersect with the boundary. (a) Approximate stable and unstable manifolds of the saddle in $0 < \theta < \pi/2$ are shown as green and red curves, respectively. A sample trajectory exemplifying boundary collision is shown as a black curve, with the start and endpoints shown as a red circle and a blue diamond, respectively. The separatrix, partitioning the phase plane into collision or bulk-bound configurations, is shown as a dot-dashed blue curve. (b) The phase plane corresponding to a reversal of shear direction from (a). The separatrix corresponding to the original flow direction (blue, dot-dashed) is shown superimposed upon the phase plane, a mirror of the reversed separatrix (red, dashed). The cross-hatched region lying between the two curves highlights those configurations whose characteristic long-time behaviour will be changed by a shear reversal. The smoothed path of a sample long-time simulation in a switching flow is shown (red, solid), which crosses the original separatrix from beneath. Following the crossing, when the flow direction is reversed, the dynamics become those represented in (a), changing the long-time behaviour of the swimmer, with the trajectory following the direction of the large black arrow.

parallel to the boundary, with the flow direction being such that $\dot{\theta} > 0$ in the absence of boundary effects. From the phase plane, we identify a fixed point of the system in $0 < \theta < \pi/2$, corresponding to the balance of torques from the rotational background flow and attractive hydrodynamic boundary effects. The fixed point is seen to be a saddle and, thus, unstable, with approximate stable and unstable manifolds being shown in Figure 3.3.5(a). Further, noting the periodicity of the system in θ, we observe a homoclinic orbit connecting the saddle to itself, creating a separatrix between the behaviours of boundary trapping and deflection into the bulk.

Here, with a passive no-slip solid boundary, we observe that configurations on one side of the separatrix will eventually result in boundary collision, with the lower branch of the unstable manifold preventing periodic swimming and, thus, lasting accumulation. Conversely, on the other side of the separatrix, boundary escape is predicted, with numerical simulation of the phase-plane dynamics required in order to show that trajectories located above the separatrix are not closed (not shown). Indeed, these behaviours were confirmed by long-time simulation of the full system,

and observed to be robust to perturbations in body lengthscale and flagellum beating parameters, as well as significant changes in background flow rates, where γ_d ranges between $0.01\,\mathrm{s}^{-1}$ and $2\,\mathrm{s}^{-1}$.

A reduction in shearing rate sees the separatrix retained, but situated at increased values of separation h, with the saddle moved correspondingly. An increase in shearing rate γ_d from the reference value of $1\,\mathrm{s}^{-1}$ to above a critical value, computed empirically for our virtual promastigote to be $\gamma_d \approx 1.2\,\mathrm{s}^{-1}$, results in the stationary point being in such close proximity to the boundary that configurations beneath the separatrix effectively represent immediate boundary collision. Thus, in high shear, we enter a parameter regime where the steady state approximately corresponds to collision with the surface, resultant of the large-magnitude torque exerted on the swimmer by the background flow. However, at such flow rates, the details of microswimmer morphology and flagellar beating are subdominant to the effects of the background flow and washout. Therefore, we will not consider such high flow rates further. For all flow rates of physical interest, we therefore conclude that the same behavioural dichotomy exists with no possibility of robust periodic swimming and, thus, virtual promastigotes will not in general boundary accumulate in shear flow.

3.3.4 Boundary behaviours may be controlled via variable shearing rates

Recalling from Section 3.3.3 that decreasing background flow shear reduces proximity of the separatrix to the wall, we note that toggling cell behaviour between wall escape and attraction for a given location and orientation may be effected by altering shear. In order to change the swimming behaviour, an appropriate change in shear is required. From a sample phase plane (see Figure 3.3.5(a)) we see that, in fact, an instantaneous change from a shearing rate γ_d to the reverse flow ($\gamma_d \mapsto -\gamma_d$) will achieve behaviour reversal in a large proportion of near-boundary cases, simply by noting that a reversal in shear direction is equivalent to the mapping $\theta \mapsto 2\pi - \theta$ and, thus, gives a separatrix mirrored about $\theta = \pi$. A sample trajectory illustrating this effect is presented in Figure 3.3.5(b).

Whilst instantaneous changes in background flow are acceptable in the inertia- free limit of Stokes equations, it is not clear that such immediate changes in shear can be performed in practice. However, the same behavioural change may be obtained from a continuous variation in shearing rate, again exploiting the response of the separatrix to a change in shearing rates and, in particular, without the need for an instantaneous background flow reversal (not shown). Hence, we conclude that the

long-time boundary behaviours of a large-bodied puller may be dynamically adjusted via background flow calibration.

3.3.5 Repulsive boundary character combined with shear flow may give rise to boundary swimming in virtual promastigotes

Whilst we have observed that a shear flow alone is not sufficient to induce stable boundary swimming in a large-bodied puller like the virtual promastigote, we investigate a boundary of different character by introducing a short-range repulsive boundary potential, simulating a contact force or other strong repulsion close to the boundary, as discussed in Section 3.2.4. Due to the short range of the repulsion and as remarked in Chapter 2, it is not in general appropriate to use the method of phase-averaging to study the near-boundary behaviour of flagellates due to the flagellar beat, which typically possesses an amplitude larger than the characteristic range of the boundary force and, thus, renders phase-averaging unreliable. However, in the medium to far-field of the boundary, the use of the phase-averaged dynamics is justified, as the surface potential is of negligible magnitude away from the boundary. Hence, we use long-time simulation in conjunction with the phase planes of Section 3.2.3 to investigate the effects of a repulsive boundary potential on monoflagellate swimming.

Simulating the long-time motion of a virtual promastigote in close proximity to the boundary in significant shear flow, we observe a qualitative change in overall swimmer behaviour. To see this, we consider the example phase plane of Figure 3.3.6, computed for shearing rate $\gamma_d = 1\,\mathrm{s}^{-1}$ for the promastigote-type swimmer, along with the full simulation of the near-boundary dynamics exemplified in Figures 3.3.6(b) and 3.3.6(c). Beginning from any of the given initial configurations (examples shown in red in Figure 3.3.6), we simulate the full system to accurately determine the motion induced by the boundary repulsion. As the flagellum approaches the boundary, promoted by the tip-first swimming of the flagellate, the strong boundary force exerts a torque on the swimmer, causing it to rotate away from the surface. Following this reorientation, the swimmer evolves to a configuration away from the surface in which the repulsive force is again subdominant, with the flagellum directed into the bulk. For swimmers initially near $\theta = 3\pi/2$, we then note from the phase plane that the resulting configuration (shown in blue) is greatly beneath the separatrix; thus, the motion that follows will entail the swimmer again drawing close to the boundary (shown in black), where the process will repeat, following an apparent limit cycle. For configurations that are initially close to the saddle point at $\theta \approx \pi/2$, as can be seen

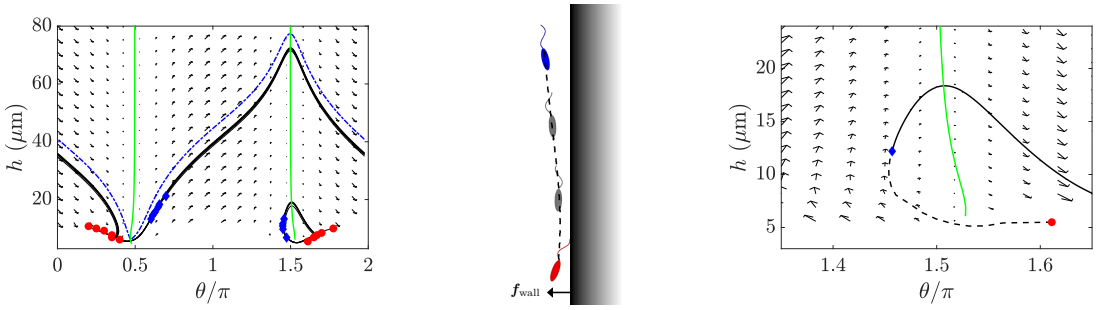

(a) (b) (c)

Figure 3.3.6: Motion of virtual promastigotes in a shear flow near a repulsive planar boundary. (a) With the h nullcline displayed in green and the separatrix displayed as a blue dot-dashed curve, multiple trajectories are shown across the phase plane, with start and endpoints of full simulations being shown as red circles and blue diamonds, respectively. Shown in black are smoothed traces of motion, resultant of simulating the full dynamics, in addition to their phase-averaged continuations, demonstrating a repeated washout tumbling for configurations beginning near the saddle point, and downstream quasiperiodic behaviour for those around $\theta = 3\pi/2$. (b) Results of a full simulation of motion, with the first and last frames displayed in red and blue, respectively. (c) A region of the phase plane representing the motion of (b), with the endpoints of the full simulation highlighted. The h nullcline is shown in green, with the smoothed trajectory shown in black, dashed. At the end of the full simulation, the repulsive boundary force becomes negligible, so the dynamics then follow the phase plane on a collision-bound trajectory (black, solid).

in Figure 3.3.6(a), we observe a repeated tumbling motion, with the repulsive surface force allowing swimmers to cross the unstable manifold of the saddle in phase space and remain beneath the separatrix. The swimmer then moves off into the bulk, but is still captured by the shear flow and again draws close to the boundary. During this cycle, the swimmer is largely far from the boundary and facing downstream ($\theta > \pi$), hence is convected predominantly with the background flow.

Thus, we have identified two modes of downstream quasiperiodic boundary swimming of virtual promastigotes in the plane, one in which swimmers remain facing downstream, and another in which the virtual flagellate tumbles. In the former case, the rotational effects of the shearing flow cause the forward-facing flagellum of the puller to approach the boundary, where it is then subject to significant repulsive forces and subsequently reoriented back away from the boundary. This repeated behaviour is not seen in pushers in the same way, exemplified by the well known upstream stable boundary swimming of the human spermatozoon in a shear flow [14, 38, 115, 177, 178]. We do, however, retain the quasiperiodic swimming observed here in pullers with reduced body lengthscales, having repeated the above analysis for a swimmer with body lengthscale decreased by 80% from that of the virtual promastigote. This suggests that the presence of such a behaviour is reliant on hydrodynamic mechanism and independent of body lengthscale.

3.4 Discussion and conclusions

In this Chapter, we have explored the response of idealised virtual microswimmers to a shearing flow. We have compared the planar orbits of virtual monoflagellates aligned with shear flow to the Jeffery's orbits of passive ellipsoidal particles, observing remarkable agreement and thereby justifying the use of the latter as an approximation of the angular evolution of the former, at least at shear rates that are both large enough to elicit appreciable rotation and small enough to not routinely result in swimmer washout. Considering the resulting period of orbit as a function of the body lengthscale, we observed a scaling that gives rise to virtual promastigotes undergoing a maximal period of rotation, for typical parameters used in the study of *Leishmania mexicana* promastigotes [156, 171], suggesting some notion of optimality in *Leishmania mexicana* morphology. However, due to morphological differences and natural variation in promastigotes within the cell cycle and across life cycle stages [156, 183], there may be little biological significance of this property, if indeed the property holds for non-idealised swimmers *in vivo*.

Following the discovery of Jeffery's orbits as an appropriate approximation to the angular motion of our monoflagellates, we then demonstrated that the linearity inherent in the rotation of these passive particles may be exploited to enable computationally feasible approximation of long-time trajectories of the planar motion of monoflagellates. In turn, this may be utilised for flow-driven swimmer guidance in the bulk, a topic that has since been explored in more detail using the theoretical framework of controllability. Whilst variations in body lengthscales were considered here, the effects of symmetry-breaking morphology were not examined in detail. Indeed, due to the rich character of Jeffery's orbits for non-axisymmetric particles, as reported classically by Hinch and Leal [184], we expect the effects of asymmetry to depend strongly on the particular morphology of the swimmer, a topic for future consideration.

Nonetheless, for axisymmetric swimmers moving in a plane, we have demonstrated that swimming paths may be predicted with significant accuracy and low computational cost, enabling further study of swimmer response to bulk guidance cues. Additionally, as explicitly demonstrated in Appendix 3.A, such dynamics also track the projection onto phase space of trajectories that are not initiated in the plane of shear. Furthermore, the Jeffery's orbit dynamics, coupled with progressive velocity, lead to a verified description of the monoflagellated swimmers that is very simple, with there being further possibilities in exploring such approximations in more complex

background flows, applied to other swimmers, and population dynamics. Indeed, the phenomenological model of rheotaxis proposed by Kantsler et al. [115] is here justified physically (at least in projection for out-of-plane dynamics) by our comparison of monoflagellate rotation with Jeffery's orbits, verified by the phase-averaged path analysis of Section 3.3.2. We further propose that the two-dimensional models of Bearon and Grünbaum [121] and the continuum formulation of Pedley and Kessler [5] may be augmented with the analytic solution of Jeffery's orbits in order to simulate the approximate collective motion of a population of flagellated swimmers.

Further, we have investigated the impacts of shearing flows on how a passive planar no-slip boundary affects monoflagellates. In particular, we have observed a lack of stable boundary swimming in the planar behaviours of virtual *Leishmania mexicana* promastigotes, additionally demonstrating that swimming stability is not qualitatively dependent on moderate changes in body lengthscale. Following from the pusher-puller duality of microscale swimming, which arises from the time-reversibility of the Stokes equations and accompanying boundary conditions, in this case, we may identify the behaviour of a puller as the time-reversal of the morphologically equivalent pusher. From this, we see that the lack of stable swimming behaviour observed here in pullers is consistent with the recent analysis of monoflagellated pushers [40, 54, 63, 100, 185], which are seen to stably accumulate near boundaries, though the findings here may not be immediately inferred due to the large cell body of *Leishmania* compared to pusher monoflagellates such as sperm.

We have explored and classified the behaviours via the use of a separatrix, a feature of the phase-averaged planar dynamics that partitions the swimmer behaviour based on its instantaneous configuration. Analysis of the dependence on shearing rate of this curve in two-dimensional configuration space suggested a method for controlling a swimmer near boundaries, providing a quantitative description of the effects of time-varying background flows on long-time swimming behaviour. Indeed, we have demonstrated that flow reversal may be capable of switching swimmer behaviour between boundary escape and attraction *in vitro*, noting that similar results may be obtained by continuous changes to background flow rates.

Changing the character of the planar boundary from a passive to a repulsive surface, we have noted the exhibition of boundary swimming in the behaviours of idealised pullers exposed to shear flow. Identifying this virtual swimmer with the *Leishmania mexicana* promastigote suggests a potential accumulation behaviour of *in vivo* parasites in flow, although the effects of symmetry-breaking morphology and non-Newtonian media remain to be investigated in detail. Nevertheless, following the

direction of the background flow, this downstream shear-resultant taxis is markedly different from the documented upstream rheotaxis of flagellated pushers [40, 54, 63, 99, 100, 185], and notably is exhibited across a range of body lengthscales.

As detailed in Appendix 3.A, we have seen that the rich and complex dynamics of the two-dimensional subspace that we have considered is highly representative of the full dynamics for behaviour near boundaries, at least in projection onto the height, h, and the angle, θ. Furthermore, the observed lack of dependence of the behaviours on the details of the swimmer body suggests that the nature of boundary accumulation in monoflagellates is more significantly dependent on the hydrodynamic classification of the swimmer, with the boundary swimming of pullers only quantitatively reliant on body lengthscales.

In summary, we have considered in detail the responses of virtual monoflagellated swimmers to a shearing background flow, exploring the effects of varying body lengthscales, shear strengths, and the hydrodynamic classification of the swimmer. We have seen that, in the bulk, we may reliably utilise the Jeffery's orbits of passive particles to approximate the rotational dynamics of both hydrodynamic pushers and pullers, having demonstrated the efficacy of phase-averaged approximations of motion and a proposed method of bulk swimmer control. Having sought to determine the impact of a passive planar boundary on swimming, we have observed an absence of boundary swimming in virtual promastigotes, in contrast to the widely reported behaviours of monoflagellated pushers. Further, the identification of a phase-averaged separatrix highlighted a dichotomy of behaviours, with configurations split between unimpeded motion in the bulk and collision-bound swimming. Introducing a repulsive surface potential, we saw the emergence of quasiperiodic downstream rheotactic boundary swimming in idealised promastigotes, driven by oscillatory switching in the dominance of boundary forces and shear-induced rotation. Finally, we have demonstrated a potentially general method for realising individual swimmer guidance, in principle enabling the dynamic guidance of a variety of motile monoflagellates in microfluidic devices.

Appendix

3.A Relevance of phase-averaged subspace to full dynamics

We establish the relevance of the two-dimensional phase-averaged subspace described in Section 3.2.3 to the full dynamical system representing monoflagellate motion near a boundary. To fully describe the three-dimensional orientation of a monoflagellate, we utilise the Tait-Bryan angles ψ, ϕ, and θ. These are taken to represent successive rotations about the laboratory axes $\hat{x}_1$, $\hat{x}_2$, and $\hat{x}_3$, respectively, and with θ the analogue to that defined in Figures 3.2.1 and 3.2.2, where the inertial frame axes are oriented relative to the shear flow in the absence of a wall (Figure 3.2.2) and relative to the wall in its presence (Figure 3.2.1). In particular, the orientation of the swimmer before rotation is such that the axes of the laboratory and swimmer-fixed frames align, so that $\psi = \phi = \theta = 0$ describes a configuration with the swimmer beat plane parallel to the plane of the shear flow and perpendicular to the boundary. As in the rest of this Chapter, we denote the separation of the origin of the swimmer-fixed frame from the wall by h.

In Figure 3.A.1, we present three examples of unrestricted virtual promastigote motion in the presence of a repulsive or passive planar boundary, along with a shear flow as described in Section 3.2.2, in each case the initial orientation of the swimmer being taken to be a perturbation away from a planar configuration (see Figure 3.A.1 for details). Comparison of the trajectory of Figure 3.A.1(a) with the periodic downstream swimming of Figure 3.3.6(a) demonstrates clear agreement between the behaviours of the full and restricted systems, with the projection of the full dynamics onto the h-θ space closely matching the computed trajectories of the two-dimensional subspace. The approximate periodicity and non-planar nature of the motion in the full system is evident from the angular evolution shown in Figures 3.A.1(a) and 3.A.1(d), where we observe an initial transient from an arbitrary initial state to an apparent periodic non-planar motion, with multiple cycles of this repeating behaviour being

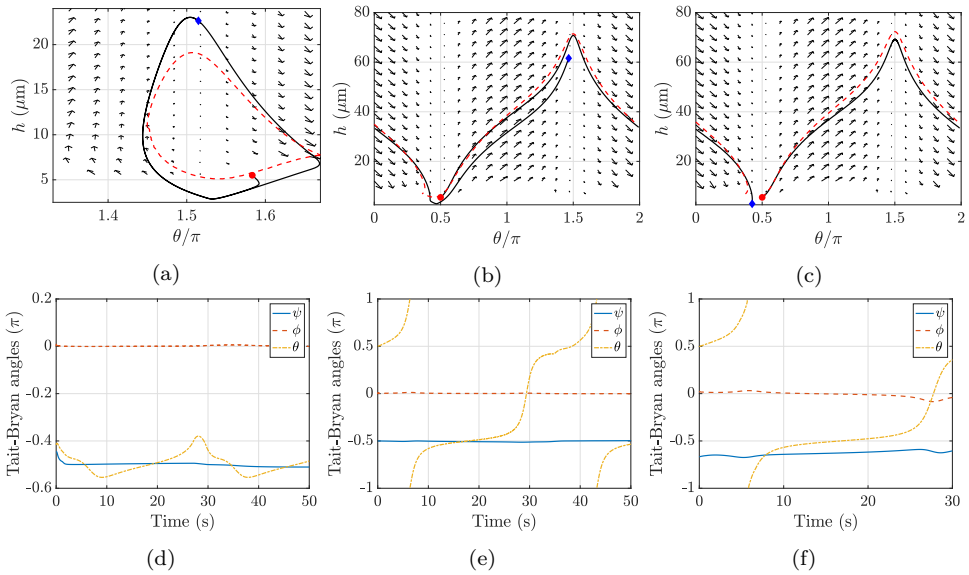

Figure 3.A.1: Sample long-time simulations of the motion of a virtual promastigote near a planar wall in shear flow from various non-planar initial configurations. (a)–(c) Projections of the motion onto the h-θ space, allowing direct comparison of trajectories with those of Figures 3.3.5 and 3.3.6. The start and endpoints of the motion are shown as red circles and blue diamonds, respectively, with the projected, smoothed path displayed as a black curve and showing remarkable qualitative agreement with those presented in Figures 3.3.5 and 3.3.6. Sample paths of the planar system are shown as dashed red curves for comparison. Here, (a) and (b) correspond to the repulsive boundary of Figure 3.3.6, whilst (c) corresponds to the passive boundary of Figure 3.3.5. The trajectory shown in (c) is truncated at 30 s as the swimmer collides with the boundary. (d)–(f) The smoothed evolution of the swimmer Tait-Bryan angles corresponding to the trajectories of (a)–(c). Periodic non-planar motion is exemplified in (d), whilst the angles corresponding to out-of-plane rotation in (e) and (f) can be seen to evolve in general on a slower timescale than the in-plane angle θ, in agreement with the general observation of Ishimoto [114]. Initial conditions are (a) $(\psi, \phi, \theta) = (-1.40, 0.02, -1.31)$, (b) $(\psi, \phi, \theta) = (-1.57, 0, 1.57)$, (c) $(\psi, \phi, \theta) = (-2.10, -0.05, 1.58)$, with angles given in radians and $h = 5.5\,\mu\text{m}$ in all cases. Discontinuities in (e) and (f) arise as the range of θ in the lower plots is $[-\pi, \pi)$, chosen for visual clarity though distinct from the upper panels.

shown. This remarkably demonstrates the existence and approximate stability of a downstream swimming behaviour in the full dynamics, corresponding to the periodic motion reported in Section 3.3.5.

Similarly, in comparison with Figure 3.3.6(a), the phase-plane projections and time series of Figures 3.A.1(b) and 3.A.1(e) highlight the existence of quasiperiodic tumbling in virtual monoflagellates in the full dynamics, as found as a feature of the planar dynamics in Section 3.3.5. We observe little change in ψ or ϕ in comparison to the large variation in θ throughout the motion, supporting the conclusion of Ishimoto [114] that out-of-plane dynamics proceed on a slower timescale than the in-plane dynamics. The same level of agreement is also present in the case of a passive boundary, as in part demonstrated by Figures 3.A.1(c) and 3.A.1(f), showing the projection of a non-planar swimming path that ends in collision with the boundary, as predicted by the planar dynamics. Further, and in supplement to the agreement seen in the far field in Figure 3.A.1, clear correspondence between the behaviour of virtual swimmers in the bulk is exemplified in Figure 3.A.2, where good agreement between the angular evolution of planar and non-planar swimming can be seen.

Thus, the simplified dynamics are here seen to capture, predict, and correspond to complex behaviours of the higher-dimensional system, in the cases of near-boundary and bulk swimming, and, hence, the study of monoflagellate motion restricted to the given planes is evidenced to be remarkably descriptive of, and pertinent to, the details of the unconstrained motion of the swimmer. Understanding why the full dynamical system approximately collapses onto the reduced system, and whether it does for other swimmers more generally, warrants detailed further study.

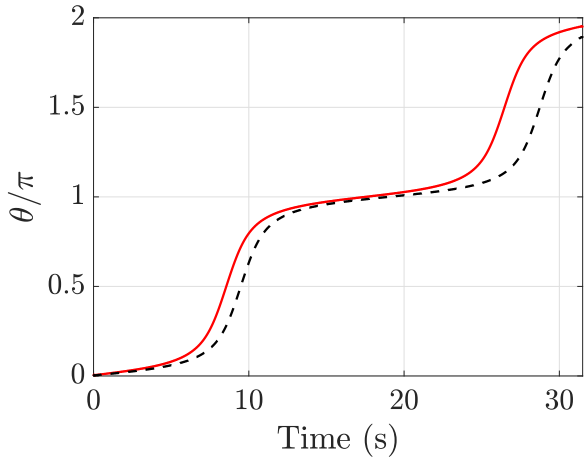

Figure 3.A.2: Sample long-time simulations of the motion of a virtual promastigote in the bulk in a background shear flow. The smoothed evolution of the planar Tait-Bryan angle θ is shown for a swimmer oriented within the plane of the shear flow (red, solid) and for a swimmer with a non-planar initial configuration (black, dashed), demonstrating good agreement over a long timescale. Initially, $(\psi, \phi, \theta) = (-0.79, 0, 0)$ for the non-planar swimmer, with all angles being given in radians.

Chapter 4

The pairwise interactions of synchronised spermatozoa

Thus far, we have explored the dynamics of a single flagellated swimmer. However, as one might expect, microswimmers are often found in significant multiplicity, potentially in populations on the order of tens of millions of swimmers. Therefore, with the effects of additional swimmers in a shared environment having the potential to influence individual behaviours and give rise to rich collective dynamics, the motion of nearby swimmers warrants investigation. Hence, in this Chapter, we will consider the interactions and resulting behaviours of a pair of synchronised human spermatozoa, capturing their complex geometry via boundary element computations as in Chapters 2 and 3. With the dynamics of two swimmers expanding the inherent dimensionality of the swimming problem, we will once again seek a system of reduced dimension, hoping to well approximate the pairwise swimming behaviours whilst affording tractability. The content of this Chapter has been published in Physical Review Fluids (Walker et al. [186]).

4.1 Introduction

Rarely found in isolation, mammalian spermatozoa commonly swim as part of large cell populations, including both artificial and biological microenvironments [85, 187–189]. Indeed, a single human spermatozoon can be one of hundreds of millions of individuals in a single fertile ejaculate [190]. Despite the relevance of these circumstances to areas of scientific research, such as fertility diagnostics, where an understanding of the collective behaviours of spermatozoa may be applicable to assisted reproductive therapies and enable more-efficient experimentation [191–193], many investigations have considered only the behaviours of a lone spermatozoon. Such studies range from

examining the motion of individual swimmers in non-trivial background flows to their behaviour in confined geometries [40, 63, 99–101, 194]. However, there have been comparatively few theoretical studies that have considered the collective behaviours of multiple spermatozoa, recent examples being the large-scale numerical simulations of Schoeller and Keaveny [123] and Yang et al. [195], with notable additional work pertaining to swimming in two dimensions, though there remains significant scope for investigating the complex near-field interactions of swimmers in detail. The latter investigations include classical two-dimensional swimming sheet models, which were introduced in the study of Taylor [84] and later used by Fauci and McDonald [100] to study the interactions of model spermatozoa via the immersed boundary method with two-dimensional hydrodynamics. Restricted to motion in a plane, but capturing three-dimensional hydrodynamics, Yang et al. [122] simulated swimmer interactions via multiparticle collision dynamics, utilising a simple bead model of spermatozoa. A key result of their study was the observation of hydrodynamic attraction between two neighbouring spermatozoa, affirmed by the computations of Simons et al. [196] and Llopis et al. [197]. These studies allowed for swimmer motion in three dimensions and were based on regularised Stokeslet slender-body theory and bead and spring models, respectively, which neglect the potential hydrodynamic effects of the swimmer cell body on pairwise swimming. Interactions between swimmers and boundaries have previously been reported to be highly sensitive to swimmer morphology [113, 138], with the relatively large cell body of model *Leishmania mexicana* contributing to their flagellum-first boundary approach, as identified in Chapter 2; thus, it is not clear *a priori* that the pairwise interactions of spermatozoa will be independent of their geometry. Hence, as a first objective of this Chapter, we will aim to elucidate any behaviours of attraction and repulsion of neighbouring spermatozoa that are not bound and without confining the cell swimming dynamics to a plane, utilising a high-accuracy boundary element method to capture the swimmer body.

Llopis et al. [197] found that pairwise swimming was unstable for their model swimmers, studying model microswimmers in configurations directly above or beside one another. Further to remarking on the attraction and repulsion of their driven bead chains, Llopis et al. noted a surprising dependence of swimming speed on swimmer configuration, with swimming speed increasing only for swimmers directly above one another, and decreasing for side-by-side swimmers. The experimental study of Woolley et al. [93], concerning bovine spermatozoa, supports this conclusion that relative swimmer position impacts on changes to the speed of progression effected by proximity. However, a detailed theoretical exploration of this result that accounts for

complex hydrodynamics and spermatozoan geometry is lacking. Thus, as a second objective of this Chapter, we will aim to determine the effects of swimmer configuration on swimming speed from a kinematic representation of spermatozoa, in particular noting if the inclusion of the non-trivial geometry of human spermatozoa invalidates qualitative conclusions drawn from simpler models.

Also significant to the interaction of nearby spermatozoa is the phenomenon of flagellar synchronization, in which the coupling of hydrodynamics and filament mechanics can result in out-of-phase beating swimmers rapidly adopting a common beat pattern and phase. Synchronization has been observed in various flagellated organisms [93, 95, 198], with extensive theoretical study supporting the role of hydrodynamics in filament synchronization [88, 89, 92, 122, 199, 200]. However, in this Chapter, we will consider spermatozoa swimming in very close proximity, with separations typically being less than one cell length, and will therefore assume throughout that flagellar beating has been synchronised. In turn, this circumvents the need for elastohydrodynamic calculations, which generally suffer from severe numerical stiffness, preventing detailed exploration of the parameter space associated with the numerous degrees of freedom characterizing the relative motion of two interacting sperm cells, whilst exploring extensive regions of parameter space underpins the aims of this Chapter. In Chapters 5 and 6, however, we will begin to explore and develop filament elastohydrodynamics in light of such difficulties.

There has been significant study pertaining to the collective behaviours of swimmers, ranging from the characteristics of bacterial suspensions to active colloidal particles [201–207]. The flow field surrounding an individual spermatozoon is often approximated by that of the force dipole, with the constant singularity strength of a pusher-type swimmer [31]. The pairwise interactions between such simple model swimmers result in hydrodynamic attraction irrespective of the configuration of the swimmers, owing to the symmetry of the flow field representation, though this may not be realistic due to the aforementioned impacts of cell morphology on swimming. Indeed, swimmer morphology is largely neglected by such a method. Recently, a theoretical coarse-grained approach for the simulation of swimmer populations was suggested by Ishimoto et al. [72] and later implemented by Ishimoto and Gaffney [74], seeking to refine the most basic singularity representation of a spermatozoon. This methodology aims to approximate the flow field induced by a lone swimmer by a small number of regularised singularities [75] with time-varying coefficients for use in large-scale simulations, seeking to improve upon simple far-field singularity

representations. This approach has also recently been adapted to model the detailed hydrodynamics of swimming bacteria [208]. Ishimoto and Gaffney simulated a population of spermatozoa moving in two dimensions, with the coarse-grained model well distinguishing between spermatozoan clustering behaviours that emerge from the prescription of different flagellar waveforms, considering detailed waveforms that are representative of those that are observed in spermatozoa in various rheological media. The efficacy of utilising their approach in order to qualitatively capture short range swimmer-swimmer interactions is unknown, as is the ability of the methodology to approximate dynamics in three spatial dimensions. Therefore, as an additional objective of this Chapter, we will evaluate the success of this approach when it is applied to three-dimensional motion, comparing against boundary element computations and ascertaining the degree of qualitative agreement between the two models. As a final objective, we will aim to interpret the computational results of the coarse-grained model in terms of fundamental singularity solutions of Stokes equations, assessing the utility and accuracy of such simple descriptions in approximating swimmer-swimmer interactions.

Hence, in this Chapter, we will examine in detail the hydrodynamic interactions of a pair of virtual spermatozoa, represented by an idealised but representative and commonly used geometry. Prescribing synchronised flagellar kinematics, we will simulate the motion of our virtual swimmers using a high-accuracy boundary element method, aiming to quantify pairwise swimming behaviours in detail, with particular focus on the direction and speeds of relative progression of the pair. After demonstrating that relative swimmer motion may be reduced to an approximate two-dimensional dynamical system, we analyse such a system to discern long-time swimming behaviours. Further, we will draw comparison of simulated behaviours with established experimental results and determine the level of accuracy to which the simple swimmer representations of Ishimoto and Gaffney [74] predict the interactions of virtual spermatozoa.

4.2 Methods

4.2.1 Virtual spermatozoa

In order to model the interactions of two spermatozoa, modifying the general approach of Chapters 2 and 3 by name only, we introduce the neutrally buoyant *virtual kinematic spermatozoon* following Ishimoto and Gaffney [63], formed of an ellipsoid-like head connected to a long slender flagellum. For the head, we adopt the idealised

geometry of Smith et al. [40], forming a computational triangular mesh of the surface as parameterised in Appendix 4.A. This is given with respect to a swimmer-fixed frame with right-handed orthogonal coordinate axes $x_{i1}x_{i2}x_{i3}$, where $i \in \{1, 2\}$ labels each individual swimmer. These axes are taken such that the $x_{i1}x_{i2}$ plane coincides with the plane of the flagellar beat of swimmer i, with the corresponding head-tail junction situated at $(x_{i1}, x_{i2}, x_{i3}) = \mathbf{0}$. The head-tail junctions have locations $\hat{\boldsymbol{x}}_0^i$ in the inertial laboratory frame $\hat{x}_1\hat{x}_2\hat{x}_3$. Unit vectors of the swimmer-fixed frames expressed in the laboratory frame are denoted by $\hat{\boldsymbol{e}}_{x_{ij}}$ for swimmer $i \in \{1, 2\}$ and direction $j \in \{1, 2, 3\}$, with these directions being further specified below.

Each flagellum is represented by a spherically capped cylinder of radius 0.125 µm and length $L_\mathrm{f} = 56\,\mu\mathrm{m}$, a standard scale for human spermatozoa [209], and their motion is prescribed in their respective swimmer-fixed frames. Here, we utilise the representative beat pattern of Dresdner and Katz [210], as adopted in previous studies of spermatozoon behaviour [63], with the flagellar beat parameterised by $s \in [0, s^\star]$ as

$$\begin{aligned} x'_{i1} &= s\,, \\ x'_{i2} &= (A - Bs)\sin(ks - \omega t + \psi_i)\,, \\ x'_{i3} &= 0\,, \end{aligned} \tag{4.1}$$

for wavenumber k, frequency ω, and phase shift ψ_i, where we take $A = 0.0543L_\mathrm{f}$ and $B = 0.1087$. Here, $x'_{i1}x'_{i2}x'_{i3}$ denotes a flagellum-fixed reference frame [40, 210], related to the respective swimmer-fixed frame by a time-dependent rotation and translation that ensures that the local flagellum tangent at the base of the flagellum is parallel to $\hat{\boldsymbol{e}}_{x_{i1}}$, consistent with previous computational studies of human spermatozoa [40, 63] and distinct from the approach used to model *Leishmania mexicana* in Chapters 2 and 3. The quantity $s^\star$ is taken such that the total length of the flagellum is constant, whilst the angular frequency of the beating is fixed such that $\omega/2\pi = 14\,\mathrm{Hz}$, in alignment with observations of spermatozoa in Newtonian media [160]. We note that the results that follow are qualitatively independent of this chosen beat frequency, as adjustments to this frequency simply correspond to performing a rescaling in time. Throughout, we will consider flagellar beating with wavenumber $k = 3\pi/L_\mathrm{f}$ as in Dresdner and Katz [210], though we additionally remark that the presented results are not qualitatively affected by small changes in wavenumber, having briefly explored this. With reference to the widely documented synchronization of flagellar beating when swimmers are in close proximity, as remarked in Section 4.1, we prescribe $\psi_1 = \psi_2 = \psi$ for some constant phase shift $\psi \in [0, 2\pi)$ and hereafter assume in

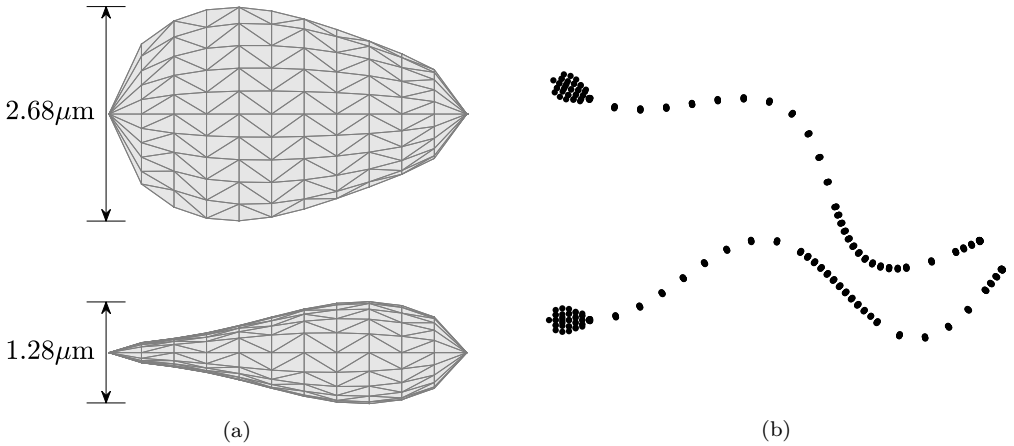

Figure 4.2.1: Computational meshes representing spermatozoan geometry. (a) Views of a triangular mesh representing the head of a spermatozoon, with vertices created in bands and equally spaced around each ellipse-like cross-section, following the parameterisation given in Appendix 4.A. (b) An example of adaptive meshing based on swimmer proximity, with vertices shown as points and elements omitted. The distal portions of the flagella have been partially re-meshed to increase local accuracy whilst retaining computational efficiency. The mesh is shown at reduced resolution for visual clarity and the numerous vertices at each cross-section of the flagellum are effectively amalgamated into one ellipsoidal marker point due to the resolution of the image. Finally, note that these flagella correspond to a flagellum length of 56 µm, a standard scale for human spermatozoa [209].

this kinematic study that the beating of nearby swimmers is synchronous. For convenience, we take ψ such that the free-space headings of the swimmers are parallel to $\hat{\boldsymbol{e}}_{x_{11}}$ and $\hat{\boldsymbol{e}}_{x_{21}}$, respectively, at time $t = 0$. Here and throughout, the term *free-space heading* refers to the direction of net progression over a beat cycle for a lone swimmer in free space and is used as a reference from which we describe the orientation of a swimmer.

4.2.2 Governing equations and numerical solution

As in the case of *Leishmania* in the previous Chapters, the microscale swimming of spermatozoa in an incompressible Newtonian fluid is governed by the three-dimensional Stokes equations. The familiar reader may safely skip to the final paragraph of this section. Recapitulating these now-familiar equations, for pressure p and fluid velocity $\boldsymbol{u}$, expressed in the laboratory frame, the governing equations are given by

$$\mu\nabla^2\boldsymbol{u} = \nabla p\,, \quad \nabla\cdot\boldsymbol{u} = 0\,, \tag{4.2}$$

where μ is the viscosity of the fluid and these equations hold throughout the fluid domain Ω with boundary $\partial\Omega$. Here, we take the fluid domain to be the exterior of the virtual spermatozoa and apply a no-slip boundary condition on the swimmer

surface, additionally enforcing that the fluid velocity decays to zero at spatial infinity in the absence of any non-trivial background flow. Following the boundary element formulation of Pozrikidis [45, 67], the solution for the fluid velocity $\boldsymbol{u}$ relative to the laboratory frame at a point $x^\star$ on the boundary $\partial\Omega$ is given by

$$\begin{aligned} u_j(\boldsymbol{x}^\star) = &- \frac{1}{4\pi\mu} \int_{\partial\Omega} G_{ij}(\boldsymbol{x}, \boldsymbol{x}^\star) f_i(\boldsymbol{x}) \, \mathrm{d}S(\boldsymbol{x}) \\ &+ \frac{1}{4\pi} \overset{PV}{\int_{\partial\Omega}} u_i(\boldsymbol{x}) T_{ijk}(\boldsymbol{x}, \boldsymbol{x}^\star) n_k(\boldsymbol{x}) \, \mathrm{d}S(\boldsymbol{x}) \,, \end{aligned} \tag{4.3}$$

where $i, j, k \in \{1, 2, 3\}$ and Einstein summation convention is assumed. Here, G_{ij} and T_{ijk} are the standard free-space velocity and stress Green's functions of Stokes flow, which inherently satisfy the condition of far-field decay, $\boldsymbol{n}$ is the surface normal directed into the fluid, f_i are the components of surface traction, and $\int^{PV}$ denotes a Cauchy principal value integral. Application of the no-slip condition at the nodes of the computational mesh representing the surface of the swimmers yields a linear system of equations in the *a priori* unknown surface tractions and the cell linear and angular velocities, where the angular velocity of each cell is measured relative to its own head-tail junction. Closure of this underspecified system results from imposing force and torque–free conditions on each swimmer, in addition to removing the gauge freedom in pressure by enforcing that the mean of the normal component of the traction over the boundary of the entire domain be zero, without loss of generality.

Given an initial swimmer configuration and prescribed flagellar kinematics, the instantaneous linear and angular velocities of the swimmers are computed and swimmer positions and orientations updated via a predictor-corrector scheme, Heun's method, with timestep $\mathrm{d}t$, which, for swimmer position $\hat{\boldsymbol{x}}_0^i(t)$ and linear velocity $\boldsymbol{U}^i(t)$, is given explicitly by

$$\hat{\boldsymbol{x}}_0^i(t + \mathrm{d}t) = \hat{\boldsymbol{x}}_0^i(t) + \frac{\mathrm{d}t}{2} \left[\boldsymbol{U}^i(t) + \boldsymbol{U}^i(t + \mathrm{d}t) \right] , \tag{4.4}$$

with a predictor step being used to approximate $\boldsymbol{U}^i(t+\mathrm{d}t)$, as described in Chapter 2. In this Chapter, we focus on the hydrodynamic interactions of the swimming pair and do not include any swimmer-swimmer contact interactions in our model, halting numerical simulations prior to collision, noting that both short range attractive and repulsive forces are of physical relevance but are typically only modelled phenomenologically [138, 166, 167, 196]. Computational meshes consisting of $2,848$ triangular elements per swimmer are adaptively refined based on swimmer proximity, with quantities linearly interpolated over elements. Example meshes demonstrating swimmer head geometry and proximity-based adaptive meshing are shown in Figure 4.2.1. The

suitability of computational meshes was established by numerical convergence, with numerical procedures being validated against the boundary element methods of Chapters 2 and 3. The timestep dt is typically taken such that there are 100 timesteps per beating period, though temporal refinement is increased by an order of magnitude when swimmers are in very close proximity.

4.2.3 Swimmer configurations

The interactions of swimming spermatozoa with synchronised flagellar beats naively form a thirteen-dimensional system, with six scalar quantities representing the location and orientation of each individual swimmer, in addition to the phase of the shared flagellar beat. Consideration of only their relative motion eliminates six degrees of freedom, though full exploration of even this reduced system is computationally prohibitive. We will consider the motion of swimmers initiated in one of two configurations, termed *side-by-side* and *above-below*, akin to the work of Llopis et al. [197] and each of relevance to the wealth of captured videomicroscopy of spermatozoa, in which nearby swimmers commonly share a beat plane or lie closely above one another in the plane of imaging, as can be seen in the Supplementary Information of [23, 211]. From these initial configurations, swimmer motion is simulated unconstrained, allowing for full three-dimensional interactions between swimmers. In Figure 4.2.2(a), we show a side-by-side configuration of swimmers, in which the spermatozoa share a beat plane and their relative motion may be in part described by the separation of their head-tail junctions, $h = |\hat{\boldsymbol{x}}_0^1 - \hat{\boldsymbol{x}}_0^2|$, and the relative angle between their free-space headings, θ, where we are neglecting an additional degree of freedom describing their relative in-plane displacement, to be justified *a posteriori* in Section 4.3.1 given initial conditions with swimmers directly beside one another. This neglected degree of freedom includes, in part, deviation of the swimmer from its average path during its beat cycle, due to cell yaw, for instance.

In Figure 4.2.2(b), we exemplify the above-below configuration of swimmers, in which virtual spermatozoa beat planes are parallel to each other except for rotations about the swimmer-fixed x_{i2}-axes. Notably, $\theta = 0$ corresponds to agreement between the free-space headings of the swimmers, with the beat planes being parallel and any rotations within the plane of beating being neglected. Indeed, we hypothesise that consideration of such in-plane rotations is of limited physical relevance due to the minimal magnitude of swimmer interactions in this configuration, a hypothesis that we will examine in detail in Section 4.3.3. Throughout, and common to both

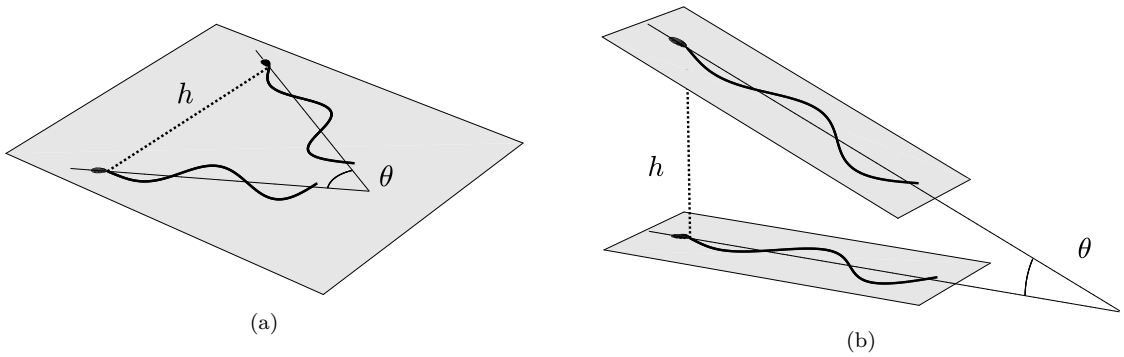

Figure 4.2.2: Schematic of virtual spermatozoa configurations and accompanying parameterisations, with free-space headings being shown as solid lines and their separation h represented by a dotted line. (a) Swimmers share a common beat plane in the side-by-side configuration, with θ defined as the signed planar angle between their free-space headings. (b) In the above-below configuration, the swimmers' relative heading is defined as the signed angle between their beat planes, as shown, where we are making the approximation that the relative motion of the swimmers is expressible solely by the quantities h and θ, justified *a posteriori* in Sections 4.3.1 to 4.3.3. In both configurations, $\theta = 0$ corresponds to the virtual spermatozoa sharing both beat plane orientation and free-space heading, so that the beat planes in the above-below configuration are in fact parallel, and we adopt the sign convention that $\theta > 0$ denotes spermatozoa facing away from one another.

configurations, we will adopt the convention that $\theta > 0$ denotes spermatozoa facing away from one another.

4.2.4 Reduction of behaviour to an approximate low-dimensional dynamical system

In order to systematically capture the complex behaviours of interacting spermatozoa, adapting the principles of previous Chapters, we simulate the motion of the two swimmers for a single period of their synchronised flagellar beats, recording their change in separation h and relative heading θ and initially enforcing that the swimmers are directly beside or above each other. We note that the dependence of the relative motion of the swimmers on the initial phase ψ is expected to be minimal, as is confirmed by numerical simulation; thus, we do not consider such variations in ψ when performing phase averaging. This effectively reduces the swimming motion to an approximate two-dimensional dynamical system in h and θ, enabling the application of a dynamical systems framework as in Chapters 2 and 3. Validity of this methodology is established by direct comparison with long-time simulations of swimmer interactions, which highlights, in particular, that the relative displacement of swimmers along their respective headings does not qualitatively impact on the h–θ dynamics on relevant timescales from initial conditions of zero displacement. We will see further evidence of the validity and utility of these reduced dynamics in Section 4.3.

4.2.5 Coarse-grained singularity representations of swimmers

We will aim to evaluate the accuracy of a recent regularised singularity representation [72, 212, 213], as used by Ishimoto and Gaffney [74] to simulate population-level behaviours of spermatozoa confined to a plane, specifically considering its natural extension to motion in three spatial dimensions. We briefly recapitulate the key principles of the methodology, and direct the interested reader to the original publications [72, 74, 208, 212, 213] for further and complete details. Simulations using this approach were performed by Prof. Kenta Ishimoto, Kyoto University.

Given the flow field generated by a swimmer in the absence of any other fluid boundaries or background flows, principal component analysis (PCA) is used to extract high-variance modes of the velocity field. The two most significant modes, which in this case capture 91.6% of the variance of the flow field, are approximated via a small distribution of regularised Stokeslets [75], yielding a low-dimensional representation of the time-varying flow field associated with a single isolated swimmer that has previously been validated to reasonable accuracy even in the presence of a planar boundary. This representation, which will be shown graphically in Section 4.3.5, allows for efficient simulation of multiple swimmers in the same domain, with the velocity of any individual swimmer being determined via force and torque-balance equations, with the drag on a given swimmer being approximated by the sum of the strengths of its constituent regularised Stokeslets, for example.

4.3 Results

4.3.1 Swimming in close proximity is transient for side-by-side spermatozoa

The long-time motion of two virtual spermatozoa in close proximity in a side-by-side configuration was simulated using the boundary element method over numerous beat cycles, where both swimmers are equipped with the same in-phase flagellar beat and are swimming within the same plane. Simulations from various initial configurations demonstrated that nearby swimming in a side-by-side configuration is transient, with the swimmers either colliding with or deflecting away from one another. Initial separations of the head-tail junctions were sampled in the range $h \in [2.5\,\mu\text{m}, 50\,\mu\text{m}]$, with the relative angle of free-space progression θ ranging from $-\pi/4$ to $\pi/4$. Typical traces showing the location of the head-tail junction of each

swimmer over time are presented in Figure 4.3.1(a), demonstrating both collision and deflection of the swimmers depending on their initial relative configurations.

In order to systematically classify these behaviours of collision and deflection, we proceed by considering the approximate dynamical system as described in Section 4.2.4. The resulting phase plane is shown in Figure 4.3.1(b), along with projections of long-time simulations of unconstrained swimmer motion, demonstrating very good agreement between swimmer motion and the approximate reduction to a plane autonomous system. In particular, this agreement validates *a posteriori* the use of such a phase plane in studying the dynamics of a swimming pair in this configuration, and highlights that any relative motion of the swimmers along their respective axes of progression does not significantly alter their behaviours on reasonable timescales from these initial conditions; indeed, the sample long-time trajectories shown in Figure 4.3.1(a) exemplify that such displacement is minimal. Absent from the plane autonomous system is a stable swimming configuration or limit cycle, meaning that trajectories either result in collision or represent swimmers separating off into the bulk; thus, pairwise side-by-side swimmer motion is transient. Remarkably, we observe from the phase plane that even swimmers initially facing away from one another may eventually collide as the result of proximity-induced reorientation, with the magnitude of this effect decreasing as the separation h between their head-tail junctions increases.

4.3.2 Above-below swimming dynamics approach a stable spiral

Having examined the interactions of swimmers that share a common beat plane, we repeat the phase plane quantification of pairwise swimmer dynamics for virtual spermatozoa in an above-below configuration, with swimmers initially situated directly above one another. The reduced system, shown in Figure 4.3.2, exhibits convergence to a stable spiral in the h–θ space from a wide range of initial configurations in the phase space, assuming that, initially, the free space headings of the swimmers lie within the same vertical plane and that the virtual spermatozoa begin located directly above one another. With the central fixed point located at $(h, \theta) \approx (19.1\,\mu\text{m}, 0.0076\pi)$, this spiral corresponds to swimmers slowly oscillating about a configuration where they are oriented almost parallel to one another and represents a stable mode of pairwise swimming in close proximity. The existence of a stationary point in the h–θ space may be explained intuitively by a simple balance of hydrodynamic attraction between swimmers and their progression along their free-space headings, noting that

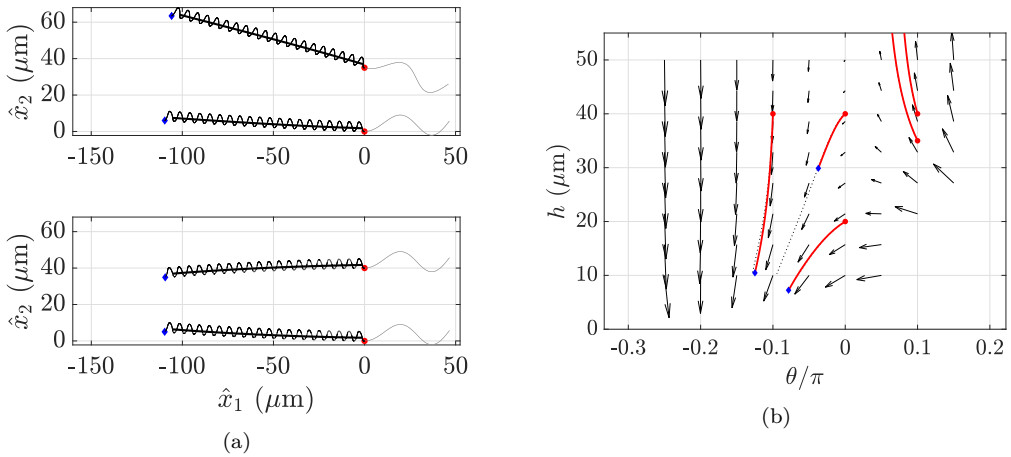

Figure 4.3.1: The transient dynamics of side-by-side swimming, with trajectory start and endpoints shown as red circles and blue diamonds, respectively. (a) The positions of the head-tail junctions $\hat{\boldsymbol{x}}_0^i$ of a pair of spermatozoa are shown as thin curves in the laboratory frame $\hat{x}_1\hat{x}_2\hat{x}_3$ for side-by-side swimmers with initial conditions $(h, \theta) = (35\,\mu\text{m}, 0.1\pi)$ and $(h, \theta) = (40\,\mu\text{m}, 0)$, corresponding to the upper and lower panels, respectively, and simulated over twenty periods of the flagellar beat. Averaged swimmer paths are shown as heavy black curves, highlighting separation in the upper panel and convergence of the swimmers in the lower panel. Shown in grey are the swimmers in their original configurations, with the cell bodies omitted here for clarity. (b) Pairwise dynamics in the h–θ space, with the projections of sample long-time simulations, typically simulated for 20 periods of the flagellar beat, shown as solid red curves. Solutions of the approximate plane autonomous system are shown dotted with the same initial conditions as the long-time simulations, demonstrating very good agreement between the full and reduced systems, serving as *a posteriori* validation of the reduction to h–θ space. Further, the dynamics as predicted by the phase plane exhibit no stable pairwise swimming, merely the behaviours of eventual collision or separation off into the bulk, though sperm initially heading away from one another are predicted to sometimes still be on a path that will result in eventual collision.

the swimmers are oriented slightly away from each other in the stable configuration, though it is *a priori* unclear that such mutual attraction should be present at all.

In order to validate the existence of this stable swimming behaviour in the full dynamics, a number of long-time simulations of unconstrained swimmer motion were performed, with sample projections onto the h–θ space shown as red curves in Figure 4.3.2. As was the case for side-by-side swimmers, excellent agreement is observed in general between trajectories predicted from the plane autonomous system and those projected from long-time simulations. In particular, a simulation of above-below swimmers beginning in the steady-state configuration predicted by the reduced dynamics demonstrates pairwise swimming behaviour corresponding to the stable spiral in the h–θ space, and is robust to perturbations out of an initial above-below configuration. Thus, from consideration of a validated reduction of the dynamics to a plane autonomous system, we have identified a stable form of pairwise swimming in virtual spermatozoa, present for swimmers in an above-below configuration and corresponding to approximately parallel motion. Further, and most remarkably, we have observed that this mode of behaviour is indeed exhibited in long-time simulations of the full pairwise dynamics.

4.3.3 Timescales of pairwise interaction are configuration dependent

Further to enabling an analysis of the overall behaviours of swimming spermatozoa, identifying collision, deflection, or stable relative motion, the long-time simulations and approximate phase plane computations of Sections 4.3.1 and 4.3.2 reveal a disparity in timescales between swimmer configurations. Whilst this may be deduced from detailed consideration of the phase planes of Figures 4.3.1 and 4.3.2, this is most clearly exemplified by focusing on the relative motion of swimmers in each configuration with $\theta = 0$ initially. In Figure 4.3.3, we report the change in separation between their head-tail junctions along with the difference in relative heading over a single beat period as a function of initial separation, as used to generate the profiles of the reduced systems in Sections 4.3.1 and 4.3.2. From this, we note that the change in both swimmer separation and relative heading over a beat period are significantly greater for side-by-side swimming than for swimmers in an above-below configuration, with the change in heading, in particular, being approximately an order of magnitude less for above-below swimmers over a range of separations. Hence, we conclude that the hydrodynamic effects of proximity on swimming behaviour are most prominent for virtual spermatozoa that share a plane of beating, in contrast to the relatively

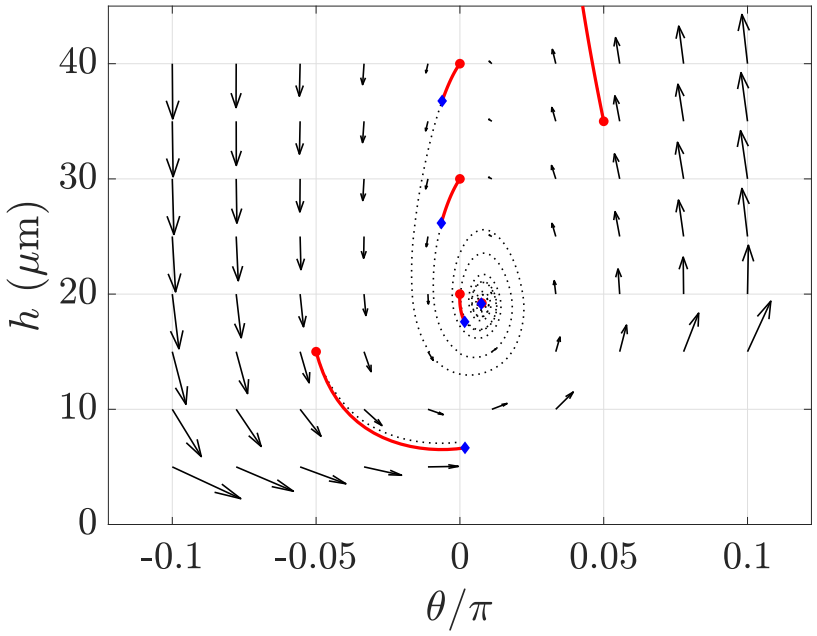

Figure 4.3.2: The approximate dynamics of above-below swimming, highlighting a pairwise swimming mode that corresponds to stable long-time motion in close proximity, represented here by the existence of an attracting stable spiral around $h \approx 19.1\mu$m, $\theta \approx 0.0076\pi$. Beat-averaged projections of long-time simulations, computed for twenty periods of the flagellar beat and serving as *a posteriori* validation of the phase plane, are shown as red curves, with start and endpoints displayed as red circles and blue diamonds, respectively. In particular, a long-time simulation initiated from approximately the stationary point of the autonomous system shows that swimmers indeed undergo negligible relative motion, verifying the existence of a stable swimming configuration. Solutions of the approximate plane autonomous system are shown dotted with the same initial conditions as the long-time simulations, demonstrating very good agreement between the full and reduced systems. Trajectories can be seen to spiral inwards, approaching the stationary point on timescales on the order of hundreds of beat cycles.

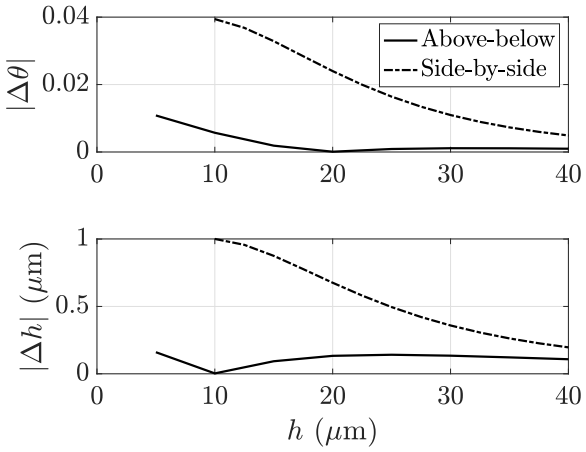

Figure 4.3.3: Change in swimmer separation and relative heading over a single beating period as a function of initial separation h, denoted Δh and $\Delta\theta$, respectively. Initially, the swimmers are situated directly above or beside one another, with $\theta = 0$. Above-below swimmers, shown as solid curves, can be seen to undergo reduced changes in relative heading and separation when compared to side-by-side swimmers, shown dot-dashed, highlighting a disparity in the timescales of relative motion between swimmer configurations.

weak effects experienced by swimmers in an above-below configuration, highlighting a stark anisotropy in the interactions of neighbouring swimmers.

In particular, the reduced magnitude of swimmer interactions in the above-below configuration justifies *a posteriori* our consideration of above-below swimming only where there is no relative rotation within the swimmers' planes of beating. Indeed, were there to be such a relative rotation, virtual spermatozoa may be expected to simply pass over each other and separate with little observable interaction, owing to the noted relative subdominance of out-of-plane hydrodynamic interactions in this configuration.

4.3.4 Effects of proximity on swimming speed are anisotropic and commonly inhibit progression

With swimming stable in above-below configurations and transient over long timescales for side-by-side swimmers, we consider in more detail the effects of low cell separation on swimmer progression. In particular, for swimmer pairs in each of the side-by-side and above-below configurations with $\theta = 0$, we compute the average linear velocity of the swimmers over a single beating period, where, as above, the flagellar beats are assumed to be in synchrony.

Considering first the case of side-by-side swimming, with the swimming speed being shown as a dot-dashed curve in Figure 4.3.4, we see that a reduction in swimmer

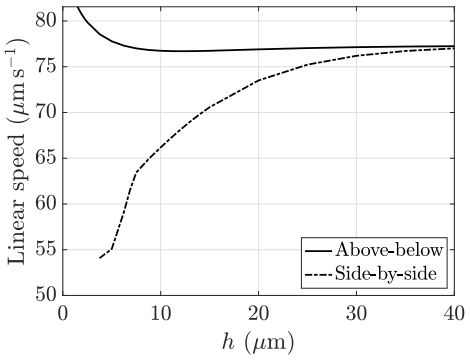

Figure 4.3.4: The linear velocity of a swimmer over a single beating period as a function of separation, h, in both above-below and side-by-side configurations. With swimmers initially directly above/beside one another, and shown here with $\theta = 0$, observed in both configurations is a reduction in swimming speed with separation between swimmer head-tail junctions, though the magnitude of such reduction is notably greater in the case of side-by-side swimming than for above-below swimmers, the change in the latter being difficult to observe on the scale of the above plot. At further-reduced separations, below approximately 10 µm, remarkably, virtual spermatozoa in an above-below configuration can be seen to increase in speed, surpassing even their free-space swimming speed of approximately $77\,\mu\mathrm{m\,s^{-1}}$.

separation yields a substantially reduced average swimming speed, with each swimmer inhibiting the progression of the other. The same general trend may be observed for virtual sperm in an above-below configuration, with speed shown as a solid curve, though reductions in swimming speed are much less in this case. However, in contrast to side-by-side swimming, in the above-below configuration, we observe a notable increase in linear speed when they are in very close proximity to one another, with separations of less than approximately 6.25 µm giving rise to average speeds greater even than those attained by lone swimmers in the bulk. The magnitude of this effect increases further as separation is reduced, with an increase of around $4\,\mu\mathrm{m\,s^{-1}}$ over the bulk speed when at a separation of 1.5 µm, with swimmers nearing contact in this configuration. Thus, in addition to the aforementioned anisotropy of timescales, the effects of proximity on the speed of progression of the virtual spermatozoa are also configuration dependent, in qualitative agreement with the results of Llopis et al. [197] though here observed accounting for the swimmer body and an idealised spermatozoan beating pattern. We observe that side-by-side swimming invariably results in reduced swimming speed, whilst close virtual spermatozoa in an above-below configuration have increased linear speed compared to both side-by-side swimmers and even lone cells in the bulk.

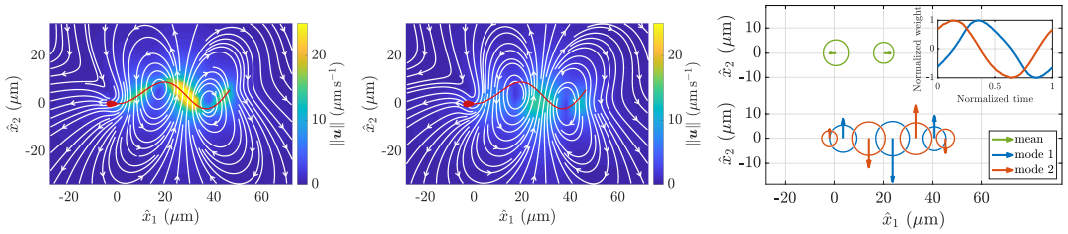

(a) (b) (c)

Figure 4.3.5: Instantaneous flow field in the plane of beating for an individual virtual spermatozoon in the laboratory frame $\hat{x}_1\hat{x}_2\hat{x}_3$, with the swimmer shown in red and situated at the origin of the laboratory frame. The flow field as computed by the boundary element method is given in (a), with the corresponding regularised singularity representation flow field shown in (b). (c) An illustration of the low-dimensional regularised singularity representation, comprising of the lowest two PCA modes and the mean over a beating period, with arrow size and direction corresponding to the strength and direction of the regularised Stokeslets. The circle size corresponds to the regularisation parameter taken for each regularised Stokeslet and inset is the normalised weighting of each of the PCA modes over a single beating period. Each regularised Stokeslet lies on the line $\hat{x}_2 = 0$ by the symmetry of the flagellar beat, with those corresponding to the mean flow here being shown offset along the vertical axis for visual clarity. Qualitative details of the instantaneous flow field can be seen to be well approximated by the low-order regularised singularity representation. The magnitudes of the flow fields are given by the intensity of the shading, with projected streamlines shown in white.

4.3.5 Efficacy of PCA-derived singularity representations is limited in three-dimensional interactions

We simulate the motion of a single swimmer in an unbounded domain to determine the swimmer's characteristic time-varying flow field and form the PCA-derived singularity representation of the swimmer as described in Section 4.2.5, with both flow fields and the accompanying regularised singularity representation being shown in Figure 4.3.5. Simulating pairwise swimmer motion as in Ishimoto and Gaffney [74], we proceed to evaluate the accuracy of using such singularity representations for the simulation of swimmer interaction by repeating the analysis of Sections 4.3.1, 4.3.2, and 4.3.4 using this approximate framework.

Firstly, we consider the predictions of this methodology with regards to separation-dependent swimming speed, reported above using the boundary element method as strongly dependent on swimmer configuration. With the results shown in Figure 4.3.6(a) as blue curves, we observe that the singularity representation is unable to capture even the qualitative effects of swimmer proximity on swimming speed in the above-below configuration, highlighting a subtlety in the mechanism by which swimmers may mutually benefit from pairwise swimming. However, for side-by-side swimmers, the concordance is fair, particularly as swimmer separation increases, suggesting a potential efficacy of this simple singularity representation in describing all

but the closest of swimmer interactions in this configuration. Unsurprisingly, at large separations, the cases of above-below and side-by-side swimming converge to the free-space speed of our virtual spermatozoa, as do the results of both the boundary element method and singularity representation computations, with swimmer-swimmer interactions decaying in magnitude as separation increases.

With reasonable agreement in swimming speed seen for side-by-side swimmers, we examine the long-time behaviours of pairwise swimmers in this configuration as in Section 4.3.1, instead using the PCA-derived singularity representations, simulating swimmer motion over a single beating period from various initial orientations and separations and forming the reduced dynamical system of Section 4.2.4. Shown in Figure 4.3.6(b) are the dynamics in the h–θ space, with projections of long-time boundary element simulations superimposed as red curves for direct comparison. Here, for side-by-side swimming, we observe very good qualitative agreement in overall swimmer behaviour between the predictions of the boundary element method and the singularity representations, consistent with that noted for linear swimming speeds above. This consensus suggests that the singularity-based methodology provides a description of side-by-side dynamics that is capable of capturing qualitative swimmer behaviour and, thus, may be widely applicable to studies of large-scale population interactions.

Now considering swimmers in an above-below configuration and repeating the construction of the approximate plane autonomous system as above, by drawing comparison with Figure 4.3.2 we see that the singularity representation fails to capture the characteristics of the motion as predicted by the boundary element method. Most notably, no stable swimming is present as a mode of pairwise swimming, with swimmers moving off into the bulk or colliding. Further, the overall dynamics of the reduced system computed via the singularity representation are not dissimilar to those predicted for side-by-side swimmers, suggesting that the anisotropy seen in boundary element simulations of our virtual spermatozoa is not captured by the low-order singularity representation.

Overall, we have seen good agreement between methodologies for swimmers in a side-by-side configuration, but little coherence in predicted behaviours for virtual spermatozoa in above-below configurations. Hence, we may conclude that the PCA-derived singularity representations should not be relied upon in their current form for the simulation of three-dimensional interactions in generality, though provide remarkable qualitative agreement with computationally expensive high-accuracy methods for planar swimmers sharing a beating plane.

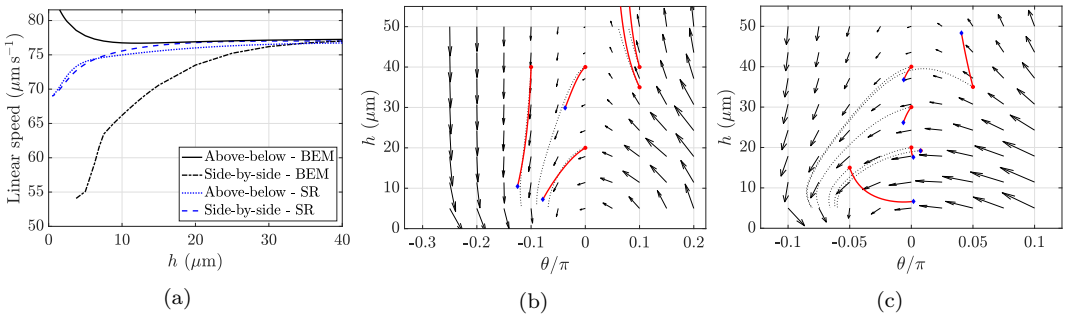

(a) (b) (c)

Figure 4.3.6: Comparison of swimmer behaviours as predicted by the boundary element method and PCA-derived singularity representations. (a) The PCA-derived singularity representations (SR), shown here as blue curves, agree qualitatively with the boundary element method (BEM) predictions for linear swimming speed in the case of side-by-side swimming, though no such agreement is present in close proximity for swimmers in an above-below configuration. (b, c) Evolution in h–θ space for (b) side-by-side and (c) above-below swimmers as predicted by singularity representations, shown as black arrows, with trajectories of the plane autonomous system shown as dotted black curves. Superimposed as solid red curves are projections of boundary element simulations onto the reduced space, with start and endpoints shown as red circles and blue diamonds respectively. We note good agreement in the case of side-by-side swimming, though there is little correspondence between the predictions of the boundary element method and the singularity representations for swimmers in an above-below configuration. Levels of agreement are further evidenced by comparison with Figures 4.3.1 and 4.3.2.

4.4 Discussion and conclusions

This Chapter has considered the motion of two virtual spermatozoa in close proximity, focussing on planar beating and two configurations of interest: side-by-side and above-below swimming. In doing so, we have identified a significant anisotropy in their relative motion, not simply limited to quantitative effects. On examining the linear swimming speed attained by our virtual synchronised swimmers over a single beat period, we have observed that side-by-side spermatozoa make less progress along their respective headings than they would achieve in isolation. Whilst the same, albeit substantially weaker, general trend may be noted in above-below swimmers at separations greater than approximately 10 µm, for reduced separations we note a remarkable increase in swimming speed, above that attained by lone swimmers in the bulk. We hypothesise that the pairwise attachment of spermatozoa in an above-below configuration may afford them a competitive advantage over non-bound individuals, with proximity increasing their speed of progression in-line with the predictions of our computational model. In agreement with the predictions of the bead-and-spring model of Llopis et al. [197], our findings, however, are in part distinct from the similar computational results of Olson and Fauci [89] concerning side-by-side elastic filaments, which predict that swimming speeds increase with proximity for planar

such filaments. This disparity in conclusions suggests that the inclusion of swimmer head geometry may have significant impact on the predicted qualitative behaviours of the swimming pair, with care being necessitated in future theoretical works to accurately capture such effects.

Further anisotropy is present in the timescales of relative motion. We have seen that swimmers in an above-below scenario undergo greatly reduced changes to their configurations over a beating cycle when compared to the motion of swimmers sharing a beat plane. This slow evolution in relative position and direction for swimmers situated in an above-below configuration appears to be in approximate concordance with the general experimental observation that motile spermatozoa frequently appear to cross one another with little visible interaction, with examples being found in the Supplementary Movies accompanying the recent works of Tung et al. [23] and Gadêlha et al. [211], concerning bovine and human spermatozoa, respectively. Further evidenced in the Supplementary Movies of Tung et al. [23], and additionally in those accompanying the work of Ishimoto et al. [72], are the limited effects of noise on swimming behaviours, with Brownian noise typically insignificant on the lengthscale of spermatozoa and synchronization persisting over reasonable timescales. However, thorough exploration of the impacts of inter-spermatozoon variation on the pairwise behaviours reported in this Chapter represents significant and pertinent future study, in addition to detailed investigations into the effects of background flows and confined geometries.

We have seen that the pairwise dynamics of virtual spermatozoa in side-by-side and above-below configurations may be described with notable accuracy by a plane autonomous system, motivating potential future consideration of pairwise interactions of further flagellated microswimmers in this way, extending in principle the approach of Ishikawa et al. [108] though here restricted to particular swimmer configurations due to the absence of symmetry. Most significantly, analysis of these reduced systems revealed a marked disparity between the long-time dynamics of above-below and side-by-side swimming, with the latter only exhibiting behaviours of collision and separation off into the bulk fluid. Consideration of above-below dynamics led to the identification of a remarkable mode of stable pairwise swimming in virtual spermatozoa, corresponding to a stable spiral in the plane autonomous system and whose existence was confirmed *in silico* by long-time simulation of a swimming pair. These behaviours are in partial agreement with general classical conclusions drawn from representing swimmers as a force dipole, valid in the far-field for lone swimmers, which predicts that pushers like our virtual spermatozoa will in general attract one

another [31], evidenced here by the noted reorientation of side-by-side swimmers. We have further seen that near-field effects are significant in determining swimmer interactions and indeed give rise to a behavioural anisotropy that is not a feature of this most simple of far-field swimmer representations, with stable swimming only being observed here for above-below spermatozoa. The similar study of Llopis et al. [197], concerning active bead chains, found that both above-below and side-by-side swimmers ultimately swim away from one another, further suggesting that the predicted interactions of nearby swimmers are sensitive to the inclusion or neglect of complex cellular morphology.

The existence of a stable swimming mode *in silico* raises the hypothesis that *in vitro* spermatozoa may swim stably as pairs even without adhering to one another, though the potentially complex effects of variation between individual swimmers are unclear and require detailed consideration. Indeed, throughout, we have considered spermatozoa equipped with a synchronised kinematic description of their flagellar beating. Relaxation of this assumption necessitates careful treatment of the governing elastohydrodynamics and the internal molecular motor dynamics in order to fully capture the complex interactions between flow field and flagella and is particularly likely to be a topic of significant future study, as is the study of bound swimming sperm in the context of rodent sperm trains [188, 214].

Having simulated the behaviours of nearby swimmers using a high-accuracy boundary element method, we have explored the qualitative accuracy of a simplified coarse-grained approach for multi-swimmer simulation, as implemented by Ishimoto and Gaffney [74]. We have seen that this simplified approach is sufficient to capture qualitative features of side-by-side swimming, supporting its use in such circumstances. However, poor agreement between this methodology and the boundary element calculations was noted for above-below swimmers, with the singularity representation failing to reproduce the anisotropy associated with our planar beaters. This highlights the complexity of the near-field interactions of these flagellated swimmers, which are more intricate than is captured by our intuitive physical interpretation of the flow field via such a low-dimensional singularity representation, though differences between methodologies in predicted flow-field magnitude in the very near field, as seen in Figure 4.3.5, may also contribute to the observed behavioural disparity. As the singularity method utilises only regularised Stokeslets in its low-dimensional representations of the swimmers, we hypothesise that the inclusion of higher-order singularities may render enhanced anisotropy and improve its efficacy for simulating the motion of out-of plane swimming pairs, which is a potential direction for the

refinement of this methodology. Without such an augmentation, the methodology of Ishimoto and Gaffney [74] appears unreliable for three-dimensional pairwise interactions in general, though is suitably accurate for in-plane interactions whilst affording significant computational simplicity and scalability to population-level models.

In summary, we have examined the behavioural consequences of hydrodynamic interactions between two synchronised flagellated swimmers moving in three dimensions, identifying a range of complex and subtle pairwise behaviours in virtual spermatozoa. Long-time considerations using high-accuracy boundary element simulations revealed diverse behavioural modes that are configuration dependent, with side-by-side swimming invariably resulting in collision or separation into the bulk. Throughout, we have seen evidenced an anisotropy in the dynamics of nearby swimming, with proximity able to effect both increases and decreases in swimming speed depending on swimmer configuration, though such subtleties may not be captured by simulations using only low-order singularity representations of swimmers. Further, we have found a disparity in the timescales of relative motion between above-below and side-by-side swimming, and have also noted that reductions to low-dimensional autonomous systems can well describe pairwise swimmer dynamics. Finally, from analysis of such systems we have identified a remarkable swimming mode in synchronised virtual spermatozoa, one corresponding to stable pairwise swimming.

Appendix

4.A Parameterisation of the virtual spermatozoon head

With respect to the swimmer-fixed reference frame of spermatozoon $i \in \{1, 2\}$, denoted $x_{i1}x_{i2}x_{i3}$, as defined in the main text, we parameterise the swimmer head by length parameter $\xi \in [0, L_\mathrm{h}]$ and $\eta \in [0, 2\pi)$, where L_h denotes the length of the virtual spermatozoon head, taken to be 4.5 µm. Adopting the idealised geometry of Smith et al. [40], the surface of the spermatozoon head is parameterised by $(x_{i1}, x_{i2}, x_{i3}) = (-\xi, r\sin\eta, r\cos\eta)$, where r is given in terms of ξ and η by

$$r^2 = \frac{1 - (2\xi/L_h - 1)^2}{\beta_1^2 \sin\eta^2 + \beta_2^2 \cos\eta^2}\beta_1^2\beta_2^2\,, \tag{4.5}$$

$$\beta_1 = r_1 - \hat{r}\sin\left(4\xi/L_h - 2\right), \tag{4.6}$$

$$\beta_2 = r_2 + \hat{r}\sin\left(4\xi/L_h - 2\right). \tag{4.7}$$

We specify the constant morphological parameters as $r_1 = 0.5\,\mu\mathrm{m}$, $r_2 = 1.25\,\mu\mathrm{m}$, and $\hat{r} = 0.28\,\mu\mathrm{m}$, representing a model human spermatozoon following Ishimoto and Gaffney [63]. Such parameters yield ellipse-like cross-sections with maximal major and minor axes of approximately 2.68 µm and 1.28 µm, respectively, as shown in Figure 4.2.1(a).

Chapter 5

Regularised non-uniform segments and no-slip elastohydrodynamics

In the previous Chapters, along with a large body of research into the dynamics and behaviours of flagellated microswimmers, we have opted to prescribe the relative motions of attached flagella based on observations from experiments. Whilst this commonplace approach has the advantage of enabling conceptually simple and computationally efficient study, it fundamentally and knowingly neglects the complex fluid-structure interactions that can occur between the viscous fluid and the elastic flagella. In the remainder of thesis, we will move away from such kinematic descriptions of flagella, instead seeking to address two core problems that arise when considering the so-called coupled *elastohydrodynamics* of an elastic filament in a viscous fluid: that of accuracy and that of computational efficiency. In this Chapter, we will look to improve upon the hydrodynamic accuracy of recent frameworks for simulating the elastohydrodynamics of a planar filament, making use of and extending my recently published slender-body theory (Walker et al. [83]). The content of this Chapter has been published in the Journal of Fluid Mechanics (Walker and Gaffney [215]).

5.1 Introduction

The coupled elastohydrodynamics of flexible slender filaments are of intense interest to a breadth of active research communities, encompassing both theoretical and experimental studies and with perspectives ranging from synthetic sensors to the biology and mechanics of cilia and flagella [85, 196, 216–220]. A comprehensive summary of the field is given in the recent review of du Roure et al. [134], which notes a particular need for further theoretical development in this area. Indeed, up until

recently, problems involving filament elastohydrodynamics have been largely out of reach due to the severe numerical stiffness associated with the dynamics of a slender body in a viscous fluid, with few studies being able to utilise large computing resources to combat this issue [123, 221, 222]. However, the work of Moreau et al. [51] sought to address such problems, integrating the governing equations of elasticity in space in order to generate a coarse-grained framework with greatly reduced numerical stiffness. Despite being a recent development in the field, this approach has already been extended by Hall-McNair et al. [135] and Walker et al. [55] to include improved non-local hydrodynamics and has been applied to the model biological problem of flagellar efficiency [136].

Common to these recent models, as well as to other treatments of slender filaments at zero Reynolds number, are simplified representations of slender-body hydrodynamics. The aforementioned work of Moreau et al. [51] utilises the resistive force theory described in Section 1.2.1, which we recall is a local relation between motion and drag that has seen widespread use since its advent in the 1950s [13, 41]. A natural path to augmenting this work is, therefore, to replace the resistive force theory with a more refined slender-body theory, such as that introduced in Section 1.2.2. However, the use of these slender theories in numerical applications often necessitates the use of many-point quadrature rules or specialised techniques to evaluate the integral of a rapidly varying kernel, such as that induced by the cancellation of terms that would otherwise result in singularities [60]. Analogous issues of cancelling singularities also plague the numerical performance of methods derived from the boundary integral formulation of Stokes equations, such as that employed in the previous Chapters. However, in the early 2000s, Cortez [75] circumvented such issues of numerical complexity by instead considering solutions of the regularly forced Stokes equations, leading to a regularised Green's function and an associated regularised theory. In turn, drawing from significant earlier study of singular slender-body theories, this led to commonplace use of a regularised slender-body theory ansatz for flow around a slender filament in terms of a force density $\boldsymbol{f}$, typically an integral over the centreline of the filament of the form

$$\boldsymbol{u}(\boldsymbol{x}) = \int \boldsymbol{K}^{\epsilon}(\boldsymbol{x}, s')\boldsymbol{f}(s')\,\mathrm{d}s'\,, \tag{5.1}$$

where $\boldsymbol{u}(\boldsymbol{x})$ is the fluid velocity at a point $\boldsymbol{x}$ and $\boldsymbol{K}^{\epsilon}$ is a regular integral kernel. Notation aside, this ansatz retains the form of the singular slender-body theory ansatz of Equation (1.7), differing only by the now-regularised nature of the kernel $\boldsymbol{K}$. The

parameter ϵ represents a lengthscale of the regularisation and the associated flow-field error, which has often been taken to be the filament radius without rigorous justification in studies of filament dynamics [55, 70, 82, 135, 223], with circular cross-sections invariably assumed. The general ansatz of Equation (5.1) is also commonly used in conjunction with the hydrodynamic no-slip condition, though is evaluated not on the surface of the body but on the filament centreline. With many approaches taking the integral kernel $\boldsymbol{K}^{\epsilon}$ to simply be the regularised point force Green's function in the appropriate domain, application of this approximate relation does not guarantee that the no-slip boundary condition is satisfied on the surface of the body. Particular issues arise at the endpoints of the filament, where more than a velocity Green's function can be required [42].

Building upon the singular work of Johnson [52] and the classical solution of Chwang and Wu [42] for a prolate ellipsoid, the recent theory of Walker et al. [83] surpasses these general shortfalls and leverages a particular choice of kernel $\boldsymbol{K}^{\chi}$, along with a systematically justified and spatially dependent regularisation parameter χ, to satisfy the no-slip boundary condition on the surface of a slender body up to errors algebraic in the body aspect ratio. This theory retains the non-singular nature and accompanying numerical simplicity of the general regularised ansatz, whilst expanding upon the scope of Johnson's work and affording systematically justified accuracy and parameterisation to a wide range of slender bodies with circular cross-sections. With such features having been absent from the recent efficient frameworks of Moreau et al. [51], Hall-McNair et al. [135], and Walker et al. [55], the primary aim of this Chapter is to incorporate the recent theory of Walker et al. [83] into the coarse-grained elastohydrodynamic framework of Walker et al. [55], enabling the efficient simulation of slender bodies with asymptotically justified hydrodynamic accuracy in the no-slip condition. In doing so, we will additionally attempt to address concerning oscillations present in the force density solutions of these frameworks, which reportedly persist even with improved filament discretisations [55, 223] and will be illustrated later.

However, whilst the incorporation of the simple ansatz of Walker et al. [83] may be achieved with relative ease, integration of the regular but rapidly varying kernels may limit the speed of computation if performed with quadrature, as implemented in the original work of Walker et al. [83]. Having built upon the works of Smith [70] and Cortez [223], respectively, Hall-McNair et al. [135] and Walker et al. [55] avoid such expensive computation by analytically integrating the kernel over the straight line segments that form the discretised centreline of the slender body, which we will refer to as the regularised Stokeslet segment (RSS) approach. Though complicated

here by a non-constant regularisation parameter χ, we will aim to proceed in a similar fashion and remove the reliance on quadrature rules in order to realise a highly efficient numerical framework for the study of slender-body elastohydrodynamics.

Hence, we will proceed by first defining the non-uniform filament problem, adopting and unifying the notation of Walker et al. [55] and Walker et al. [83] for slender-body kinematics. We will then describe a modification of the coarse-grained framework of Moreau et al. [51], similar in form to that of Walker et al. [55], and present the slender-body theory of Walker et al. [83] cast in dimensionless quantities. Having adopted a piecewise-constant discretisation of viscous force density, we then seek to perform the slender-body integrals analytically, Taylor expanding the regularisation parameter χ to yield symbolic tractability. We will then numerically evidence the improved satisfaction of the no-slip boundary condition on the surface of the filament attained with the presented methodology. In turn, we will then consider the computed profiles of force density along the centreline of the filament and their behaviour near the endpoints of the slender body.

5.2 Geometry and set-up

In this Chapter, we will consider the planar motions of a thin inextensible unshearable untwistable filament with circular cross-sections in a viscous fluid, denoting the filament centreline by $\boldsymbol{x}(s,t) = x(s,t)\boldsymbol{e}_x + y(s,t)\boldsymbol{e}_y$, without loss of generality, where $\boldsymbol{e}_x$ and $\boldsymbol{e}_y$ are constant orthogonal unit vectors in a fixed inertial reference frame and span the plane of motion. Here, $s \in [0, L]$ is an arclength parameter and L is the length of the slender object, whilst t denotes time. Subtly distinct from the notation of Section 5.1, this slenderness is captured by the dimensionless parameter ϵ, defined explicitly as

$$\epsilon = \frac{2\max_{s\in[0,L]}\{\eta(s)\}}{L} \ll 1\,, \tag{5.2}$$

where $\eta(s)$ is the non-negative radius of the filament at arclength s, having assumed local axisymmetry about the centreline. With the shape therefore entirely defined by the centreline and radius function, we may describe points on the surface of the filament as

$$\boldsymbol{x}^S(s,\phi) = \boldsymbol{x}(s) + \eta(s)\boldsymbol{e}_r(s,\phi)\,, \tag{5.3}$$

where ϕ is a cross-sectional angle. Here, $\boldsymbol{e}_r$ is a radial unit vector embedded in a transverse cross-section to the centreline. For unit tangent, normal, and binormal

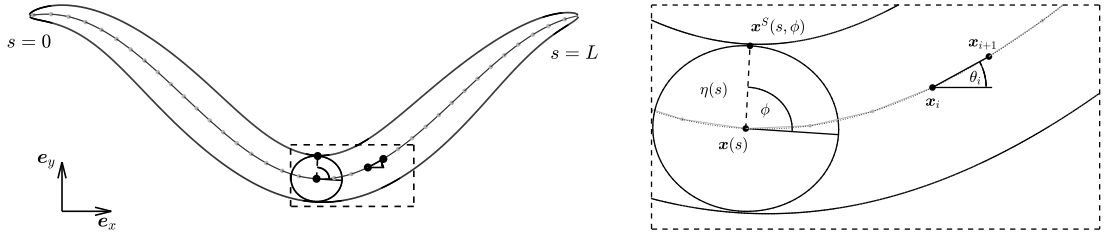

(a) (b)

Figure 5.2.1: Filament set-up and notation. (a) A general locally axisymmetric filament of total length L, with its centreline contained in a plane spanned by $\boldsymbol{e}_x$ and $\boldsymbol{e}_y$. (b) A zoomed view of the slender body, with centreline $\boldsymbol{x}(s)$ and associated surface points $\boldsymbol{x}^S(s,\phi)$ parameterised by angle ϕ at a distance $\eta(s)$ from the centreline. Discrete points are shown as grey circles, connected by solid straight line segments that approximate the smooth dotted centreline. Example such discrete points $\boldsymbol{x}_i$ and $\boldsymbol{x}_{i+1}$ are highlighted in black, with the connecting line segment defining the angle θ_i relative to the fixed $\boldsymbol{e}_x$ direction.

vectors defined by the Frenet-Serret relations

$$\boldsymbol{e}_t(s) = \frac{\partial \boldsymbol{x}}{\partial s}, \qquad \frac{\partial \boldsymbol{e}_t}{\partial s} = \theta_s \boldsymbol{e}_n(s), \qquad \boldsymbol{e}_b(s) = \boldsymbol{e}_t(s) \times \boldsymbol{e}_n(s)\,, \tag{5.4}$$

where $\theta(s,t)$ defines the filament tangent angle relative to $\boldsymbol{e}_x$, we define

$$\boldsymbol{e}_r(s,\phi) = \boldsymbol{e}_n(s)\cos\phi + \boldsymbol{e}_b(s)\sin\phi\,. \tag{5.5}$$

Here, and throughout, subscripts of s denote derivatives with respect to arclength and we have omitted writing the inherent time dependence of the filament centreline and all derived quantities. These definitions are illustrated in Figure 5.2.1.

We discretise the filament centreline into N linear segments, with the endpoints of these segments denoted by $\boldsymbol{x}(s_i)$ for uniformly spaced arclengths $s_i = (i-1)L/N \in [0, L]$, where $i = 1, \ldots, N+1$. We write $\boldsymbol{t}_i$ for the unit tangent on each linear segment, noting that this is an approximation of $\boldsymbol{e}_t(s)$ on the i^{th} segment, and parameterise these discrete tangents by $\theta(s)$, itself discretised as $\theta(s) \approx \theta_i$ on the i^{th} segment such that $\boldsymbol{t}_i = \cos\theta_i \boldsymbol{e}_x + \sin\theta_i \boldsymbol{e}_y$ for $i = 1, \ldots, N$. With this piecewise linear discretisation of $\boldsymbol{x}$ in arclength, or equivalently a piecewise constant discretisation of θ, we may describe the position of the filament with only the $N+2$ quantities $x_1, y_1, \theta_1, \ldots, \theta_N$, where $\boldsymbol{x}_1 = x_1 \boldsymbol{e}_x + y_1 \boldsymbol{e}_y$. Explicitly, for $j = 1, \ldots, N+1$, we have

$$\boldsymbol{x}_j = \boldsymbol{x}_1 + \sum_{i=1}^{j-1} (\cos\theta_i \boldsymbol{e}_x + \sin\theta_i \boldsymbol{e}_y)\Delta \mathrm{s}\,, \tag{5.6}$$

where $\Delta \mathrm{s}$ is the constant segment length, equivalently defined as $\Delta \mathrm{s} = L/N$. Differentiating with respect to time, denoting time derivatives with a dot, this gives the

linear velocity of the material point $\boldsymbol{x}_j$ as

$$\dot{\boldsymbol{x}}_j = \dot{\boldsymbol{x}}_1 + \sum_{i=1}^{j-1}(-\sin\theta_i \boldsymbol{e}_x + \cos\theta_i \boldsymbol{e}_y)\dot{\theta}_i \Delta \mathrm{s}\,. \tag{5.7}$$

We may concisely write this latter linear relation as

$$\boldsymbol{Q}\dot{\boldsymbol{\theta}} = \dot{\boldsymbol{X}}\,, \tag{5.8}$$

where $\boldsymbol{\theta} = [x_1, y_1, \theta_1, \ldots, \theta_N]^T$, $\boldsymbol{X} = [x_1, y_1, \ldots, x_{N+1}, y_{N+1}]^T$, and $\boldsymbol{Q}$ is the linear operator encoding Equation (5.7), the latter having dimension $(2N+2) \times (N+2)$ and given explicitly in the work of Walker et al. [55]. Hence, we may readily cast expressions involving $\dot{\boldsymbol{X}}$ in terms of the reduced variables $\boldsymbol{\theta}$ and their time derivatives.

The equations governing the surrounding fluid medium will be the familiar Newtonian Stokes equations, valid in the inertia-free limit of zero Reynolds number, which we will assume throughout. Previously noted for flagellated swimmers though true more generally, this limit is relevant to a broad range of biological and physical circumstances, such as the bending of cilia in flow. Once again, the Stokes equations may be briefly restated as

$$\mu\nabla^2\boldsymbol{u} = \nabla p\,, \quad \nabla\cdot\boldsymbol{u} = 0\,, \tag{5.9}$$

where $\boldsymbol{u}$ is the fluid velocity, μ is the associated viscosity, and p is the pressure. Here, we will also assume that the flow is in an unbounded domain in the exterior of the filament and decays to zero in the far field.

5.3 No-slip elastohydrodynamics

5.3.1 Coarse-grained mechanics

We follow Moreau et al. [51], stating the governing equations of elasticity for this slender inextensible unshearable filament in pointwise form as

$$\boldsymbol{n}_s - \boldsymbol{f} = \boldsymbol{0}\,, \tag{5.10}$$

$$\boldsymbol{m}_s + \boldsymbol{x}_s \times \boldsymbol{n} = \boldsymbol{0}\,, \tag{5.11}$$

for contact force and couple denoted $\boldsymbol{n}$ and $\boldsymbol{m}$, respectively, and where a subscript of s again denotes differentiation with respect to arclength. Here, and throughout, the filament is passive, with no driving internal couple, and $\boldsymbol{f}$ denotes the force per unit length applied on the surrounding fluid by the filament. Note that the external

couple per unit length exerted by the fluid on the filament is $O(\epsilon^2)$, following the result of Chwang and Wu [224] for a circular cylinder, which will be negligible at the level of asymptotic approximation that we will consider in this Chapter. To proceed, we integrate these equations with respect to arclength s, yielding

$$-\sum_{j=1}^{N} \int_{s_j}^{s_{j+1}} \boldsymbol{f}(s)\,\mathrm{d}s = \boldsymbol{n}(0)\,, \tag{5.12}$$

$$-\sum_{j=i}^{N} \int_{s_j}^{s_{j+1}} (\boldsymbol{x}(s) - \boldsymbol{x}_i) \times \boldsymbol{f}(s)\,\mathrm{d}s = \boldsymbol{m}(s_i)\,, \quad i = 1, \ldots, N\,, \tag{5.13}$$

where we have decomposed the integrals into those over discrete segments and integrated the pointwise moment balance from $s = s_i$ to $s = s_{N+1} = L$ for $i = 1, \ldots, N$. In writing Equations (5.12) and (5.13), we have assumed that the filament is force and moment free at $s = L$, equivalent to imposing $\boldsymbol{n}(L) = \boldsymbol{m}(L) = \boldsymbol{0}$. We will additionally assume that these conditions hold at the base, so that $\boldsymbol{n}(0) = \boldsymbol{m}(0) = \boldsymbol{0}$, though each of these boundary conditions may be readily replaced with those appropriate for particular problem settings, for example, the clamping of one end of the filament. Recalling that the considered filament motion is purely planar, each term of Equation (5.13) is proportional to $\boldsymbol{e}_x \times \boldsymbol{e}_y = \boldsymbol{e}_z$, with $\boldsymbol{m}(s_i) = m(s_i)\boldsymbol{e}_z$, so that Equation (5.13) collapses onto N scalar equations. We adopt a simple constitutive law, writing $m(s_i) = EI\theta_s(s_i) \approx EI(\theta_i - \theta_{i-1})/\Delta\mathrm{s}$ for bending stiffness EI, valid for $i = 2, \ldots, N$.

Illustrated in Figure 5.3.1, we discretise the force density $\boldsymbol{f}$, adopting a piecewise constant representation that is distinct from that of θ, which we will justify below. Denoting the value taken by $\boldsymbol{f}$ at the segment endpoints $\boldsymbol{x}_j$ by $\boldsymbol{f}_j$, for $j = 1, \ldots, N+1$, we discretise $\boldsymbol{f}$ as

$$\boldsymbol{f}(s) = \begin{cases} \boldsymbol{f}_i\,, & s \in [s_i, s_i + \frac{\Delta\mathrm{s}}{2})\,, \\ \boldsymbol{f}_{i+1}\,, & s \in [s_i + \frac{\Delta\mathrm{s}}{2}, s_{i+1})\,, \end{cases} \tag{5.14}$$

where $i \in \{2, \ldots, N-1\}$ is such that $s \in [s_i, s_{i+1})$. This is equivalent to stating that, on segments $i = 2, \ldots, N-1$, the value taken by $\boldsymbol{f}$ is equal to that at the closest segment endpoint, with the i^{th} segment effectively split into two halves. The definition on the first and last segments is similar, though the segment is not precisely split into two equal parts, which will enable a concise description of the slender-body theory in Section 5.3.2. Defining $e = \sqrt{1-\epsilon^2}$ to be the effective filament eccentricity, on the first segment we take

$$\boldsymbol{f}(s) = \begin{cases} \boldsymbol{f}_1\,, & s \in [s_1, s_L^\star)\,, \\ \boldsymbol{f}_2\,, & s \in [s_L^\star, s_2) \end{cases} \qquad \text{for } s_L^\star = \frac{1}{2}\left(\frac{L(1-e)}{2} + \Delta\mathrm{s}\right)\,, \tag{5.15}$$

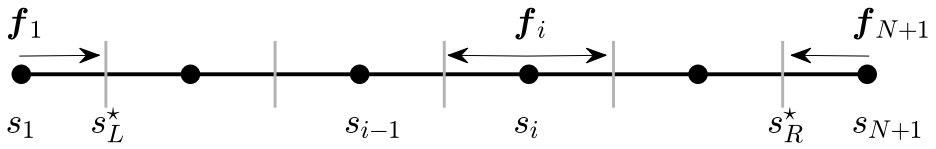

Figure 5.3.1: Illustration of the piecewise-constant force density discretisation. The horizontal line represents arclength s, with the discrete arclengths s_i corresponding to segment endpoints shown as black circles. The force density $\boldsymbol{f}$ is approximated as taking the value $\boldsymbol{f}_i$ in a neighbourhood of the arclength s_i, typically between the midpoints $(s_{i-1} + s_i)/2$ and $(s_i + s_{i+1})/2$ of the adjacent segments, which are shown as vertical grey lines. The exceptional cases are on the first and final segments, where the midpoints are replaced with $s_L^\star$ and $s_R^\star$, respectively, in order to simplify the later description of the hydrodynamic slender-body theory.

whilst on the last segment we analogously have

$$\boldsymbol{f}(s) = \begin{cases} \boldsymbol{f}_N\,, & s \in [s_N, s_R^\star)\,, \\ \boldsymbol{f}_{N+1}\,, & s \in [s_R^\star, s_{N+1}) \end{cases} \qquad \text{for } s_R^\star = \frac{1}{2}\left(\frac{L(3+e)}{2} - \Delta\mathrm{s}\right). \tag{5.16}$$

The dependence of the discretisation on the filament aspect ratio is inherited from the particular slender-body ansatz that we will later make use of in Section 5.3.2, with there otherwise being no obvious geometrical motivation for making this choice here.

Overall, whilst this discretisation is somewhat cumbersome, with the first and last segments being treated differently to the others, we have found that it yields significant advantages over simpler piecewise constant and linear schemes found in the literature. In particular, attempts at a piecewise linear approximation, as in Walker et al. [55], result in large endpoint oscillations in the computed values of $\boldsymbol{f}$, akin to those found in the regularised Stokeslet segment methodology of Cortez [223], which are examined further in Section 5.4.3.2, where we evidence a lack of such oscillations in the approach presented in this Chapter. A natural alternative, in which $\boldsymbol{f}$ is constant on each segment, yields equivalently undesirable results, with the methodology becoming numerically intractable due to stiffness when considering nearly straight filaments. Indeed, the same issue is present in the scheme proposed by Hall-McNair et al. [135], which utilises this intuitive discretisation. Though these issues are circumvented by the approach presented in this Chapter, the source of this sensitive numerical dependence of the filament problem on discretisation remains unclear and warrants future investigation.

Returning to the now-discretised filament problem, the force-density dependence of Equations (5.12) and (5.13) may be cast as a simple linear operator, denoted by $\boldsymbol{B}$, allowing us to write

$$-\boldsymbol{B}\boldsymbol{F} = \boldsymbol{R}\,, \tag{5.17}$$

where $\boldsymbol{R} = [0, 0, m(s_1), \ldots, m(s_N)]^T$ encodes the bending moments and total force acting on the filament, whilst $\boldsymbol{F} = [\boldsymbol{f}_1 \cdot \boldsymbol{e}_x, \boldsymbol{f}_1 \cdot \boldsymbol{e}_y, \ldots, \boldsymbol{f}_{N+1} \cdot \boldsymbol{e}_x, \boldsymbol{f}_{N+1} \cdot \boldsymbol{e}_y]^T$ is the vector of discretised force densities. The first two rows $\boldsymbol{B}_1$ and $\boldsymbol{B}_2$ of $\boldsymbol{B}$ represent total force balance over the filament and are given explicitly by

$$\boldsymbol{B}_1 = \frac{\Delta \mathrm{s}}{2}[1 + d, 0, 2 - d, 0, 2, 0, \ldots, 2, 0, 2 - d, 0, 1 + d, 0]\,, \tag{5.18}$$

$$\boldsymbol{B}_2 = \frac{\Delta \mathrm{s}}{2}[0, 1 + d, 0, 2 - d, 0, 2, 0, \ldots, 2, 0, 2 - d, 0, 1 + d]\,, \tag{5.19}$$

where $d = L(1 - e)/(2\Delta \mathrm{s})$. The remaining rows $\boldsymbol{B}_{i+2}$ encode the integrated moment balance equations for $i = 1, \ldots, N$, the expressions for which are given in Appendix 5.A.

We now suppose that an invertible linear operator $\boldsymbol{A}$ may be constructed such that

$$\dot{\boldsymbol{X}} = \boldsymbol{A}\boldsymbol{F}(1 + O(\epsilon))\,, \tag{5.20}$$

which we will find explicitly in Section 5.3.2 and links filament kinematics to viscous forces. Upon substitution of Equation (5.20) into Equation (5.17), also making use of Equation (5.8), we obtain the leading-order coarse-grained linear system

$$-\boldsymbol{B}\boldsymbol{A}^{-1}\boldsymbol{Q}\dot{\boldsymbol{\theta}} = \boldsymbol{R}\,, \tag{5.21}$$

where $\boldsymbol{B}$ encodes the integrated equations of elasticity, $\boldsymbol{A}$ represents the hydrodynamic relation between velocity and force density, $\boldsymbol{Q}$ links the kinematic descriptions of the filament, and $\boldsymbol{R}$ is the elastic response of the filament to bending[1].

Finally, we non-dimensionalise lengths by filament half-length $L/2$, forces with $4EI/L^2$, and time with some characteristic timescale T. This yields the dimensionless system

$$-E_h\hat{\boldsymbol{B}}\hat{\boldsymbol{A}}^{-1}\hat{\boldsymbol{Q}}\dot{\hat{\boldsymbol{\theta}}} = \hat{\boldsymbol{R}}\,, \quad E_h = \frac{\pi\mu L^4}{2EI\,T}\,, \tag{5.22}$$

where the notation $\hat{\cdot}$ denotes dimensionless quantities and we note that the rescaled arclength parameter is $\hat{s} = 2s/L \in [0, 2]$. The elastohydrodynamic number E_h here is analogous to that of Walker et al. [55], though differs by a factor of 16 due to differing choices of lengthscale. We have the explicit relations

$$\boldsymbol{B} = \frac{L^2}{4}\hat{\boldsymbol{B}}\,, \quad \boldsymbol{A} = \frac{1}{8\pi\mu}\hat{\boldsymbol{A}}\,, \quad \boldsymbol{Q}\dot{\boldsymbol{\theta}} = \frac{L}{2T}\hat{\boldsymbol{Q}}\dot{\hat{\boldsymbol{\theta}}}\,, \quad \boldsymbol{R} = \frac{2EI}{L}\hat{\boldsymbol{R}}\,, \tag{5.23}$$

between dimensional and dimensionless quantities, having multiplied the force balance equations by $\Delta \mathrm{s}/2$ and absorbed the dimensional scalings of x_1, y_1 into $\boldsymbol{Q}$ for

[1]Note that $\boldsymbol{R}$ also encodes the total force acting on the filament.

convenience, writing $\hat{\boldsymbol{\theta}} = (\hat{x}_1, \hat{y}_1, \theta_1, \ldots, \theta_N)^T$. In what follows, we will drop the $\hat{\cdot}$ notation for dimensionless variables, though for later convenience we first write

$$\eta(s) = \frac{L}{2}\hat{\eta}(\hat{s}) = \frac{\epsilon L}{2}\tilde{\eta}(\hat{s}) \tag{5.24}$$

and immediately drop the tilde on $\tilde{\eta}(\hat{s}) \sim O(1)$. For clarity, the points on the surface of the filament may now be written in terms of dimensionless quantities as

$$\boldsymbol{x}^S(s, \phi) = \boldsymbol{x}(s) + \epsilon\eta(s)\boldsymbol{e}_r(s, \phi)\,. \tag{5.25}$$

5.3.2 Non-uniform hydrodynamics

Before describing the slender-body theory of Walker et al. [83] that we will use to relate forces and flow, we first recapitulate the well known regularised singularities of Cortez [75] and Ainley et al. [76] on which it is built. Following Walker et al. [83], for points $\boldsymbol{\alpha}$ and $\boldsymbol{\beta}$ and the particular choices of mollifier given in Appendix 5.B, the regularised Stokeslet $\boldsymbol{S}^\chi$ and potential dipole $\boldsymbol{D}^\chi$ are given by

$$\boldsymbol{S}^\chi(\boldsymbol{\alpha}, \boldsymbol{\beta}) = \frac{(|\boldsymbol{\alpha} - \boldsymbol{\beta}|^2 + 2\chi)\boldsymbol{I}}{(|\boldsymbol{\alpha} - \boldsymbol{\beta}|^2 + \chi)^{3/2}} + \frac{\boldsymbol{T}(\boldsymbol{\alpha}, \boldsymbol{\beta})}{(|\boldsymbol{\alpha} - \boldsymbol{\beta}|^2 + \chi)^{3/2}}\,, \tag{5.26}$$

$$\boldsymbol{D}^\chi(\boldsymbol{\alpha}, \boldsymbol{\beta}) = -\frac{(|\boldsymbol{\alpha} - \boldsymbol{\beta}|^2 - 2\chi)\boldsymbol{I}}{(|\boldsymbol{\alpha} - \boldsymbol{\beta}|^2 + \chi)^{5/2}} + \frac{3\boldsymbol{T}(\boldsymbol{\alpha}, \boldsymbol{\beta})}{(|\boldsymbol{\alpha} - \boldsymbol{\beta}|^2 + \chi)^{5/2}}\,, \tag{5.27}$$

where $\boldsymbol{T}(\boldsymbol{\alpha}, \boldsymbol{\beta}) = (\boldsymbol{\alpha} - \boldsymbol{\beta}) \otimes (\boldsymbol{\alpha} - \boldsymbol{\beta})$, $\boldsymbol{I}$ is the 3×3 identity tensor, and χ is the regularisation parameter.

Throughout this section, it will be convenient to consider functions of filament arclength instead as functions of a shifted arclength parameter $s' \in [-1, 1]$, which will greatly simplify the notation associated with the slender-body theory of Walker et al. [83]. We will consistently abuse notation and write $\boldsymbol{x}(s) \equiv \boldsymbol{x}(s')$, where $s = s' + 1$ and other functions of arclength are treated analogously. In particular, this enables us to concisely define the arclength-dependent regularisation parameter $\chi = \chi(s')$, which may be written as

$$\chi(s') = \epsilon^2[(1 - s'^2) - \eta^2(s')]\,. \tag{5.28}$$

This choice of regularisation parameter ensures a convenient form of the regularised Stokeslet and potential dipole when evaluated on the surface of the slender body, as discussed in detail in the work of Walker et al. [83].

The analysis of Walker et al. [83] imposed a restriction on the derivative of $\chi(s')$, requiring $\mathrm{d}\chi(s')/\mathrm{d}s' = O(\epsilon^2)$ in order to Taylor expand $\chi(s')$ with sufficiently small

error in an inner region. However, we remark that this may in fact be relaxed to a Lipschitz condition on $\chi(s')$, with differentiability of $\chi(s')$ no longer required by the slender theory. Precisely, the error analysis of Walker et al. [83, Eq. 3.21] still holds if $\chi(s')$ satisfies a Lipschitz condition with constant $L_\chi = O(\epsilon^2)$, which in turn is satisfied if $\eta^2(s')$ is Lipschitz with an $O(1)$ constant. This serves to explain the numerical explorations of Walker et al., in which the consideration of non-differentiable $\chi(s')$ was noted to not result in large errors in the slender theory, despite the violation of differentiability assumptions.

Returning to our hydrodynamic formulation and recalling the effective filament eccentricity as $e = \sqrt{1-\epsilon^2}$, the dimensionless ansatz of Walker et al. [83] for the fluid velocity at a point $\boldsymbol{y}$ in terms of the force per unit length $\boldsymbol{f}(s')$ may now be written as

$$\boldsymbol{u}(\boldsymbol{y}) = \int_{-e}^{e} \left[\boldsymbol{S}^{\chi(s')}(\boldsymbol{y}, \boldsymbol{x}(s')) - \frac{1-e^2}{2e^2}(e^2 - s'^2)\boldsymbol{D}^{\chi(s')}(\boldsymbol{y}, \boldsymbol{x}(s')) \right] \boldsymbol{f}(s')\,\mathrm{d}s' \,, \tag{5.29}$$

noting that the dimensional factor of $8\pi\mu$ has been absorbed by the scalings of Equation (5.23). Note that the limits in the integral are between $-e$ and e, rather than -1 and 1, as inherited ultimately from the Chwang and Wu [42] solution for a translating prolate ellipsoid, as detailed in Walker et al. [83]. Taking $\boldsymbol{y} = \boldsymbol{x}^S(s_i', \phi)$, where $s_i' = s_i - 1$ are the shifted dimensionless arclengths corresponding to the discrete points s_i, we may apply this ansatz at the filament surface to generate the $N+1$ vector equations

$$\begin{aligned} \boldsymbol{u}(\boldsymbol{x}^S(s_i', \phi)) = \int_{-e}^{e} \Bigg[& \boldsymbol{S}^{\chi(s')}(\boldsymbol{x}^S(s_i', \phi), \boldsymbol{x}(s')) \\ & - \frac{1-e^2}{2e^2}(e^2 - s'^2)\boldsymbol{D}^{\chi(s')}(\boldsymbol{x}^S(s_i', \phi), \boldsymbol{x}(s')) \Bigg] \boldsymbol{f}(s')\,\mathrm{d}s' \,. \end{aligned} \tag{5.30}$$

We impose the no-slip condition $\boldsymbol{u}(\boldsymbol{x}^S(s_i', \phi)) = \dot{\boldsymbol{x}}^S(s', \phi)$ on the surface of the filament and decompose

$$\dot{\boldsymbol{x}}^S(s', \phi) = \dot{\boldsymbol{x}}(s') + \epsilon\eta(s')\boldsymbol{\omega}(s') \times \boldsymbol{e}_r(s', \phi) \tag{5.31}$$

for centreline velocity $\dot{\boldsymbol{x}}(s')$ and angular velocity $\boldsymbol{\omega}(s')$ measured about $\boldsymbol{x}(s')$, recalling that the filament is assumed to be unshearable. Supposing that $\boldsymbol{\omega}$ is $O(1)$ as $\epsilon \to 0$, consistent with the filament being assumed untwistable and planar, at leading order we simply have

$$\dot{\boldsymbol{x}}^S(s', \phi) = \dot{\boldsymbol{x}}(s') + O(\epsilon) \,, \tag{5.32}$$

independent of ϕ. Finally, we arrive at the leading-order relation

$$\dot{\boldsymbol{x}}(s_i') \approx \int_{-e}^{e} \Big[\boldsymbol{S}^{\chi(s')}(\boldsymbol{x}^S(s_i', \phi), \boldsymbol{x}(s')) - \frac{1-e^2}{2e^2}(e^2 - s'^2)\boldsymbol{D}^{\chi(s')}(\boldsymbol{x}^S(s_i', \phi), \boldsymbol{x}(s')) \Big] \boldsymbol{f}(s')\,\mathrm{d}s' \,. \quad (5.33)$$

For comparison, the equivalent expression used in the method of regularised Stokeslet segments, and indeed many regularised slender-body theories [80, 82, 221], may be written as

$$\dot{\boldsymbol{x}}(s_i') \approx \int_{-1}^{1} \boldsymbol{S}^{\frac{\epsilon^2}{4}}(\boldsymbol{x}(s_i'), \boldsymbol{x}(s'))\boldsymbol{f}(s')\,\mathrm{d}s' \,, \quad (5.34)$$

where we note, in particular, that the evaluations of the regularised Stokeslet kernel are on the filament centreline, not on the surface of the slender body, and the regularisation parameter is fixed.

Though the left-hand side of Equation (5.33) is trivially independent of the cross-sectional angle ϕ, it is not clear if the integral is similarly independent. However, with the particular choice of regularisation parameter $\chi(s')$ given in Equation (5.28), Walker et al. [83] showed that the integral of Equation (5.30) is in fact independent of ϕ at leading order in ϵ, with errors linear in the aspect ratio[2]. Thus, Equation (5.33) satisfies this necessary condition. Moreover, its solution enables the no-slip condition on the surface of the filament to be satisfied to $O(\epsilon)$. With the force density $\boldsymbol{f}$ discretised as described in Section 5.3.1 and incurring errors proportional to $\Delta s\,\|\mathrm{d}\boldsymbol{f}/\mathrm{d}s\|$, which are assumed small and may be verified *a posteriori*, yields the leading-order linear system

$$\dot{\boldsymbol{X}} = \boldsymbol{A}\boldsymbol{F} \quad (5.35)$$

relating force densities on the filament to the centreline velocities.

5.3.3 Regularised non-uniform segments

The entries of $\boldsymbol{A}$ may be readily computed with quadrature, as was performed in the original work of Walker et al. [83]. However, with the integral kernels rapidly varying in some regions, this can be prohibitively expensive in elastohydrodynamic simulations, where numerous evaluations of $\boldsymbol{A}$ are typically required. Inspired by the recent method of regularised Stokeslet segments, as detailed by Cortez [223] and used in the work of Walker et al. [55], we seek to evaluate these integrals analytically on

[2]The details of this justification are lengthy, so are not repeated here.

each linear segment of the filament, in general incurring discretisation errors as a result of the arclength-dependent regularisation $\chi(s')$. We will refer to this approach as the method of *regularised non-uniform segments* (RNS).

With $\boldsymbol{f}$ approximated as piecewise constant, computation of $\boldsymbol{A}$ reduces to performing a number of integrals over the discrete straight segments of the filament. We consider such an integral over the j^{th} segment, parameterised by $\alpha \in [0,1]$, on which we write $\chi = \chi(\alpha)$ and the filament centreline is given by $\boldsymbol{x}(\alpha) = \boldsymbol{x}_j - \alpha\boldsymbol{v}$, where $\boldsymbol{v} = \boldsymbol{x}_j - \boldsymbol{x}_{j+1}$. Remarkably, this formulation is applicable even to the first and last segments, subject to the substitution of $\boldsymbol{x}_1$ by $\boldsymbol{x}(-e)$ and of $\boldsymbol{x}_{N+1}$ by $\boldsymbol{x}(e)$, owing to the chosen discretisation of $\boldsymbol{f}$. With this discretised $\boldsymbol{f}$ taking the values $\boldsymbol{f}_j$ and $\boldsymbol{f}_{j+1}$ on different halves of this segment, we require expressions for the integrals evaluated on two subdomains, $\alpha \in [0, 1/2]$ and $\alpha \in [1/2, 1]$. Further, analogous to Cortez [223] and Walker et al. [55] and given explicitly in Appendix 5.C, we note that this discretisation of $\boldsymbol{f}$ has rendered each of these integrals as linear combinations of

$$T^L_{m,q} = \int_0^{\frac{1}{2}} \alpha^m R^q \,\mathrm{d}\alpha\,, \quad T^R_{m,q} = \int_{\frac{1}{2}}^1 \alpha^m R^q \,\mathrm{d}\alpha\,, \tag{5.36}$$

where we define $R = \left(\left|\boldsymbol{x}_i^S - \boldsymbol{x}_j + \alpha\boldsymbol{v}\right|^2 + \chi(\alpha)\right)^{1/2}$ for a surface point $\boldsymbol{x}_i^S = \boldsymbol{x}^S(s_i', \phi)$, with ϕ arbitrary, as above. These integrals may be readily performed in the case that R^2 is a quadratic function of α, as in the original method of regularised Stokeslet segments though here prohibited in general by $\chi(\alpha)$.

In order to recover this desirable property, we Taylor expand $\chi(\alpha)$ about an endpoint of the segment, either $\alpha = 0$ or $\alpha = 1$, assuming sufficient smoothness of χ. The expansion point is chosen in order to minimise the error in the resulting integral, noting in particular that $R(\alpha)$ can become $O(\epsilon)$ if $\boldsymbol{x}_j - \alpha\boldsymbol{v}$ nears $\boldsymbol{x}_i^S$, such as in the trivial case of $i = j$. With χ therefore plausibly the dominant term in this $O(\epsilon)$ neighbourhood, we choose to expand $\chi(\alpha)$ about the segment endpoint that is closest to $\boldsymbol{x}_i^S$, denoting the value of α at this endpoint as $\alpha^\star$. Collecting powers of α, in each case this yields an expansion of the form

$$R(\alpha)^2 = A + B\alpha + C\alpha^2 + E\,, \quad |E| \leq \begin{cases} \frac{1}{6}\alpha^3 \left|\boldsymbol{v}\right|^3 \sup\left|\frac{\mathrm{d}^3\chi}{\mathrm{d}s'^3}\right|\,, & \alpha^\star = 0\,, \\ \frac{1}{6}(1-\alpha)^3 \left|\boldsymbol{v}\right|^3 \sup\left|\frac{\mathrm{d}^3\chi}{\mathrm{d}s'^3}\right|\,, & \alpha^\star = 1\,. \end{cases} \tag{5.37}$$

In the error term E, we have bounded the third derivative of χ over the segment, and have cast the derivative in terms of the normalised arclength s' in order to unify our phrasing of model assumptions. With $R(\alpha) = O(\epsilon)$ when $\left|\boldsymbol{x}_i^S - \boldsymbol{x}_j + \alpha\boldsymbol{v}\right| = O(\epsilon)$,

and $R(\alpha)$ strictly order unity otherwise, when $\alpha^\star = 0$ this error term is subdominant if

$$\frac{1}{6}\alpha^3 \Delta \mathrm{s}^3 \sup \left| \frac{\mathrm{d}^3 \chi}{\mathrm{d}s'^3} \right| = \begin{cases} O(\epsilon^3) , & \text{where } \left| \boldsymbol{x}_i^S - \boldsymbol{x}_j + \alpha \boldsymbol{v} \right| = O(\epsilon) , \\ O(\epsilon) , & \text{otherwise,} \end{cases} \tag{5.38}$$

noting that $|\boldsymbol{v}| \leq \Delta \mathrm{s}$, with a similar expression required for $\alpha^\star = 1$. This imposes a weak restriction on the derivatives of χ and the discretisation length $\Delta \mathrm{s}$, recalling that $\chi = O(\epsilon^2)$ everywhere, though we remark that these differentiability assumptions may be relaxed if a sufficiently accurate quadratic approximation to $\chi(s')$ was nevertheless available. Recalling Equation (5.28), these assumptions translate into similar conditions on $\eta^2(s')$, the square of the radius function.

We proceed assuming that the differentiability restrictions of Equation (5.38) hold, whereupon we drop the error term E in what follows, approximating $R(\alpha)^2$ as a quadratic function on each segment. The segment-dependent coefficients A, B and C may be readily computed when expanding with $\alpha^\star = 0$ or $\alpha^\star = 1$; for $\alpha^\star = 0$, they are given explicitly by

$$A = \left| \boldsymbol{x}_i^S - \boldsymbol{x}_j \right|^2 + \chi , \quad B = 2\boldsymbol{v} \cdot (\boldsymbol{x}_i^S - \boldsymbol{x}_j) + |\boldsymbol{v}| \frac{\mathrm{d}\chi}{\mathrm{d}s'} , \quad C = |\boldsymbol{v}|^2 \left(1 + \frac{1}{2} \frac{\mathrm{d}^2 \chi}{\mathrm{d}s'^2} \right) , \tag{5.39}$$

where evaluations of χ and its derivatives for A, B, and C are at $\alpha = 0$ and we henceforth write $R(\alpha)^2 = A + B\alpha + C\alpha^2$ for brevity. Analogous expressions arise for A, B, and C when $\alpha^\star = 1$. As noted above and written explicitly in Appendix 5.C, the integral kernel may be decomposed into a linear combination of terms $\alpha^m R^q$ for $(m, q) \in \{(0,-1), (0,-3), (0,-5), (1,-3), (1,-5), (2,-3), (2,-5), (3,-5), (4,-5)\}$. The computation of these quantities for $m > 0$ may be performed simply via the recurrence relations

$$T^L_{m+1,q-2} = \left. \frac{\alpha^m R^q}{qC} \right|_0^{\frac{1}{2}} - \frac{m}{qC} T^L_{m-1,q} - \frac{B}{2C} T^L_{m,q-2} , \tag{5.40}$$

$$T^R_{m+1,q-2} = \left. \frac{\alpha^m R^q}{qC} \right|_{\frac{1}{2}}^1 - \frac{m}{qC} T^R_{m-1,q} - \frac{B}{2C} T^R_{m,q-2} , \tag{5.41}$$

where $qC \neq 0$. These are analogous to the recurrence of Cortez [223] and are similarly derived via integration by parts. Thus, explicit calculation of $T^L_{m,q}$ and $T^R_{m,q}$ is required only for $m = 0$, with the relevant antiderivatives given in Appendix 5.D.

Hence, the construction of the operator $\boldsymbol{A}$ proceeds simply and efficiently: the coefficients A, B, and C are evaluated from precomputed values of χ and its derivatives; the integrals $T^L_{m,q}$ and $T^R_{m,q}$ are computed for $m = 0$ using the given antiderivatives; further integrals for $m > 0$ are computed via the recurrences of Equations (5.40)

and (5.41); the entries of $\boldsymbol{A}$ are formed as linear combinations of these terms following Appendix 5.C. We additionally note that this process may be readily generalised to evaluation points that do not lie on the surface of the filament, with the only modification being to Taylor expand $\chi(\alpha)$ about the segment endpoint that is closest to the evaluation point, again seeking to minimise error when approximating $R(\alpha)$, though we do not explore this further in this Chapter.

5.4 Verification and examples

5.4.1 Efficiency and accuracy against quadrature

Construction of the operator $\boldsymbol{A}$ via the method of regularised non-uniform segments introduces local approximations of the regularisation parameter χ wherever it is not simply a quadratic function of arclength, enabling analytic integration. We now compare this approach with quadrature in terms of both accuracy and efficiency in a practical parameter regime, considering three dimensionless radius functions $\eta(s')$ of varying complexity:

$$\begin{aligned} &\text{(a)} \quad \sqrt{1-s'^2}\,, \\ &\text{(b)} \quad \sqrt{1-s'^2}(1-0.1\cos 2\pi s')\,, \\ &\text{(c)} \quad \sqrt{1-s'^2}(1.1+\sin 9\pi s')\,, \end{aligned} \tag{5.42}$$

each subject to normalisation and shown in Figure 5.4.1. Considering a filament with a curved centreline, corresponding to the initial condition of Figure 5.4.2a, with $N = 100$ and $\epsilon = 0.02$ we compute $\boldsymbol{A}$ using both the RNS methodology and the inbuilt `quadv` routine in MATLAB®, with the numerical quadrature set to a tolerance of 10^{-12} and denoting the results of these computations by $\boldsymbol{A}_{\mathrm{RNS}}$ and $\boldsymbol{A}_{\mathrm{Q}}$, respectively. We write $\mathcal{E}$ for the relative matrix infinity norm error between these two results, defined explicitly as

$$\mathcal{E} = \frac{\|\boldsymbol{A}_{\mathrm{RNS}} - \boldsymbol{A}_{\mathrm{Q}}\|_{\infty}}{\|\boldsymbol{A}_{\mathrm{Q}}\|_{\infty}}\,. \tag{5.43}$$

These relative errors are shown in Figure 5.4.1, each of which can be seen to be orders of magnitude lower than the asymptotic slenderness parameter. The rapidly varying curvature of case (c) gives rise to the largest error, consistent with the restrictions imposed on the derivatives of χ in Equation (5.38), with the derivatives of χ in case (c) being orders of magnitude greater than in cases (a) and (b). Computations were performed on modest hardware (Intel® Core™ i7-6920HQ CPU), with the wall time for the RNS methodology being over two orders of magnitude less than that of the quadrature implementation, representing a significant improvement in computational

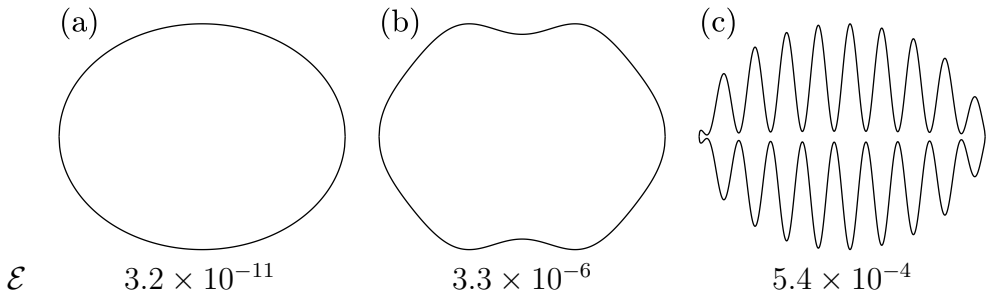

Figure 5.4.1: Example radius functions and the relative error $\mathcal{E}$ of using the RNS methodology in constructing the operator $\boldsymbol{A}$ compared with a quadrature rule of tolerance 10^{-12}. In each of the three cases, we note a small matrix infinity norm error $\mathcal{E}$, largest in case (c) where curvature of the radius function is rapidly varying. Here, we have considered a curved filament in a dimensionless framework with $N = 100$ segments, having taken $\epsilon = 0.02$ and radius functions corresponding to Equation (5.42). The filament centreline corresponds to the initial condition of Figure 5.4.2a, and shapes are shown stretched vertically for visual clarity.

efficiency for minimal reduction in accuracy. These observations of efficiency and accuracy hold for a range of considered body centrelines and radius functions, and are robust to variations in the slenderness parameter ϵ.

5.4.2 Invariants of free-filament motion

The coarse-grained framework for filament elasticity is similar to that presented and derived in the recent work of Walker et al. [55], where it was extensively verified and benchmarked, utilising the stiff solver `ode15s` provided in MATLAB® with relative and absolute tolerances of 10^{-6} [225]. However, due to the modification of considering a piecewise constant discretisation of the force density $\boldsymbol{f}$, akin to the study of Moreau et al. [51], we additionally verify the presented methodology in the case of a relaxing symmetric filament. Having taken $N = 40$ and $\epsilon = 0.02$, in Figure 5.4.2 we showcase the simulated dynamics of an initially symmetric filament relaxing to a straight configuration, during which we see that symmetry is preserved. Owing to the filament having no net force or torque act upon it, the centre of mass should not deviate from its initial position. Computing the translation of the centre of mass over the motion, a quantitative measure of framework accuracy, in Figure 5.4.2b we see that this approximate constancy is preserved numerically with errors on the order of $10^{-3}L$, improved by an order of magnitude when compared to the previous methodology of Walker et al. [55].

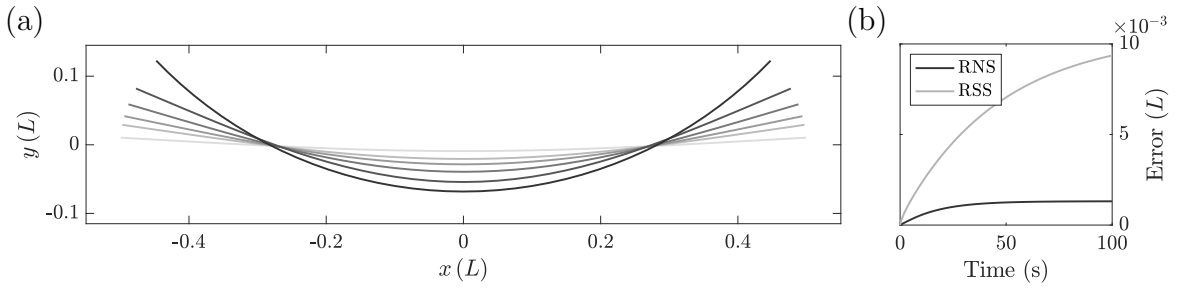

Figure 5.4.2: The relaxation of a symmetric filament, simulated with $N = 40$ segments for $E_h = 9600$. (a) Relaxation dynamics qualitatively match those of Walker et al. [55], in agreement with intuition and preserving the symmetry of the initial condition. (b) Distance translated by the centre of mass of the filament, as computed by the presented RNS methodology and the RSS approach of Walker et al. [55], analytically zero and captured approximately here, having taken $N = 40$ and $\epsilon = 0.02$. Here, we have considered a filament with dimensionless shape $\eta(s') = \sqrt{1 - s'^2}$, corresponding to a prolate ellipsoid, though note that this information is not captured by the typical slender-body ansatz, as implemented in Walker et al. [55].

5.4.3 Comparison against existing theories

We now more thoroughly compare and contrast the presented elastohydrodynamic framework against two existing approaches, specifically the published regularised Stokeslet segment (RSS) methodology of Walker et al. [55] and a resistive force theory (RFT) formulation based on that of Moreau et al. [51]. The latter RFT methodology is as described in the work of Walker et al. [55], though we make use of the resistive coefficients of Gray and Hancock [13, 41], with the normal resistive coefficient being twice that of the tangential coefficient. A detailed comparison of the existing RFT and RSS hydrodynamic methodologies is presented in the work of Walker et al. [55].

5.4.3.1 A relaxing filament

We simulate the free relaxation of a bent filament, with the θ_i initially equally spaced and increasing between $-\pi/4$ and $\pi/4$ to correspond to a filament of constant curvature, via each of the three methodologies, picking a common but arbitrary elastohydrodynamic number of $E_h = 9600$ and setting $N = 40$. The filament has aspect ratio 1:100, corresponding to $\epsilon = 0.02$ in the RNS framework and $\epsilon = 0.01$ in the RFT and RSS approaches, noting that these latter frameworks define ϵ to be the aspect ratio of the slender body. Simulating until a dimensional time of 100 s, at which point the RNS solution is nearing complete relaxation to a straight configuration, we display snapshots of the computed solutions and some associated metrics in Figure 5.4.3. Immediately evident is a qualitative similarity between the computations, though there is some pairwise disagreement throughout the motion. Most prominent are differ-

ences in the timescale of relaxation, as can be seen in the maximum curvature plot of Figure 5.4.3b, with the RFT solution relaxing more slowly than the predictions by non-local theories. We more concretely quantify the overall differences between methodologies at a given time t via the measure D, defined for a computed solution $\boldsymbol{x}(s,t)$ by

$$D(t)^2 = \frac{1}{L}\int_0^L \|\boldsymbol{x}(s,t) - \boldsymbol{x}_{\mathrm{RNS}}(s,t)\|_2^2 \,\mathrm{d}s\,, \tag{5.44}$$

relative to the RNS solution $\boldsymbol{x}_{\mathrm{RNS}}$. The evolution of this distance measure for the RFT and RSS approaches is shown in Figure 5.4.3c, and demonstrates that, whilst differences between solutions are indeed small, being on the scale of ϵ in this particular case, these distinctions persist throughout the motion.

With elastohydrodynamic simulations appearing broadly similar at the level of detail considered thus far, we also note a common computational efficiency of the frameworks, with even the more complex regularised non-uniform segments approach computing the relaxation dynamics in a number of seconds. Indeed, this is replicated throughout further testing for each of a wide array of initial conditions, and is robust to variations in the radius function $\eta(s')$ and the filament aspect ratio. Thus, despite employing a more sophisticated slender-body ansatz, we see retained in the RNS methodology the desirable efficiency associated with the existing coarse-grained frameworks, which would not be present if we were to simply apply the quadrature-based approach of Walker et al. [83].

5.4.3.2 A simple filament in flow

From the agreement seen above in the case of a relaxing filament, one might expect that the theoretical refinement offered by the RNS approach over the simpler and cruder RSS methodology is minimal in practice. However, more significant differences are indeed present.

We consider perhaps the most simple possible filament simulation: the dynamics of an initially straight filament in a uniform background flow, with a background flow $\boldsymbol{u}_b$ incorporated into the current framework via the mapping $\boldsymbol{u} \mapsto \boldsymbol{u} - \boldsymbol{u}_b$ as in the work of Walker et al. [55]. The simulated filament should exhibit trivial motion and deformation, merely translating with the background flow and retaining its straight configuration. Both the RNS and RSS methodologies successfully replicate this behaviour and solution time is negligible. However, a noted issue of methods based on regularised Stokeslet segments and similar approaches are endpoint oscillations in the

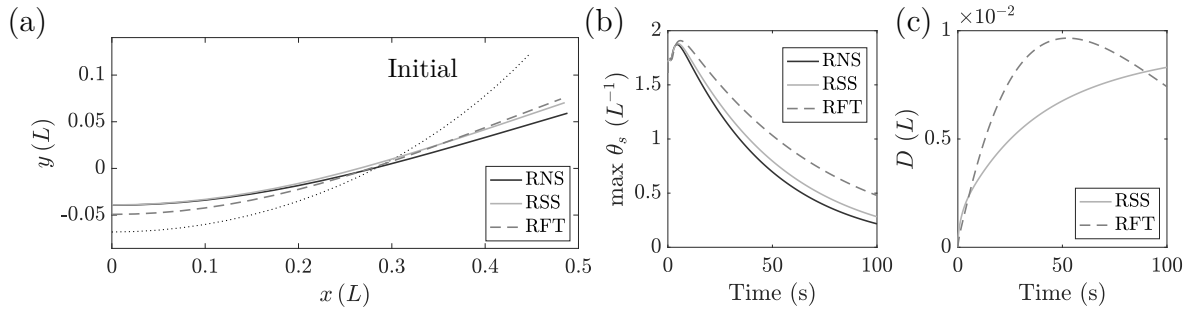

Figure 5.4.3: Comparing methodologies via the relaxation of a symmetric filament, simulated with $N = 40$ segments for $E_h = 9600$. Each starting from an initial curved configuration, shown dotted in (a), we simulate the relaxation dynamics via a resistive force theory (RFT), regularised Stokeslet segment (RSS), and regularised non-uniform segment (RNS) methodology. (a) Shown at the same instant in time (30 s) are the filament configurations as computed by the three methodologies, with the filament shapes broadly similar though showing some minor differences. Only half of the filament is shown, appealing to the preserved symmetry, and the shared initial condition is shown as a dotted curve. (b) The maximum filament curvature as a function of time, highlighting greater distinctions between the methodologies. (c) The difference between filament configurations at time t, defined by $D^2 = \int \|\boldsymbol{x} - \boldsymbol{x}_{\mathrm{RNS}}\|_2^2 \,\mathrm{d}s/L$, quantifies the difference between the RNS methodology, denoted $\boldsymbol{x}_{\mathrm{RNS}}$, and the results of the other frameworks, denoted $\boldsymbol{x}$ in turn. With a filament aspect ratio of 1:100 here, overall differences between computations appear only slight, with the exception of the longer timescale of the RFT solution compared to the non-local methodologies in (b). In the RNS framework, we have considered a filament with dimensionless shape $\eta(s') = \sqrt{1 - s'^2}$, corresponding to a prolate ellipsoid, though note that this information is not captured by the RFT or RSS frameworks.

computed force density $\boldsymbol{f}$, present in each of the works of Walker et al. [55], Cortez [223], and Hall-McNair et al. [135], which persist even with mesh refinement.

Here, we explicitly compute the force density on a straight filament of aspect ratio 1:100 in a unit background flow $\boldsymbol{u}_b = \boldsymbol{e}_y$ using both the RNS and RSS approaches, where $\boldsymbol{e}_y$ is perpendicular to the filament tangent. In Figure 5.4.4a-c, we present the magnitude of the computed force density on the filament for the body radius functions of Figure 5.4.1a-c, respectively, noting that the force density is identically zero in the direction of the filament tangent. In each case, we observe the oscillations of the RSS force density near the endpoints of the slender body, with the RSS solution being fundamentally independent of the radius function even at filament endpoints, whilst the piecewise-constant RNS solution essentially eliminates these oscillations. We have taken $N = 200$ in Figure 5.4.4c in order to capture the highly oscillatory radius function of Figure 5.4.1c, consistent with the error analysis of Section 5.3.3, taking $N = 100$ in the other cases.

Perhaps more pertinent, and indeed the motivation behind the use of the ansatz of Walker et al. [83], is the velocity boundary condition on the filament. We explicitly evaluate the flow velocity on the surface of the filament via both the RNS and RSS methods, sampling at 1000 uniformly spaced points on the surface, and show the infinity norm error in the computed velocity in Figure 5.4.4d-f as a function of dimensionless shifted arclength s'. Notably, the RSS approach is consistently inaccurate along the length of the slender body, yielding approximately 5% errors over the entire surface, corresponding to five times the regularisation parameter of the RSS method. The RNS methodology significantly improves upon this, with limitingly small error along the majority of each of the slender bodies in both Figure 5.4.4d and Figure 5.4.4e, with errors of approximately 2ϵ near the endpoints of the slender body in Figure 5.4.4e. In particular, these errors are on the same order as those found in the original evaluation of the slender-body theory by Walker et al. [83], with the impact of moving away from quadrature therefore minimal in all but Figure 5.4.4f, which is improved by reducing Δs to once again accommodate the oscillatory radius function. Thus, we observe that the use of the RNS methodology affords significant gains in the accuracy of the no-slip boundary condition over other approaches, in line with the quadrature-based findings of Walker et al. [83], though significantly improves on the efficiency of this existing quadrature-based approach. Convergence of this velocity error as a function of N and ϵ is illustrated in Appendix 5.E for the case of Figure 5.4.1b.

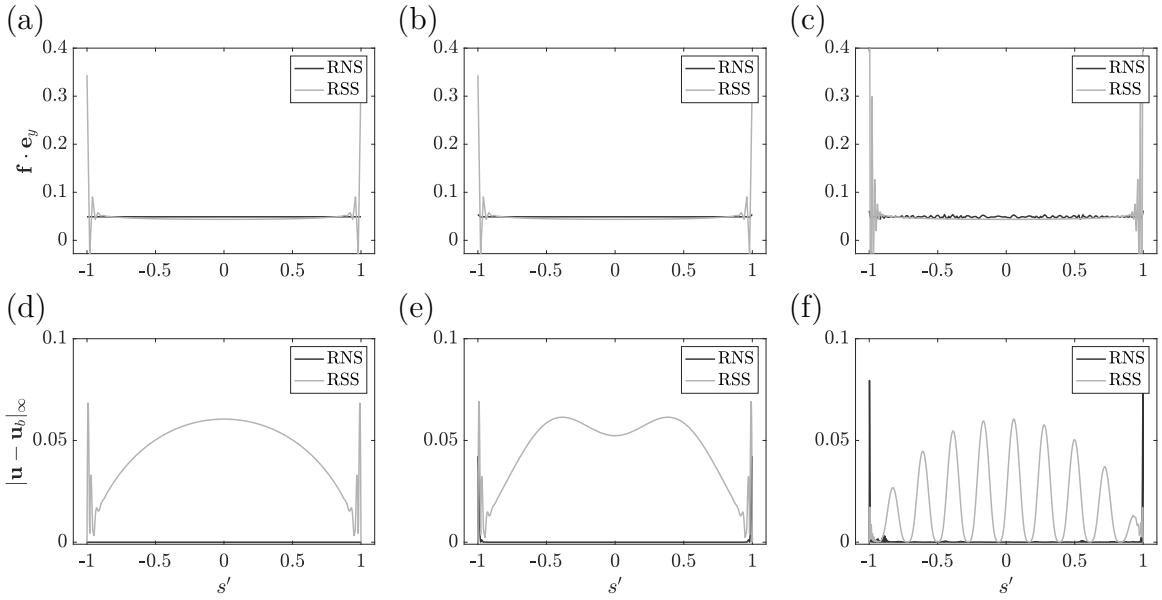

Figure 5.4.4: The computed force densities and errors in surface velocity for straight filaments in unit uniform flow. Panels (a,d), (b,e), and (c,f) correspond to the shapes shown in panels (a), (b), and (c) of Figure 5.4.1, respectively. Here, we have used an aspect ratio of 1:100, corresponding to $\epsilon = 0.02$ for the RNS methodology, and we recall that the slender-body theory upon which it is based is accurate to $O(\epsilon)$. In panels (a)-(c), we note the presence of significant oscillations near the ends of the filament for the RSS solution, absent from the RNS computation. Panels (d)-(f) report the error in the surface velocity for a unit magnitude background flow $\boldsymbol{u}_b = \boldsymbol{e}_y$, from which we note the significant improvement in accuracy afforded by the RNS methodology over the RSS approach. In particular, the RNS error is at least an order of magnitude less than the RSS error, except perhaps at the very endpoints of the filament, with the RSS methodology making little systematic attempt to satisfy the boundary condition on the surface. We have taken $N = 100$ in (a,b,d,e), whilst in (c) and (f) we have taken $N = 200$, with the highly curved radius function of Figure 5.4.1c requiring reduced Δs to yield comparable accuracy to the other, simpler cases.

5.5 Discussion and conclusions

Though the study of Moreau et al. [51] vastly increased the computational efficiency of filament simulations, it did so whilst employing resistive force theory, with this leading-order hydrodynamic relation typically conferring errors logarithmic in the filament aspect ratio. Subsequent works have extended this framework to feature improved hydrodynamics [55, 135], each making use of a simple but non-local regularised ansatz. However, even these works neglect the boundary condition on the body surface, instead evaluating velocities along the centreline when linking fluid velocity to applied force density. Via the evaluations performed in Section 5.4.3.2 of this work, we have evidenced the relative inaccuracy of such approaches, observing non-negligible errors in the computed surface velocity over the entire length of the slender body, with these hydrodynamic errors being a fundamental weakness of previous methodologies. Incorporating a refined hydrodynamic ansatz, the presented regularised non-uniform segment methodology significantly improves upon such errors, with discrepancies in the velocity boundary condition present only at the filament endpoints, given adequate discretisation to account for the level of variation in the cross-sectional radius function. In particular, the slender-body theory employed here inherently takes into account the complex shape of the filament, enabling the study of realistic slender-body geometries and replacing previous imprecise justifications with analytically derived quantifications of accuracy. Further, we noted that the differentiability assumptions in the slender theory of Walker et al. [83] may be replaced with weaker continuity conditions on the regularisation parameter χ, which represents a promising avenue for expanding the range of geometries admissible in the theory and is a direction for likely future investigation.

However, a naive incorporation of the slender-body theory of Walker et al. [83] into a coarse-grained framework of filament elasticity yielded large computation times, sacrificing the efficiency typically associated with the underlying approach of Moreau et al. [51]. Indeed, whilst the use of adaptive quadrature rules may allow computation of the hydrodynamic operator to any desired degree of numerical accuracy, the rapidly varying integral kernel of the ansatz of Walker et al. [83] prohibited rapid computation on par with the existing frameworks of Moreau et al. [51], Walker et al. [55], and Hall-McNair et al. [135]. Thus, exploiting a low-degree approximation of the unknown force density $\boldsymbol{f}$, we instead computed the necessary integrals analytically, mimicking the approach of Cortez [223] after Taylor expanding the generally non-quadratic regularisation parameter χ. Quantifying the errors associated with

this approximation, we have evidenced a remarkable accuracy and efficiency of this approach, yielding a scheme for elastohydrodynamic simulation that is comparable in computational cost to existing methodologies, whilst simultaneously improving upon their accuracy. Thus, the presented framework will enable rapid solution of the forward elastohydrodynamic problem, pertinent to modern Bayesian parameter inference techniques, for example, along with explorations of fluid-structure interactions in slender-body systems. Further, the method of regularised non-uniform segments will more generally enable rapid application of the slender-body theory of Walker et al. [83], facilitating future investigative and explorative studies into filament dynamics.

Whilst efficiency gains were made by adopting the general principle of the method of regularised Stokeslet segments, the regularised non-uniform segment approach avoids a pertinent issue associated with the principles of the former theory. Present in the works and published codes of Walker et al. [55], Cortez [223], and Hall-McNair et al. [135] are severe variations in the computed force density $\boldsymbol{f}$ near the endpoints of the considered filaments, persisting or indeed worsening with increased refinement of approximation. With force density a fundamental component of such elastohydrodynamic frameworks, these apparent errors may contribute non-negligibly to simulated dynamics and applications, particularly given the reported significance of distal activity in recent model spermatozoa [136]. Thus, the absence of comparable oscillations in the RNS solutions represents a significant advantage over these existing methodologies. Curiously, the insertion of the slender-body theory of Walker et al. [83] alone into the framework of Walker et al. [55] was not sufficient to achieve this, as discovered during an initial attempt at formulating the RNS methodology, which differs to the presented approach only by using a piecewise linear discretisation of force density $\boldsymbol{f}$. However, the combination of this improved ansatz and a lower-order discretisation of $\boldsymbol{f}$ successfully removed the unphysical oscillations from the computed solutions, yielding the smooth profiles seen in Figure 5.4.4, though detailed investigation of the Fredholm integral equation of Equation (5.1) is required in order to ascertain the source of such pervasive errors and methods for their avoidance. Future work may also include trivial extensions to the study of active filaments and general background flows, affording justified accuracy to the wide range of elastohydrodynamic problems made tractable by the work of Moreau et al. [51].

In summary, we have integrated the fundamental advance of Moreau et al. [51] and the regularised slender-body theory of Walker et al. [83], overcoming their respective shortfalls to yield a framework for the efficient and accurate simulation of slender-body elastohydrodynamics. The so-called regularised non-uniform segment approach

retains the flexibility of its parent models and, hence, may be applied to a wide variety of biological and biophysical problems to afford increased accuracy over earlier approaches. Further, complex axisymmetric filament geometries may now be reliably modelled using this framework, previously only realisable with reduced fidelity or drastically increased computational effort. Applicable even more generally, the study of this Chapter has markedly improved the efficiency of the slender-body theory of Walker et al. [83], with this work overall facilitating both the accurate quantification and large-scale no-slip simulation of slender elasticity and hydrodynamics.

Appendix

5.A Moment balance as a linear system

For $i = 1, \ldots, N$, the rows $\boldsymbol{B}_{i+2}$ of $\boldsymbol{B}$ encode the integrated moment balance in terms of the $\boldsymbol{f}_j$, resultant of integrating over segments i through N. For each i, the summation of Equation (5.13) may be written simply as

$$\sum_{j=i}^{N} \boldsymbol{I}_j \tag{5.45}$$

for integrals $\boldsymbol{I}_j$, which depend linearly on the discretised force density. For $j = 2, \ldots, N-1$, these are given by

$$\boldsymbol{I}_j = \frac{\Delta \mathrm{s}}{2}\left[\boldsymbol{x}_j - \boldsymbol{x}_i - \frac{1}{4}\boldsymbol{v}_j\right] \times \boldsymbol{f}_j + \frac{\Delta \mathrm{s}}{2}\left[\boldsymbol{x}_j - \boldsymbol{x}_i - \frac{3}{4}\boldsymbol{v}_j\right] \times \boldsymbol{f}_{j+1}\,, \tag{5.46}$$

where $\boldsymbol{v}_j = \boldsymbol{x}_j - \boldsymbol{x}_{j+1}$. For $j = 1$, again writing $d = L(1-e)/(2\Delta \mathrm{s})$, we have the modified expression

$$\begin{aligned}\boldsymbol{I}_1 = \frac{\Delta \mathrm{s}}{2}\left[(1+d)(\boldsymbol{x}_j - \boldsymbol{x}_i) - \frac{1}{4}(1+d)^2\boldsymbol{v}_1\right] \times \boldsymbol{f}_1 \\ + \frac{\Delta \mathrm{s}}{2}\left[(1-d)(\boldsymbol{x}_j - \boldsymbol{x}_i) + \left(\frac{1}{4}(1+d)^2 - 1\right)\boldsymbol{v}_1\right] \times \boldsymbol{f}_2\,,\end{aligned} \tag{5.47}$$

whilst for $j = N$ we have

$$\begin{aligned}\boldsymbol{I}_N = \frac{\Delta \mathrm{s}}{2}\left[(1-d)(\boldsymbol{x}_j - \boldsymbol{x}_i) - \frac{1}{4}(1-d)^2\boldsymbol{v}_N\right] \times \boldsymbol{f}_N \\ + \frac{\Delta \mathrm{s}}{2}\left[(1+d)(\boldsymbol{x}_j - \boldsymbol{x}_i) + \left(\frac{1}{4}(1-d)^2 - 1\right)\boldsymbol{v}_N\right] \times \boldsymbol{f}_{N+1}\,.\end{aligned} \tag{5.48}$$

These expressions are self-consistent, as taking $d = 0$ in the latter two yields expressions analogous to that of $\boldsymbol{I}_j$, and are clearly linear in the discretised force density.

5.B Choices of mollifier

In order to generate the regularised Stokeslet and potential dipole of Equations (5.26) and (5.27), we employ the mollifiers ϕ^S_χ and ϕ^D_χ, respectively. For a displacement $\boldsymbol{x}$, these are defined as

$$\phi^S_\chi(\boldsymbol{x}) = \frac{15\chi^2}{8\pi(|\boldsymbol{x}|^2+\chi)^{7/2}}\,, \quad \phi^D_\chi(\boldsymbol{x}) = \frac{3\chi}{4\pi(|\boldsymbol{x}|^2+\chi)^{5/2}}\,, \tag{5.49}$$

following Cortez [75] and Ainley et al. [76], to which we direct the interested reader for full details and the derivation of the resulting expressions.

5.C Integrals as a linear combination

We decompose the integral of Equation (5.33) over a straight segment with endpoints $\boldsymbol{x}_j$ and $\boldsymbol{x}_{j+1}$, adopting a piecewise constant discretisation of the force density $\boldsymbol{f}$, such that it takes the value $\boldsymbol{f}_j$ on the half of the segment nearest to $\boldsymbol{x}_j$, and $\boldsymbol{f}_{j+1}$ otherwise[3]. The limits of integration are determined by seeking either the coefficient of $\boldsymbol{f}_j$ or that of $\boldsymbol{f}_{j+1}$ and, for brevity, we omit such limits here and will refer instead to the placeholder $T_{m,q}$ in lieu of $T^L_{m,q}$ and $T^R_{m,q}$ in what follows, which should be appropriately substituted (see Equation (5.36)). Parameterising the straight segment by $\alpha \in [0,1]$, with $\boldsymbol{x}(\alpha) = \boldsymbol{x}_j - \alpha\boldsymbol{v}$, where $\boldsymbol{v} = \boldsymbol{x}_j - \boldsymbol{x}_{j+1}$, and taking $\boldsymbol{K}^\chi$ to be the kernel of Equation (5.33), we may write the integral over the part of the segment as

$$\int \boldsymbol{K}^\chi(\boldsymbol{x}, s')\boldsymbol{f}(s')\,\mathrm{d}s' = \boldsymbol{K}^\chi_I \boldsymbol{f}^\star\,, \tag{5.50}$$

where $\boldsymbol{f}^\star$ is the constant force density over the domain of integration, which is either $\alpha \in [0, 1/2]$ or $\alpha \in [1/2, 1]$. The operator $\boldsymbol{K}^\chi_I$ is given explicitly by

$$\boldsymbol{K}^\chi_I = |\boldsymbol{v}|\left(\boldsymbol{K}_{\boldsymbol{S}} - \frac{1-e^2}{2e^2}\left[(e^2 - s_j'^2)\boldsymbol{K}_{\boldsymbol{D}_0} - 2s_j'\,|\boldsymbol{v}|\,\boldsymbol{K}_{\boldsymbol{D}_1} - |\boldsymbol{v}|^2\,\boldsymbol{K}_{\boldsymbol{D}_2}\right]\right)\,, \tag{5.51}$$

where the outermost $|\boldsymbol{v}|$ term arises due to the change of integration variable from s' to α. In turn, the terms $\boldsymbol{K}_{\boldsymbol{S}}, \boldsymbol{K}_{\boldsymbol{D}_0}, \boldsymbol{K}_{\boldsymbol{D}_1}$, and $\boldsymbol{K}_{\boldsymbol{D}_2}$ are given by

$$\boldsymbol{K}_{\boldsymbol{S}} = +\boldsymbol{C}_{0,1}T_{0,-1} + 1(\boldsymbol{C}_{0,3}T_{0,-3} + \boldsymbol{C}_{1,3}T_{1,-3} + \boldsymbol{C}_{2,3}T_{2,-3})\,, \tag{5.52}$$

$$\boldsymbol{K}_{\boldsymbol{D}_0} = -\boldsymbol{C}_{0,1}T_{0,-3} + 3(\boldsymbol{C}_{0,3}T_{0,-5} + \boldsymbol{C}_{1,3}T_{1,-5} + \boldsymbol{C}_{2,3}T_{2,-5})\,, \tag{5.53}$$

$$\boldsymbol{K}_{\boldsymbol{D}_1} = -\boldsymbol{C}_{0,1}T_{1,-3} + 3(\boldsymbol{C}_{0,3}T_{1,-5} + \boldsymbol{C}_{1,3}T_{2,-5} + \boldsymbol{C}_{2,3}T_{3,-5})\,, \tag{5.54}$$

$$\boldsymbol{K}_{\boldsymbol{D}_2} = -\boldsymbol{C}_{0,1}T_{2,-3} + 3(\boldsymbol{C}_{0,3}T_{2,-5} + \boldsymbol{C}_{1,3}T_{3,-5} + \boldsymbol{C}_{2,3}T_{4,-5})\,. \tag{5.55}$$

[3]Here, we have replaced $\boldsymbol{x}_1$ and $\boldsymbol{x}_{N+1}$ with $\boldsymbol{x}(-e)$ and $\boldsymbol{x}(e)$, respectively, as described in the main text.

Finally, the coefficients $\boldsymbol{C}_{0,1}$, $\boldsymbol{C}_{0,3}$, $\boldsymbol{C}_{1,3}$, and $\boldsymbol{C}_{2,3}$ are determined by the choice of Taylor expansion point for χ, it being either the left or right endpoint of the segment as motivated in Section 5.3. When expanding about the left endpoint, where the shifted rescaled arclength parameter is s'_j, we have

$$\boldsymbol{C}_{0,1} = \boldsymbol{I}\,, \tag{5.56}$$

$$\boldsymbol{C}_{0,3} = \chi(s'_j)\boldsymbol{I} + \boldsymbol{w}\boldsymbol{w}^T\,, \tag{5.57}$$

$$\boldsymbol{C}_{1,3} = |\boldsymbol{v}|\,\frac{\mathrm{d}\chi}{\mathrm{d}s'}(s'_j)\boldsymbol{I} + \boldsymbol{w}\boldsymbol{v}^T + \boldsymbol{v}\boldsymbol{w}^T\,, \tag{5.58}$$

$$\boldsymbol{C}_{2,3} = \frac{1}{2}\,|\boldsymbol{v}|^2\,\frac{\mathrm{d}^2\chi}{\mathrm{d}s'^2}(s'_j)\boldsymbol{I} + \boldsymbol{v}\boldsymbol{v}^T\,, \tag{5.59}$$

with $\boldsymbol{v}$ as defined previously. Here, $\boldsymbol{w}$ joins the evaluation point to the left endpoint of the segment, which, in the case of Equation (5.33), is given as $\boldsymbol{w} = \boldsymbol{x}^S(s'_i, \phi) - \boldsymbol{x}_j$ but may be readily generalised to evaluation points off the surface of the filament, as briefly noted in Section 5.3.3. The corresponding expressions for expansion about the right endpoint are

$$\boldsymbol{C}_{0,1} = \boldsymbol{I}\,, \tag{5.60}$$

$$\boldsymbol{C}_{0,3} = \left(\chi(s'_{j+1}) - |\boldsymbol{v}|\,\frac{\mathrm{d}\chi}{\mathrm{d}s'}(s'_{j+1}) + \frac{1}{2}\,|\boldsymbol{v}|^2\,\frac{\mathrm{d}^2\chi}{\mathrm{d}s'^2}(s'_{j+1})\right)\boldsymbol{I} + \boldsymbol{w}\boldsymbol{w}^T\,, \tag{5.61}$$

$$\boldsymbol{C}_{1,3} = \left(|\boldsymbol{v}|\,\frac{\mathrm{d}\chi}{\mathrm{d}s'}(s'_{j+1}) - |\boldsymbol{v}|^2\,\frac{\mathrm{d}^2\chi}{\mathrm{d}s'^2}(s'_{j+1})\right)\boldsymbol{I} + \boldsymbol{w}\boldsymbol{v}^T + \boldsymbol{v}\boldsymbol{w}^T\,, \tag{5.62}$$

$$\boldsymbol{C}_{2,3} = \frac{1}{2}\,|\boldsymbol{v}|^2\,\frac{\mathrm{d}^2\chi}{\mathrm{d}s'^2}(s'_{j+1})\boldsymbol{I} + \boldsymbol{v}\boldsymbol{v}^T\,. \tag{5.63}$$

5.D Explicit antiderivatives

We recall the notation of Section 5.3.3, with R being defined following Equation (5.36) and expanded in Equation (5.37) via the constants A, B, C and the normalised integration variable α, which is itself defined in the discussion preceding Equation (5.36). Writing $\beta = \beta(\alpha) = B + 2C\alpha$ for brevity, the antiderivatives of $\alpha^m R^q$ for $m = 0, q \in \{-1, -3, -5\}$ may be readily computed as

$$\int R^{-1}\,\mathrm{d}\alpha = C^{-\frac{1}{2}}\log\left(\beta + 2C^{\frac{1}{2}}R(\alpha)\right), \tag{5.64}$$

$$\int R^{-3}\,\mathrm{d}\alpha = -\frac{2}{B^2 - 4AC}\,\frac{\beta}{R(\alpha)}\,, \tag{5.65}$$

$$\int R^{-5}\,\mathrm{d}\alpha = -\frac{2}{3(B^2 - 4AC)^2}\,\frac{(B^2 - 8BC\alpha - 4C(3A + 2C\alpha^2))\beta}{R(\alpha)^3}\,, \tag{5.66}$$

unless we are in the degenerate case, where $B^2 - 4AC = 0$, which yields

$$\int R^{-1} \, \mathrm{d}\alpha = C^{-\frac{1}{2}} \operatorname{sgn}(\beta) \log(\beta), \tag{5.67}$$

$$\int R^{-3} \, \mathrm{d}\alpha = -2C^{\frac{1}{2}} \frac{\operatorname{sgn}(\beta)}{\beta^2}, \tag{5.68}$$

$$\int R^{-5} \, \mathrm{d}\alpha = -4C^{\frac{3}{2}} \frac{\operatorname{sgn}(\beta)}{\beta^4}. \tag{5.69}$$

Here, we have assumed that $C > 0$, consistent with our assumptions on the derivatives of χ and the definition of C in Equation (5.39). The analysis of Walker et al. [83] and the assumptions of Equation (5.38) are sufficient to guarantee that the $R(\alpha)$ is non-zero on $\alpha \in [0, 1]$; thus, these integrals are indeed well defined.

5.E Convergence of surface velocity

For the radius function in Figure 5.4.1b, we compute the error in the surface velocity of a straight filament in unit background flow using the RNS methodology, as in Section 5.4.3.2, though here sampling at 2000 points on the surface. The maximum error over the filament surface is reported in Figure 5.E.1, showing substantial refinement as N increases for common values of slenderness parameter ϵ. Similar to the method of regularised Stokeslet segments [55, 223], for regimes with both large ϵ and N, we see that the error increases dramatically, such that the method is highly inaccurate, occurring when the parameters are approximately past the threshold $\epsilon\sqrt{N} = 1$, which is illustrated as a black dashed line in Figure 5.E.1, though this relation is purely empirical. Notably, this typical breakdown occurs outside regimes of common relevance. Regions marked with crosses correspond to errors larger than the range of the colour axis.

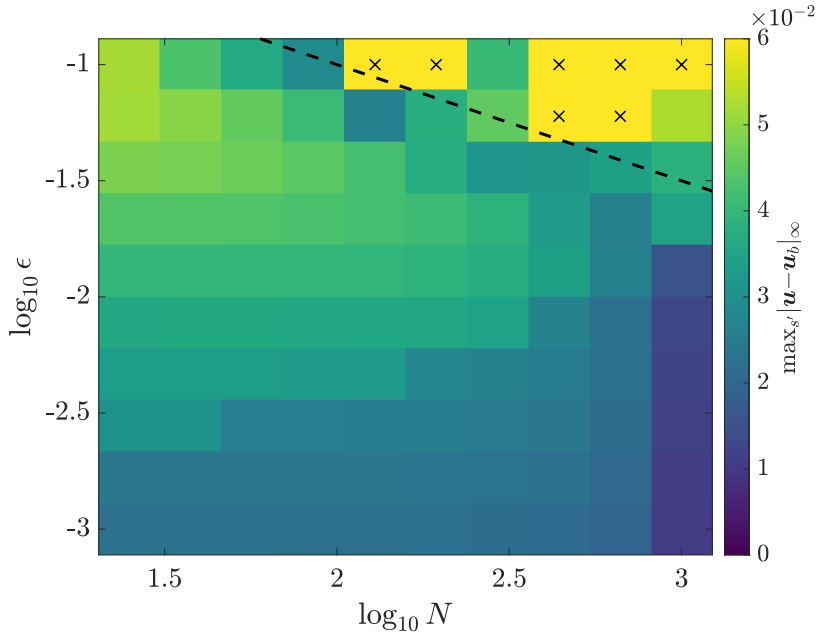

Figure 5.E.1: Surface velocity error as a function of the slenderness parameter and discretisation. We compute the maximum infinity norm error in the surface velocity over 2000 points for a straight filament with radius function as in Figure 5.4.1b and a unit background flow $\boldsymbol{u}_b = \boldsymbol{e}_y$ using the method of regularised non-uniform segments. We show in colour the error as a function of ϵ and N, with convergence apparent as N increases for most common values of ϵ. For both ϵ and N large, we see a drastic increase in error, approximately in the region bounded below by the black dashed line, which is empirically given as $\epsilon\sqrt{N} = 1$. Sections marked with a cross exhibit errors significantly larger than the range of the colour axis, though these also lie outside parameter regimes of typical relevance.

Chapter 6

Efficient simulation of filament elastohydrodynamics in three dimensions

A clear and overt shortfall of the elastohydrodynamic method described in the previous Chapter is its inherent restriction to two spatial dimensions. Indeed, such a limitation is present across contemporary efficient methodologies of this kind. The restriction to two-dimensional motion simplifies the considerations of both the filament elasticity and the slender-body hydrodynamics, with planar motion admitting concise filament representations as well as torque-free hydrodynamics. However, with the motion of biological and synthetic filaments in general not simply occurring in a plane, there remains significant scope for the development of a simulation framework that captures three-dimensional motion whilst maintaining the efficiency of these recent works. Therefore, in this final research Chapter, we will seek to lift efficient two-dimensional elastohydrodynamic approaches into three dimensions, focussing in particular on the treatment of the elastic equations. In doing so, we will generalise the work of Moreau et al. [51], encountering and circumventing issues of parameterisation with the objective of realising a framework with comparable efficiency to that of recent two-dimensional works. The content of this Chapter has been published in Physical Review Fluids (Walker et al. [226]).

6.1 Introduction

As we have seen and remarked upon throughout this thesis, the coupled elasticity and hydrodynamics of flexible inextensible filaments on the microscale are of significance to much of biology, as well as to biophysics and soft matter physics

[41, 60, 85, 216, 218, 227–230]. A fundamental barrier to much numerical investigation into this topic has been the severe stiffness associated with the equations of filament elasticity when coupled to viscous fluid dynamics. Recently, significant progress has been made in resolving the dynamics of planar filaments, with the aforementioned work of Moreau et al. [51] presenting a coarse-grained model of filament elasticity that overcame much of the stiffness previously associated with slender elastohydrodynamics. Key to this approach was the integration of the pointwise force and moment balance equations, the spatial discretisation of which yielded a relatively simple system of ordinary differential equations to solve in order to describe filament motion. However, being confined to two dimensions limits the potential scope and applicability of such a method, with three-dimensional filament motion being readily and frequently observed in a plethora of biophysical systems, such as the complex flagellar beating found in spermatozoa or the helically driven monotrichous bacterium *Escherichia coli* [227, 231].

However, for non-planar filaments in three dimensions, there is currently no methodology analogous to that of Moreau et al., with state-of-the-art frameworks still plagued by extensive numerical stiffness, necessitating costly computation to the extent that practical simulation studies have been limited and parameter space studies are largely prohibited. With three dimensions being inherently more challenging than lower dimensional settings, this field has seen developments such as the recent work of Schoeller et al. [232], which utilises a quaternion representation of filament orientation to parameterise the three-dimensional shape of the slender body. However, in this framework, numerical care is required to satisfy the inextensibility condition, with similar such consideration necessary in earlier methodologies [196, 221, 222, 233], each of which is equipped with non-local slender-body hydrodynamics and considers nearly inextensible filaments. Consequently, these existing approaches often require the use of sophisticated computing hardware in order to simulate filament motion, with typical simulations of Ishimoto and Gaffney [222] having a runtime of multiple hours on high-performance computing clusters. The recent work of Jabbarzadeh and Fu [234] compared and contrasted such nearly inextensible approaches with a truly inextensible scheme, concluding that both accuracy and efficiency were afforded by the latter in a range of biological and biophysical modelling scenarios. Despite their improved efficiency, typical wall times for these filament simulations are measured on a timescale of hours on typical hardware. Thus, there remains significant scope for the development of an efficient framework for the simulation of inextensible elastic filaments in three dimensions, one in which filament dynamics can be rapidly

computed on non-specialised hardware on timescales of seconds or minutes, thus facilitating a wealth of future studies and explorations into complex multi-parametric and previously intractable biological and physical systems.

Hence, the fundamental objective of this Chapter is to develop and describe an efficient framework for the numerical simulation of filament mechanics in three dimensions. We will build upon the recent and significant work of Moreau et al. [51], extending their approach to include an additional spatial dimension via a generalisation of the Frenet triad and integration of the governing equations of elasticity, though here we restrict the consideration of hydrodynamics to resistive force theory. We will overcome fundamental issues with simple single parameterisations of a filament in three dimensions, presenting an effective computational approach utilising adaptive reparameterisation and basis selection. We will then validate the presented framework by consideration of three candidate test problems, simulating well documented behaviours of filaments in a viscous fluid and including a side-by-side comparison against the existing and recent methodology of Ishimoto and Gaffney [222]. Finally, we will showcase the flexibility and general applicability of the presented approach by describing and exemplifying a number of methodological extensions.

6.2 Methods

6.2.1 Equations of elasticity

We consider a slender, inextensible, unshearable, cylindrical filament in a viscous Newtonian fluid, with its centreline described by $\boldsymbol{x}(s)$, parameterised by arclength $s \in [0, L]$ for dimensional filament length L. We model the filament as a Kirchhoff rod with arclength-independent material parameters, circular cross-sections, and, in the first instance, no intrinsic curvature or intrinsic torsion. Both the filament and fluid inertia are negligible for the physical scales associated with many applications, especially those associated with cellular flagella and cilia; thus, there is no inertia here and throughout. Along the filament, we have the pointwise conditions of force and moment balance, given explicitly by

$$\boldsymbol{n}_s - \boldsymbol{f} = \boldsymbol{0}\,, \tag{6.1}$$

$$\boldsymbol{m}_s + \boldsymbol{x}_s \times \boldsymbol{n} - \boldsymbol{\tau} = \boldsymbol{0}\,, \tag{6.2}$$

for contact force and torque denoted $\boldsymbol{n}$ and $\boldsymbol{m}$, respectively, and where a subscript of s denotes differentiation with respect to arclength. The quantity $\boldsymbol{f}$ is the force per

unit length applied on the fluid medium by the filament, which we will later express in terms of the filament velocity $\dot{\boldsymbol{x}}$, where here a dot denotes a time derivative. Similarly, $\boldsymbol{\tau}$ is the torque per unit length applied on the fluid medium by the filament. The inclusion of this torque in the moment balance is a key point of distinction between two and three-dimensional filaments, with this term not present in two-dimensional frameworks, such as that in Chapter 5. Whilst any standard boundary condition may be considered in the formalism below, throughout, we impose zero force and torque at the filament ends, so that

$$\boldsymbol{n}(0) = \boldsymbol{n}(L) = \boldsymbol{m}(0) = \boldsymbol{m}(L) = \boldsymbol{0}\,. \tag{6.3}$$

In the Kirchhoff framework, note that the contact force is not constitutive, but simply an undetermined Lagrange multiplier for the intrinsic constraints of inextensibility and no shearing of the filament cross-section in any direction [235]. Thus, we may eliminate $\boldsymbol{n}(s)$ at the earliest opportunity; using the boundary condition $\boldsymbol{n}(L) = 0$ and Equation (6.1) we have

$$\boldsymbol{n}(s) = -\int_s^L \boldsymbol{f}(\tilde{s})\,\mathrm{d}\tilde{s}\,. \tag{6.4}$$

This relation is also subject to the constraint that the boundary condition $\boldsymbol{n}(0) = \boldsymbol{0}$ is satisfied, generating a global force balance constraint for the applied force per unit length,

$$\boldsymbol{0} = \int_0^L \boldsymbol{f}(\tilde{s})\,\mathrm{d}\tilde{s}, \tag{6.5}$$

which we carry forward into the formalism below together with the elimination of $\boldsymbol{n}(s)$ via Equation (6.4). Thus, and as originally considered by Moreau et al. [51], integration of Equation (6.2) and use of the boundary condition $\boldsymbol{m}(L) = \boldsymbol{0}$ reveals the integrated moment balance

$$-\int_s^L \left[(\boldsymbol{x}(\tilde{s}) - \boldsymbol{x}(s)) \times \boldsymbol{f}(\tilde{s}) + \boldsymbol{\tau}(\tilde{s})\right] \mathrm{d}\tilde{s} = \boldsymbol{m}(s)\,. \tag{6.6}$$

Given a right-handed orthonormal director basis $\{\boldsymbol{d}_1(s), \boldsymbol{d}_2(s), \boldsymbol{d}_3(s)\}$, generalising the Frenet triad such that $\boldsymbol{d}_3$ corresponds to the local filament tangent, following Nizette and Goriely [236] we define the twist vector $\boldsymbol{\kappa}$ by

$$\frac{\partial \boldsymbol{d}_\alpha}{\partial s} = \boldsymbol{\kappa} \times \boldsymbol{d}_\alpha \tag{6.7}$$

for $\alpha = 1, 2, 3$. Writing $\boldsymbol{\kappa} = \sum_\alpha \kappa_\alpha \boldsymbol{d}_\alpha$, for uniform bending stiffness EI we use the Euler-Bernoulli constitutive relation of the Kirchhoff formalism to relate the contact torque $\boldsymbol{m}$ and the twist vector $\boldsymbol{\kappa}$ [235], via

$$\boldsymbol{m} = EI \left(\kappa_1 \boldsymbol{d}_1 + \kappa_2 \boldsymbol{d}_2 + \frac{1}{1+\sigma} \kappa_3 \boldsymbol{d}_3 \right) , \tag{6.8}$$

where σ is the Poisson ratio [236], assumed to be constant. With this constitutive relation, the integrated moment balance equations in the $\boldsymbol{d}_\alpha$ directions are simply

$$-\boldsymbol{d}_\alpha(s) \cdot \int_s^L \left[(\boldsymbol{x}(\tilde{s}) - \boldsymbol{x}(s)) \times \boldsymbol{f}(\tilde{s}) + \boldsymbol{\tau}(\tilde{s}) \right] \mathrm{d}\tilde{s} = \frac{EI}{1 + \delta_{\alpha,3}\sigma} \kappa_\alpha(s) , \tag{6.9}$$

for $\alpha = 1, 2, 3$ and where $\delta_{a,b}$ denotes the Kronecker delta.

6.2.2 Filament discretisation

In discretising the filament, we follow the approach of Walker et al. [55], as previously applied to planar filaments and itself building upon the earlier work of Moreau et al. [51]. We approximate the filament shape with N linear segments, each of constant length Δs, with segment endpoints having positions denoted by $\boldsymbol{x}_1, \ldots, \boldsymbol{x}_{N+1}$ and the constraints of inextensibility and the absence of cross-section shear are satisfied inherently. The endpoints of the i^{th} segment correspond to $\boldsymbol{x}_i$ and $\boldsymbol{x}_{i+1}$ for $i = 1, \ldots, N$, with the local tangent $\boldsymbol{d}_3$ being constant on each segment and denoted $\boldsymbol{d}_3^i$. In what follows, we will consider a discretisation of $\boldsymbol{d}_1$ and $\boldsymbol{d}_2$ such that they are also constant on each segment and we denote these constants similarly as $\boldsymbol{d}_1^i$ and $\boldsymbol{d}_2^i$.

We will also require the values of the $\boldsymbol{d}_\alpha$ at the endpoints of the segments, which we will similarly denote by $\bar{\boldsymbol{d}}_\alpha^j$ at the j^{th} endpoint. These are constructed from the $\boldsymbol{d}_\alpha^i$ by first considering an elementwise linear approximation, denoted by $\boldsymbol{a}_\alpha^j$, using the unique piecewise-linear interpolant[1], linearly extrapolating to yield approximations at the endpoints of the filament. However, the $\boldsymbol{a}_\alpha^j$ need not form an orthonormal basis, though such a basis may readily be constructed. Explicitly, we compute a standard singular value decomposition of the matrix representation $M_{\boldsymbol{a}} \coloneqq \left[\boldsymbol{a}_1^j, \boldsymbol{a}_2^j, \boldsymbol{a}_3^j \right]$, yielding $M_{\boldsymbol{a}} = U \Sigma V$, where the singular values of $M_{\boldsymbol{a}}$ are captured by the diagonal matrix Σ and U, V are orthogonal matrices. Owing to the linear approximation, the non-zero entries of Σ will generally be close to unity, given a sufficiently fine filament discretisation. Thus, replacing Σ with the corresponding identity matrix yields an

[1] In computing the interpolant, we assume that $\boldsymbol{d}_\alpha$ takes the value $\boldsymbol{d}_\alpha^i$ at the midpoint of the i^{th} segment.

approximation $M_{\boldsymbol{a}} \approx UV$ with column vectors that are necessarily orthonormal. The node approximations to $\boldsymbol{d}_\alpha$ are then obtained via $UV = \left[\bar{\boldsymbol{d}}_1^j, \bar{\boldsymbol{d}}_2^j, \bar{\boldsymbol{d}}_3^j\right]$.

Writing s_i for the constant arclength associated with each material point $\boldsymbol{x}_i$, so that $s_1 = 0$, for instance, we apply Equation (6.9) at each of the s_i for $i = 1, \ldots, N$, splitting the integral at the segment endpoints to give

$$-\bar{\boldsymbol{d}}_\alpha^i \cdot \sum_{j=i}^{N} \int_{s_j}^{s_{j+1}} \left[(\boldsymbol{x}(\tilde{s}) - \boldsymbol{x}_i) \times \boldsymbol{f}(\tilde{s}) + \boldsymbol{\tau}(\tilde{s})\right] \mathrm{d}\tilde{s} = \frac{EI}{1 + \delta_{\alpha,3}\sigma} \kappa_\alpha(s_i)\,, \tag{6.10}$$

for $\alpha = 1, 2, 3$. On the j^{th} segment, $\boldsymbol{x}$ may be written as $\boldsymbol{x}(s) = \boldsymbol{x}_j + \eta(\boldsymbol{x}_{j+1} - \boldsymbol{x}_j)$, where $\eta \in [0, 1]$ is given by $\eta = (s - s_j)/\Delta\mathrm{s}$. Additionally discretising the force per unit length as a continuous piecewise-linear function, with η as above, we have $\boldsymbol{f}(s) = \boldsymbol{f}_j + \eta(\boldsymbol{f}_{j+1} - \boldsymbol{f}_j)$ on the segment, where we write $\boldsymbol{f}_j = \boldsymbol{f}(s_j)$. This is distinct from the discretisation of Chapter 5, chosen for algebraic convenience. Substitution of these parameterisations into Equation (6.10) and subsequent integration yields, after simplification,

$$-\bar{\boldsymbol{d}}_\alpha^i \cdot \left(\boldsymbol{I}_i^f + \boldsymbol{I}_i^\tau\right) = \frac{EI}{1 + \delta_{\alpha,3}\sigma} \kappa_\alpha(s_i)\,, \tag{6.11}$$

where the integral contribution of the force and torque densities are denoted $\boldsymbol{I}_i^f$ and $\boldsymbol{I}_i^\tau$, respectively. With this discretisation, $\boldsymbol{I}_i^f$ has reduced to

$$\boldsymbol{I}_i^f = \sum_{j=i}^{N} \left\{ \left[\frac{\Delta\mathrm{s}}{2} (\boldsymbol{x}_j - \boldsymbol{x}_i) + \frac{\Delta\mathrm{s}^2}{6} \boldsymbol{d}_3^j \right] \times \boldsymbol{f}_j + \left[\frac{\Delta\mathrm{s}}{2} (\boldsymbol{x}_j - \boldsymbol{x}_i) + \frac{\Delta\mathrm{s}^2}{3} \boldsymbol{d}_3^j \right] \times \boldsymbol{f}_{j+1} \right\}, \tag{6.12}$$

in agreement with expressions for planar filaments found in Moreau et al. [51] and Walker et al. [55]. As we will highlight below, the contributions of the applied torque per unit length are relatively small given the slenderness of the filament, motivating a less refined discretisation for $\boldsymbol{I}_i^\tau$. Hence, taking the piecewise constant discretisation $\boldsymbol{\tau} = \boldsymbol{\tau}_j$ on the j^{th} segment, we have the simple expression

$$\boldsymbol{I}_i^\tau = \sum_{j=i}^{N} \Delta\mathrm{s} \boldsymbol{\tau}_j\,. \tag{6.13}$$

From the above, we see explicitly that the integral component of each moment balance equation may be written as a linear operator acting on the $\boldsymbol{f}_j$ and the $\boldsymbol{\tau}_j$. Similarly, with this piecewise-linear force discretisation, the integrated force balance of Equation (6.5) simply reads

$$-\frac{\Delta\mathrm{s}}{2} \sum_{j=1}^{N} (\boldsymbol{f}_j + \boldsymbol{f}_{j+1}) = \boldsymbol{0}\,. \tag{6.14}$$

We write $\boldsymbol{F} = [f_{1,x}, f_{1,y}, f_{1,z}, \ldots, f_{N+1,x}, f_{N+1,y}, f_{N+1,z}]^\top$ for components $f_{j,x}$, $f_{j,y}$, and $f_{j,z}$ of $\boldsymbol{f}_j$ with respect to some fixed laboratory frame with basis $\{\boldsymbol{e}_x, \boldsymbol{e}_y, \boldsymbol{e}_z\}$, and similarly $\boldsymbol{T}$ for the vector of components of applied torque per unit length. Here, and throughout, force and torque components are written relative to the laboratory reference frame. With this notation, we may write the equations of force and moment balance as

$$-\mathcal{B}\begin{bmatrix}\boldsymbol{F}\\ \boldsymbol{T}\end{bmatrix} = \boldsymbol{R}\,, \tag{6.15}$$

where $\mathcal{B}$ is a matrix of dimension $(3N+3)\times(6N+3)$ with rows $\mathcal{B}_k$. For $k = 1, 2, 3$, the first $3N+3$ columns are given by

$$\begin{aligned}
\mathcal{B}_1 &= \frac{\Delta \mathrm{s}}{2}[1,0,0,2,0,0,2\ldots,2,0,0,1,0,0]\,,\\
\mathcal{B}_2 &= \frac{\Delta \mathrm{s}}{2}[0,1,0,0,2,0,0,2\ldots,2,0,0,1,0]\,,\\
\mathcal{B}_3 &= \frac{\Delta \mathrm{s}}{2}[0,0,1,0,0,2,0,0,2\ldots,2,0,0,1]\,,
\end{aligned} \tag{6.16}$$

corresponding to the force balance of Equation (6.14), with the remaining $3N$ columns being zero. The remaining rows of $\mathcal{B}$ encode the moment balance of Equation (6.11) as expanded in Equation (6.12), organised in triples such that $\mathcal{B}_{3(i-1)+3+\alpha}$ projects the i^{th} moment balance equation onto $\bar{\boldsymbol{d}}^i_\alpha$, in that this $(3i+\alpha)^{\text{th}}$ row of $\mathcal{B}$ captures the $\bar{\boldsymbol{d}}^i_\alpha$ component of $-(\boldsymbol{I}^f_i + \boldsymbol{I}^\tau_i)$. The cross products inherited from Equation (6.12) may now be notationally simplified by use of the cyclic property of the scalar triple product, explicitly giving

$$\begin{aligned}
\bar{\boldsymbol{d}}^i_\alpha \cdot \boldsymbol{I}^f_i = \sum_{j=i}^{N}\Bigg\{ &\bar{\boldsymbol{d}}^i_\alpha \cdot \left[\frac{\Delta \mathrm{s}}{2}(\boldsymbol{x}_j - \boldsymbol{x}_i) + \frac{\Delta \mathrm{s}^2}{6}\boldsymbol{d}^j_3\right]\times \boldsymbol{f}_j \\
&+\bar{\boldsymbol{d}}^i_\alpha \cdot \left[\frac{\Delta \mathrm{s}}{2}(\boldsymbol{x}_j - \boldsymbol{x}_i) + \frac{\Delta \mathrm{s}^2}{3}\boldsymbol{d}^j_3\right]\times \boldsymbol{f}_{j+1}\Bigg\}
\end{aligned} \tag{6.17}$$

$$\begin{aligned}
= \sum_{j=i}^{N}\Bigg\{ &\bar{\boldsymbol{d}}^i_\alpha \times \left[\frac{\Delta \mathrm{s}}{2}(\boldsymbol{x}_j - \boldsymbol{x}_i) + \frac{\Delta \mathrm{s}^2}{6}\boldsymbol{d}^j_3\right]\cdot \boldsymbol{f}_j \\
&+\bar{\boldsymbol{d}}^i_\alpha \times \left[\frac{\Delta \mathrm{s}}{2}(\boldsymbol{x}_j - \boldsymbol{x}_i) + \frac{\Delta \mathrm{s}^2}{3}\boldsymbol{d}^j_3\right]\cdot \boldsymbol{f}_{j+1}\Bigg\}\,,
\end{aligned} \tag{6.18}$$

with the latter expression readily transcribed as a linear operator acting on the $\boldsymbol{f}_j$ for $j = i, \ldots, N$. Analogously, we have

$$\bar{\boldsymbol{d}}^i_\alpha \cdot \boldsymbol{I}^\tau_i = \Delta \mathrm{s}\bar{\boldsymbol{d}}^i_\alpha \cdot \sum_{j=i}^{N}\boldsymbol{\tau}_j\,, \tag{6.19}$$

from which a linear operator acting on the $\boldsymbol{\tau}_j$ for $j = i, \ldots, N$ can be constructed. Accordingly, the $(3N+3)$-vector $\boldsymbol{R}$ is given by

$$\boldsymbol{R} = \frac{EI}{1+\delta_{\alpha,3}\sigma}[0,0,0,\kappa_1(s_1),\kappa_2(s_1),\kappa_3(s_1),\kappa_1(s_2),\ldots,\kappa_3(s_N)]^\top\,, \tag{6.20}$$

so that the local moment balance is expressed relative to the local director basis. We remark that each of the quantities involved in the construction of $\mathcal{B}$ and $\boldsymbol{R}$ are well defined for a general filament in three dimensions, given the local directors $\boldsymbol{d}_1$ and $\boldsymbol{d}_2$ and computing the components of the twist vector as $\kappa_1 = \boldsymbol{d}_3 \cdot \partial_s \boldsymbol{d}_2$, $\kappa_2 = \boldsymbol{d}_1 \cdot \partial_s \boldsymbol{d}_3$, and $\kappa_3 = \boldsymbol{d}_2 \cdot \partial_s \boldsymbol{d}_1$. In terms of the discretised filament, these arclength derivatives are approximated via finite differences in practice, typically low-order schemes in order to suppress small numerical oscillations in solutions[2]. As noted earlier, we will proceed assuming that the filament is moment-free at the base, which is equivalent in this formulation to enforcing $\kappa_1(s_1) = \kappa_2(s_1) = \kappa_3(s_1) = 0$, though this may be readily replaced with other conditions, such as an externally applied basal torque.

6.2.3 Coupling hydrodynamics

We now relate the force density $\boldsymbol{f}$ acting on the fluid to the velocity of each segment endpoint, utilising the aforementioned and commonly applied method of resistive force theory, typically incurring errors logarithmic in the aspect ratio of the filament, though errors worsen near the filament endpoints. Here taking the constant radius of the filament to be $\epsilon = 10^{-2}L$, which more generally is assumed to be small in comparison to the filament length, simple resistive force theory gives the leading-order relation between filament velocity and force density as

$$\boldsymbol{f}_t = C_t \boldsymbol{u}_t\,, \quad \boldsymbol{f}_n = C_n \boldsymbol{u}_n\,. \tag{6.21}$$

Here, $\boldsymbol{f}_t$ and $\boldsymbol{f}_n$ denote the components of the force density that are tangential and normal to the filament, with analogous definitions of $\boldsymbol{u}_t$ and $\boldsymbol{u}_n$. We will utilise the expressions of Gray and Hancock [13], with

$$C_t = \frac{2\pi\mu}{\log(2L/\epsilon) - 0.5}\,, \quad C_n = \frac{4\pi\mu}{\log(2L/\epsilon) - 0.5}\,, \tag{6.22}$$

where μ is the medium viscosity, noting the relation $C_n = 2C_t$. By linearity, and again assuming a piecewise-linear force density along segments, we may write the coupling of translational kinematics to hydrodynamics as

$$\dot{\boldsymbol{X}} = A\boldsymbol{F}\,, \tag{6.23}$$

[2]High-order schemes effectively smooth out such oscillations before computing the elastic restoring moments, which prevents these moments from suppressing unphysical oscillations.

where A is a square matrix of dimension $3(N+1) \times 3(N+1)$ and is a function only of the segment endpoints $\boldsymbol{x}_i$. Of dimension $3(N+1)$, the vector $\dot{\boldsymbol{X}}$ corresponds to the linear velocities of the segment endpoints and is constructed analogously to $\boldsymbol{F}$ with respect to the laboratory frame. This relation results from the application of the no-slip condition at the segment endpoints, coupling the filament to the surrounding fluid. We note that this hydrodynamic condition is being applied here with considerably less care than in the previous Chapter, though may be improved upon in future work, subject to the existence of an appropriate three-dimensional slender-body theory that includes the contributions of non-trivial torques. Such a hydrodynamic theory is currently lacking, but is under development and is expected to supplement this elastohydrodynamic theory in future work.

Thus, here, in order to relate the rate of rotation of each segment to the viscous torque $\boldsymbol{\tau}_i$ acting on the fluid, we consider an approximation of the finite segment as an infinite rotating cylinder, associating the torque per unit length on the i^{th} segment with the rate of rotation ω_i about its local tangent $\boldsymbol{d}_3^i$ via the relation of Chwang and Wu [224]:

$$\boldsymbol{\tau}_i = 4\pi\mu\epsilon^2\omega_i\boldsymbol{d}_3^i \tag{6.24}$$

In particular, the ϵ^2 scaling entails the torque per unit length contributions are relatively small, unless the angular velocity is $O(\epsilon^{-2})$. Here, we recall that μ is the viscosity of the fluid medium and ϵ is the radius of the filament. We may write this relation as a linear operator on $\boldsymbol{\omega} = [\omega_1, \ldots, \omega_N]^\top$, written simply as $\boldsymbol{T} = \tilde{A}\boldsymbol{\omega}$. Finally, combining Equations (6.15), (6.23), and (6.24) now yields the linear system

$$-\mathcal{B}\begin{bmatrix} A^{-1} & 0 \\ 0 & \tilde{A} \end{bmatrix}\begin{bmatrix} \dot{\boldsymbol{X}} \\ \boldsymbol{\omega} \end{bmatrix} = -\mathcal{B}\mathcal{A}\begin{bmatrix} \dot{\boldsymbol{X}} \\ \boldsymbol{\omega} \end{bmatrix} = \boldsymbol{R}, \tag{6.25}$$

where A is invertible and $\mathcal{A}$ is defined to be a block matrix of dimension $(6N+3) \times (4N+3)$ with non-zero diagonal blocks A^{-1} and $\tilde{A}$.

6.2.4 Parameterisation

We may parameterise the tangents $\boldsymbol{d}_3^i$ on each linear segment by the Euler angles $\theta_i \in [0, \pi]$, $\phi_i \in (-\pi, \pi]$, $\psi_i \in (-\pi, \pi]$ for $i = 1, \ldots, N$ [235]. With this parameterisation, we may make a choice of $\boldsymbol{d}_1$ and $\boldsymbol{d}_2$, taking here the three orthonormal vectors to be

$$\boldsymbol{d}_1^i = \left[-s_\phi c_\psi - c_\theta c_\phi s_\psi, +c_\phi c_\psi - c_\theta s_\phi s_\psi, s_\theta s_\psi\right]^\top, \tag{6.26}$$

$$\boldsymbol{d}_2^i = \left[+s_\phi s_\psi - c_\theta c_\phi c_\psi, -c_\phi s_\psi - c_\theta s_\phi c_\psi, s_\theta c_\psi\right]^\top, \tag{6.27}$$

$$\boldsymbol{d}_3^i = \left[s_\theta c_\phi, s_\theta s_\phi, c_\theta\right]^\top, \tag{6.28}$$

written with respect to the laboratory frame and where $s_\theta \equiv \sin\theta_i$, $c_\theta \equiv \cos\theta_i$, and analogously for s_ϕ, c_ϕ, s_ψ, and c_ψ. From the directors, we recover

$$\theta_i = \arccos\left(\boldsymbol{d}_3^i \cdot \boldsymbol{e}_z\right), \quad \phi_i = \arctan\left(\frac{\boldsymbol{d}_3^i \cdot \boldsymbol{e}_y}{\boldsymbol{d}_3^i \cdot \boldsymbol{e}_x}\right), \quad \psi_i = \arctan\left(\frac{\boldsymbol{d}_1^i \cdot \boldsymbol{e}_z}{\boldsymbol{d}_2^i \cdot \boldsymbol{e}_z}\right). \tag{6.29}$$

As the discretised filament is piecewise linear, for $j = 1, \ldots, N+1$ we may write

$$\boldsymbol{x}_j = \boldsymbol{x}_1 + \Delta s \sum_{i=1}^{j-1} \boldsymbol{d}_3^i, \quad \dot{\boldsymbol{x}}_j = \dot{\boldsymbol{x}}_1 + \Delta s \sum_{i=1}^{j-1} \dot{\boldsymbol{d}}_3^i. \tag{6.30}$$

With $\boldsymbol{d}_3^i$ parameterised as above, we can thus express $\dot{\boldsymbol{x}}_j$ as a linear combination of the derivatives of θ_i and ϕ_i for $i = 1, \ldots, j-1$, in addition to including the time derivative of the base point $\boldsymbol{x}_1$. Hence, we may write

$$Q\dot{\boldsymbol{\Theta}} = \dot{\boldsymbol{X}}, \tag{6.31}$$

$$\boldsymbol{\Theta} = [x_{1,x}, x_{1,y}, x_{1,z}, \theta_1, \ldots, \theta_N, \phi_1, \ldots, \phi_N, \psi_1, \ldots, \psi_N]^\top, \tag{6.32}$$

where Q is a $3(N+1) \times 3(N+1)$ matrix and $x_{1,x}$, $x_{1,y}$, and $x_{1,z}$ are the components of $\boldsymbol{x}_j$ in the basis $\{\boldsymbol{e}_x, \boldsymbol{e}_y, \boldsymbol{e}_z\}$. Explicitly, Q may be constructed via

$$\tilde{Q} = \left[\begin{array}{c|c|c|c} Q_{11} & Q_{12} & Q_{13} & \\ \hline Q_{21} & Q_{22} & Q_{23} & 0 \\ \hline Q_{31} & Q_{32} & Q_{33} & \end{array}\right], \quad Q = [\tilde{Q}]_P, \tag{6.33}$$

where the matrices Q_{k1} are of dimension $(N+1) \times 3$, with Q_{k2} and Q_{k3} being of dimension $(N+1) \times N$, for $k = 1, 2, 3$. In the definition of Q, the subscript P denotes that the i^{th} row of $\tilde{Q}$ is permuted to the $P(i)^{\text{th}}$ row of Q, where

$$P(i) = \begin{cases} 3(i-1)+1, & i = 1, \ldots, N+1, \\ 3(i-N-2)+2, & i = N+2, \ldots, 2N+2, \\ 3(i-2N-3)+3, & i = 2N+3, \ldots, 3N+3. \end{cases} \tag{6.34}$$

This permutation of $\tilde{Q}$ allows us to define the sub-blocks simply, given explicitly as

$$
\begin{aligned}
Q^{i,j}_{k1} &= \begin{cases} 1\,, & j = k\,, \\ 0\,, & \text{otherwise}\,, \end{cases} \qquad k = 1,2,3\,, \\
Q^{i,j}_{12} &= \Delta\mathrm{s} \begin{cases} +\cos\theta_j \cos\phi_j\,, & j < i\,, \\ 0\,, & j \geq i\,, \end{cases} \\
Q^{i,j}_{13} &= \Delta\mathrm{s} \begin{cases} -\sin\theta_j \sin\phi_j\,, & j < i\,, \\ 0\,, & j \geq i\,, \end{cases} \\
Q^{i,j}_{22} &= \Delta\mathrm{s} \begin{cases} +\cos\theta_j \sin\phi_j\,, & j < i\,, \\ 0\,, & j \geq i\,, \end{cases} \\
Q^{i,j}_{23} &= \Delta\mathrm{s} \begin{cases} +\sin\theta_j \cos\phi_j\,, & j < i\,, \\ 0\,, & j \geq i\,, \end{cases} \\
Q^{i,j}_{32} &= \Delta\mathrm{s} \begin{cases} -\sin\theta_j\,, & j < i\,, \\ 0\,, & j \geq i\,, \end{cases} \\
Q^{i,j}_{33} &= 0\,.
\end{aligned}
$$

Further, in this parameterisation, we may readily relate the local rate of rotation about $\boldsymbol{d}^i_3$, denoted ω_i as in Equation (6.24), to θ, ϕ, ψ, and their time derivatives. Explicitly, this relationship is $\omega = \cos(\theta)\dot{\phi} + \dot{\psi}$, which can be deduced from simple but lengthy calculation using the parameterised expressions for the directors, and is notably linear in the derivatives of the Euler angles. Thus, we form the composite matrix

$$
\mathcal{Q} = \left[\begin{array}{c|c|c} Q & & \\ \hline 0 & C & I_N \end{array}\right]\,, \tag{6.35}
$$

where I_N is the $N \times N$ identity matrix and the $N \times N$ matrix C has diagonal elements $C_i = \cos(\theta_i)$ for $i = 1, \ldots, N$, with all other elements zero. The upper block, Q, maps the parameterisation into the laboratory frame, whilst the lower blocks convert between the parameterisation and the local rate of rotation about $\boldsymbol{d}_3$ as written in director basis. The $(4N+3) \times 3(N+1)$ matrix $\mathcal{Q}$ now encodes the expressions of velocities and rotation rates in terms of the parameterisation, via

$$
\mathcal{Q}\dot{\boldsymbol{\Theta}} = \left[\begin{array}{c} \dot{\boldsymbol{X}} \\ \boldsymbol{\omega} \end{array}\right]\,, \tag{6.36}
$$

noting that the representation of $\boldsymbol{\omega}$ is relative to the director basis, whilst the representation of $\dot{\boldsymbol{X}}$ is relative to the basis of the laboratory frame.

Having constructed $\mathcal{Q}$, we now combine Equations (6.25) and (6.36) to give

$$
-\mathcal{B}\mathcal{A}\mathcal{Q}\dot{\boldsymbol{\Theta}} = \boldsymbol{R}\,, \tag{6.37}
$$

noting in particular that the matrix $\mathcal{BAQ}$ is square and of dimension $(3N+3) \times (3N+3)$. Each constituent of this linear system is readily interpretable and closely resembles the two-dimensional formulation of Chapter 5. Naively, this system of ordinary differential equations can be readily solved numerically to give the evolution of the filament in the surrounding fluid. However, the use of a single parameterisation to describe the filament will in general lead to degeneracy of the linear system and ill-defined derivatives in both space and time, issues that we will explore and resolve numerically in the subsequent sections.

6.2.5 Coordinate singularities

Consider a straight filament aligned with the $\boldsymbol{e}_z$ axis, with each of the $\boldsymbol{d}_3^i = [0,0,1]^\top$ written in the laboratory frame. For this filament, $\theta_i = 0$ for all i, whilst the ϕ_i are undetermined, arbitrary, and, notably, need not be the same on each segment. Were we to attempt to formulate and solve the linear system of Equation (6.37), both ϕ and its derivatives would be ill-defined and, correspondingly, we would be unable to solve the system for the filament dynamics, which are physically trivial in this particular set-up. In more generality, if a filament were to have any segment pass through one of the poles $\theta = \{0, \pi\}$ of this coordinate system, ϕ would be undetermined on the segment and arbitrary, with attempts to solve our parameterised system of ordinary differential equations failing. Further, were a segment to pass close to but not through a pole, time derivatives of ϕ would necessarily become large, with ϕ well defined but varyingly rapidly as the segment moves close to the pole of the coordinate system. These large derivatives would artificially introduce additional stiffness to the elastohydrodynamical problem, inherent only to the parameterisation and not to the underlying physics. This problem is well known for Euler angle parameterisations and is commonly referred to as the 'gimbal lock' [235]. Analogous issues with arclength derivatives occur when considering neighbouring segments, with the value of ϕ varying rapidly and artificially between segments that reside near the pole of the coordinate system. In this latter case, however, our formulation of the elastohydrodynamical problem circumvents the need for evaluation of ϕ_s, instead considering only derivatives of the smooth quantities $\boldsymbol{d}_\alpha$, though we are not able to resolve issues with temporal derivatives in the same way.

In order to avoid the numerical and theoretical problems associated with singular points in the filament parameterisation, we exploit the finiteness of the set of angles θ_i, along with the independence of the underlying elastohydrodynamical problem from the parameterisation. Throughout this work, we have assumed a fixed laboratory

frame with basis $\{\boldsymbol{e}_x, \boldsymbol{e}_y, \boldsymbol{e}_z\}$, present only so that vector quantities may be written component-wise for convenience. Our choice of such a basis is arbitrary, with the physical problem of filament motion being independent of our selection of particular basis vectors. It is with respect to this basis that we have defined the Euler angles θ, ϕ, and ψ, from which the aforementioned coordinate singularities appear if any of the θ_i approach zero or π. Thus, if one makes a choice of basis $\{\boldsymbol{e}_x^\star, \boldsymbol{e}_y^\star, \boldsymbol{e}_z^\star\}$ such that the corresponding Euler angles $\theta_i^\star$ are some δ-neighbourhood away from the poles of the new parameterisation, the system of ordinary differential equations given in Equation (6.37) may be readily solved, at least initially. Should the solution in the new coordinate system approach one of the new poles $\theta^\star = 0, \pi$, a new basis can again be chosen, and this process iterated until the filament motion has been captured over a desired interval.

We note that, for sufficiently small $\delta > 0$, such a choice of basis $\{\boldsymbol{e}_x^\star, \boldsymbol{e}_y^\star, \boldsymbol{e}_z^\star\}$ necessarily exists due to the finiteness of the set of θ_i, with δ in practice able to be sufficiently large so as to limit the effects of coordinate singularities. Thus, subject to reasonable assumptions of smoothness of the filament position $\boldsymbol{x}$, such a process of repeatedly changing basis when necessary will prevent issues associated with the parameterisation described above and will, in practice, enable the efficient simulation of filament motion without introducing significant artificial stiffness or singularities.

6.3 Implementation, verification, and extensions

6.3.1 Selecting a new basis

Initially choosing an arbitrary laboratory basis $\{\boldsymbol{e}_x, \boldsymbol{e}_y, \boldsymbol{e}_z\}$, the above formulation is implemented in MATLAB®, with the system of ordinary differential equations (ODEs) of Equation (6.37) being solved using the inbuilt stiff solver `ode15s`, as described in detail by Shampine and Reichelt [225]. This standard variable-step, variable-order solver allows for configurable error tolerances, typically set here at 10^{-5} for absolute error and 10^{-4} for relative error, in general significantly below the error associated with the piecewise-linear filament discretisation. Initially and at each timestep, the values of θ_i are checked to determine if they are within δ of a coordinate singularity, typically with $\delta = \pi/50$. Should the parameterisation be approaching a singularity, a new basis is chosen and the problem recast in this basis.

A natural method of selecting a new basis is perhaps to choose one uniformly at random. Indeed, by considering the worst-case scenario of the N tuples (θ_i, ϕ_i) uniformly and disjointly covering the surface of the unit sphere, which together θ

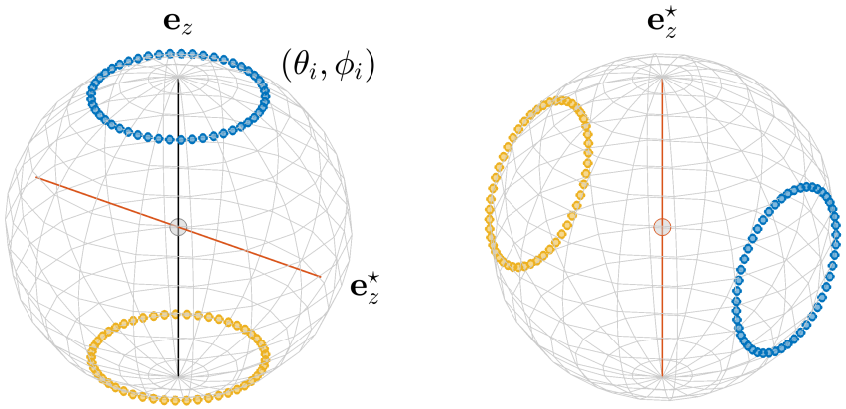

(a) (b)

Figure 6.3.1: An example choice of a new parameterisation in order to avoid coordinate singularities. Shown in blue are the points on the unit sphere corresponding to (θ_i, ϕ_i), with their antipodes displayed in yellow. (a) Before a change of basis and subsequent reparameterisation, we see that these points are located near to the $\theta = 0$ and $\theta = \pi$ axes, which are shown as black vertical lines. A new potential location for the $\theta = 0$ axis is shown in orange, selected so as to maximise the distance from the (θ_i, ϕ_i) and their antipodes. (b) Following reparameterisation, the points and antipodes are located maximally away from the new axis. This example scenario corresponds to a helical filament initially with $\theta_i = \pi/6$ for $i = 1, \ldots, 50$.

and ϕ parameterise, the probability that any random basis results in a scenario with $\min_i \{\theta_i, \pi - \theta_i\} < \delta$ is crudely bounded by $2N \sin^2(\delta/2)$, a consequence of elementary geometry[3]. With this quantity being significantly less than unity for a wide range of N with δ large enough to avoid severe artificial numerical stiffness, as discussed above, a practical implementation for the simulation of filament elastohydrodynamics as formulated above may simply select a new basis randomly, repeating until a suitable basis is found. With $\delta = \pi/50$ and $N = 50$, the probability of rejecting a candidate new basis is bounded above by 0.1; thus, in practice, one should expect to find an appropriate basis within few iterations of the proposed procedure.

Alternatively, and as we will do throughout this Chapter, one may instead proceed in a deterministic manner, selecting a near-optimal basis from knowledge of the existing parameterisation. Given the set of parameters θ_i and ϕ_i, we may choose a $\hat{\theta} \in [0, \pi]$ and $\hat{\phi} \in [0, 2\pi)$ so as to maximise the distance of $(\hat{\theta}, \hat{\phi})$ from each of the (θ_i, ϕ_i) and their antipodes. In practice, an approximate solution to this problem is obtained by selecting $(\hat{\theta}, \hat{\phi})$ from a selection of preset test points in order to maximise

[3]The surface area of a spherical cap of polar half-angle δ on a unit sphere is given by $4\pi \sin^2(\delta/2)$. Placing such caps at the locations of the N tuples (θ_i, ϕ_i) and their antipodes, this covers an area of at most $8N\pi \sin^2(\delta/2)$, a bound that crudely assumes that the caps are disjoint. Thus, the proportion of the sphere covered by the caps is at most $2N \sin^2(\delta/2)$.

the distance from the (θ_i, ϕ_i), where distance is measured on the surface of the unit sphere that θ and ϕ naturally parameterise, as shown in Figure 6.3.1. It should be noted that this process of selection impacts negligibly on computational efficiency with 10,000 test points. With these choices of $\hat{\theta}$ and $\hat{\phi}$, we form a new basis by mapping the original basis vector $\boldsymbol{e}_z$ to the vector $\boldsymbol{e}_z^\star$, given explicitly by

$$\boldsymbol{e}_z^\star = [\sin\hat{\theta}\cos\hat{\phi}, \sin\hat{\theta}\sin\hat{\phi}, \cos\hat{\theta}]^\top . \tag{6.38}$$

Choosing the other members of the orthonormal basis $\boldsymbol{e}_x^\star$ and $\boldsymbol{e}_y^\star$ arbitrarily, expressed in this new basis the accompanying filament parameterisation will be removed from any coordinate singularities by construction, as exemplified in Figure 6.3.1(b).

6.3.2 Validation

In what follows, we validate the presented methodology against known filament behaviours and a sample three-dimensional simulation via an existing methodology. Initial configurations and parameter values for each can be found in Appendix 6.A, with behaviours qualitatively independent of these parameter choices and filament set-ups.

6.3.2.1 Relaxation of a planar filament

Noting that there is no analytical test solution for the dynamics of a fully 3D Kirchhoff rod in a viscous fluid, to the best of our knowledge, we consider validations by comparison with numerical studies in the literature, though we additionally utilise invariance of the centre of mass as a gold standard below, where applicable. Firstly, we validate the presented approach by considering the problem of filament relaxation in two dimensions, a natural and well studied subset of the three-dimensional framework. We consider the simple case of a symmetric curved filament in the $\boldsymbol{e}_x\boldsymbol{e}_y$ plane, which will provide a test of symmetry preservation, integrated moment balance, and hydrodynamics via qualitative comparisons with the earlier works of Moreau et al. [51] and Hall-McNair et al. [135]. Simulating the relaxation of such a filament to a straight equilibrium condition with $N = 40$ segments takes less than 2 s on modest hardware (Intel® Core™ i7-6920HQ CPU), from which we immediately see retained the computational efficiency of the framework of Moreau et al. that this Chapter generalises. Present throughout the computed motion is the left-right symmetry of the initial condition, with the filament shape evolving smoothly even with a small number of segments, as shown in Figure 6.3.2. Further, the centre of mass, which in

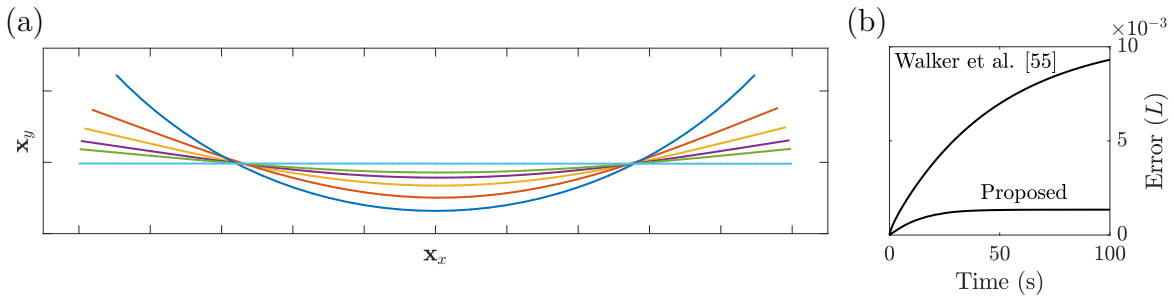

Figure 6.3.2: The two-dimensional relaxation of a symmetric planar filament, simulated with $N = 40$ segments. (a) Symmetry is preserved throughout the dynamics, with the relaxation in qualitative agreement with that used for verification in the two-dimensional works of Moreau et al. [51], Walker et al. [55], and Hall-McNair et al. [135]. (b) Translation of the centre of mass throughout the motion, analytically zero, is captured numerically with errors on the order of $10^{-3}L$ by the proposed methodology, notably the same order of magnitude as that attained with the two-dimensional methodology of Walker et al. [55]. Axes $\boldsymbol{x}_x$ and $\boldsymbol{x}_y$ correspond to the unit vectors $\boldsymbol{e}_x$ and $\boldsymbol{e}_y$, respectively.

exact calculation would be fixed in space due to the overall force-free condition on the filament, is captured numerically with errors on the order of $10^{-3}L$, demonstrating very good quantitative satisfaction of this condition. Of note, in Figure 6.3.2b, we have verified that this error is of the same order of magnitude as that generated by the two-dimensional methodology of Walker et al. [55].

6.3.2.2 Planar bending of a filament in shear flow

Further, whilst the above is reassuring and serves to validate a subset of the implementation, we note from Equations (6.26) and (6.27) that motion cast in the $\boldsymbol{e}_x\boldsymbol{e}_y$ plane of the laboratory frame may often render the evolution of one of the directors $\boldsymbol{d}_1$ and $\boldsymbol{d}_2$ trivial. In order to avoid this, we may consider planar problems in slightly more generality, posing a problem that is planar though not aligned with the $\boldsymbol{e}_x\boldsymbol{e}_y$ plane. As an exemplar such problem, we attempt to recreate a typical but complex behaviour of a flexible filament in a shear flow, that of the *J-shape* and *U-turn* [65], aligning both the filament and the background flow in a plane spanned by $\boldsymbol{e}_y$ and $\boldsymbol{e}_x + \boldsymbol{e}_z$. In order to ensure the absence of alignment of the parameterisation with the $\boldsymbol{e}_x\boldsymbol{e}_y$ plane, we disable the adaptive system of basis selection for the purpose of this example, and simulate the motion of a filament in a shear flow. The background flow with velocity $\boldsymbol{u}_b$ and vorticity $\boldsymbol{\Omega}$ is incorporated into the framework via the transformation $\boldsymbol{u} \mapsto \boldsymbol{u} - \boldsymbol{u}_b$, $\omega_i \mapsto \omega_i - \boldsymbol{\Omega} \cdot \boldsymbol{d}_3^i/2$, yielding the modified system

$$-\mathcal{B}\mathcal{A}\mathcal{Q}\dot{\boldsymbol{\Theta}} = \boldsymbol{R} - \mathcal{B}\mathcal{A}\boldsymbol{U}_b \tag{6.39}$$

for a vector $\boldsymbol{U}_b$ of background flows and vorticities evaluated at segment endpoints and midpoints, respectively. Details of the flow field and initial set-up are given in

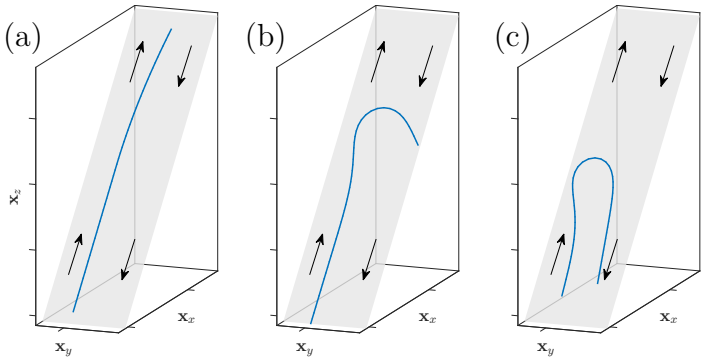

Figure 6.3.3: The planar evolution of a filament in shear, exhibiting a rich and well documented dynamics. (a) Having aligned both the filament and shear flow in a plane not parallel to the $\boldsymbol{e}_x\boldsymbol{e}_y$ plane, with the directors non-trivial in this set-up, we simulate the motion of the filament through two distinct morphological transitions: (b) the characteristic *J-shape* and (c) the subsequent *U-turn* (cf. Liu et al. [65, Fig. 1, Movies S5, S6]). We note that the selection of an improved basis for computation has been disabled for this example and yields a twofold increase in computational efficiency if enabled. Arrows indicate the direction of the background shear flow. Axes $\boldsymbol{x}_x$, $\boldsymbol{x}_y$, and $\boldsymbol{x}_z$ correspond to the unit vectors $\boldsymbol{e}_x$, $\boldsymbol{e}_y$, and $\boldsymbol{e}_z$, respectively. The plane containing the filament and the shear flow is shown in grey.

Appendix 6.A, along with a non-dimensionalisation of the problem.

Adopting the timescale T to be the inverse of the shearing rate of the flow, we consider a parameter regime in which one would expect to see the formation of a J-shape and subsequently a U-turn, defined by their characteristic morphologies in Liu et al. [65, Figure 1, Movies S5, S6] and from which an appropriate parameter choice is obtained. Notably, the impact of thermal noise perturbations is not considered here, in contrast to Liu et al. [65], preventing a quantitative comparison. In Figure 6.3.3, we present the initial, J-shape, and U-turn configurations of the filament as simulated via the proposed methodology, with computation requiring approximately 20 s with $N = 50$ segments. The simulated filament shapes are in qualitative agreement with those shown in Liu et al. [65, Figure 1] and serve as further validation of the coarse-grained methodology. Notably, enabling the described method of basis selection effectively casts this problem in the $\boldsymbol{e}_x\boldsymbol{e}_y$ plane, affording a twofold increase in computational efficiency and highlighting the benefits of adaptive reparameterisation.

6.3.2.3 Relaxation of a non-planar filament

Finally, we consider truly non-planar relaxation of filaments in three dimensions. Typical simulations of such a relaxation with $N = 50$ segments have a runtime of approximately 10 s on the modest hardware described above, often requiring at most one choice of basis though naturally problem dependent, and provide reasonable accuracy. Thus, even when considering inherently three-dimensional problems, we see retained

in this methodology the low computational cost of the formulation of Moreau et al. [51], representing significant improvements in computational efficiency over recent studies in three dimensions [196, 221, 222]. This is particularly evident when directly comparing the presented coarse-grained methodology with the results of Ishimoto and Gaffney [222], considering in this case the relaxation of a helical configuration to a straight equilibrium. A side-by-side comparison of the relaxation dynamics as computed by the proposed methodology and that presented by Ishimoto and Gaffney is shown in Figure 6.3.4, noting that the work of Ishimoto and Gaffney [222] considers an actively driven nearly inextensible filament, of which relaxation dynamics are a natural subset. Figure 6.3.4 highlights good agreement between methodologies that is in line with the level of accuracy typically afforded by the resistive force theories used here, recalling errors logarithmic in the filament aspect ratio. Figure 6.3.4e shows a quantitative evaluation of the computed solutions, with the deviation of the filament centre of mass from the initial condition shown as solid black curves for each methodology. With the force-free condition implying that the filament centre of mass should not move throughout the relaxation dynamics, this measured deviation serves as an assessment of the accuracy of both frameworks, with each exhibiting variation only on the order of $10^{-2}L$. Also shown in Figure 6.3.4e is a dimensional measure of the difference between the two computed solutions, here denoted $E(t)$ and defined as the non-negative root of

$$E(t)^2 = \frac{1}{L}\int_0^L \|\boldsymbol{x}_P(s,t) - \boldsymbol{x}_{IG}(s,t)\|_2^2 \,\mathrm{d}s\,, \tag{6.40}$$

where $\boldsymbol{x}_P(s,t)$ and $\boldsymbol{x}_{IG}(s,t)$ denote the filament centreline as computed by the proposed methodology and that used by Ishimoto and Gaffney, respectively. Numerically approximating this integral with quadrature and noting that this error is consistently on the order of $10^{-2}L$ throughout the relaxation, we see evidenced good quantitative agreement between the two frameworks, thus validating the proposed methodology. We also remark that the solution of Ishimoto and Gaffney [222] does not perfectly satisfy filament inextensibility, with variation in total length of approximately 1%, which may have some impact on the computed dynamics. Thus, when computing $E(t)$ as defined above, we treat $s \in [0, L]$ as a material parameter, with the differences in position $\boldsymbol{x}_P(s,t) - \boldsymbol{x}_{IG}(s,t)$ therefore capturing discrepancies between the simulated locations of the material point with undeformed arclength s at time t, with s not necessarily equal to the deformed arclength in the solution of Ishimoto and Gaffney [222].

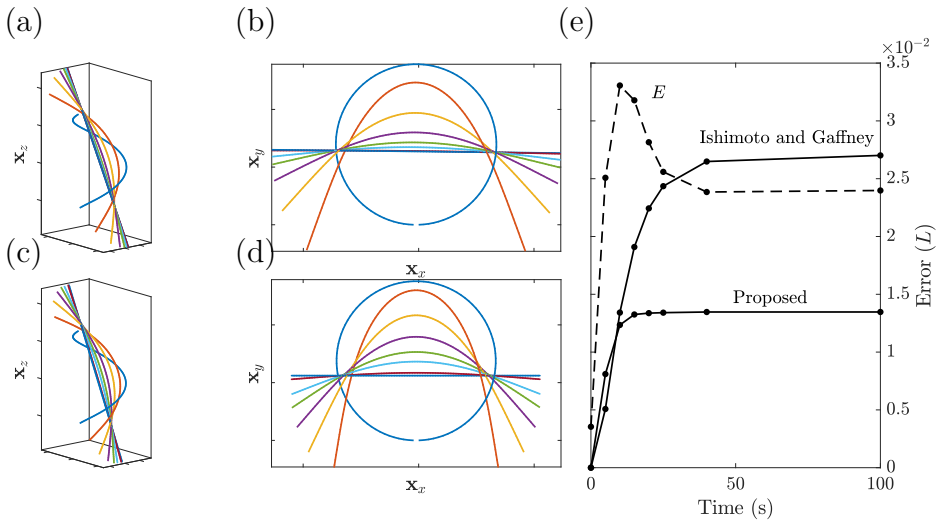

Figure 6.3.4: The relaxation of a filament in three dimensions. Shown are the results of simulating this motion via (a,b) the proposed framework and (c,d) the methodology presented in Ishimoto and Gaffney [222], in turn heavily based on the work of Olson et al. [221], shown from multiple perspectives at multiple timepoints. In both cases, we observe relaxation from a non-planar, helical configuration to a straight filament and good agreement between the two computed solutions, particularly given the logarithmic accuracy of resistive force theories. (e) A quantitative comparison between the two frameworks, with solid lines showing the Euclidean distance of the filament centre of mass from its initial location, analytically zero by the force-free condition though here on the order of $10^{-2}L$. The dashed curve quantifies the error between the computed solutions, denoted E, with the square of this error defined as $E^2 = \int \|\boldsymbol{x}_P - \boldsymbol{x}_{IG}\|_2^2 \, \mathrm{d}s/L$, where $\boldsymbol{x}_P$ and $\boldsymbol{x}_{IG}$ are the locations of the filament centreline as computed by the proposed methodology and that used by Ishimoto and Gaffney, respectively. Computation with the presented methodology took approximately 30 s on a modest laptop computer, in comparison to the multiple hours required on sophisticated cluster hardware for the methodology of Ishimoto and Gaffney. Here, we have simulated filament motion with $N = 100$ segments. Axes $\boldsymbol{x}_x$, $\boldsymbol{x}_y$, and $\boldsymbol{x}_z$ correspond to the unit vectors $\boldsymbol{e}_x$, $\boldsymbol{e}_y$, and $\boldsymbol{e}_z$, respectively.

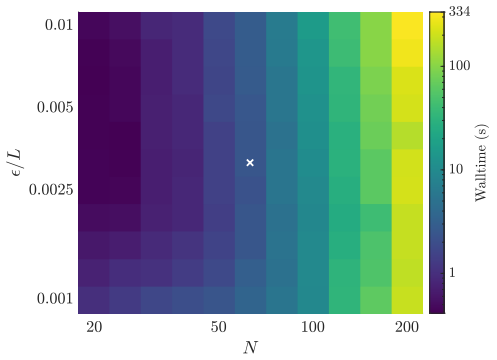

Figure 6.3.5: Wall times associated with the 3D filament relaxation of Figure 6.3.4 for various choices of the parameters ϵ and N. With $N = 200$ corresponding to a very fine discretisation of the filament, we observe a maximum wall time of under 6 minutes on a modest laptop computer, approximately 25x faster than the similar computations of Ishimoto and Gaffney [222] on sophisticated cluster hardware, albeit for different parameter values. There is a strong dependence of the wall time on the level of discretisation N, as expected. Here, the absolute and relative error tolerances of the ODE solver are set to 10^{-5} and 10^{-4}, respectively. All axes, including the colour axis, are logarithmically scaled for visual clarity. The parameter combination signified by a cross corresponds to a wall time of 2.5 s, with $N = 63$ and $\epsilon/L \approx 3.2 \times 10^{-3}$, chosen for illustration purposes only.

In contrast to the agreement between solutions, there is a stark difference between the associated time required for computation. Taking $N = 100$ segments and computing until relaxation, the coarse-grained framework calculated the solution in approximately 30 s on personal computing hardware with ODE error tolerances of 10^{-5}, whilst the computations utilising the implementation of Ishimoto and Gaffney required 2.5 h on a high performance computing cluster. A thorough investigation of the time required for computation with the presented methodology for various choices of the parameters ϵ and N is showcased in Figure 6.3.5, from which we note the remarkable performance of this simple implementation across parameter regimes, with the wall time naturally dependent on the discretisation parameter N.

6.3.3 Model extensions

6.3.3.1 Intrinsic curvature

In order to showcase the versatility of the presented framework, we demonstrate its simple extension to filaments with non-zero intrinsic or reference curvature, which can exhibit complex buckling behaviours [237]. Recalling the constitutive relation of Equation (6.8), the effect of an intrinsic curvature $\boldsymbol{\kappa}^0$ is to alter the bending moments, yielding the modified constitutive relation

$$\boldsymbol{m} = EI\left([\kappa_1 - \kappa_1^0]\boldsymbol{d}_1 + [\kappa_2 - \kappa_2^0]\boldsymbol{d}_2 + \frac{1}{1+\sigma}[\kappa_3 - \kappa_3^0]\boldsymbol{d}_3\right), \tag{6.41}$$

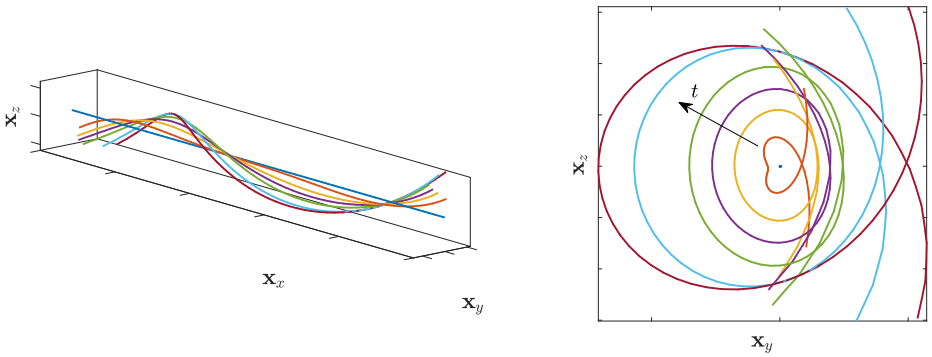

Figure 6.3.6: The relaxation of a straight filament with non-zero intrinsic curvature to a helical configuration, with reference curvature specified as $\boldsymbol{\kappa}^0 = \pi\boldsymbol{d}_2 + 2\pi\boldsymbol{d}_3$. Having taken $N = 70$ segments and $\epsilon = 10^{-2}L$, we observe the smooth relaxation of the filament away from its initial straight configuration, computed in 15 s on a modest laptop computer. Axes $\boldsymbol{x}_x, \boldsymbol{x}_y$, and $\boldsymbol{x}_z$ correspond to the unit vectors $\boldsymbol{e}_x, \boldsymbol{e}_y$, and $\boldsymbol{e}_z$, respectively.

where we have written $\boldsymbol{\kappa}^0 = \sum_\alpha \kappa^0_\alpha \boldsymbol{d}_\alpha$ in the local director basis. Notably, the reference curvature can plausibly depend on a variety of quantities, including time, arclength, and spatial position, with an example being the modelling of an internally driven filament by a time-dependent intrinsic curvature [221, 232].

Practically, the inclusion of such an intrinsic curvature amounts to a simple subtraction of the reference curvature from the computed components of $\boldsymbol{\kappa}$ at each instant, with $\boldsymbol{R}$ as given in Equation (6.20) being modified accordingly. Doing so, we simulate the relaxation of a straight filament with a non-zero intrinsic curvature, with the reference curvature of $\boldsymbol{\kappa}^0 = \pi\boldsymbol{d}_2 + 2\pi\boldsymbol{d}_3$ corresponding to a helical configuration. As shown in Figure 6.3.6, the filament indeed relaxes to a helix, with the wall time of this simulation being 15 s on a laptop computer, having taken $\epsilon = 10^{-2}L$ and $N = 70$ segments, noting that the filament shape has been sufficiently resolved with this discretisation.

6.3.3.2 Clamped and internally driven filaments

Finally, we consider the simple extensions to both clamped filaments and to those with actively generated internal moments, the latter being akin to the active beating of biological cilia and flagella [211]. For time and arclength-dependent active moment density $\boldsymbol{m}^a$, its inclusion into the presented framework acts to modify the moment balance of Equation (6.2) to

$$\boldsymbol{m}_s + \boldsymbol{x}_s \times \boldsymbol{n} - \boldsymbol{\tau} + \boldsymbol{m}^a = \boldsymbol{0}\,. \tag{6.42}$$

Repeating the integration of the pointwise moment balance from $s = s_i$ to $s = L$, as in Section 6.2, leads to a modified form of Equation (6.11), explicitly given as

$$-\bar{\boldsymbol{d}}^i_\alpha \cdot \left(\boldsymbol{I}^f_i + \boldsymbol{I}^\tau_i\right) = \frac{EI}{1+\delta_{\alpha,3}\sigma}\kappa_\alpha(s_i) - \bar{\boldsymbol{d}}^i_\alpha \cdot \boldsymbol{I}^a_i \,, \tag{6.43}$$

where the integrated active moment density is written as

$$\boldsymbol{I}^a_i = \int_{s_i}^{L} \boldsymbol{m}^a \,\mathrm{d}\tilde{s} \,. \tag{6.44}$$

For a given active moment density, assumed to be integrable, $\boldsymbol{I}^a_i$ may be readily computed either analytically or numerically, with its components in the local $\bar{\boldsymbol{d}}^i_\alpha$ direction then modifying $\boldsymbol{R}$ from Equation (6.20) accordingly.

Clamping the filament at the base is somewhat simpler, in that the overall force and moment balance conditions on the filament are merely replaced by enforcing no motion or rotation at the base. These conditions may be stated concisely as

$$\dot{\boldsymbol{x}}(0) = \boldsymbol{0} \,, \quad \dot{\theta}_1 = \dot{\phi}_1 = \dot{\psi}_1 = 0 \,, \tag{6.45}$$

supplanting the force and moment-free conditions of Equations (6.5) and (6.6), on taking $s = 0$ in the latter. Implementing these minor modifications, as an example, we specify a travelling wave of internal moment given by $\boldsymbol{m}^a = 5\sin(s-t)\boldsymbol{d}_1 + 5\cos(s-t)\boldsymbol{d}_2$ and simulate the active motion of a clamped filament, taking $N = 50$ and $\epsilon = 10^{-2}L$. Snapshots of this eventually periodic motion are shown in Figure 6.3.7, with the motion simulated up until a dimensionless time of $t = 8\pi$ from a straight initial configuration and with a wall time of around 8 s.

6.4 Discussion and conclusions

In this Chapter, we have seen that the motion of inextensible unshearable filaments in three dimensions can be concisely described by a coarse-grained framework, building upon the principles of Moreau et al. [51] in order to minimise numerical stiffness associated with the governing equations of elastohydrodynamics. This representation was readily implemented via an Euler angle parameterisation, with adaptive basis selection and reparameterisation overcoming coordinate singularities associated with a fixed representation of the dynamics. We have further demonstrated the efficacy of the proposed deterministic method for basis selection by explicit simulation of non-planar filament dynamics, which is able to afford reductions in numerical stiffness

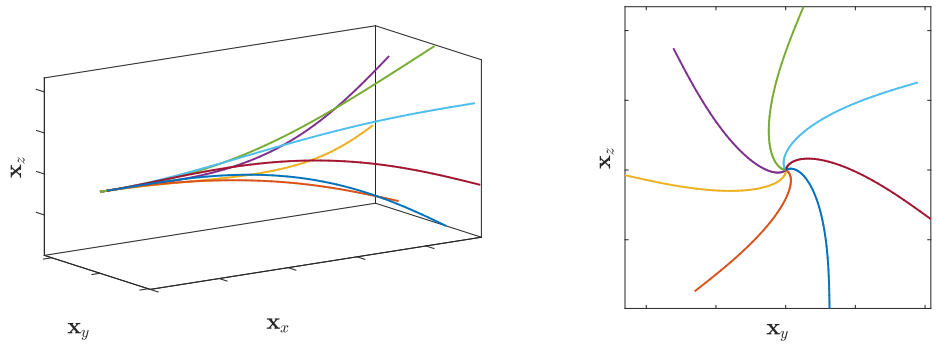

Figure 6.3.7: The 3D beating of a clamped filament driven by prescribed active internal moments. Having specified a travelling wave of out-of-phase sinusoidal active moments $\boldsymbol{m}^a = 5\sin(s-t)\boldsymbol{d}_1 + 5\cos(s-t)\boldsymbol{d}_2$, an initially straight filament deforms to a periodic driven motion, with the tip of the filament following a circular path. Here, we have taken $\epsilon = 10^{-2}L$ and $N = 50$, noting that the filament shape has been resolved smoothly with this level of discretisation. Computation required approximately 8 s on modest hardware, simulating up until $t = 8\pi$. Axes $\boldsymbol{x}_x$, $\boldsymbol{x}_y$, and $\boldsymbol{x}_z$ correspond to the unit vectors $\boldsymbol{e}_x$, $\boldsymbol{e}_y$, and $\boldsymbol{e}_z$, respectively.

even when the filament set-up is separated from singularities of the parameterisation. The presented framework retains the flexibility and extensibility of the formulations of Moreau et al. [51], Walker et al. [55], and Hall-McNair et al. [135], with background flows, active moment generation, body forces, and other effects or constraints being simple to include in this representation. The simplicity of these possible extensions speaks to the broad utility of the proposed approach, with potential for use in the simulation of both single and multiple filamentous bodies in fluid under a wide variety of circumstances and conditions.

In formulating our methodology, we have made the simplifying assumption of coupling fluid dynamics to forces via resistive force theory, which is well known to incur errors logarithmic in the filament aspect ratio, though variations remain in widespread use [51, 103, 211, 220, 238–240]. Resistive force theories additionally suffer from locality, in that portions of the filament do not directly interact with one another through the fluid. A natural development of the presented approach would therefore be the inclusion of non-local hydrodynamics, perhaps via the regularised Stokeslet segment methodology of Cortez [75] as included in the work of Walker et al. [55], or lightweight singular slender-body theories such as those of Johnson [52] and Tornberg and Shelley [60]. Such improvements may also include the consideration of confined geometries, with motion in a half space of particular pertinence to typical microscopy of flagellated organisms. Despite the many possible directions for hydrodynamic refinement, we note that the linearity of Stokes flows necessitates that any relations between forces and velocities be linear, with explicit formulations simply giving rise to modified linear operators $\mathcal{A}$ that may be readily inserted into the

described framework.

In the wider context of methods for soft filament simulation, the scope of which is illustrated by the generality of the approach of Gazzola et al. [241], the proposed framework enables rapid simulation of the subclass of purely inextensible filaments. This modelling assumption has been demonstrated to be a valid approximation of nearly inextensible filaments in a variety of contexts [234], affording greatly improved computational efficiency over previous approaches that we have compounded here, albeit with reduced hydrodynamic fidelity. However, we expect that the addition of improved hydrodynamics will have minimal impact on the computational efficiency of the presented methodology, with this efficiency not being derived from our use of simple resistive force theory, as noted by Walker et al. [55] and Hall-McNair et al. [135] for their non-local refinements of the two-dimensional theory of Moreau et al. [51], which we also observed in Chapter 5.

In summary, we have presented, verified, and exemplified a novel framework for the rapid simulation of inextensible unshearable filaments in a viscous fluid at zero Reynolds number in three dimensions. Despite the improved generality of this methodology over existing two-dimensional approaches, we have retained the computational efficiency and simplicity of the work of Moreau et al. [51], affording significant extensibility and, thus, facilitating a vast range of previously unrealisable biological and biophysical studies into filament dynamics on the microscale.

The computer code used and generated in this Chapter is freely available from `https://gitlab.com/bjwalker/3d-filaments.git`.

Appendix

6.A Parameters and initial conditions

We non-dimensionalise the system of Equation (6.37) as in Chapter 5 and Walker et al. [55], differing from Chapter 5 only in that the lengthscale chosen here is that of L rather than $L/2$. This results in a dimensionless system of the form

$$-E_h\hat{\mathcal{B}}\hat{\mathcal{A}}\hat{\mathcal{Q}}\dot{\hat{\Theta}} = \hat{\boldsymbol{R}}\,, \quad E_h = \frac{8\pi\mu L^4}{EI\,T} \tag{6.46}$$

for timescale T and elastohydrodynamic number E_h, where dimensionless counterparts are given by

$$\mathcal{B} = L^2\hat{\mathcal{B}}\,, \quad \mathcal{A} = \frac{1}{8\pi\mu}\hat{\mathcal{A}}\,, \quad \mathcal{Q}\dot{\boldsymbol{\theta}} = \frac{L}{T}\hat{\mathcal{Q}}\dot{\hat{\boldsymbol{\theta}}}\,, \quad \boldsymbol{R} = \frac{EI}{L}\hat{\boldsymbol{R}}\,, \tag{6.47}$$

having multiplied the force balance equations by Δs to unify dimensions. All examples begin with the filament base, $\boldsymbol{x}_1$, coincident with the origin of the laboratory frame, and we set Poisson's ratio to zero, i.e. $\sigma = 0$, throughout, though note a lack of sensitivity of results to this choice.

6.A.1 Relaxation of a planar filament

In simulating the relaxation of a filament in the $\boldsymbol{e}_x\boldsymbol{e}_y$ plane, we impose the initial filament shape as

$$\theta_i = \pi/2\,, \quad \phi_i = \frac{\pi}{2}\left(\frac{i-1}{N-1} - \frac{1}{2}\right)\,, \quad \psi_i = 0\,, \quad \text{for } i = 1,\ldots,N \tag{6.48}$$

with respect to standard laboratory Euler angles. Filament motion is simulated with $E_h \approx 1.6\times10^5$, though this choice is arbitrary given the invariance of the dynamics to rescalings in time (assuming that the rescaling is not so extreme as to break the inertialess assumption).

6.A.2 Planar bending of a filament in shear flow

In order to generate the characteristic behaviours of the *J-shape* and *U-turn*, we initialise the filament via

$$\theta_i = \pi/4\,, \quad \phi_i = -\frac{\pi}{12}\frac{i-1}{N-1}\,, \quad \psi_i = 0\,, \quad \text{for } i = 1, \ldots, N\,. \tag{6.49}$$

We align a background shear flow in the same plane as the filament, proportional in strength to the coordinate in the $\boldsymbol{e}_y$ direction, denoted y. Explicitly, this flow $\boldsymbol{u}_b$ is given in the laboratory frame in dimensionless form by

$$\boldsymbol{u}_b = \frac{1}{\sqrt{2}} y(\boldsymbol{e}_x + \boldsymbol{e}_z)\,, \tag{6.50}$$

having taken the timescale T to be the inverse of the dimensional shear rate. Simulation proceeds with $E_h \approx 4.7 \times 10^5$, consistent with the regime found in Liu et al. [65], and we note that the tip of the filament initially curves into the oncoming background flow in $y < 0$.

6.A.3 Relaxation of a non-planar filament

Taking $N = 100$ segments, we impose the helical initial condition

$$\theta_i = \pi/3\,, \quad \phi_i = 2\pi\frac{i-1}{N-1}\,, \quad \psi_i = 0\,, \quad \text{for } i = 1, \ldots, N\,. \tag{6.51}$$

We simulate filament motion with $E_h \approx 3.1 \times 10^4$, with results insensitive to this choice. The parameters used in the implementation of Ishimoto and Gaffney [222] are as in their publication, with the image system for a plane wall accordingly removed and the actively generated torques set to zero to allow for filament relaxation in free space. In particular, whilst the filaments of Ishimoto and Gaffney [222] are extensible, the extensional modulus of these filaments is sufficiently high so as to provide near inextensibility in their results, enabling meaningful comparison. Simulations using this methodology were performed by Prof. Kenta Ishimoto, Kyoto University.

6.A.4 Relaxation of a non-straight filament

Taking $N = 70$ segments, we impose the straight initial condition

$$\theta_i = \pi/2\,, \quad \phi_i = 0\,, \quad \psi_i = 0\,, \quad \text{for } i = 1, \ldots, N\,. \tag{6.52}$$

The intrinsic curvature is specified as $\boldsymbol{\kappa}^0 = \pi\boldsymbol{d}_2 + 2\pi\boldsymbol{d}_3$. We simulate filament motion with $E_h \approx 1.5 \times 10^5$, with results insensitive to this choice.

6.A.5 Active beating of a clamped filament

Taking $N = 50$ segments, we impose the straight initial condition

$$\theta_i = \pi/2\,, \quad \phi_i = 0\,, \quad \psi_i = 0\,, \quad \text{for } i = 1, \ldots, N\,. \tag{6.53}$$

The active moment density is specified as $\boldsymbol{m}^a = 5\sin(s-t)\boldsymbol{d}_1 + 5\cos(s-t)\boldsymbol{d}_2$. We simulate filament motion with $E_h = 10^3$ up until $t = 8\pi$.

Chapter 7

Discussion

The principal and overarching aim of this thesis has been to explore a number of open problems related to the modelling and simulation of flagellate motility. Through the varied computational and theoretical explorations of Chapters 2 to 6, we have indeed realised this aim, considering the behaviours of individual swimmers in a range of environments, the pairwise behaviours of two idealised canonical microswimmers, and the complex fluid-structure interactions that shape the way in which flagella beat.

We began this thesis with the study of a largely unexplored organism, the parasite *Leishmania mexicana*. Morphologically distinct from better-studied swimmers, the behaviours of this large-bodied puller microswimmer were unknown, despite the role of motility in its life cycle. Further, even its observable flagellar beat was unquantified, with knowledge of its motion vital for the pursuit of kinematic studies. Seeking to address this, we devised and employed a morphology-driven method for automatic identification of flagella from videomicroscopy, as described in detail by Walker et al. [125], removing the need for prolonged researcher input and promising general applicability [159]. Here, this approach enabled us to identify a particularly simple flagellar kinematics in *Leishmania*, providing the necessary footing for informed kinematic study.

In Chapters 2 and 3, we conducted such enquiry, examining the response of a virtual *Leishmania mexicana* promastigote to both a no-slip boundary and a background shearing flow, observing complex interplays between morphology, mode of locomotion, and the swimmer environment. In order to make progress via high-accuracy boundary element methods, which incurred significant computational costs, we devised and utilised approximate low-dimensional dynamical systems to capture the motion of these swimmers, averaging the full dynamics over the short period of the flagellar beat. This approach, though initially motivated by practical necessity,

proved to be a powerful tool for the analysis of long-time swimmer behaviours, revealing tendencies of boundary-induced reorientation and mechanisms of sustained near-boundary swimming, for instance. Indeed, we translated this remarkable utility into a multiswimmer setting, quantifying the pairwise motion of two model spermatozoa in Chapter 4. These low-dimensional representations, *a priori* unknown to be reminiscent of the projections of the high-dimensional dynamics for *Leishmania* and spermatozoa, were surprisingly evidenced to capture swimmer behaviour and, further, enabled the evaluation of the stability of pairwise swimming in biologically pertinent configurations. With the appropriateness of this technique being afforded, in part, by the time-independence of the Stokes equations, we foresee generalised notions of this approach being used more widely in the kinematic study of microswimmers that are driven by periodic flagellar or ciliary beating.

Each of the kinematic Chapters of this thesis sought to investigate a particular biological setting or organism, duly motivated by their particular scientific contexts. For example, we have studied the behaviours of *Leishmania mexicana* in a range of conditions, observing a perhaps surprising absence of stable boundary swimming, even in the presence of either repulsive surface forces or background flows, each of which can lead to stable swimming in other organisms [40, 100, 101, 168]. The lack of stable swimming in this environment may serve to explain a particular aspect of the *Leishmania* life cycle, with these organisms known to move away from the boundaries of the sandfly-vector midgut upon detachment from these surfaces, though this naturally warrants significant future experimental investigation.

Progressing to the multiswimmer study of Chapter 4, a natural extension of single-swimmer considerations and as motivated by the overwhelming multiplicity and density of spermatozoa in many biological settings, we observed a remarkable anisotropy of pairwise swimming, with both stability and an increase in swimming speed afforded by above-below configurations, whilst neither were present in side-by-side swimming. This is in apparent concordance with the experimental study of Woolley et al. [93], in which synchronised spermatozoa with visually overlapping heads were observed to move at an increased speed, though a direct comparison between experiment and theory is currently out of reach. However, a significant limitation of the study of Chapter 4 is the assumed synchrony of the flagellar beats of the swimmers, with full and proper treatment of the elastohydrodynamics warranted. Indeed, our kinematic investigation has recently been partially replicated in an elastohydrodynamic setting [242], though the associated computational costs limit a similarly thorough investigation of the pairwise dynamics.

The anisotropy of the two-swimmer problem considered in this thesis also gave rise to an ideal test problem for the evaluation of a recent coarse-grained methodology for swimmer approximation, that of Ishimoto et al. [72], as used by Ishimoto and Gaffney [74]. Repeating our analysis of the multiswimmer setting using this approach, we noted a failure of this recent coarse-grained framework to capture the dynamics accurately, with little to no anisotropy evident in the low-dimensional dynamical systems that were derived using Ishimoto and Gaffney's methodology, in contrast to those obtained via boundary element computations. We speculate that this is a direct result of the form of the inherent anisotropy of a single swimmer, with relatively low magnitude flow fields produced outside of the plane of the flagellar beat. Indeed, with the flow approximation of Ishimoto et al. [72] utilising principal component analysis, the small out-of-plane flows are unlikely to be present in the prominent principal components. We anticipate that this may be rectified by appropriate rescaling of the generated flows, sacrificing the coordinate invariance enjoyed by the previous approach, though this modification has yet to be evaluated and represents a promising avenue of future study.

Returning to Chapter 3, in addition to its biologically interpretable results, this kinematic and scientifically motivated study has also yielded a number of theoretical contributions, perhaps the most significant of which is a suggestion of swimmer control. These remarks only briefly touch upon the rich and complex theory of the control and controllability of swimmers, significantly distinct from the largely behavioural and methodological studies conducted in this thesis. In particular, via an empirical observation of concordance between a detailed and an idealised swimmer model, we suggested and minimally exemplified the efficacy of utilising a background fluid flow to effect swimmer guidance. This motivates a detailed and precise quantification of the controllability of microswimmers via imposed background flows, with such a method of control applicable to all swimmers in appropriate environments. This is in stark contrast to the range of existing controllability studies that rely on exploitable properties of particular swimmers, for example, the magnetic microswimmers considered by Giraldi and Pomet [243] and Moreau [244]. With broad applicability and hypothesised utility, the investigation into the plausibility and robustness of flow-mediated control represents a direction for significant future exploration.

With the first three research Chapters of this thesis having explored a sequence of kinematic microswimming problems, the concluding research Chapters have instead considered the elastohydrodynamic problem, which seeks to couple the fluid flow around the flagellum to its elastic response. Investigation in this manner aims to

overcome the inherent shortfall of kinematic studies, furthering the level of detail used in biophysical investigation and enabling the incorporation of refined mechanisms for the internal driving of flagella, with the details of this regulation currently unknown and the subject of competing hypotheses. As we remarked in the Introduction, this promising and potentially transformational avenue of research has been classically prohibited by computational resource and numerical stiffness of the governing elastohydrodynamic equations, with the work of Moreau et al. [51] newly enabling efficient study of planar filament elastohydrodynamics. Despite the work of Moreau et al. [51] having been augmented multiple times over the past two years, no such studies have justified or established the accuracy of their employed hydrodynamic ansaetze. Hence, in Chapter 5 of this thesis, we have sought to improve upon this apparent paradigm by incorporating a recent and asymptotically justified slender-body ansatz [83]. Whilst its inclusion was simple, the reliance on quadrature rules to evaluate nearly singular integrals sacrificed much of the characteristic efficiency of Moreau's approach. Thus, we further sought to hybridise this methodology with the ideas of Cortez [223], producing an accurate and computationally efficient approach for planar elastohydrodynamics. An in-depth evaluation of the developed 'regularised non-uniform segment' approach validated the accuracy that we had hoped to inherit from the work of Walker et al. [83], with such an evidenced verification of an efficient method envisaged to form a part of future elastohydrodynamic studies across the community.

With the work of Moreau and our subsequent refinement both confined to the study of planar filaments, we then sought to remove this significant restriction whilst retaining the characteristic efficiency of these two-dimensional schemes. In Chapter 6, we successfully generalised this approach to three dimensions, affording a remarkable speed-up in computational simulations of multiple orders of magnitude over existing methodologies. Key to this was the circumvention of a numerical and theoretical singularity inherent to the Euler angle parameterisation of the sphere, though we only achieved this algorithmically. A more satisfying resolution would perhaps be to overcome this problem of parameterisation analytically, though the use of existing approaches, such as quaternion representation, is expected to sacrifice much of the efficiency gained as part of this generalised framework. For instance, future work could consider alternative methods of resolving this, such as the use of multiple charts and smooth transition maps to describe the surface of the sphere. A further promising avenue for practical development is the incorporation of local segment bases, as opposed

to the currently employed global parameterisation, which is likely to afford both additional scalability and improved computational performance. There is also significant scope to conduct a broad range of biologically and biophysically motivated studies, including considerations of the three-dimensional helical beating mode exhibited by spermatozoa and the swirling motion of nodal cilia.

In this thesis, we have moved between biologically driven enquiry and the abstract development of theoretical and computational approaches, at the same time transitioning from kinematic to elastohydrodynamic study. Indeed, with the recent advances in elastohydrodynamic methods, such as that presented in Chapter 6 and the transformational study of Moreau et al. [51], we envisage that much future microswimmer research will similarly move towards considerations of elastohydrodynamics, though kinematic studies will likely remain a fundamental contributor to the investigation of inertia-free swimming. Perhaps the most significant barrier to such a transition will be the discrepancy of data availability between the two approaches, with kinematic data in relative abundance. However, with the continuing development of micro-experimental techniques and an improving mechanical understanding of the flagellum, this gap has the potential to close rapidly.

That being said, a necessary precursor to the advent of widespread adoption of elastohydrodynamic methods is the proof of their reliability and accuracy. For the case of planar motion, both recent and classical theories can afford such validity when coupled to elastohydrodynamic frameworks, as we demonstrated in Chapter 5 for the regularised theory of Walker et al. [83]. Whilst the flexibility of these frameworks enables the ready insertion of alternate hydrodynamic theories and ansaetze, accuracy in efficient three-dimensional elastohydrodynamic frameworks, such as that developed in Chapter 6, remains out of reach. This is due to the absence of an efficient theory suited to capturing the flow around a filament that is locally rotating, something of little consequence in planar studies though highly relevant to general three-dimensional motion. Owing to the presumed subdominance of rotational effects by essentially all slender hydrodynamic theories, including each of those introduced and discussed throughout this thesis, the torque acting on a slender body invariably goes unquantified. Therefore, in order to enable reliable three-dimensional elastohydrodynamic study, such a hydrodynamic slender-body theory that captures local rotation is necessitated and is expected to be the subject of future work.

Once again returning to the kinematic studies of the early research Chapters of this thesis, we have only begun to touch upon the breadth of such enquiries that could be conducted. For instance, having considered the effects of a no-slip boundary on

the swimming of *Leishmania mexicana* in Chapters 2 and 3, it remains to investigate the impacts of a free or no-shear surface on near-boundary swimming, with surface boundary character noted to have significant effects on the swimming of bacteria [104], for example. Another promising avenue of future research concerns multiswimmer behaviours, though detailed and thorough explorations of the high-dimensional space of swimmer configurations are expected to be very computationally demanding, perhaps prohibitively so. Whilst we circumvented the need for complete consideration of the phase-dependent dynamics of two swimmers in Chapter 4, the same approach of dimensionality reduction and phase averaging may not yield similar such improvements in the many-swimmer case, with systems of reduced dimension likely still beyond the scope of modern computational resources. Future investigations could also seek to link recent theoretical developments with modern experimental approaches, with one such direction being the rigorous evaluation of the impacts of genetic factors on the form and function of cilia and flagella, enabled by advances in elastohydrodynamics and genomics. This, in turn, has the broad potential to inform our biological and mechanical understanding of the wealth of ciliary systems that can be found throughout eukaryotic organisms. Such systems include the densely packed cilia of the human airway, though significant theoretical developments are required in order to more faithfully model many biological systems, including improvements to our understanding of non-Newtonian fluids and the formulation of methodologies for the accurate elastohydrodynamic simulation of multiple filaments.

In summary, we have considered many different facets of flagellated swimming, from the interactions of multiple swimmers to the coupling between the elastic flagellum and the surrounding fluid. In doing so, we have designed and adopted new methodologies and approaches for the theoretical investigation of microswimming, systematically interrogated kinematic swimmer models via approximate techniques, and, perhaps most significantly, enabled simple and efficient numerical study of the complex three-dimensional behaviours of elastic filaments in a viscous fluid.

Bibliography

[1] I. Manton and B. Clarke. An electron microscope study of the spermatozoid of Sphagnum. *Journal of Experimental Botany*, 3(9):265–275, 1952.

[2] P. Sartori, V. F. Geyer, A. Scholich, F. Jülicher, and J. Howard. Dynamic curvature regulation accounts for the symmetric and asymmetric beats of Chlamydomonas flagella. *eLife*, 5:1–26, 2016.

[3] V. Mukundan, P. Sartori, V. F. Geyer, F. Jülicher, and J. Howard. Motor regulation results in distal forces that bend partially disintegrated chlamydomonas axonemes into circular arcs. *Biophysical Journal*, 106(11):2434–2442, 2014.

[4] B. Qin, A. Gopinath, J. Yang, J. P. Gollub, and P. E. Arratia. Flagellar kinematics and swimming of algal cells in viscoelastic fluids. *Scientific Reports*, 5:1–7, 2015.

[5] T. J. Pedley and J. O. Kessler. A new continuum model for suspensions of gyrotactic microorganisms. *Journal of Fluid Mechanics*, 212:155, 1990.

[6] K. Drescher, R. E. Goldstein, N. Michel, M. Polin, and I. Tuval. Direct measurement of the flow field around swimming microorganisms. *Physical Review Letters*, 105(16):1–4, 2010.

[7] K. L. Hill. Biology and mechanism of trypanosome cell motility. *Eukaryotic Cell*, 2(2):200–208, 2003.

[8] P. Bastin, T. J. Pullen, F. F. Moreira-Leite, and K. Gull. Inside and outside of the trypanosome flagellum: A multifunctional organelle. *Microbes and Infection*, 2(15):1865–1874, 2000.

[9] G. Ballesteros-Rodea, M. Santillán, S. Martínez-Calvillo, and R. Manning-Cela. Flagellar motility of Trypanosoma cruzi epimastigotes. *Journal of Biomedicine and Biotechnology*, 2012:1–9, 2012.

[10] C. Gadelha, B. Wickstead, and K. Gull. Flagellar and ciliary beating in trypanosome motility. *Cell Motility and the Cytoskeleton*, 64(8):629–643, 2007.

[11] R. Broadhead, H. R. Dawe, H. Farr, S. Griffiths, S. R. Hart, N. Portman, M. K. Shaw, M. L. Ginger, S. J. Gaskell, P. G. McKean, and K. Gull. Flagellar motility is required for the viability of the bloodstream trypanosome. *Nature*, 440(7081):224–227, 2006.

[12] T. Omori and T. Ishikawa. Upward swimming of a sperm cell in shear flow. *Physical Review E*, 93(3):32402, 2016.

[13] J. Gray and G. J. Hancock. The propulsion of sea-urchin spermatozoa. *Journal of Experimental Biology*, 32(4):802–814, 1955.

[14] K. Miki and D. E. Clapham. Rheotaxis guides mammalian sperm. *Current Biology*, 23(6): 443–452, 2013.

[15] L. Chauvaud, J. Cosson, M. Suquet, and R. Billard. Sperm motility in turbot, Scophthalmus marimus: initiation of movement and changes with time of swimming characteristics. *Environmental Biology of Fishes*, 43(4):341–349, 1995.

[16] L. Scharer, D. T. J. Littlewood, A. Waeschenbach, W. Yoshida, and D. B. Vizoso. Mating behavior and the evolution of sperm design. *Proceedings of the National Academy of Sciences*, 108(4):1490–1495, 2011.

[17] E. E. Wallach, D. Y. Liu, and H. W. G. Baker. Tests of human sperm function and fertilization in vitro. *Fertility and Sterility*, 58(3):465–483, 1992.

[18] K. Coetzee, T. F. Kruge, and C. J. Lombard. Predictive value of normal sperm morphology: a structured literature review. *Human Reproduction Update*, 4(1):73–82, 1998.

[19] T. K. Chaudhury. On swimming in a visco-elastic liquid. *Journal of Fluid Mechanics*, 95(01): 189, 1979.

[20] G. R. Fulford, D. F. Katz, and R. L. Powell. Swimming of spermatozoa in a linear viscoelastic fluid. *Biorheology*, 35(4, 5):295–309, 1998.

[21] E. Lauga. Propulsion in a viscoelastic fluid. *Physics of Fluids*, 19(8):083104, 2007.

[22] H. C. Fu, C. W. Wolgemuth, and T. R. Powers. Swimming speeds of filaments in nonlinearly viscoelastic fluids. *Physics of Fluids*, 21(3):033102, 2009.

[23] C.-K. Tung, C. Lin, B. Harvey, A. G. Fiore, F. Ardon, M. Wu, and S. S. Suarez. Fluid viscoelasticity promotes collective swimming of sperm. *Scientific Reports*, 7(1):3152, 2017.

[24] C. Datt, B. Nasouri, and G. J. Elfring. Two-sphere swimmers in viscoelastic fluids. *Physical Review Fluids*, 3(12):123301, 2018.

[25] C. Li, B. Qin, A. Gopinath, P. E. Arratia, B. Thomases, and R. D. Guy. Flagellar swimming in viscoelastic fluids: role of fluid elastic stress revealed by simulations based on experimental data. *Journal of The Royal Society Interface*, 14(135):20170289, 2017.

[26] L. Li and S. E. Spagnolie. Swimming and pumping by helical waves in viscous and viscoelastic fluids. *Physics of Fluids*, 27(2):021902, 2015.

[27] B. Thomases and R. D. Guy. The role of body flexibility in stroke enhancements for finite-length undulatory swimmers in viscoelastic fluids. *Journal of Fluid Mechanics*, 825:109–132, 2017.

[28] B. Liu, T. R. Powers, and K. S. Breuer. Force-free swimming of a model helical flagellum in viscoelastic fluids. *Proceedings of the National Academy of Sciences*, 108(49):19516–19520, 2011.

[29] X. N. Shen and P. E. Arratia. Undulatory swimming in viscoelastic fluids. *Physical Review Letters*, 106(20):208101, 2011.

[30] J. Teran, L. Fauci, and M. Shelley. Viscoelastic fluid response can increase the speed and efficiency of a free swimmer. *Physical Review Letters*, 104(3):038101, 2010.

[31] E. Lauga and T. R. Powers. The hydrodynamics of swimming microorganisms. *Reports on Progress in Physics*, 72(9), 2009.

[32] C. B. Lindemann and K. A. Lesich. Flagellar and ciliary beating: the proven and the possible. *Journal of Cell Science*, 123(4):519–528, 2010.

[33] E. A. Gaffney, H. Gadêlha, D. J. Smith, J. R. Blake, and J. C. Kirkman-Brown. Mammalian sperm motility: observation and theory. *Annual Review of Fluid Mechanics*, 43(1):501–528, 2011.

[34] D. F. Katz, J. W. Overstreet, S. J. Samuels, P. W. Niswander, T. D. Bloom, and E. L. Lewis. Morphometric analysis of spermatozoa in the assessment of human male fertility. *Journal of Andrology*, 7(4):203–10, 1986.

[35] W. V. Holt, H. D. M. Moore, and S. G. Hillier. Computer-assisted measurement of sperm swimming speed in human semen: correlation of results with in vitro fertilization assays. *Fertility and sterility*, 44(1):112–119, 1985.

[36] C. S. Chen, H. T. Chao, C. H. Leng, R. L. Pan, and Y. H. Wei. Direct measurement of the tail beat frequency of human sperm by flash light synchronization. *Andrologia*, 30(1):49–54, 1998.

[37] C. W. Oseen. Uber die Stokes' sche formel und uber eine verwandte aufgabe in der hydrodynamik. *Arkiv för Matematik, Astronomi och Fysik*, 6:1, 1910.

[38] H. Winet, G. S. Bernstein, and J. Head. Observations on the response of human spermatozoa to gravity, boundaries and fluid shear. *Reproduction*, 70(2):511–523, 1984.

[39] T. J. Pedley and J. O. Kessler. Hydrodynamic phenomena in suspensions of swimming microorganisms. *Annual Review of Fluid Mechanics*, 24(1):313–358, 1992.

[40] D. J. Smith, E. A. Gaffney, J. R. Blake, and J. C. Kirkman-Brown. Human sperm accumulation near surfaces: a simulation study. *Journal of Fluid Mechanics*, 621:289–320, 2009.

[41] G. J. Hancock. The self-propulsion of microscopic organisms through liquids. *Proceedings of the Royal Society of London. Series A. Mathematical and Physical Sciences*, 217(1128):96–121, 1953.

[42] A. T. Chwang and T. Y.-T. Wu. Hydromechanics of low-Reynolds-number flow. Part 2. Singularity method for Stokes flows. *Journal of Fluid Mechanics*, 67(4):787–815, 1975.

[43] J. R. Blake. A note on the image system for a stokeslet in a no-slip boundary. *Mathematical Proceedings of the Cambridge Philosophical Society*, 70(02):303, 1971.

[44] H. Hasimoto. On the periodic fundamental solutions of the Stokes equations and their application to viscous flow past a cubic array of spheres. *Journal of Fluid Mechanics*, 5(02):317, 1959.

[45] C. Pozrikidis. *Boundary integral and singularity methods for linearized viscous flow*. Cambridge University Press, 1992.

[46] J. J. L. Higdon. A hydrodynamic analysis of flagellar propulsion. *Journal of Fluid Mechanics*, 90(04):685, 1979.

[47] G. G. Stokes. *On the effect of the internal friction of fluids on the motion of pendulums*, volume 9. Pitt Press Cambridge, 1851.

[48] R. G. Cox. The motion of long slender bodies in a viscous fluid Part 1. General theory. *Journal of Fluid Mechanics*, 44(04):791–810, 1970.

[49] R. E. Johnson and C. J. Brokaw. Flagellar hydrodynamics. A comparison between resistive-force theory and slender-body theory. *Biophysical Journal*, 25(1):113–127, 1979.

[50] J. Lighthill. Flagellar hydrodynamics. *SIAM review*, 18(2):161–230, 1976.

[51] C. Moreau, L. Giraldi, and H. Gadêlha. The asymptotic coarse-graining formulation of slender-rods, bio-filaments and flagella. *Journal of The Royal Society Interface*, 15(144):20180235, 2018.

[52] R. E. Johnson. An improved slender-body theory for Stokes flow. *Journal of Fluid Mechanics*, 99(2):411–431, 1980.

[53] C. Brennen and H. Winet. Fluid mechanics of propulsion by cilia and flagella. *Annual Review of Fluid Mechanics*, 9(1):339–398, 1977.

[54] M. Ramia, D. L. Tullock, and N. Phan-Thien. The role of hydrodynamic interaction in the locomotion of microorganisms. *Biophysical Journal*, 65(2):755–778, 1993.

[55] B. J. Walker, K. Ishimoto, H. Gadêlha, and E. A. Gaffney. Filament mechanics in a half-space via regularised Stokeslet segments. *Journal of Fluid Mechanics*, 879:808–833, 2019.

[56] Y. Man, L. Koens, and E. Lauga. Hydrodynamic interactions between nearby slender filaments. *EPL (Europhysics Letters)*, 116(2):24002, 2016.

[57] J. Lighthill. Mathematical biofluiddynamics. In *Regional Conference Series in Applied Mathematics, no. 17*. SIAM, 1975.

[58] J. B. Keller and S. I. Rubinow. Slender-body theory for slow viscous flow. *Journal of Fluid Mechanics*, 75(4):705–714, 1976.

[59] T. Y. Wu and G. Yates. Finite-amplitude unsteady slender-body flow theory. In *11th Symposium on Naval Hydrodynamics*, 1976.

[60] A. K. Tornberg and M. J. Shelley. Simulating the dynamics and interactions of flexible fibers in Stokes flows. *Journal of Computational Physics*, 196(1):8–40, 2004.

[61] M. J. Shelley and T. Ueda. The Stokesian hydrodynamics of flexing, stretching filaments. *Physica D: Nonlinear Phenomena*, 146(1-4):221–245, 2000.

[62] L. Li, H. Manikantan, D. Saintillan, and S. E. Spagnolie. The sedimentation of flexible filaments. *Journal of Fluid Mechanics*, 735:705–736, 2013.

[63] K. Ishimoto and E. A. Gaffney. A study of spermatozoan swimming stability near a surface. *Journal of Theoretical Biology*, 360:187–199, 2014.

[64] D. J. Smith, E. A. Gaffney, and J. R. Blake. Discrete cilia modelling with singularity distributions: application to the embryonic node and the airway surface liquid. *Bulletin of Mathematical Biology*, 69(5):1477–1510, 2007.

[65] Y. Liu, B. Chakrabarti, D. Saintillan, A. Lindner, and O. du Roure. Morphological transitions of elastic filaments in shear flow. *Proceedings of the National Academy of Sciences*, 115(38): 9438–9443, 2018.

[66] G. K. Youngren and A. Acrivos. Stokes flow past a particle of arbitrary shape: a numerical method of solution. *Journal of Fluid Mechanics*, 69(02):377, 1975.

[67] C. Pozrikidis. *A practical guide to boundary element methods with the software library BEMLIB*. CRC Press, 2002.

[68] W. Varnhorn. Efficient quadrature for a boundary element method to compute three-dimensional Stokes flow. *International Journal for Numerical Methods in Fluids*, 9(2):185–191, 1989.

[69] H. Shum, E. A. Gaffney, and D. J. Smith. Modelling bacterial behaviour close to a no-slip plane boundary: the influence of bacterial geometry. *Proceedings of the Royal Society A: Mathematical, Physical and Engineering Sciences*, 466(2118):1725–1748, 2010.

[70] D. J. Smith. A boundary element regularized Stokeslet method applied to cilia- and flagella-driven flow. *Proceedings of the Royal Society A: Mathematical, Physical and Engineering Sciences*, 465(2112):3605–3626, 2009.

[71] K. Ishimoto, J. Cosson, and E. A. Gaffney. A simulation study of sperm motility hydrodynamics near fish eggs and spheres. *Journal of Theoretical Biology*, 389:187–197, 2016.

[72] K. Ishimoto, H. Gadêlha, E. A. Gaffney, D. J. Smith, and J. Kirkman-Brown. Coarse-graining the fluid flow around a human sperm. *Physical Review Letters*, 118(12):124501, 2017.

[73] T. D. Montenegro-Johnson and E. Lauga. Optimal swimming of a sheet. *Physical Review E*, 89(6):060701, 2014.

[74] K. Ishimoto and E. A. Gaffney. Hydrodynamic clustering of human sperm in viscoelastic fluids. *Scientific Reports*, 8(1):15600, 2018.

[75] R. Cortez. The method of regularized Stokeslets. *SIAM Journal on Scientific Computing*, 23 (4):1204–1225, 2001.

[76] J. Ainley, S. Durkin, R. Embid, P. Boindala, and R. Cortez. The method of images for regularized Stokeslets. *Journal of Computational Physics*, 227(9):4600–4616, 2008.

[77] R. Cortez, L. Fauci, and A. Medovikov. The method of regularized Stokeslets in three dimensions: analysis, validation, and application to helical swimming. *Physics of Fluids*, 17(3): 031504, 2005.

[78] S. E. Spagnolie and E. Lauga. Hydrodynamics of self-propulsion near a boundary: predictions and accuracy of far-field approximations. *Journal of Fluid Mechanics*, 700:105–147, 2012.

[79] H. Flores, E. Lobaton, S. Mendezdiez, S. Tlupova, and R. Cortez. A study of bacterial flagellar bundling. *Bulletin of Mathematical Biology*, 67(1):137–168, 2005.

[80] E. A. Gillies, R. M. Cannon, R. B. Green, and A. A. Pacey. Hydrodynamic propulsion of human sperm. *Journal of Fluid Mechanics*, 625:445–474, 2009.

[81] A. Buchmann, L. J. Fauci, K. Leiderman, E. Strawbridge, and L. Zhao. Mixing and pumping by pairs of helices in a viscous fluid. *Physical Review E*, 97(2):1–11, 2018.

[82] R. Cortez and M. Nicholas. Slender body theory for Stokes flows with regularized forces. *Communications in Applied Mathematics and Computational Science*, 7(1):33–62, 2012.

[83] B. J. Walker, M. P. Curtis, K. Ishimoto, and E. A. Gaffney. A regularised slender-body theory of non-uniform filaments. *Journal of Fluid Mechanics*, 899:A3, 2020.

[84] G. Taylor. Analysis of the swimming of microscopic organisms. *Proceedings of the Royal Society of London. Series A. Mathematical and Physical Sciences*, 209(1099):447–461, 1951.

[85] J. Gray. *Ciliary movement.* Cambridge University Press, Cambridge [England], 1928.

[86] W. S. Perrin. Researches upon the life-history of Trypanosoma balbianii (CERTES). *Archiv für Protistenkunde*, 7:131–156, 1906.

[87] G. J. Elfring and E. Lauga. Hydrodynamic phase locking of swimming microorganisms. *Physical Review Letters*, 103(8):088101, 2009.

[88] N. Uchida, R. Golestanian, and R. R. Bennett. Synchronization and collective dynamics of flagella and cilia as hydrodynamically coupled oscillators. *Journal of the Physical Society of Japan*, 86(10):101007, 2017.

[89] S. D. Olson and L. J. Fauci. Hydrodynamic interactions of sheets vs filaments: Synchronization, attraction, and alignment. *Physics of Fluids*, 27(12):121901, 2015.

[90] N. Osterman and A. Vilfan. Finding the ciliary beating pattern with optimal efficiency. *Proceedings of the National Academy of Sciences*, 108(38):15727–15732, 2011.

[91] H. Guo, L. Fauci, M. Shelley, and E. Kanso. Bistability in the synchronization of actuated microfilaments. *Journal of Fluid Mechanics*, 836:304–323, 2018.

[92] R. E. Goldstein, E. Lauga, A. I. Pesci, and M. R. E. Proctor. Elastohydrodynamic synchronization of adjacent beating flagella. *Physical Review Fluids*, 1(7):073201, 2016.

[93] D. M. Woolley, R. F. Crockett, W. D. I. Groom, and S. G. Revell. A study of synchronisation between the flagella of bull spermatozoa, with related observations. *Journal of Experimental Biology*, 212(14):2215–2223, 2009.

[94] I. H. Riedel. A self-organized vortex array of hydrodynamically entrained sperm cells. *Science*, 309(5732):300–303, 2005.

[95] D. R. Brumley, K. Y. Wan, M. Polin, and R. E. Goldstein. Flagellar synchronization through direct hydrodynamic interactions. *eLife*, 3(3):1–15, 2014.

[96] R. E. Goldstein, M. Polin, and I. Tuval. Emergence of synchronized beating during the regrowth of eukaryotic flagella. *Physical Review Letters*, 107(14):148103, 2011.

[97] V. Kantsler, J. Dunkel, M. Polin, and R. E. Goldstein. Ciliary contact interactions dominate surface scattering of swimming eukaryotes. *Proceedings of the National Academy of Sciences*, 110(4):1187–1192, 2013.

[98] K. Y. Wan and R. E. Goldstein. Coordinated beating of algal flagella is mediated by basal coupling. *Proceedings of the National Academy of Sciences*, 113(20):E2784–E2793, 2016.

[99] K. Ishimoto and E. A. Gaffney. Fluid flow and sperm guidance: a simulation study of hydrodynamic sperm rheotaxis. *Journal of The Royal Society Interface*, 12(106):20150172, 2015.

[100] L. J. Fauci and A. McDonald. Sperm motility in the presence of boundaries. *Bulletin of Mathematical Biology*, 57(5):679–699, 1995.

[101] J. Elgeti, U. B. Kaupp, and G. Gompper. Hydrodynamics of sperm cells near surfaces. *Biophysical Journal*, 99(4):1018–1026, 2010.

[102] D. Smith, E. Gaffney, H. Shum, H. Gadêlha, and J. Kirkman-Brown. Comment on the Article by J. Elgeti, U. B. Kaupp, and G. Gompper: Hydrodynamics of sperm cells near surfaces. *Biophysical Journal*, 100(9):2318–2320, 2011.

[103] E. Lauga, W. R. DiLuzio, G. M. Whitesides, and H. A. Stone. Swimming in circles: motion of bacteria near solid boundaries. *Biophysical Journal*, 90(2):400–412, 2006.

[104] D. Lopez and E. Lauga. Dynamics of swimming bacteria at complex interfaces. *Physics of Fluids*, 26(7):071902, 2014.

[105] J. R. Blake. A spherical envelope approach to ciliary propulsion. *Journal of Fluid Mechanics*, 46(01):199, 1971.

[106] M. J. Lighthill. On the squirming motion of nearly spherical deformable bodies through liquids at very small Reynolds numbers. *Communications on Pure and Applied Mathematics*, 5(2): 109–118, 1952.

[107] V. Magar and T. J. Pedley. Average nutrient uptake by a self-propelled unsteady squirmer. *Journal of Fluid Mechanics*, 539:93, 2005.

[108] T. Ishikawa, M. P. Simmonds, and T. J. Pedley. Hydrodynamic interaction of two swimming model micro-organisms. *Journal of Fluid Mechanics*, 568:119, 2006.

[109] O. S. Pak and E. Lauga. Generalized squirming motion of a sphere. *Journal of Engineering Mathematics*, 88(1):1–28, 2014.

[110] E. M. Purcell. Life at low Reynolds number. *American Journal of Physics*, 45(1):3–11, 1977.

[111] A. Najafi and R. Golestanian. Simple swimmer at low Reynolds number: three linked spheres. *Physical Review E*, 69(6):062901, 2004.

[112] S. Suarez and A. A. Pacey. Sperm transport in the female reproductive tract. *Human Reproduction Update*, 12(1):23–37, 2006.

[113] K. Ishimoto and E. A. Gaffney. Squirmer dynamics near a boundary. *Physical Review E*, 88 (6):062702, 2013.

[114] K. Ishimoto. Guidance of microswimmers by wall and flow: Thigmotaxis and rheotaxis of unsteady squirmers in two and three dimensions. *Physical Review E*, 96(4):043103, 2017.

[115] V. Kantsler, J. Dunkel, M. Blayney, and R. E. Goldstein. Rheotaxis facilitates upstream navigation of mammalian sperm cells. *eLife*, 3:e03521, 2014.

[116] C.-K. Tung, F. Ardon, A. Roy, D. L. Koch, S. S. Suarez, and M. Wu. Emergence of upstream swimming via a hydrodynamic transition. *Physical Review Letters*, 114(10):108102, 2015.

[117] Marcos, H. C. Fu, T. R. Powers, and R. Stocker. Bacterial rheotaxis. *Proceedings of the National Academy of Sciences*, 109(13):4780–4785, 2012.

[118] M. Molaei and J. Sheng. Succeed escape: Flow shear promotes tumbling of Escherichia colinear a solid surface. *Scientific Reports*, 6(1):35290, 2016.

[119] M. Molaei, M. Barry, R. Stocker, and J. Sheng. Failed escape: solid surfaces prevent tumbling of Escherichia coli. *Physical Review Letters*, 113(6):068103, 2014.

[120] G. B. Jeffery. The motion of ellipsoidal particles immersed in a viscous fluid. *Proceedings of the Royal Society A: Mathematical, Physical and Engineering Sciences*, 102(715):161–179, 1922.

[121] R. Bearon and D. Grünbaum. From individual behaviour to population models: a case study using swimming algae. *Journal of Theoretical Biology*, 251(4):679–697, 2008.

[122] Y. Yang, J. Elgeti, and G. Gompper. Cooperation of sperm in two dimensions: synchronization, attraction, and aggregation through hydrodynamic interactions. *Physical Review E*, 78 (6):061903, 2008.

[123] S. F. Schoeller and E. E. Keaveny. From flagellar undulations to collective motion: predicting the dynamics of sperm suspensions. *Journal of the Royal Society Interface*, 15(140), 2018.

[124] S. Lomholt and M. R. Maxey. Force-coupling method for particulate two-phase flow: Stokes flow. *Journal of Computational Physics*, 184(2):381–405, 2003.

[125] B. J. Walker, K. Ishimoto, and R. J. Wheeler. Automated identification of flagella from videomicroscopy via the medial axis transform. *Scientific Reports*, 9(1):5015, 2019.

[126] M. T. Gallagher, G. Cupples, E. H. Ooi, J. C. Kirkman-Brown, and D. J. Smith. Rapid sperm capture: high-throughput flagellar waveform analysis. *Human Reproduction*, 34(7):1173–1185, 2019.

[127] P. V. Bayly and K. S. Wilson. Equations of interdoublet separation during flagella motion reveal mechanisms of wave propagation and instability. *Biophysical Journal*, 107(7):1756–1772, 2014.

[128] P. V. Bayly and K. S. Wilson. Analysis of unstable modes distinguishes mathematical models of flagellar motion. *Journal of The Royal Society Interface*, 12(106):20150124, 2015.

[129] C. B. Lindemann. A 'geometric clutch' hypothesis to explain oscillations of the axoneme of cilia and flagella. *Journal of Theoretical Biology*, 168(2):175–189, 1994.

[130] I. H. Riedel-Kruse and A. Hilfinger. How molecular motors shape the flagellar beat. *HFSP Journal*, 1(3):192–208, 2007.

[131] S. Camalet and F. Jülicher. Generic aspects of axonemal beating. *New Journal of Physics*, 2 (24), 2000.

[132] K. E. Machin. Wave propagation along flagella. *Journal of Experimental Biology*, 35(May): 796–806, 1958.

[133] M. Hines and J. Blum. Bend propagation in flagella. I. Derivation of equations of motion and their simulation. *Biophysical Journal*, 23(1):41–57, 1978.

[134] O. du Roure, A. Lindner, E. N. Nazockdast, and M. J. Shelley. Dynamics of flexible fibers in viscous flows and fluids. *Annual Review of Fluid Mechanics*, 51(1):539–572, 2019.

[135] A. L. Hall-McNair, T. D. Montenegro-Johnson, H. Gadêlha, D. J. Smith, and M. T. Gallagher. Efficient implementation of elastohydrodynamics via integral operators. *Physical Review Fluids*, 4(11):1–24, 2019.

[136] C. V. Neal, A. L. Hall-McNair, J. Kirkman-Brown, D. J. Smith, and M. T. Gallagher. Doing more with less: The flagellar end piece enhances the propulsive effectiveness of human spermatozoa. *Physical Review Fluids*, 5(7):073101, 2020.

[137] B. J. Walker and R. J. Wheeler. High-speed multifocal plane fluorescence microscopy for three-dimensional visualisation of beating flagella. *Journal of Cell Science*, 132(16):jcs231795, 2019.

[138] B. J. Walker, R. J. Wheeler, K. Ishimoto, and E. A. Gaffney. Boundary behaviours of Leishmania mexicana: a hydrodynamic simulation study. *Journal of Theoretical Biology*, 462:311–320, 2019.

[139] B. L. Herwaldt. Leishmaniasis. *The Lancet*, 354(9185):1191–1199, 1999.

[140] J. R. Herricks, P. J. Hotez, V. Wanga, L. E. Coffeng, J. A. Haagsma, M.-G. Basáñez, G. Buckle, C. M. Budke, H. Carabin, E. M. Fèvre, T. Fürst, Y. A. Halasa, C. H. King, M. E. Murdoch, K. D. Ramaiah, D. S. Shepard, W. A. Stolk, E. A. Undurraga, J. D. Stanaway, M. Naghavi, and C. J. L. Murray. The global burden of disease study 2013: what does it mean for the NTDs? *PLOS Neglected Tropical Diseases*, 11(8):e0005424, 2017.

[141] P. A. Bates. Complete developmental cycle of Leishmania mexicana in axenic culture. *Parasitology*, 108(01):1, 1994.

[142] C. Branche. Conserved and specific functions of axoneme components in trypanosome motility. *Journal of Cell Science*, 119(16):3443–3455, 2006.

[143] S. F. Goldstein, M. E. Holwill, and N. R. Silvester. The effects of laser microbeam irradiation on the flagellum of Crithidia (Strigomonas) oncopelti. *The Journal of Experimental Biology*, 53(2):401–9, 1970.

[144] M. E. Holwill and J. L. McGregor. Micromanipulation of the flagellum of Crithidia oncopelti. I. Mechanical effects. *The Journal of Experimental Biology*, 60(2):437–44, 1974.

[145] M. E. Holwill and J. L. McGregor. Effects of calcium on flagellar movement in the trypanosome Crithidia oncopelti. *The Journal of Experimental Biology*, 65(1):229–42, 1976.

[146] D. N. Johnston, N. R. Silvester, and M. E. Holwill. An analysis of the shape and propagation of waves on the flagellum of Crithidia oncopelti. *Journal of Experimental Biology*, 80(1):299–315, 1979.

[147] A. Cuvillier, F. Redon, J. C. Antoine, P. Chardin, T. DeVos, and G. Merlin. LdARL-3A, a Leishmania promastigote-specific ADP-ribosylation factor-like protein, is essential for flagellum integrity. *Journal of cell science*, 113(11):2065–74, 2000.

[148] A. Dostálová and P. Volf. Leishmania development in sand flies: parasite-vector interactions overview. *Parasites & Vectors*, 5(1):276, 2012.

[149] P. A. Bates. Leishmania sand fly interaction: progress and challenges. *Current Opinion in Microbiology*, 11(4):340–344, 2008.

[150] B. A. Butcher, S. J. Turco, B. A. Hilty, P. F. Pimenta, M. Panunzio, and D. L. Sacks. Deficiency in β1,3-galactosyltransferase of a Leishmania major lipophosphoglycan mutant adversely influences the Leishmania-sand fly interaction. *Journal of Biological Chemistry*, 271 (34):20573–20579, 1996.

[151] P. F. Pimenta, S. J. Turco, M. J. McConville, P. G. Lawyer, P. V. Perkins, and D. L. Sacks. Stage-specific adhesion of Leishmania promastigotes to the sandfly midgut. *Science*, 256(5065): 1812–1815, 1992.

[152] P. F. Pimenta, E. M. Saraiva, E. Rowton, G. B. Modi, L. A. Garraway, S. M. Beverley, S. J. Turco, and D. L. Sacks. Evidence that the vectorial competence of phlebotomine sand flies for different species of Leishmania is controlled by structural polymorphisms in the surface lipophosphoglycan. *Proceedings of the National Academy of Sciences of the United States of America*, 91(19):9155–9159, 1994.

[153] R. P. Soares, M. E. Macedo, C. Ropert, N. F. Gontijo, I. C. Almeida, R. T. Gazzinelli, P. F. Pimenta, and S. J. Turco. Leishmania chagasi: Lipophosphoglycan characterization and binding to the midgut of the sand fly vector Lutzomyia longipalpis. *Molecular and Biochemical Parasitology*, 121(2):213–224, 2002.

[154] R. P. Soares, C. Margonari, N. C. Secundino, M. E. Macêdo, S. M. Da Costa, E. F. Rangel, P. F. Pimenta, and S. J. Turco. Differential midgut attachment of Leishmania (Viannia) braziliensis in the sand flies Lutzomyia (Nyssomyia) whitmani and Lutzomyia (Nyssomyia) intermedia. *Journal of Biomedicine and Biotechnology*, 2010, 2010.

[155] R. J. Wheeler, J. D. Sunter, and K. Gull. Flagellar pocket restructuring through the Leishmania life cycle involves a discrete flagellum attachment zone. *Journal of Cell Science*, 129 (4):854–867, 2016.

[156] R. J. Wheeler, E. Gluenz, and K. Gull. The cell cycle of Leishmania: morphogenetic events and their implications for parasite biology. *Molecular Microbiology*, 79(3):647–662, 2011.

[157] S. Werner, J. C. Rink, I. H. Riedel-Kruse, and B. M. Friedrich. Shape mode analysis exposes movement patterns in biology: flagella and flatworms as case studies. *PLoS ONE*, 9(11): e113083, 2014.

[158] R. Ma, G. S. Klindt, I. H. Riedel-Kruse, F. Jülicher, and B. M. Friedrich. Active phase and amplitude fluctuations of flagellar beating. *Physical Review Letters*, 113(4):1–5, 2014.

[159] B. J. Walker, S. Phuyal, K. Ishimoto, C.-K. Tung, and E. A. Gaffney. Computer-assisted beat-pattern analysis and the flagellar waveforms of bovine spermatozoa. *Royal Society Open Science*, 7(6):200769, 2020.

[160] D. J. Smith, E. A. Gaffney, H. Gadêlha, N. Kapur, and J. C. Kirkman-Brown. Bend propagation in the flagella of migrating human sperm, and its modulation by viscosity. *Cell Motility and the Cytoskeleton*, 66(4):220–236, 2009.

[161] S. Lacomble, S. Vaughan, C. Gadelha, M. K. Morphew, M. K. Shaw, J. R. McIntosh, and K. Gull. Three-dimensional cellular architecture of the flagellar pocket and associated cytoskeleton in trypanosomes revealed by electron microscope tomography. *Journal of Cell Science*, 122(8):1081–1090, 2009.

[162] S. Lacomble, S. Vaughan, C. Gadelha, M. K. Morphew, M. K. Shaw, J. R. McIntosh, and K. Gull. Basal body movements orchestrate membrane organelle division and cell morphogenesis in Trypanosoma brucei. *Journal of Cell Science*, 123(17):2884–2891, 2010.

[163] R. J. Wheeler. Use of chiral cell shape to ensure highly directional swimming in trypanosomes. *PLoS Computational Biology*, 13(1):e1005353, 2017.

[164] J. Nocedal and S. J. Wright. *Numerical optimization*, volume 11 of *Springer Series in Operations Research and Financial Engineering*. Springer-Verlag, New York, 1999.

[165] B. J. Walker. *Aspects of simulating microswimmers*. Masters thesis, University of Oxford, 2017.

[166] J. D. Klein, A. R. Clapp, and R. B. Dickinson. Direct measurement of interaction forces between a single bacterium and a flat plate. *Journal of Colloid and Interface Science*, 261(2): 379–385, 2003.

[167] K. Ishimoto and E. A. Gaffney. Mechanical tuning of mammalian sperm behaviour by hyperactivation, rheology and substrate adhesion: a numerical exploration. *Journal of The Royal Society Interface*, 13(124):20160633, 2016.

[168] D. J. Smith and J. R. Blake. Surface accumulation of spermatozoa: a fluid dynamic phenomenon. *The Mathematical Scientist*, 2009.

[169] P. A. Bates. Transmission of Leishmania metacyclic promastigotes by phlebotomine sand flies. *International Journal for Parasitology*, 37(10):1097–1106, 2007.

[170] A. Ambit, K. L. Woods, B. Cull, G. H. Coombs, and J. C. Mottram. Morphological events during the cell cycle of Leishmania major. *Eukaryotic Cell*, 10(11):1429–1438, 2011.

[171] B. J. Walker, K. Ishimoto, R. J. Wheeler, and E. A. Gaffney. Response of monoflagellate pullers to a shearing flow: a simulation study of microswimmer guidance. *Physical Review E*, 98(6):063111, 2018.

[172] G. P. Arnold. Rheotropism in fishes. *Biological reviews of the Cambridge Philosophical Society*, 49(4):515–76, 1974.

[173] D. A. Lytle, J. D. Olden, and L. E. McMullen. Drought-escape behaviors of aquatic insects may be adaptations to highly variable flow regimes characteristic of desert rivers. *The Southwestern Naturalist*, 53(3):399–402, 2008.

[174] W. E. Uspal, M. N. Popescu, S. Dietrich, and M. Tasinkevych. Rheotaxis of spherical active particles near a planar wall. *Soft Matter*, 11(33):6613–6632, 2015.

[175] N. G. Chisholm, D. Legendre, E. Lauga, and A. S. Khair. A squirmer across Reynolds numbers. *Journal of Fluid Mechanics*, 796(May):233–256, 2016.

[176] G. Lott. *Zur anatomie und physiologie des cervix uteri.* Ferdinand Enke, Stuttgart, Germany, 1872.

[177] F. P. Bretherton and Rothschild. Rheotaxis of spermatozoa. *Proceedings of the Royal Society B: Biological Sciences*, 153(953):490–502, 1961.

[178] A. M. Roberts. Motion of spermatozoa in fluid streams. *Nature*, 228(5269):375–376, 1970.

[179] M. E. Rogers, T. Ilg, A. V. Nikolaev, M. A. J. Ferguson, and P. A. Bates. Transmission of cutaneous leishmaniasis by sand flies is enhanced by regurgitation of fPPG. *Nature*, 430(6998): 463–467, 2004.

[180] C. Bechinger, R. Di Leonardo, H. Löwen, C. Reichhardt, G. Volpe, and G. Volpe. Active particles in complex and crowded environments. *Reviews of Modern Physics*, 88(4), 2016.

[181] K. Ishimoto and D. G. Crowdy. Dynamics of a treadmilling microswimmer near a no-slip wall in simple shear. *Journal of Fluid Mechanics*, 821:647–667, 2017.

[182] A. Zöttl and H. Stark. Nonlinear dynamics of a microswimmer in Poiseuille flow. *Physical Review Letters*, 108(21):218104, 2012.

[183] M. E. Rogers, M. L. Chance, and P. A. Bates. The role of promastigote secretory gel in the origin and transmission of the infective stage of Leishmania mexicana by the sandfly Lutzomyia longipalpis. *Parasitology*, 124(5):495–507, 2002.

[184] E. J. Hinch and L. G. Leal. Rotation of small non-axisymmetric particles in a simple shear flow. *Journal of Fluid Mechanics*, 92:591–608, 1979.

[185] A. P. Berke, L. Turner, H. C. Berg, and E. Lauga. Hydrodynamic attraction of swimming microorganisms by surfaces. *Physical Review Letters*, 101(3):038102, 2008.

[186] B. J. Walker, K. Ishimoto, and E. A. Gaffney. Pairwise hydrodynamic interactions of synchronized spermatozoa. *Physical Review Fluids*, 4(9):093101, 2019.

[187] L. Rothschild. Measurement of sperm activity before artificial insemination. *Nature*, 163 (4140):358–359, 1949.

[188] H. Moore, K. Dvoráková, N. Jenkins, and W. Breed. Exceptional sperm cooperation in the wood mouse. *Nature*, 418(6894):174–177, 2002.

[189] A. Creppy, O. Praud, X. Druart, P. L. Kohnke, and F. Plouraboué. Turbulence of swarming sperm. *Physical Review E*, 92(3):032722, 2015.

[190] M. J. Zinaman, C. C. Brown, S. G. Selevan, and E. D. Clegg. Semen quality and human fertility: a prospective study with healthy couples. *Journal of Andrology*, 21(1):145–153, 2000.

[191] D. Lai, G. D. Smith, and S. Takayama. Lab-on-a-chip biophotonics: its application to assisted reproductive technologies. *Journal of Biophotonics*, 5(8-9):650–660, 2012.

[192] J. E. Swain, D. Lai, S. Takayama, and G. D. Smith. Thinking big by thinking small: application of microfluidic technology to improve ART. *Lab on a Chip*, 13(7):1213, 2013.

[193] C.-K. Tung, F. Ardon, A. G. Fiore, S. S. Suarez, and M. Wu. Cooperative roles of biological flow and surface topography in guiding sperm migration revealed by a microfluidic model. *Lab Chip*, 14(7):1348–1356, 2014.

[194] B. M. Friedrich, I. H. Riedel-Kruse, J. Howard, and F. Julicher. High-precision tracking of sperm swimming fine structure provides strong test of resistive force theory. *Journal of Experimental Biology*, 213(8):1226–1234, 2010.

[195] Y. Yang, V. Marceau, and G. Gompper. Swarm behavior of self-propelled rods and swimming flagella. *Physical Review E*, 82(3):031904, 2010.

[196] J. Simons, L. Fauci, and R. Cortez. A fully three-dimensional model of the interaction of driven elastic filaments in a Stokes flow with applications to sperm motility. *Journal of Biomechanics*, 48(9):1639–1651, 2015.

[197] I. Llopis, I. Pagonabarraga, M. Cosentino Lagomarsino, and C. P. Lowe. Cooperative motion of intrinsic and actuated semiflexible swimmers. *Physical Review E*, 87(3):032720, 2013.

[198] B. M. Friedrich and I. H. Riedel-Kruse. Flagellar beating: row with the flow. *eLife*, 3, 2014.

[199] G. J. Elfring and E. Lauga. Passive hydrodynamic synchronization of two-dimensional swimming cells. *Physics of Fluids*, 23(1):011902, 2011.

[200] L. J. Fauci. Interaction of oscillating filaments: a computational study. *Journal of Computational Physics*, 86(2):294–313, 1990.

[201] A. Sokolov and I. S. Aranson. Physical properties of collective motion in suspensions of bacteria. *Physical Review Letters*, 109(24):248109, 2012.

[202] A. Zöttl and H. Stark. Hydrodynamics determines collective motion and phase behavior of active colloids in quasi-two-dimensional confinement. *Physical Review Letters*, 112(11):118101, 2014.

[203] D. Saintillan and M. J. Shelley. Orientational order and instabilities in suspensions of self-locomoting rods. *Physical Review Letters*, 99(5):058102, 2007.

[204] N. Oyama, J. J. Molina, and R. Yamamoto. Purely hydrodynamic origin for swarming of swimming particles. *Physical Review E*, 93(4):043114, 2016.

[205] G. Li and A. M. Ardekani. Collective motion of microorganisms in a viscoelastic fluid. *Physical Review Letters*, 117(11):118001, 2016.

[206] B. Ezhilan, M. J. Shelley, and D. Saintillan. Instabilities and nonlinear dynamics of concentrated active suspensions. *Physics of Fluids*, 25(7):070607, 2013.

[207] M. C. Marchetti, J. F. Joanny, S. Ramaswamy, T. B. Liverpool, J. Prost, M. Rao, and R. A. Simha. Hydrodynamics of soft active matter. *Reviews of Modern Physics*, 85(3):1143–1189, 2013.

[208] K. Ishimoto, E. A. Gaffney, and B. J. Walker. Regularized representation of bacterial hydrodynamics. *Physical Review Fluids*, 5(9):093101, 2020.

[209] J. M. Cummins and P. F. Woodall. On mammalian sperm dimensions. *Journal of Reproduction and Fertility*, 75(1):153–175, 1985.

[210] R. D. Dresdner and D. F. Katz. Relationships of mammalian sperm motility and morphology to hydrodynamic aspects of cell function. *Biology of Reproduction*, 25(5):920–930, 1981.

[211] H. Gadêlha, E. A. Gaffney, D. J. Smith, and J. C. Kirkman-Brown. Nonlinear instability in flagellar dynamics: a novel modulation mechanism in sperm migration? *Journal of The Royal Society Interface*, 7(53):1689–1697, 2010.

[212] K. Ishimoto, H. Gadêlha, E. A. Gaffney, D. J. Smith, and J. Kirkman-Brown. Human sperm swimming in a high viscosity mucus analogue. *Journal of Theoretical Biology*, 446:1–10, 2018.

[213] B. Chakrabarti and D. Saintillan. Spontaneous oscillations, beating patterns, and hydrodynamics of active microfilaments. *Physical Review Fluids*, 4(4):043102, 2019.

[214] H. S. Fisher and H. E. Hoekstra. Competition drives cooperation among closely related sperm of deer mice. *Nature*, 463(7282):801–803, 2010.

[215] B. Walker and E. Gaffney. Regularised non-uniform segments and efficient no-slip elastohydrodynamics. *Journal of Fluid Mechanics*, 915:A51, 2021.

[216] C. Pozrikidis. Shear flow over cylindrical rods attached to a substrate. *Journal of Fluids and Structures*, 26(3):393–405, 2010.

[217] D. J. Smith, T. D. Montenegro-Johnson, and S. S. Lopes. Symmetry-breaking cilia-driven flow in embryogenesis. *Annual Review of Fluid Mechanics*, 51(1):105–128, 2019.

[218] M. Roper, R. Dreyfus, J. Baudry, M. Fermigier, J. Bibette, and H. A. Stone. On the dynamics of magnetically driven elastic filaments. *Journal of Fluid Mechanics*, 554:167–190, 2006.

[219] L. Guglielmini, A. Kushwaha, E. S. G. Shaqfeh, and H. A. Stone. Buckling transitions of an elastic filament in a viscous stagnation point flow. *Physics of Fluids*, 24(12):123601, 2012.

[220] M. P. Curtis, J. C. Kirkman-Brown, T. J. Connolly, and E. A. Gaffney. Modelling a tethered mammalian sperm cell undergoing hyperactivation. *Journal of Theoretical Biology*, 309:1–10, 2012.

[221] S. D. Olson, S. Lim, and R. Cortez. Modeling the dynamics of an elastic rod with intrinsic curvature and twist using a regularized Stokes formulation. *Journal of Computational Physics*, 238:169–187, 2013.

[222] K. Ishimoto and E. A. Gaffney. An elastohydrodynamical simulation study of filament and spermatozoan swimming driven by internal couples. *IMA Journal of Applied Mathematics*, 83 (4):655–679, 2018.

[223] R. Cortez. Regularized Stokeslet segments. *Journal of Computational Physics*, 375:783–796, 2018.

[224] A. Chwang and T. Y.-T. Wu. Hydromechanics of low-Reynolds-number flow. Part 1. Rotation of axisymmetric prolate bodies. *Journal of Fluid Mechanics*, 63(3):607–622, 1974.

[225] L. F. Shampine and M. W. Reichelt. The MATLAB ODE Suite. *SIAM Journal on Scientific Computing*, 18(1):1–22, 1997.

[226] B. J. Walker, K. Ishimoto, and E. A. Gaffney. Efficient simulation of filament elastohydrodynamics in three dimensions. *Physical Review Fluids*, 5(12):123103, 2020.

[227] H. C. Berg and R. A. Anderson. Bacteria swim by rotating their flagellar filaments. *Nature*, 245(5425):380–382, 1973.

[228] C. Pozrikidis. Shear flow past slender elastic rods attached to a plane. *International Journal of Solids and Structures*, 48(1):137–143, 2011.

[229] S. Tottori, L. Zhang, F. Qiu, K. K. Krawczyk, A. Franco-Obregón, and B. J. Nelson. Magnetic helical micromachines: fabrication, controlled swimming, and cargo transport. *Advanced Materials*, 24(6):811–816, 2012.

[230] F. Meng, D. Matsunaga, and R. Golestanian. Clustering of magnetic swimmers in a poiseuille flow. *Physical Review Letters*, 120(18):188101, 2018.

[231] R. Yanagimachi. The movement of golden hamster spermatozoa before and after capacitation. *Reproduction*, 23(1):193–196, 1970.

[232] S. F. Schoeller, A. K. Townsend, T. A. Westwood, and E. E. Keaveny. Methods for suspensions of passive and active filaments. *Journal of Computational Physics*, page 109846, 2020.

[233] E. L. Bouzarth, A. T. Layton, and Y.-N. Young. Modeling a semi-flexible filament in cellular stokes flow using regularized Stokeslets. *International Journal for Numerical Methods in Biomedical Engineering*, 27(12):2021–2034, 2011.

[234] M. Jabbarzadeh and H. C. Fu. A numerical method for inextensible elastic filaments in viscous fluids. *Journal of Computational Physics*, 418:109643, 2020.

[235] S. S. Antman. *Nonlinear problems of elasticity*, volume 107 of *Applied Mathematical Sciences*. Springer-Verlag, New York, 2005.

[236] M. Nizette and A. Goriely. Towards a classification of Euler-Kirchhoff filaments. *Journal of Mathematical Physics*, 40(6):2830–2866, 1999.

[237] S. Lim. Dynamics of an open elastic rod with intrinsic curvature and twist in a viscous fluid. *Physics of Fluids*, 22(2):024104, 2010.

[238] J. Sznitman, X. Shen, R. Sznitman, and P. E. Arratia. Propulsive force measurements and flow behavior of undulatory swimmers at low Reynolds number. *Physics of Fluids*, 22(12): 121901, 2010.

[239] R. D. Schulman, M. Backholm, W. S. Ryu, and K. Dalnoki-Veress. Undulatory microswimming near solid boundaries. *Physics of Fluids*, 26(10), 2014.

[240] A. S. Utada, R. R. Bennett, J. C. N. Fong, M. L. Gibiansky, F. H. Yildiz, R. Golestanian, and G. C. L. Wong. Vibrio cholerae use pili and flagella synergistically to effect motility switching and conditional surface attachment. *Nature Communications*, 5(1):4913, 2014.

[241] M. Gazzola, L. H. Dudte, A. G. McCormick, and L. Mahadevan. Forward and inverse problems in the mechanics of soft filaments. *Royal Society Open Science*, 5(6):171628, 2018.

[242] N. Taketoshi, T. Omori, and T. Ishikawa. Elasto-hydrodynamic interaction of two swimming spermatozoa. *Physics of Fluids*, 32(10):101901, 2020.

[243] L. Giraldi and J.-B. Pomet. Local controllability of the two-link magneto-elastic micro-swimmer. *IEEE Transactions on Automatic Control*, 62(5):2512–2518, 2017.

[244] C. Moreau. Local controllability of a magnetized Purcell's swimmer. *IEEE Control Systems Letters*, 3(3):637–642, 2019.